# Identifying Exoplanets and Unmasking False Positives with NGTS
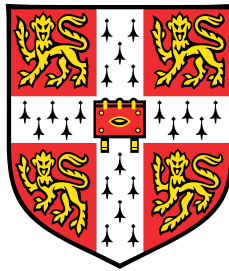
Maximilian Norbert Günther

Department of Physics

University of Cambridge

This dissertation is submitted for the degree of

Doctor of Philosophy

Girton College

July 2018

Für meine Familie,

für meine Freunde,

für das Unbekannte

und das Surreale.

Declaration

This dissertation is the result of my own work and includes nothing which is the outcome of work done in collaboration, except as declared below and specified in the text and acknowledgements. It is not substantially the same as any that I have submitted, or is being concurrently submitted for a degree or diploma or other qualification at the University of Cambridge or any other University or similar institution, except as declared below and specified in the text and acknowledgements. I further state that no substantial part of my dissertation has already been submitted, or, is being concurrently submitted for any such degree, diploma or other qualification at the University of Cambridge or any other University or similar institution, except as declared below and specified in the text and acknowledgements. This dissertation does not exceed the prescribed word limit for the Degree Committee of Physics and Chemistry. It contains fewer than 60,000 words including abstract, tables, footnotes and appendices, and has fewer than 150 figures.

Chapter 3 and parts of Chapter 1 were published as 'A New Yield Simulator for Transiting Planets and False Positives: Application to the Next Generation Transit Survey' in *Monthly Notices of the Royal Astronomical Society* (Günther et al., 2017a). This original work was performed by myself in correspondence with members of the NGTS consortium, unless where stated otherwise. It was published with Didier Queloz, Brice-Olivier Demory and Francois Bouchy.

Chapter 4 and parts of Chapter 1 were published as 'Centroid vetting of transiting planet candidates from the Next Generation Transit Survey' in *Monthly Notices of the Royal Astronomical Society* (Günther et al., 2017b). This original work was performed by myself in correspondence with members of the NGTS consortium, unless where stated otherwise.

It was published with Didier Queloz, Edward Gillen, James McCormac, Daniel Bayliss, Francois Bouchy, Simon. R. Walker, Richard G. West, Philipp Eigmüller, Alexis M. S. Smith, David J. Armstrong, Matthew Burleigh, Sarah L. Casewell, Alexander P. Chaushev, Michael R. Goad, Andrew Grange, James Jackman, James S. Jenkins, Tom Louden, Maximiliano Moyano, Don Pollacco, Katja Poppenhaeger, Heike Rauer, Liam Raynard, Andrew P. G. Thompson, Stéphane Udry, Christopher A. Watson and Peter J. Wheatley.

Chapter 5 and parts of Chapter 1 and Chapter 2 were published as 'Unmasking the hidden NGTS-3Ab: a hot Jupiter in an unresolved binary system' in *Monthly Notices of the Royal Astronomical Society* (Günther et al., 2018). This original work was performed by myself in correspondence with members of the NGTS consortium, unless where stated otherwise. Spectral analyses of the HARPS data were performed by Barry Smalley. Reduction of SPECULOOS data was performed by Laetitia Delrez, Michaël Gillon, and Artem Burdanov. The spectral energy distribution fit was performed by Edward Gillen. This work was submitted for publication with Didier Queloz, Edward Gillen, Laetitia Delrez, François Bouchy, James McCormac, Barry Smalley, Yaseen Almleaky, David J. Armstrong, Daniel Bayliss, Artem Burdanov, Matthew Burleigh, Juan Cabrera, Sarah L. Casewell, Benjamin F. Cooke, Szilárd Csizmadia, Elsa Ducrot, Philipp Eigmüller, Anders Erikson, Boris T. Gänsicke, Neale P. Gibson, Michaël Gillon, Michael R. Goad, Emmanuël Jehin, James S. Jenkins,, Tom Louden, Maximiliano Moyano, Catriona Murray, Don Pollacco, Katja Poppenhaeger, Heike Rauer, Liam Raynard, Alexis M. S. Smith, Sandrine Sohy, Samantha J. Thompson, Stéphane Udry, Christopher A. Watson, Richard G. West, and Peter J. Wheatley.

<div align="right">

Maximilian Norbert Günther

July 2018

</div>

Acknowledgements

Personal acknowledgements

First of all, I would like to thank my superivsor Didier Queloz, who has provided mentorship and guidance with grand future vision, while giving me freedom and space to explore new approaches and set my own path. Moreover, Didier's support has granted me remarkable experiences, from working on the NGTS telescope hardware in Paranal, Chile, to numerous international conferences, at which I could present my research and set my own mark. Didier, your mentorship has truly brought me to where I am today.

I would also like to thank Brice-Olivier Demory and Edward Gillen, who have been there supporting me at various stages in my PhD, and from whom I have learned more than I can ever remember. Thanks to Didier, Brice, Ed and the entire Cambridge exoplanets team, my PhD was always a pleasure and full of rewards for my work, and I do not remember a single day I was not motivated to thrive as a scientist.

Equally, many thanks to the NGTS consortium for all the fruitful discussion and collaborative projects over the past years. Working in this community was always a joyful and encouraging experience. In particular, I would like to thank Peter Wheatley, who has provided strong support for my academic growth and future career.

I further wish to express my gratitude to my former supervisors, teachers and mentors. With George Shubeita I embarked on a journey into the world of fruit flies and genetic diseases during my unforgettable time as a Master's student at the University of Texas. This work gave me the confidence in my scientific abilities that enabled my PhD in first place. Matthias Kadler not only supervised my work on Megamasers as a Bachelor's student at the

Julius-Maximilians-Universität Würzburg, but also sparked my interest in astrophysics and exploring the unknown.

I also send my thanks to my former high school and university teachers, particularly Thomas Carl and Winfred Bogdahn. While I do not dare to re-read my very first 'academic' work on prime numbers, receiving encouragement at a very young age has made me believe in myself, and motivated me to embark on this life journey.

Most importantly, I am grateful for my family and friends, who always supported me in my education, academic work, travels and personal life. Every interaction with you on this long journey has formed me and let me thrive further. I especially thank my partner, Jessica Santivañéz, for her support over the last three years in Cambridge, for sharing joyful times, and for fruitful discussions about our research. – *Von ganzem Herzen danke ich meiner Familie und meinen Freunden, die mich stets in meiner Bildung, meiner akademischen Arbeit, bei meinen Reisen und in meinem persönlichem Leben unterstützten. Jeder Austausch mit Euch auf diesem langen Weg hat mich geformt und weiter wachsen lassen. Besonders danke ich meiner Partnerin, Jessica Santivañéz, für Ihre Unterstütztung über die letzten drei Jahre in Cambridge, für die freudenreichen Zeiten und die hilfreichen Diskussionen über unsere Forschung.*

Scientific acknowledgements

(1974a,b) and Milne (1926). This research also makes use of IRAF. IRAF is distributed by the National Optical Astronomy Observatory, which is operated by the Association of Universities for Research in Astronomy, Inc., under cooperative agreement with the National Science Foundation. Throughout my PhD, I have been supported by the UK Science and Technology Facilities Council (STFC) award reference 1490409 as well as an Isaac Newton Studentship.

Abstract

In my PhD, I advanced the scientific exploration of the Next Generation Transit Survey (NGTS), a ground-based wide-field survey operating at ESO's Paranal Observatory in Chile since 2016. My original contribution to knowledge is the development of novel methods to 1) estimate NGTS' yield of planets and false positives; 2) disentangle planets from false positives; and 3) accurately characterise planets.

If an exoplanet passes (transits) in front of its host star, we can measure a periodic decrease in brightness. The study of transiting exoplanets gives insight into their size, formation, bulk composition and atmospheric properties. Transit surveys are limited by their ability to identify false positives, which can mimic planets and out-number them by a hundredfold.

First, I designed a novel yield simulator to optimise NGTS' observing strategy and identification of false positives (published in Günther et al., 2017a). This showed that NGTS' prime targets, Neptune- and Earth-sized signals, are frequently mimicked by blended eclipsing binaries, allowing me to quantify and prepare strategies for candidate vetting and follow-up.

Second, I developed a centroiding algorithm for NGTS, achieving a precision of 0.25 milli-pixel in a CCD image (published in Günther et al., 2017b). With this, one can measure a shift of light during an eclipse, readily identifying unresolved blended objects.

Third, I innovated a joint Bayesian fitting framework for photometry, centroids, and radial velocity cross-correlation function profiles. This allows to disentangle which object (target or blend) is causing the signal and to characterise the system. My method has already unmasked numerous false positives. Most importantly, I confirmed that a signal which was almost erroneously rejected, is in fact an exoplanet (published in Günther et al., 2018).

The presented achievements minimise the contamination with blended false positives in NGTS candidates by 80%, and show a new approach for unmasking hidden exoplanets. This research enhanced the success of NGTS, and can provide guidance for future missions.

Nomenclature

Telescopes/Instruments/Facilities

NGTS	Next Generation Transit Survey
SPECULOOS	Search for habitable Planets EClipsing ULtra-cOOl Stars
WASP	Wide Angle Search for Planets
MEarth	(transit survey)
HAT	Hungarian-made Automated Telescope
TESS	Transiting Exoplanet Survey Satellite
Kepler	(transit survey named after Johannes Kepler)
CoRoT	COnvection ROtation and planetary Transits
ESPRESSO	Echelle SPectrograph for Rocky Exoplanet- and Stable Spectroscopic Observations
HARPS	High Accuracy Radial velocity Planet Searcher
Coralie	(spectrograph)
Gaia	(all-sky survey)
2MASS	Two Micron All-Sky Survey
UCAC	United States Naval Observatory CCD Astrograph Catalog
APASS	American Association of Variable Star Observers Photometric All-Sky Survey
WISE	Wide-field Infrared Survey Explorer

Methodology (astrophysical)

RV	Radial Velocity
CCD	Charge Coupled Device
PSF	Point Spread Function
SED	Spectral Energy Distribution
TTV	Transit-Timing Variations

Methodology (statistical)

PDF	Probability Density Function
MCMC	Markov Chain Monte Carlo
GP	Gaussian Process
CCF	Cross-Correlation Function
FWHM	Full Width Half Maximum
RMSE	Root Mean Squared Error

Units

$R_{\odot}$	Nominal equatorial radius of the Sun, 6.957×10^8 m
$M_{\odot}$	Nominal mass of the Sun, 1.988×10^{30} kg
R_J	Nominal equatorial radius of Jupiter, 7.1492×10^7 m
M_J	Nominal mass of Jupiter, 1.898×10^{27} kg
$R_{\oplus}$	Nominal equatorial radius of the Earth, 6.3781×10^6 m
$M_{\oplus}$	Nominal mass of the Earth, 5.972×10^{24} kg

Table of contents

List of figures

List of tables

Chapter 1

Introduction

"If you thought that science was certain
- well, that is just an error on your part."

— Richard Feynman

1.1 History of exoplanet detection

Long before humans started to observe extra-solar planets ('exoplanets'), our ancestors were intrigued by the variety of planets in our own solar system. Mercury, Venus, Mars, Jupiter and Saturn - the five planets visible to the naked eye - were among the first celestial objects studied in history. They inherited their names as a tribute to Greek and Roman gods, and their classification from the old Greek word 'planetes' (the wanderers). The development of telescopes allowed a first breakthrough, leading to the discovery of Uranus (Herschel, 1781), Neptune (Le Verrier & Galle, 1846) and dwarf-planets like Ceres (Piazzi, 1801) and Pluto (Tombaugh, 1930). It took another hundred years until astronomical instruments reached the precision to explore worlds outside of our own solar system.

The first evidence for an exoplanet was found in 1988 in a binary star system by Campbell et al., yet not verified until 2003 by Hatzes et al.. In 1992, Wolszczan & Frail discovered two planetary-mass objects around the pulsar PSR 1257+12. A breakthrough happened in 1995 with the discovery of 51 Peg b by Mayor & Queloz. Admittedly, 51 Peg b was far from being

a second Earth; it was the first 'hot Jupiter'[1], a fiery gas giant orbiting its star in only four days. Yet, having found the first exoplanet orbiting a Sun-like star, the search for Earth-twins and signatures of extraterrestrial life came within reach. In the last 25 years we have seen an 'exoplanet gold rush' (Fig. 1.1), bringing us close to answering fundamental questions humans had for millenia: is there another Earth? How probable is extraterrestrial life? How special is our planet and solar system? How did our Earth form?

The exoplanet field has developed a variety of detection techniques over the years. While it all started with ground-based radial velocity (RV) surveys, which led to the 1995 discovery, techniques used nowadays additionally encompass direct imaging, microlensing observations, and especially transit surveys. In this thesis, I focus on transit detections with RV follow-up measurements, as both combined are needed to confirm and characterise a planet (see Sections 1.2 and 1.3).

The first transit event of a planet, HD 209458b, was detected in 2000 (Charbonneau et al., 2000; Henry et al., 2000), although the planet was already known from RV measurements beforehand. The first planet to be discovered by the transit method, OGLE-TR-56 b, followed two years later (Udalski et al., 2002). This feasibility demonstration then led to a paradigm shift in the field, with the transit technique becoming the most efficient exoplanet detection method. Dedicated wide-field transit surveys, both from the ground (e.g. HAT, Bakos et al. 2002 and WASP, Pollacco et al. 2006) and from space (e.g. CoRoT, Baglin et al. 2002 and *Kepler*, Borucki et al. 2010), have discovered 2900 of the 3700 currently known exoplanets[2]. This was especially supported by the launch of the *Kepler* spacecraft in 2009. *Kepler*'s detections account for the two spikes in detection rates seen in Fig. 1.1. However, these have to be taken with a grain of salt. As *Kepler*'s targets are usually faint, the two major candidate releases relied on a probabilistic evaluation rather than follow-up observations to verify these planets (see Section 1.6.2).

In 2016, the Next Generation Transit Survey started its hunt for new exoplanets from ESO's Paranal Observatory in Chile (Section 1.9). In the next years, the impact of the transit method will be furthered by the 'Transiting Exoplanet Survey Satellite' (TESS, Ricker et al.,

---

[1] a Jupiter-sized planet on a short orbit, usually $\lesssim 5$ days
[2] http://exoplanetarchive.ipac.caltech.edu/ (online 26 March 2018)
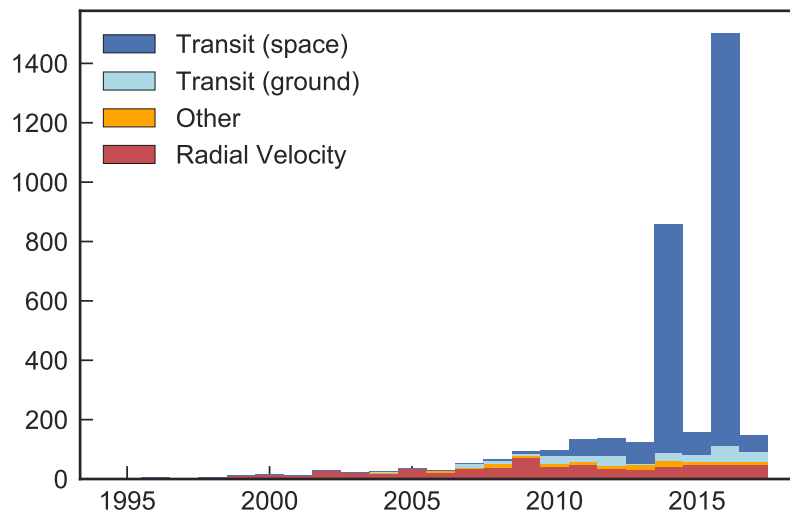
Fig. 1.1 The exoplanet gold-rush, highlighted as the number of exoplanets found per year. Data from Exoplanetarchive (http://exoplanetarchive.ipac.caltech.edu/, online 30 Jan 2018).

2014) in 2018 and the 'PLAnetary Transits and Oscillations of stars' mission (PLATO, Rauer et al., 2014) in 2026, both predicted to find tens of thousands of exoplanets. Missions like CHEOPS (Broeg et al., 2013) and JWST (Gardner et al., 2006) will provide high-precision transit follow-up of the most interesting candidates.

Over the past years, we have found a variety of planets with similar sizes and masses to Earth, such as the first terrestrial candidate, CoRoT-7b (Léger et al., 2009; Queloz et al., 2009), and the first confirmed terrestrial exoplanet, Kepler 10b (Batalha et al., 2011). We have found planets in binary systems (e.g. Kepler 16b, Doyle et al., 2011) and planets in the habitable zones of their host stars (e.g. Kepler-186f, Quintana et al., 2014). The TRAPPIST-1 system harbours seven Earth-sized planets in short orbits around their host star - an ultra-cool dwarf star barely larger than Jupiter (Gillon et al., 2017). In special cases, we can study exoplanets' atmospheres (Kaltenegger & Traub, 2009), and can even predict their weather (see e.g. Burrows, 2014; Crossfield et al., 2014). The discoveries of the first exoplanets led us to rethink our theories about planet formation and accelerated research on planet migration (e.g. Chambers, 2007; Lin et al., 1996, see Section 1.4).

The fast-growing field of exoplanets unites multi-disciplinary efforts, combining astronomy, physics, chemistry, geology, biology and computer science. Its objects of interest range from nanometre-sized molecules in planet atmospheres to gas giant planets as large as small stars. We are getting closer to finding a handle on planets' habitability, and even the first programmes sending space craft to the nearest exoplanets are being considered[3]. What counted as science fiction just a generation ago, can these days be detected and studied.

1.2 Transiting exoplanets

The transit method is a powerful tool for the detection and study of exoplanets. Through it, one can indirectly find exoplanets when they eclipse their star and periodically block out a fraction of the stellar light (see Fig. 1.2). Transit observations are not only efficient in detecting exoplanets, but also key in determining a wide range of their physical characteristics. The measured transit depth depends on the ratio of planet radius to stellar radius (see Section 1.2.1). Hence, if the stellar radius is well constrained, the planet's size can be measured. By combining information on the planet's size and RV measurements of its mass, one can estimate the planet's bulk density. This allows to constrain the planet's bulk composition (see e.g. Seager et al., 2007). Using this approach, the first transit detections could prove that known Jupiter-mass objects are indeed gas giant planets (e.g. Charbonneau et al., 2000; Henry et al., 2000). Even if the stellar radius is unknown, the surface gravity of the exoplanet can be extracted by combining transits and RVs (see Section 1.3.1).

Transmission spectroscopy of a transiting planet allows to determine its atmospheric properties. This was theoretically predicted by Seager & Sasselov (2000) and for the first time observationally achieved by Charbonneau et al. (2002). Thereby the transit depth is measured in multiple narrow bandpasses, such that different absorption by molecules in the planet's atmosphere can be detected, one of the most significant ones being water features. Hence, transmission spectroscopy has been proposed as a means to find evidence for biomarkers and traces of life in the atmospheres of Earth-like exoplanets in the future (see e.g. Seager

---

[3]https://breakthroughinitiatives.org/initiative/3, online 26 March 2018

et al., 2016). However, many of the so far measured transmission spectra have shown to be featureless. Recently, Sing et al. (2016) conducted a study of the atmospheres of ten hot Jupiters, producing the largest sample of this kind to date. Their results suggest that the absence of molecular absorption lines is caused by clouds and hazes in the planet atmosphere. In a follow-up study of WASP-39b with the Hubble Space Telescope, the team was able to obtain the most complete spectrum to date, providing evidence for strong water features (Wakeford et al., 2018). Using an atmospheric model, this allowed them to constrain the planet's effective temperature and atmospheric metallicity to unprecedented precision.

In addition, transmission spectroscopy has been proposed as a means to constrain the mass of the exoplanet (de Wit & Seager, 2013). The mass of a planet has an impact on its atmosphere. In theory, the planet mass can hence be derived from the planet's radius and its atmospheric temperature, mean molecular mass and scale height. Yet, estimating these values relies on various assumptions. The method is suggested to be readily applicable to Hot Jupiters. However, mass measurements for smaller planets require up to 200 h of in-transit observation with large space-based instruments like the upcoming James Webb Space Telescope (JWST), which might be too costly in observing time.

Moreover, transit events can give insight into the fate and disintegration of extra-solar systems. For example, Vanderburg et al. (2015) reported a disintegrating planet orbiting a white dwarf star. The tail of material behind the planet leaves a significant feature in the measured transit signal. Furthermore, planetary evaporation was detected by studying transits in the ultraviolet (see e.g. Ehrenreich et al., 2015; Vidal-Madjar et al., 2003). The authors suggest that this could mean that Neptune-like planets might lose their atmosphere over time, transforming into small, rocky planets.

A precise analysis of the timing between transits can reveal hidden non-transiting objects in multi-planet systems (see e.g. Agol & Fabrycky, 2017). As planets gravitationally influence each others' orbits, each transit will occur at a slightly off-set time. Using 'transit timing variations' (TTVs) for the discovery of non-transiting exoplanets was proposed, for example, by Holman & Murray (2005) and Agol et al. (2005). The method can further be used to determine the masses of the other planets in the same system. The first discovery of a

non-transiting exoplanet through TTVs was reported by Ballard et al. (2011). TTVs of the transiting planet *Kepler* 19b gave evidence for the non-transiting 2.2 $M_\oplus$ planet *Kepler* 19c. To date, 15 planets have been detected this way[4]. TTVs are usually on the order of seconds to minutes for multi-planet systems. In binary star systems, planetary TTVs can be on the order of hours to days, due to the strong orbital disturbance by the stars (see Section 1.5).

Planets also reflect their host stars' light depending on their orbital position (see Section 1.2.3). Studies of a planet passing behind its star ('occultation') and changing brightness on its orbit ('phase curve') allow to compute the planet's reflectivity and equilibrium temperature (see e.g. Parmentier & Crossfield, 2017). The first detections of infra-red thermal emission from an exoplanet were independently achieved for TrES-1b by Charbonneau et al. (2005) and for HD209458b by Deming et al. (2005).

1.2.1 Transit depth and shape

Transit observations make use of photometry, measuring the flux received from an object over broad wavelength bands. The measured time series of flux is referred to as the 'light curve' of the object (see Fig. 1.2). This Section describes the properties one can extract from light curves and exoplanet transit events.

Transit depth

The measured transit depth δ_{tr} (see Fig. 1.2) gives direct insight into the planet radius R_{p}, given the stellar radius $R_\star$ is known:

$$\delta_{\mathrm{tr}} \approx \left(\frac{R_{\mathrm{p}}}{R_\star}\right)^2 \tag{1.1}$$

(see e.g. Winn, 2011). The transit signal, and hence chance of detection, increases with larger planets or smaller stars. A typical hot Jupiter around a Sun-like star would cause a transit signal of $\delta_{\mathrm{tr}} \approx \left(1R_{\mathrm{jup}}/1R_\odot\right)^2 \approx 1\,\%$. With nowadays photometric precision, the detection of hot Jupiters is routinely feasible even from the ground. Likewise, a transiting Neptune

---

[4]http://exoplanetarchive.ipac.caltech.edu/ (online 26 March 2018)

$$bR_\star \sim a\cos i$$

$$\delta_{tr}$$
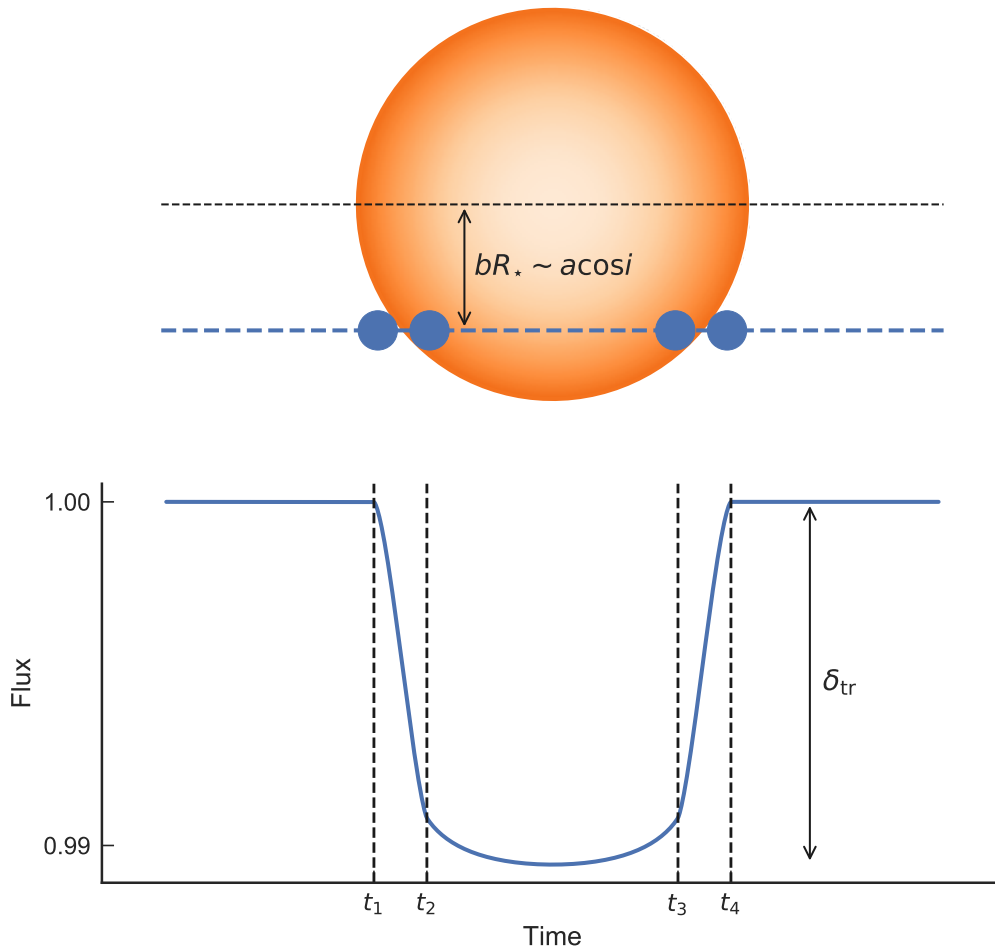
Fig. 1.2 Transit technique: whenever the exoplanet transits the star, it blocks out a fraction of the stellar flux. This example shows a hot Jupiter orbiting a Sun-like star. The shown parameters of the transit are the transit depth δ_{tr}, contact times t_1 to t_4, the impact parameter b, the stellar radius $R_\star$, the orbital semi-major axis a and the orbital inclination i.

would cause a signal of ≈ 0.1 %, and a transiting Earth would be detected at ≈ 0.01 % around a Sun-like star. This pushes the sensitivity limits of ground-based facilities, requiring space-based photometric precision.

Alternatively, one can move to smaller stars. Table 1.1 compares the transit signals around different star types. While previous ground-based surveys were limited to a precision

of $\gtrapprox$ 3 mmag, the NGTS mission pushes down into the Neptune-sized regime for Sun-like stars with a precision of 1 mmag[5]. This relation is one of the motivations for recent missions like MEarth (Nutzman & Charbonneau, 2008) and SPECULOOS (Gillon et al., in prep.) to shift to bandpasses that are more sensitive to redder wavelengths, where the emission of smaller (colder) stars peaks.

Planet / Star	G5V	K5V	M0V	M9V
Earth	0.01% ●	0.02% ●	0.03% ●	0.9% ●●
Neptune	0.1% ●●	0.3% ●●	0.4% ●●	14% ●●
Jupiter	1% ●●	2% ●●	3% ●●	100% ●●

Table 1.1 Focusing on smaller host stars leads to a gain in detectability of exoplanets. Light-blue circles indicate detectability with current ground-based surveys, foremost enabled by NGTS' 1 mmag precision. Dark blue circles indicate detectability from space.

Note that gas giant planets around M-dwarf stars are predicted to be rare by current theories of planet formation (see e.g. Laughlin et al., 2004). However, recent discoveries such as NGTS-1b (Bayliss et al., 2018, see Section 1.9.6), a $1.33^{+0.61}_{-0.33}$ R_{Jup} sized planet orbiting an M-dwarf star, have shown that these objects exist, and might be more common than previously thought (see Section 1.8 for further discussion).

Limb darkening

The relation in Eq. 1.1 is not strictly true, as it assumes the stellar light to be homogeneously emitted across the entire stellar disk. This would lead to a generally flat bottomed transit event, which is not the case in reality. The effect causing this deviation is known as 'limb darkening'. The stellar disk appears brightest at its centre, and becomes fainter and redder towards its limb (illustrated in Figs. 1.2, 1.3 and 1.4). The impact of limb darkening is strongest for blue wavelengths, and can lead to differences in the transit depth of several milli-mag.

Photons form at a certain depth in the stellar photosphere. This leads to two factors determining the limb darkening. First, until the photons can be observed, they have to travel a certain path length L through the stellar atmosphere (Fig. 1.3), along which they can be

---

[5]a photometric precision of 1 mmag is generally used synonymously to represent 0.1 % in relative flux
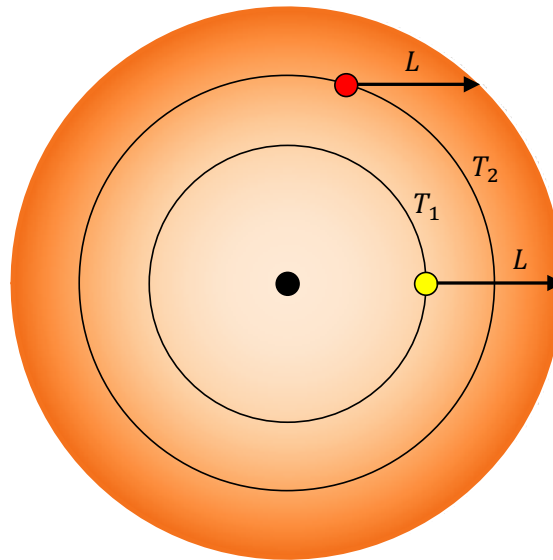
Fig. 1.3 Limb darkening describes the effect that a stellar disk appears brightest at its centre, and fainter and redder towards its limb. Here, L denotes the path length travelled by a photon before escaping the star. The maximum path length is given by the optical depth, which is defined as $1/e$ of all photons being transmitted. $T_1 > T_2$ indicate two layers of the radial temperature profile of the star. Photons observed at the centre are transmitted radially outwards, and can hence originate from deeper and hotter (T_1) layers. At the limb, photons have to escape at an angle, thus only photons forming in outer and cooler (T_2) layers can be transmitted.

absorbed or scattered. The amount of light that can be transmitted is defined by the optical depth. One optical depth corresponds to a fraction of $1/e$ of all photons being transmitted.

Second, the radial temperature profile of the star is such that it is hottest in the centre, and gets cooler with increasing distance from the centre (Fig. 1.3). At two distances $R_1 < R_2$ from the centre, the temperatures are $T_1 > T_2$. The region at R_2 (with cooler temperature T_2) is hence less emissive than at R_1 (with hotter temperature T_1).

At the centre of the stellar disk, photons are transmitted radially outwards, such that an observer can see photons from a deeper (hotter) layer of the stellar photosphere. At the limb, only the photons forming in the outer (cooler) part of the photosphere, can escape the star. The limb hence appears darker and redder.

There is an exception to this phenomena, namely if the radial temperature profile of the star is not monotonically decreasing towards the outer layers. The layers at which the

temperature increases with radius will be more emissive than the deeper layers. As the optical depth is a function of wavelength, different spectral lines probe different depths in the stellar atmosphere. For certain spectral lines, one can thus observe the effect of 'limb brightening'.

Throughout literature, the effect has been modelled in dependency of the normalised radius $r \in [0,1]$ with the functions given in Tab. 1.2. Limb darkening further depends on the stellar type and instrument bandpass (see e.g. Sing, 2010). Hence, the parameters $c_1 - c_4$ are usually fixed to tabulated values or fitted. The exoplanet community commonly uses the model by Mandel & Agol (2002), who quantified the quadratic and nonlinear limb darkening laws in a set of equations to analytically calculate transit light curves.

uniform	$I(r) = I_0$	
linear	$I(r) = I_0 \left[1 - c_1(1-r) \right]$	(Schwarzschild & Villiger, 1906)
quadratic	$I(r) = I_0 \left[1 - c_1(1-r) - c_2(1-r)^2 \right]$	(Kopal, 1950)
logarithmic	$I(r) = I_0 \left[1 - c_1(1-r) - c_2 r \ln r \right]$	(Klinglesmith & Sobieski, 1970)
square-root	$I(r) = I_0 \left[1 - c1(1-r) - c2(1 - \sqrt{r}) \right]$	(Diaz-Cordoves & Gimenez, 1992)
nonlinear	$I(r) = I_0 [1 - c_1(1 - r^{1/2}) - c_2(1-r)$ $- c_3(1 - r^{3/2}) - c_4(1 - r^2)]$	(Claret, 2000)
exponential	$I(r) = I_0 \left[1 - c_1(1-r) - c_2/(1 - e^r) \right]$	(Claret & Hauschildt, 2003)

Table 1.2 Limb darkening models.

Transit alignment

The transit alignment is described by the impact parameter b (see e.g. Winn, 2011, Figs. 1.2 and 1.4). It is defined as the projected distance between the centre of the planet and the centre of the star at mid-transit, given by

$$ b = \frac{a \cos i}{R_*} \left(\frac{1 - e^2}{1 + e \sin \omega} \right). \tag{1.2} $$

The orbital parameters are its semi-major axis a, eccentricity e, argument of periastron ω, and inclination i towards the observer.

The inclination i has a strong impact on the shape of the transit. It is defined at $90°$ for a transit through the midline of the stellar disc. Fig. 1.4 demonstrates how decreasing i leads
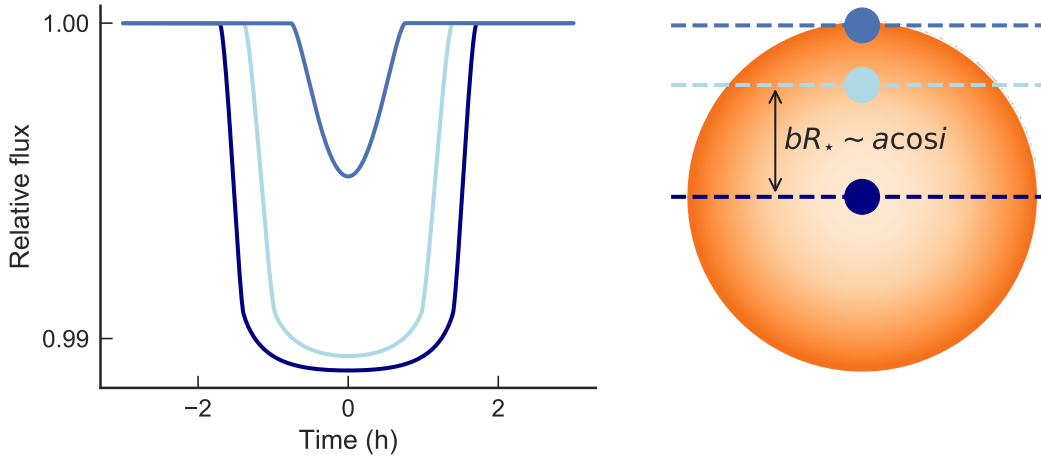
Fig. 1.4 The duration, depth and shape of the transit event depend on the transit geometry, represented by the orbital inclination i and impact parameter b. This example shows a hot Jupiter in a 5 day orbit around a Sun-like star.

to a shorter and shallower transit. Even if the planet is fully transiting ($b < 1 - R_p/R_\star$), the transit depth decreases for $i < 90°$ due the limb darkening effect (see above). The case of a grazing eclipse is commonly refereed to as a 'V-shaped' transit.

Transit duration

A non-grazing eclipse can be characterized as ingress, in-transit, and egress. These are set by the contact times t_1 to t_4, at which the planetary and stellar disk are tangent (Fig. 1.2). The duration of the transit can be quantified from the contact times as the total duration $T_{tot} = t_4 - t_1$ and the full duration $T_{full} = t_3 - t_2$:

$$T_{tot} = t_4 - t_1 = \frac{P}{\pi} \arcsin \left(\frac{R_\star}{a} \frac{\sqrt{(1+R_p/R_\star)^2 - b^2}}{\sin i} \right), \tag{1.3}$$

$$T_{full} = t_3 - t_2 = \frac{P}{\pi} \arcsin \left(\frac{R_\star}{a} \frac{\sqrt{(1-R_p/R_\star)^2 - b^2}}{\sin i} \right) \tag{1.4}$$

(see e.g. Winn, 2011).

Likewise, one can express the ingress duration $\tau_{in} = t_2 - t_1$ and egress duration $\tau_{eg} = t_4 - t_3$. These are equal for circular orbits and negligibly different for eccentric orbits, such that one commonly uses $\tau = \tau_{in} = \tau_{eg}$.

For non-grazing transits and circular orbits, one can define a characteristic transit time scale T_0 as

$$T_0 = R_* \cdot M_\star^{-1/3} \cdot P^{1/3} \cdot \left(\frac{4}{G\pi}\right)^{1/3}, \tag{1.5}$$

with the stellar radius $R_\star$, stellar mass $M_\star$, and orbital period P, and gravitational constant G. The interval between halfway points of ingress and egress $T = T_{tot} - \tau$, as well as the in/egress time τ, can be approximated as

$$T \approx T_0 \sqrt{1 - b^2}, \tag{1.6}$$

$$\tau \approx \frac{T_0}{\sqrt{1 - b^2}} \frac{R_p}{R_\star}. \tag{1.7}$$

The transit duration is hence a measure of the stellar density and the transit alignment.

1.2.2 Geometric transit probability

The geometric probability of an exoplanet to be transiting can be derived from the condition $a\cos i \leq R_\star + R_p$, which has to be fulfilled (see e.g. Winn, 2011). Here, $\cos i$ represents the sky-projection of the normal vector of the orbital plane and its prior likelihood is uniform between 0 and 1. The geometric transit probability P_{geom} is given as the fraction of transiting orbits over all orbits. It can be calculated by integrating over all possible $\cos i$ and ω, leading to:

$$P_{geom.} = \frac{R_\star + R_p}{a} \left(\frac{1}{1 - e^2}\right). \tag{1.8}$$

Consequentially, close-in planets are more likely to be transiting. Larger stars also result in a higher transit probability, but lead to shallower transit depth (Section 1.2.1). Larger planet

sizes also increase the transit probability, which is negligible for large stars ($R_\star \gg R_p$), but can be a factor for gas giant planets around small stars ($R_\star \approx R_p$).

For example, the typical transit probability of a hot Jupiter on a 4 day orbit around a Sun-like star is $P_{geom.} \approx 10\ \%$. In contrast, the transit probability of an Earth-twin around a Sun-like star in a 1 AU orbit is $P_{geom.} \approx 0.5\ \%$. This means Earth-twins are unlikely to transit - and if they transit, their signals are shallow and difficult to detect (see Section 1.2.1). This emphasises the advantage of targeting colder host stars, which allow the potential 'habitable zone' to fall closer to the star (see e.g. Gillon et al., 2017). Even though their radius is smaller, the transit probability increases due to the shorter orbit. For comparison, an Earth-twin around an M5V star in a 1 week orbit has a transit probability of $P_{geom.} \approx 2.4\ \%$.

1.2.3   Phase curves and occultation

The brightness of the planet is a function of its orbital position relative to the observer, referred to as the 'phase curve'. It is composed of the light emitted from the planet itself and the reflection of stellar light from the planet's day side. The occultation of the planet by the star can theoretically be measured as the occultation depth δ_{occ}:

$$\delta_{occ} = \left(\frac{R_p}{R_\star}\right)^2 \frac{I_{p(t)}}{I_\star} \tag{1.9}$$

(see e.g. Winn, 2011). Here, $I_{p(t)}$ and $I_\star$ are the brightness of the planet and the star.

The planet's day side receives radiation power P_{in} from the star. The fraction A of this incident light gets reflected. The remaining power $(1 - A)P_{in}$ is absorbed by the planet. This parameter A is referred to as the albedo of the planet. In equilibrium, the absorbed power gets re-emitted from the planet as black-body radiation, $P_{out} = (1 - A)P_{in}$, leading to the definition of an equilibrium temperature:

$$T_{eq} = \frac{1}{2}\left(\frac{(1 - A)L_\star}{\sigma \pi a^2}\right)^{1/4}. \tag{1.10}$$

(see e.g. Winn, 2011). Here, $L_\star$ is the star's luminosity, σ is the Stefan-Boltzmann constant and a is the orbital semimajor axis.

1.3 Radial velocity

Radial velocity (RV) detections are historically the origin of the exoplanet field. They led to the first discovery of a planet around a main sequence star, 51 Peg b (Mayor & Queloz, 1995). When the planet orbits its host, the star also performs an orbital motion but on a significantly smaller scale depending on the mass ratio of the two bodies. In general, the planet causes the star to 'wobble' in its position, leading to a Doppler shift of the star's spectral lines. By measuring this Doppler shift as a function of time, the RV technique allows indirect detection of exoplanets (see e.g. Lovis & Fischer, 2011). Due to the nature of this method, however, it is biased towards heavy, close-in planets, such as hot Jupiters (see Section 1.8.1).

In this thesis, I will discuss RV measurements from the point of view of follow-up observations. Transit surveys allow an efficient all-sky screening, and determination of planet radii relative to their host star. If the host star is bright enough, the planet mass is accessible through RV monitoring. Together, the two approaches allow the planet density and bulk composition to be determined (see Section 1.2).

In a two-body system, the equation for the RV semi-amplitude $K_{A,B}$ of the primary A and secondary/planet B follows from the binary mass function. In the most general formulation, applicable to planets orbiting stars as well as eclipsing binaries, it is given as:

$$K_{A,B} = \frac{M_{B,A} \sin i}{(M_A + M_B)^{2/3}} \frac{(2\pi G)^{1/3}}{P^{1/3}\sqrt{1-e^2}} \tag{1.11}$$

(see e.g. Hilditch, 2001). Here, $K_{A,B}$ and $M_{A,B}$ are the semi-amplitudes and masses of the primary and secondary/planet, respectively. P is the orbital period and G is the gravitational constant. The equation further depends on the inclination i and eccentricity e of the orbit, which are in general unknown and difficult to measure exactly. Hence, RV measurements generally only yield $M_{B,A} \cdot \sin i$, a lower limit for the mass of the secondary/planet or primary.

To characterise the secondary/planet by studying its density and composition, it is necessary to constrain i and gather information about its size. Both can be achieved using the transit technique.

Applying Kepler's Third Law, the RV semi-amplitude can also be expressed as:

$$K_{A,B} = \frac{2\pi a_{A,B}}{P\sqrt{1-e^2}}.$$
(1.12)

For a planetary system the primary and secondary masses from Eq. 1.11 are usually expressed as the stellar mass $M_\star$ and planetary mass M_p. As the planet does not radiate, it does not produce any visible emission lines. Assuming $M_p << M_\star$, an upper limit on the planet mass can directly be derived from Eq. 1.11 and the measurement of the semi-amplitude $K = K_\star$ of the host star:

$$M_p \sin i \approx K\, M_\star^{2/3}\, P^{1/3}\, \sqrt{1-e^2}\, (2\pi G)^{-1/3}.$$
(1.13)

The measured RV as a function of time depends on the orbit of the system (Fig. 1.5). It is parametrised by the eccentricity e, inclination i, argument of periastron ω, and true anomaly $\Theta(t)$:

$$\mathrm{RV} = K\left[\cos(\Theta+\omega) + e\cos\omega\right] + \gamma.$$
(1.14)

Here, γ is the systemic velocity of the system. The true anomaly $\Theta(t)$ can be derived from the eccentric anomaly $E(t)$ through

$$\tan\left(\frac{\Theta(t)}{2}\right) = \sqrt{\frac{1+e}{1-e}}\tan\left(\frac{E}{2}\right).$$
(1.15)

The eccentric anomaly in turn is given by Kepler's equation:

$$E - e\sin E = 2\pi(t-T)/P = M,$$
(1.16)

in which M is defined as the mean anomaly and T is the time of periastron passage. To compute the RV curve for eccentric orbits, Kepler's equation has to be solved numerically. Fig. 1.6 compares the RV curves for one circular and two eccentric orbits.
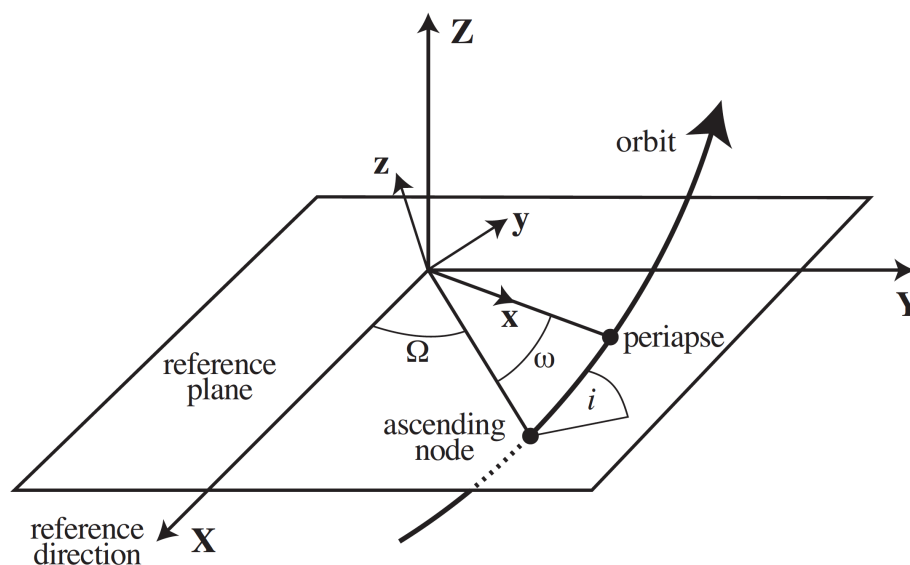
Fig. 1.5 Orbital parameters, showing the inclination i, argument of periastron ω and longitude of ascending node Θ. Figure from C. D. Murray (2011).

1.3.1   Radial velocity observations of transiting exoplanets

A transit signal gives only the ratio of planet to stellar radius, $(R_p/R_s)^2$ (see Section 1.2.1). If the stellar radius is known (for example through stellar models and precise *Gaia* (Gaia Collaboration et al., 2016a) parallax measurements), one can directly derive the exoplanet's radius. The transit observation also constrains the inclination of the system. By additionally gathering RV observations, the mass of the exoplanet can be further constrained. Combining both radius and mass measurements, allows a direct insight into the bulk density of the planet (see e.g. Seager et al., 2007).

Without constrains on the stellar radius, however, the planet's bulk density remains unknown. Yet, one can always retrieve the surface gravity g_p of the planet by combining
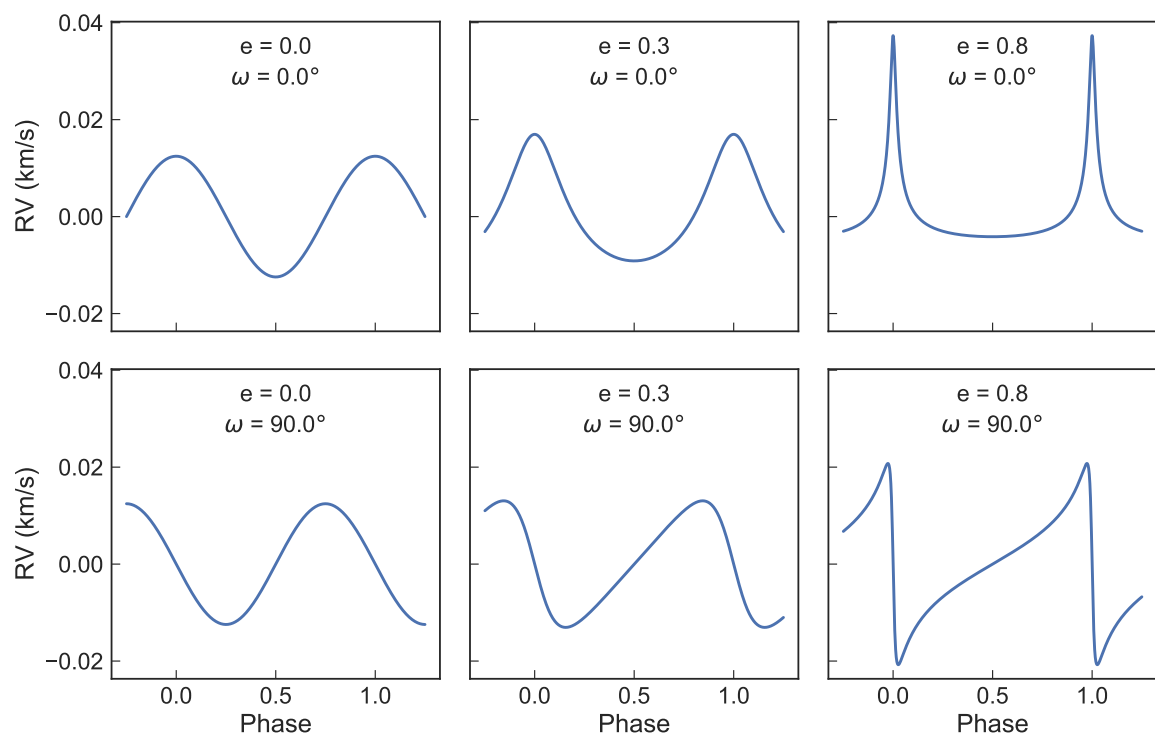
Fig. 1.6 Examples of a Jupiter-mass planet orbiting at 5 AU around a Sun-like star for different orbital parameters.

transit and RV measurements via:

$$g_{\rm p} = \frac{2\pi}{P} \frac{(1-e^2)^{1/2} K_\star}{r_{\rm p}^2 \sin i}$$

(1.17)

(Southworth et al., 2007). This only depends on five observables: period P, RV semi-amplitude of the star $K_\star$, eccentricity e, inclination i and the ratio of planet radius to orbital semi-major axis $r_{\rm p} = R_{\rm p}/a$.

1.4 The origin of exo-solar systems

After discussing the detection of exoplanet systems in the previous Sections, I here go one step back to discuss how such extra-solar systems are formed in the first place. Notably, this research fields dates back almost 300 years, as the first theories about the formation of our own solar system were developed by Emanuel Swedenborg, Pierre-Simon Laplace and others. This Section introduces the basic concepts behind proto-planetary discs, planet formation and planet migration. For a comprehensive overview see e.g. the books by Perryman (2011) and Pessah & Gressel (2017). A review paper on planet formation is provided by Kley & Nelson (2012), yet this field is progressing rapidly and constantly developing new concepts, such as for example pebble accretion mechanisms (see Section 1.4.2). The most up-to-date review of the field is provided in the lecture notes of Armitage (2017). For a review of the current research frontier and challenges, the reader is referred to e.g. Morbidelli & Raymond (2016).

1.4.1 Star formation and the proto-planetary disk

The birth of a planet is preceded by the birth of its host star. Taking our own solar system as an example, 4.6 billion years ago, our Sun and planets did not exist yet. All there was at this time, was an interstellar cloud of molecular gas and dust, known as a solar nebula, carrying all the material to later build our solar system (step 1 in Fig. 1.7; see e.g. Perryman 2011). Any new star is born out of varying densities within this cloud, such that the over-dense

regions start gravitationally accreting more material. This is given if the sum of gravitational energy E_g (negative) and kinetic energy E_k (positive) is $E_g + E_k < 0$. Clumps start forming in the cloud (step 2). This leads to a cataclysmic process, in which dense cores form via gravitational collapse. This process forms proto-stars, the precursors of stars, from within these clumps (step 3). Under the pressure of the dense material, nuclear fusion is triggered and the cores condense into young stars (step 4). Remnants of this gravitational collapse keep orbiting the young star, forming a proto-planetary disk of gas and dust. In the final step, the planet formation step, planets form from the material in the proto-planetary disk (step 5). A new solar system is born.

Fig. 1.8 shows the first direct observation of what is thought to be planets forming in a protoplanetary disk (ALMA Partnership et al., 2015). In 2015, the Atacama Large Millimeter/submillimeter Array (ALMA) observatory captured this image of the young star HL Tau, surrounded by its proto-planetary disk. Various orbital regions seem to be cut out. These gaps suggest to have formed due to orbiting planetesimals accreting gas and dust from the disk.

1.4.2 Planet formation

There are two leading theories for planet formation, explaining fundamentally different origins (see e.g. Perryman, 2011). On the one hand, the 'gas collapse' theory describes the formation of some gas giant planets and brown dwarfs, in a similar fashion to the formation of stars. On the other hand, the 'core accretion' theory explains the formation of rocky and gas planets by continuous growth of the body. The overlap of those two scenarios suggests that giant planets and brown dwarfs might either represent the low-mass tail of gas collapse, or the heavy-mass tail of core accretion.

Gas collapse

The gas collapse theory states that some giant gas planets could form following the same physical principles as stars (see e.g. Perryman, 2011). Similar to before in the proto-stellar
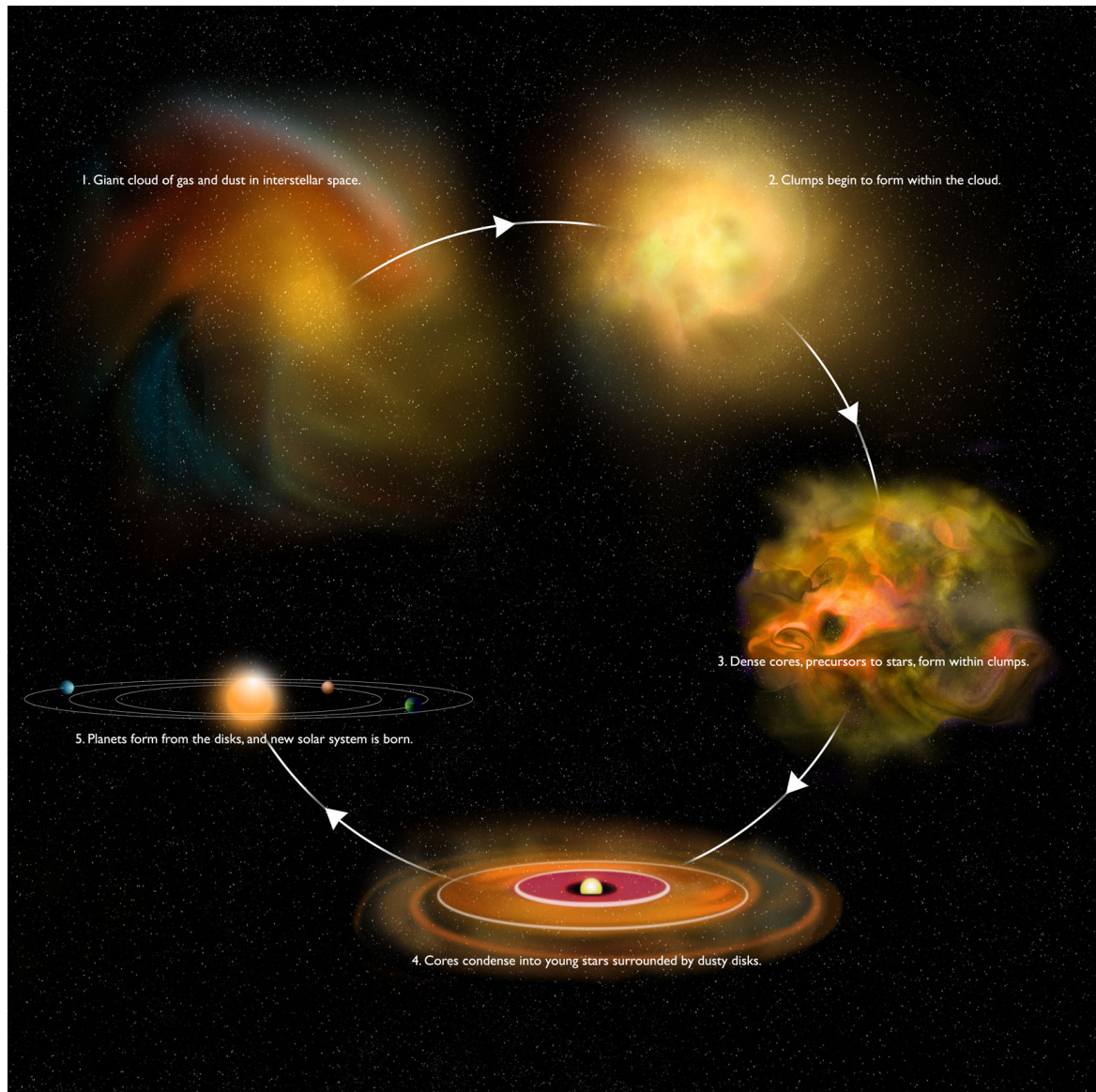
Fig. 1.7 Birth of a solar system. Credit: Bill Saxton, NRAO/AUI/NSF.
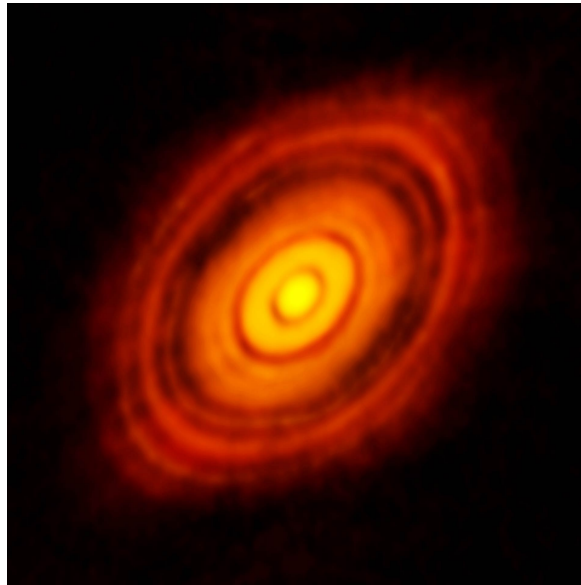
Fig. 1.8 ALMA observation the proto-planetary disk around the young star HL Tau. Orbital gaps are suggested to be formed by the formation of planetesimals. Credit: ALMA (NRAO/ESO/NAOJ); C. Brogan, B. Saxton (NRAO/AUI/NSF).

disk, there are over-dense regions being formed in the proto-planetary disk. These form clumps of gas and dust, which then gravitationally collapse into giant gas planets.

The potential gas collapse formation of gas giant planets shows that the formation mechanism is unsuitable when distinguishing a planet from a brown dwarf or small star. In this model, the only difference between stars and gas giant planets is their ability to sustain nuclear fusion. In a gas giant planet, the gravitational pull towards its centre is balanced solely by the electron degeneracy pressure. This is described by Pauli's exclusion principle, which states that two identical fermions (e.g. electrons) cannot occupy the same quantum state. Adding more mass to a gas giant planet (or brown dwarf) would hence increase its gravitational energy and further decrease its radius. The resulting increase in pressure would increase the temperature in the centre. In the case of a star, the object is so massive, that the temperature in the centre is high enough to trigger hydrogen fusion. The gravitational pull is balanced by the pressure resulting from the thermonuclear fusion. This gives an interesting insight onto the transition region between gas giant planets to brown dwarfs (which burn deuterium) to stars (which burn hydrogen).

The snow line

The planets in our own solar system seem to follow a certain pattern. The four small rocky planets (Mercury, Venus, Earth, Mars) are closest to the Sun, while the four large gas planets (Jupiter, Saturn, Uranus, Neptune) are further out. This naturally influenced early studies of planet formation long before the discovery of the first exoplanet systems. The dividing line between Mars and Jupiter was found to be motivated by the 'snow line', the distance to the Sun at which it is cold enough to form water ice (see e.g. Perryman, 2011).

This condensation temperature does not lie at 273 K like on Earth, but is corresponding to the partial pressure in the disk. Using a solar nebula model for our solar system, the partial pressure in the disk mid-plane is circa 10^{-4} bar at distances of a few AU. At this pressure, the condensation temperature for water is circa 170 K. This temperature is reached at a distance of circa 3 AU from the Sun. This distance marks the snow line, at which water condensation occurs in the disk. Likewise, the distance for the condensation of other volatiles (e.g. ammonia or carbon dioxide) can be computed and varies depending on the volatiles' properties. The snow line is an important principle for the leading formation theory of rocky bodies, the core accretion mechanism described below.

Core accretion

A probable explanation for the formation of the planets in our solar system, as well as most exoplanets, is core accretion (see e.g. Chambers, 2011; Perryman, 2011). In this process, water ice and dust clump together. This forms micrometer-sized pebbles which progressively grow on to meter-sized and kilometer-sized objects (planetesimals), finally forming planet cores. When a critical mass is reached, these planet cores gravitationally accrete surrounding gas into their atmosphere. The locally available gas in the proto-planetary disk dictates which planet will form. This depends on the planet formation time scale and location in the disk. Planet cores which formed beyond the snow line and are massive enough can accrete large gas envelopes, developing into gas giant planets. Other planet cores can only grow further by collisions with smaller bodies, eventually forming rocky planets. In the end, material in the disk will be either accreted or dissipate into space, leaving a new extra-solar system.

The growth from grains to planetesimals, is still under intense study. A possible explanation is that small particles are electrostatically attracted to each other by the van der Waals force. As they form grains and grow more massive, gravitational forces take over. Laboratory experiments have shown that for micrometer-sized grains low collision speeds can lead to a growth, but at speeds > 10 m/s the particles will fragment (see e.g. Beitz et al., 2011). When grown to centimetre-sized particles, this changes, and a minimum collision speed of 10 m/s is required, while too high speeds (>> 10 m/s) still result in disintegration. Once grown into meter-sized objects, however, the collision speeds in the gas disk are usually much higher, leading to fragmentation. This so-called 'meter-sized barrier' is still an unresolved problem.

The next step, the growth from kilometer-sized objects to planet cores, can be explained by gravitational accretion. Finally, the accretion of a gas envelope depends on the interplay of the gravitational pull exerted by the planet and the thermal escape velocity of its atmosphere. The pressure gradient in the atmosphere counteracts the contraction of the gas envelope. When the gravitational force exceeds it, it comes to a runaway effect in accretion. Tidal interactions between planet and disk slow down the accretion, which comes to an end as all surrounding gas is accreted or dissipated into space.

There are several currently unresolved challenges with the core accretion theory. For example, the proto-planetary disk typically consists of 99% H_2 molecular gas and 1% other molecules, referred to as dust. The formation of solid planet cores hence can only make use of limited material in the disk. Further, the planet formation has to happen within very short time (astronomically speaking). The entire growth process, representing a scale factor of over 10 orders of magnitudes in size, must happen within the few million years before the proto-planetary disk evaporates.

Recent studies and inclusion of concepts such as 'pebble accretion' suggest that this rapid core formation is indeed possible. This idea has been proposed by Ormel & Klahr (2010) and further elaborated by Lambrechts & Johansen (2012), and is in constant development since (see e.g. Bitsch et al., 2015). It suggests that the material in the disk does not directly form the few kilometer-sized planetesimals. Instead, numerous millimeter-sized pebbles form via collision and condensation. Next, the collision and gravitational collapse of many

pebbles can rapidly build up kilometer-sized bodies. Ongoing pebble accretion then leads to the formation of planet cores. Importantly, this build up is linked with a dynamic view of the formation, including the migration of planets (see Section 1.4.3) into the formation stage.

Giant gas planet or failed star?

There is an unknown boundary between planets and 'failed stars'. If considering the formation mechanism as a distinguishing criterion, it seems that stellar metallicity is a key factor. Objects with $< 4 - 10 \, \mathrm{M_J}$ were found to orbit metal-rich stars (Schlaufman, 2018). Their metal-rich protoplanetary disks can provide enough heavy material to enable the rapid formation of planetary cores, suggesting they form via core accretion. In contrast, objects $> 10 \, \mathrm{M_J}$ seem to orbit metal-poor stars. The lack of heavy material in the disk thus makes gravitational collapse formation more plausible. With such an formation-driven definition, objects $> 10 \, \mathrm{M_J}$ but below the brown dwarf limit (minimum mass for deuterium burning, $13 \, \mathrm{M_J}$) would not be considered planets.

1.4.3   Planet migration

The discovery of the first exoplanet, 51 Peg b (Mayor & Queloz, 1995), posed a challenge for the present theories of planet formation. How could a gas giant planet exist on an orbit of just 4 days around a Sun-like star, way closer than the snow line? This opened the route to new research, and based on previous theoretical studies, the observation of the first Hot Jupiters led to a variety of studies of planet migration (see e.g. Lin et al., 1996). Nowadays, planet formation and migration theories are usually conjoint, and models aim to reproduce not only the current state of our solar system, but also of the observed exoplanet demography (see Section 1.8).

Various migration theories have evolved, which are in praxis all interplaying with each other (see e.g. Kley & Nelson, 2012; Perryman, 2011): 1) in 'gas disk migration', a forming planet interacts with the gas and dust in the disk, resulting in a torque (see below); 2) 'planetesimal disk migration' incorporates gravitational interactions and collisions between

planets and smaller bodies in the disk; 3) 'planet-planet scattering' describes the gravitational exchange of momentum between planets. Additionally, the Kozai mechanism describes the perturbation of a planet's orbit if interacting with a highly inclined companion, leading to varying eccentricity and inclination (see e.g. Fabrycky & Tremaine, 2007). This might be the cause for misaligned planets (see e.g. Brown et al., 2012; Triaud et al., 2010). Further, tidal interaction with the host star can circularise a planet's orbit. In the case of rocky bodies, additional complex influencing factors can arise. The fate of close-in small bodies depends on the influence of gas giant planet migration, collisions, and photoevaporation of the planet's atmosphere.

A detailed discussion of all these mechanisms is beyond the scope of this thesis, and the reader can refer to the references in Perryman (2011) and Kley & Nelson (2012). In the following, I will briefly elaborate the basic concepts of disk migration, which is generally one of the major drivers for migration.

Gas disk migration

In gas disk migration models, the planet experiences a torque from the remaining gas in the disk. The effects of gas disk migration depend on the mass of the planet, leading to the following three major models.

Type I migration: low-mass planets ($\lesssim 10$ M$_\oplus$) perturb the surrounding gas, causing spiral density waves in the disk (Ward, 1997). Gas closer to the star orbits at a faster rate, gas further out at a slower rate. The gravitational pull from the planet on the gas leads to an exchange of angular momentum, generating a so-called Lindblad torque: interaction with the inner gas causes the planet to gain angular momentum and migrate outward; the interplay with the outer gas leads to a loss of angular momentum and inward migration. While this can drive both an inward and outward migration, generally the inward migration dominates. Type I migration occurs on short timescales relative to the disk lifetime ($\sim 10^5$ years; see e.g. Nelson et al., 2000; Ward, 1997).

Type II migration: a similar process as in Type I migration starts for high-mass objects, such as gas giant planets ($\gtrsim 0.3$ M$_J$). Their strong gravitational pull, however, then starts

to clear a gap in the disk (Bate et al., 2003). From then on, the planet and gap move jointly through the disk. Whenever material falls into the gap, it migrates inwards.

Type III migration: This model, also referred to as 'runaway migration', applies mainly to Saturn-sized planets. The material in the corotation zone of the planet exerts an additional torque, leading to an increasing migration rate.

A currently studied problem with planet migration is that it is an accelerating process, yet the existence of Hot Jupiters shows that the inwards motion must stop at a certain point. The most common explanation states that a braking mechanisms is introduced by tidal circularisation, which stabilises the planet's orbit (see e.g. Plavchan & Bilinski, 2013).

1.5 Planets in binary star systems

We currently know 88 (24) extra-solar binary systems (multiple systems), which contain a total of 125 (34) exoplanets[6] (Schwarz et al., 2016). Such extra-solar systems are categorised by their orbit into S-type and P-type. In an S-type system, the planet orbits only one star of the binary system on a usually short obit, while the host stars are generally widely separated (> 1000 AU). In a P-type system ('circumbinary system'), the planet orbits both stars on a usually wide orbit, while the host stars are generally close-in binaries. Both findings are strongly influenced by detection bias, but might also be restricted by planet formation and orbital stability.

Exoplanets in binary systems can be detected using the standard transit and RV techniques if the binary stars are sufficiently separated to be either visually or spectroscopically resolved. However, the binary nature can impose some complications. In the case of a transit observation, the system can show TTVs on the order of hours to days (see e.g. Armstrong et al., 2013). This is caused by the motion of the host stars orbiting their common centre of mass, and an increased precession of the planet's orbit. As the host star and planet move at different velocities, this can also affect the transit duration. Notably, around single stars, TTVs have been proven to be a successful method for detecting further planetary companions

---

[6]http://www.univie.ac.at/adg/schwarz/multiple.html, online 26 March 2018
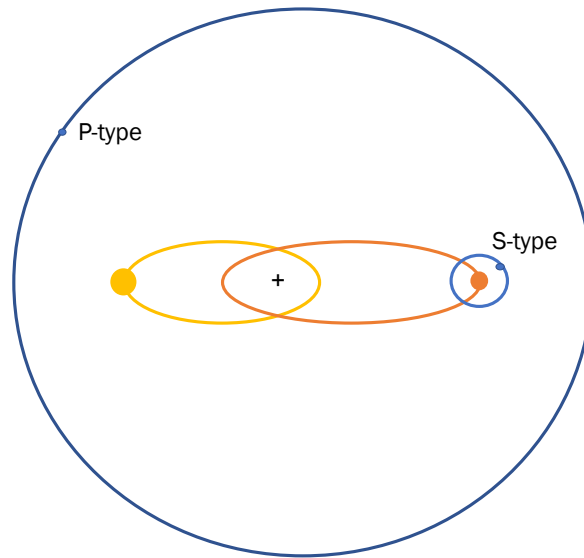
Fig. 1.9 Exoplanets in binary star systems are characterised as S-type (orbiting one star) or P-type (orbiting both stars).

in multiple star systems (see Section 1.2). In such cases, however, the TTVs are usually on the order of seconds to minutes (see e.g. Holczer et al., 2016).

The closest known orbit between stars with an S-type planet was found by the OGLE mircolensing survey (Gould et al., 2014). OGLE-2013-BLG-0341LBb is in a 1 AU orbit, while the binary stars are separated by only ~ 15 AU. Another exceptional finding is the occurrence of 'cousin' hot Jupiters in the WASP-40 binary systems (Neveu-VanMalle et al., 2014). Both WASP-40A and WASP-40B are orbited by hot Jupiters in S-type configurations.

S- and P-type systems are an excellent test bed for planet formation, migration, and orbital stability. In the context of hot Jupiters in binary systems, this raises an interesting question: are these systems 'failed' triple star systems, or did the planet form as a planet (see Section 1.4.2)? It was suggested that objects with $< 4 - 10$ M_J formed via core accretion, while objects > 10 M_J formed via gravitational collapse (Schlaufman, 2018). The transition range between $4 - 10$ M_J still remains widely unexplored, leaving giant exoplanets in binary systems to provide potentially interesting insights.

1.6   False positives mimicking transiting exoplanets

Transit-like shape variability in the light curve may not only be caused by planets. 'False positive' transit events related to an eclipsing astrophysical object can cause a transit signal of small amplitude that may be interpreted as a planetary transit (Fig. 1.10; see e.g. Cameron 2012).

Eclipsing binaries (EBs) can be very expensive in telescope time to follow up. First, low-mass companions such as Brown dwarfs and very low mass stars can be of similar size as gas giant planets. Distinguishing them from planets necessitates RV follow-up to measure the mass, and may be aided by measuring ellipsoidal effects or obtaining colour information during transit and eclipse. Second, EBs with grazing events lead to transit depths mimicking a planet-sized object even if the secondary is significantly larger.

Another class of false positives are background eclipsing binaries (BEBs), which are faint and distant EBs that are aligned along the line of sight behind a bright target star and hence diluted. The dilution reduces the apparent transit depth onto a planet-like scale, making BEBs one of the most difficult false positives to rule out. Similar to this are triple and higher-order star systems with one or more pairs of stars eclipsing, referred to as hierarchical EBs.
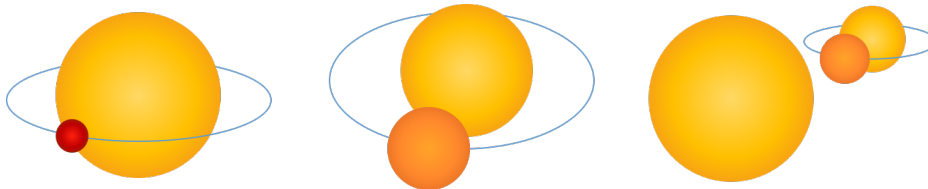
Fig. 1.10 False positives: eclipsing binaries (EBs) with a low-mass stellar companion (left panel) or a grazing eclipse (middle panel), as well as background eclipsing binaries (BEBs blended in the photometric aperture; right panel) can mimic exoplanet transits.

1.6.1   Candidate vetting methods

With typical geometric transit probabilities of only a few percent for hot Jupiters and significantly lower for planets on Earth-like orbits (see Section 1.2.2), transit surveys need to observe a multitude of possible host stars. In wide-field surveys, false positives can be

up to two orders of magnitude more prevalent than planets (see e.g. Almenara et al., 2009; Hartman et al., 2011). Identifying these objects can be costly in follow-up time. Therefore, sophisticated candidate vetting has to be performed before scheduling any additional observations.

Fortunately, various aspects of a light curve can give insight into the underlying nature of the signal, allowing to rule out false positives from transit data alone. A full transit gives a characteristic trapezoidal or U-shaped dip in the light curve. Grazing transits, however, show a typical V-shape (see Fig. 1.4). If the quality of the light curve is high enough, grazing EBs can be ruled out by this feature.

Further, the transit duration T gives a direct measure of the host star's density as shown in Eq. 1.7. If the stellar density of the target star is known, these values can be compared and indicate a possible BEB contamination (see e.g. Cameron, 2012).

In addition, different depths for even and odd eclipses give another hint (Batalha et al., 2010). Segregating and studying both series independently can prove that the supposed planet with orbital period P is actually an EB with orbital period $2P$. Moreover, shallow secondary eclipses of a binary system can be misidentified as a planet scenario if the primary eclipse is missed or not visible due to an eccentric orbit.

If the signal is caused by a planet, the combination of transit and occultation depth gives a direct measure for the ratio of planet and stellar flux (see Eq. 1.1 and 1.9). Assuming blackbody radiation, the effective temperature $T_{\text{eff,p}}$ of the planet can be estimated (see Eq. 1.10). The value of $T_{\text{eff,p}}$ can then be compared with the equilibrium temperature of a strongly irradiated planet:

$$T_{\text{eq,p}} = T_{\text{eff,}\star} \left(R_\star/2a\right)^{1/2} \left[f(1-A_B)\right]^{1/4} \tag{1.18}$$

(see e.g. Batalha et al., 2010). In here, $T_{\text{eff,}\star}$ is the effective temperature of the star, f describes the atmospheric thermal circulation, and A_B is the Bond Albedo. If the discrepancy between $T_{\text{eff,p}}$ and $T_{\text{eq,p}}$ is significant, the system is likely a grazing EB or BEB.

Kepler's precision allows to implement centroid measurements to rule out BEBs (Batalha et al., 2010). Whenever a BEB undergoes an eclipse, the pair will contribute less to the overall flux and the centre of flux in the aperture will shift towards the target star. Such variations are typically on very small scales and due to the required precision not feasible for most other surveys. In Section 4, I outline how I achieve to measure centroid shifts for the NGTS mission.

For upcoming surveys, many false positives eclipsing binaries will have been uncovered a-priori by the *Gaia* mission. With its high precision, *Gaia* can visually resolve binaries that are separated below the arc-second level. Further, the pull from unresolved companions introduces non-linear proper motions, which can be astrometrically detected. Its spectroscopic and photometric long-term campaign will further enable estimates of binary masses, and the radii of eclipsing binaries.

1.6.2 Automated vetting tools

With the era of *Kepler*, the field had to move to a probabilistic validation of planet candidates. Previously, each transit signal was followed up by with RV observations. These were able to identify eclipsing binaries and blended objects, and to determine the mass of the orbiting body. As *Kepler* planet candidates were numerous, generally faint, and often very small and low-mass (i.e. with non-detectable RV signatures), this approach was not feasible anymore. This Section presents a selection of automated vetting tools for distinguishing planets from false positives in a 'Big Data' context. This list is far from complete, but shall serve as a short overview of recent advances in the field of candidate vetting.

The BLENDER algorithm, which serves to validate whether a signal originates from a planet or from a blended object, was the first automated validation approach on a big scale (Torres et al., 2004, 2011, 2015). Thereby, the likelihood of an undiluted planet transit model is calculated and compared to the best fitting model of a diluted eclipsing binary. The code makes additional use of other information, such as the presence of centroid shifts (see e.g. Batalha et al., 2010). However, BLENDER necessitates significant computational investment

and priors that first need to be gained from high resolution follow-up. It is consequently only applicable in limited cases (see Fressin et al., 2013; Morton, 2012).

The VESPA code (Morton, 2012, 2015) was extensively used by the *Kepler* team to probabilistically validate over one thousand planets at once (Morton et al., 2016). VESPA uses a fast fit of a trapezoidal model to the light curve, simplifying the analysis to effectively three parameters: transit depth, width and in-/egress duration. The Bayesian evidence of each model is computed and used to determine the best fitting scenario. This model is computationally effective and statistically robust. However, the dimensionality reduction and simplification of the transit/eclipse shape can pose a potential issue. The VESPA code is publicly available[7].

Independently, PASTIS (Díaz et al., 2014; Santerne et al., 2015) was introduced to validate *Kepler* and CoRoT targets by comparing the Bayesian evidence and Bayesian odds factor of planet and false positive models matching the data. It follows a similar approach to VESPA, yet employs a physical transit/eclipse model and is capable of incorporating external (prior) information from astrometric and RV measurements. PASTIS hence provides a more thorough approach than BLENDER and VESPA. However, due to this, the method is only applicable to selected targets. Further, PASTIS only leads to conclusive results for a signal-to-noise-ratio $SNR > 50$, which is generally not the case for current shallow targets.

Kepler's ROBOVETTER (Coughlin et al., 2016) mimics and automates the human decision making process by incorporating some of the tests outlined in Section 1.6.1. For each of *Kepler*'s threshold-crossing events (TCEs), a series of quantitative tests are performed to decide whether a signal is 'transit-like', and whether it resembles a planet or detached eclipsing binary. The difference of the light curve from a reference transit-like light curve is used to identify sinusoidal or semi-periodic out-of-eclipse variation. Further, the Bayesian Information Criteria (BIC; Schwarz, 1978) between the fits of a transit model and discontinuity models are compared. Additionally, the best fitting transit model is slid across the phase folded light curve to identify any other decreases in light with the same shape. Finally, transit-like signals are masked and included one by one to compute the phase-folded light

---

[7]https://github.com/timothydmorton/VESPA, online 26 March 2018

curve's signal-to-noise ratio. If it does not increase with the addition of more transit signals, but is dominated by a single event, the TCE gets rejected. If a TCE passes all these steps, it is registered as a Kepler Object of Interest (KOI), containing planet candidates and detached eclipsing binaries.

All KOIs are further vetted. The ROBOVETTER code identifies detached eclipsing binaries by their secondary eclipse. If there is either a shallower transit-like signal with the same period but shifted epoch (either detected as a TCE or with the sliding transit model), or if there is a difference in the depth of odd versus even transits, a planet scenario gets rejected. Further, centroid shifts are investigated as evidence for blended objects in the aperture. If a KOI passes all these steps, it gets ranked as a planet candidate for final inspection. The ROBOVETTER code is publicly available[8].

Shallue & Vanderburg (2018) developed a machine learning classifier for candidate vetting of *Kepler* data. Their approach is different form previous ones, as it uses a convolutional deep learning network for supervised learning, a method that is common for image recognition. Rather than extracting and evaluating individual transit features, the algorithm categorises 'images' of transit-like events. The authors were able to detect two new *Kepler* planets with this method, yet the overall accuracy of the method was limited. This is likely due to the code's limitation to the transit 'image' alone, and the non-inclusion of features indicating blend scenarios, such as centroid shifts.

Recently, Armstrong et al. (2018) introduced AUTOVET, which was designed for NGTS but is generally applicable to all photometric transit searches. The software uses a combination of supervised and unsupervised machine learning to rank planet candidates by their likelihood of being real. First, self-organising maps (SOM; Kohonen, 1982) are employed to analyse the transit shape via unsupervised learning. This implementation is based on the previous TRANSITSOM algorithm (Armstrong et al., 2017). Additionally, other typical transit features are extracted, including for example the period, width and depth of the transit, noise of the light curve and secondary eclipses. All features provided by the SOM and the light curve fitting are then passed into a random forest algorithm (see e.g. Breiman, 2001) for

---

[8]https://github.com/nasa/kepler-robovetter, online 26 March 2018

supervised machine learning. A set of simulated planets and real candidates is passed for training and cross-validation of the classifier. The authors report a precision and recall of around 90%, and show that their top 10 ranked planet candidates are populated by known and to-be-published exoplanets. The AUTOVET code is publicly available[9].

1.6.3 Candidate vetting efficiency

In the case of *Kepler* KOIs, the false positive rate for hot Jupiters was found to be 35% in the first data sets (Santerne et al., 2012). The *Kepler* team consequently put significant effort into improving the pipeline to reduce false positives contamination. Still, Fressin et al. (2013) estimate that even after the extensive candidate vetting procedure, 9.4% of all KOIs are false positives. These rates are lower than for any other survey (Morton, 2012).

CoRoT, for example, was able to use its light curves to directly rule out 83% of its initially triggered signals as false positives (Almenara et al., 2009). Nevertheless, still 88% of the remaining CoRoT candidates were found to be false positives. For ground-based surveys the rates reach values of up to 95% for HAT (Hartman et al., 2011) and WASP (personal correspondence with the WASP team).

One reason for this is that *Kepler* observed the same objects continuously over four years. In the case of wide field surveys like CoRoT, the field of view is frequently changed to cover as much of the sky as possible. Ground-based surveys like WASP are additionally interrupted by a limited field visibility and weather. Another reason is the photometric precision achieved from space, with red noise levels around 0.03 mmag (Gilliland et al., 2011). Ground-based surveys in contrast are limited by red noise of several mmag. This precision allows *Kepler* to make extensive use of transit shape analyses and the centroid technique in ruling out BEBs. It also enables to detect shallower signals and secondary eclipses.

NGTS is the first ground-based survey to achieve a photometric precision of 1 mmag, enabling the detection of shallow planet signals. A sophisticated candidate vetting is hence pivotal to the success of the survey and is the main focus of my PhD work, as presented in this thesis.

---

[9]https://github.com/DJArmstrong/autovet, online 26 March 2018

1.7 False positives in radial velocity observations

Various scenarios can introduce spurious signals mimicking a centre-of-mass movement of the host star. The contamination by star spots and faculae can introduce an RV jitter, and depends on the activity, rotation rate and surface gravity of the host star (see e.g. Dravins et al., 1981; Wright, 2017). Current efforts in breaking the sensitivity limit include continuous spectroscopic observations of the Sun as an exoplanet host star, to model the jitter introduced by events in the stellar atmosphere and translate these into an exoplanet scenario (see e.g. Haywood et al., 2016).

Likewise, false positives can be introduced by unresolved blended objects whose light falls into the spectrograph fibre. For example, if the target is actually a spectroscopically unresolved binary, the third object might transit the primary or secondary. It could hence be a planet on the primary, with constant dilution from the secondary; or it could be a brown dwarf on the secondary, with constant dilution from the primary (see e.g. Santos et al., 2002).

In practice, the stellar spectrum is obtained from spectroscopic measurements and then cross-correlated with a calibrated reference spectrum ('mask'). This gives the RV cross-correlation function (CCF; see Fig. 1.11). The CCF peak is fitted with a Gaussian function, whose mean value is the reported RV value. Likewise, the full width at half maximum (FWHM) and amplitude of the Gaussian (Contrast) can be extracted.

The CCF bisector, in particular the bisector inverse slope (BIS), has been proven to be a powerful tool to both detect star spots (Queloz et al., 2001b) and blended objects (Santos et al., 2002). The bisector is defined as the mean points halfway between equal intensities on both sides of the CCF peak. The BIS is defined as $v_t - v_b$, with v_t (v_b) being the mean bisector velocity of all points between the top 10-40% (the bottom 60-90%) of the CCF peak depth (Queloz et al., 2001b). The correlation (or anti-correlation) between RV and BIS can then give insight into the true nature of the RV signal:

- **Atmospheric phenomena.** If a star shows strong atmospheric activity, such as star spots, the top of the RV CCF profile will remain mostly unaffected, while the bottom will show strong oscillations around the mean value. This leads to an anti-correlation

between the BIS and RV measurements (see e.g. Boisse et al., 2011; Queloz et al., 2001b).

- **Blended systems.** If the observed target is a multiple star system whose angular separation is smaller than the fibre of the RV instrument (1" for HARPS, see Mayor et al., 2003), each obtained spectrum will show the combined blended spectra of all objects. The measured RV is the flux-weighted average of all components. It is thereby important to distinguish the two scenarios whether the brighter or fainter object are orbited by a third body. Fig. 1.11 illustrates how the bisector and BIS can unmask a blended system.

As I demonstrate in Chapter 5, inferring the true nature of the target requires a combined modelling of photometric and RV observations.
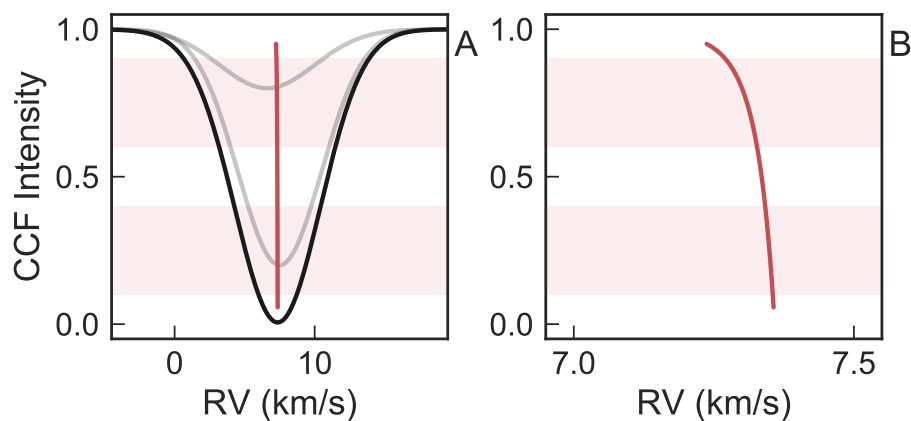
Fig. 1.11 Simulation of the CCF and bisector of a blended system. A) The (unresolvable) signals for the two blended stars are shown in grey, and the measured sum of their signal is shown in black. The red line represents the bisector. Light red shaded regions indicate the top 10-40% (v_t) and bottom 60-90% (v_b) of the profile, which are used to calculate the BIS = $v_\text{t} - v_\text{b}$. B) Zooming onto the bisector shows a clear signal, resulting in BIS = $v_\text{t} - v_\text{b} < 0$ in this example.

1.8 Exoplanet demography

1.8.1 Selection effects

Each exoplanet detection method has an intrinsic selection bias (Fig. 1.12; see e.g. Winn 2018). Transit surveys, measuring the planet radius, are biased towards large planets in short orbits around small stars (Section 1.2). The transit signal decreases quadratically with a smaller planet radius or a larger stellar radius, $\delta_{tr} \sim R_p^2 R_\star^{-2}$ (Eq. 1.1). Further, the geometric transit probability decreases with smaller stellar radius and larger period, $P_{geom} \sim R_\star a^{-1} \sim R_\star P^{-2/3}$ (Eq. 1.8; assuming $R_p << R_\star$). In the case of ground-based surveys, the day-night-cycle and the resulting observing window function additionally decrease the chances of detecting transit signals. Moreover, automated pipelines for transit surveys usually require to detect at least three transits. A strict upper limit on the orbital period is thus set by the survey duration, further biasing against long period planets.

RV surveys, measuring the planet mass, are most efficient in detecting massive exoplanets in short orbits around bright, less massive stars (Section 1.3). The RV semi-amplitude scales as $K \sim M_p M_\star^{-2/3} P^{-1/3}$ (Eq. 1.11; assuming $M_p << M_\star$). The dependency on $P^{-1/3}$ shows that RV surveys are more sensitive to longer orbit planets than transit surveys. An orbital alignment at $i \approx 90°$ is not required for RV surveys. However, the signal decreases with $\sin i$. Further, an RV detection does not rely on a single event (like a transit), but planet signals are visible even if their orbital period exceeds the survey duration. A limitation is that spectroscopic measurements require bright targets, typically $V < 15$, and have to observe target by target.

Most discovered transiting planets are too faint to be followed-up with RV instruments, and are hence lacking a mass measurement. Vice versa, many RV planets are not transiting, such that the planet radius can not be measured. This makes a comparison between the yields of both surveys difficult, as the bulk composition is unknown, and a mass-radius-relationship of exoplanets currently remains an active field of study.

Likewise, other detection methods are biased. Direct imaging is only possible for planets on very long orbits around faint, nearby stars (see e.g. Traub & Oppenheimer, 2011). The

planets have to be distant enough from their star such that the stellar light can be blended out when imaging the planets. Microlensing surveys, too, are most sensitive to planets orbiting beyond 1 AU (see e.g. Gaudi, 2011).
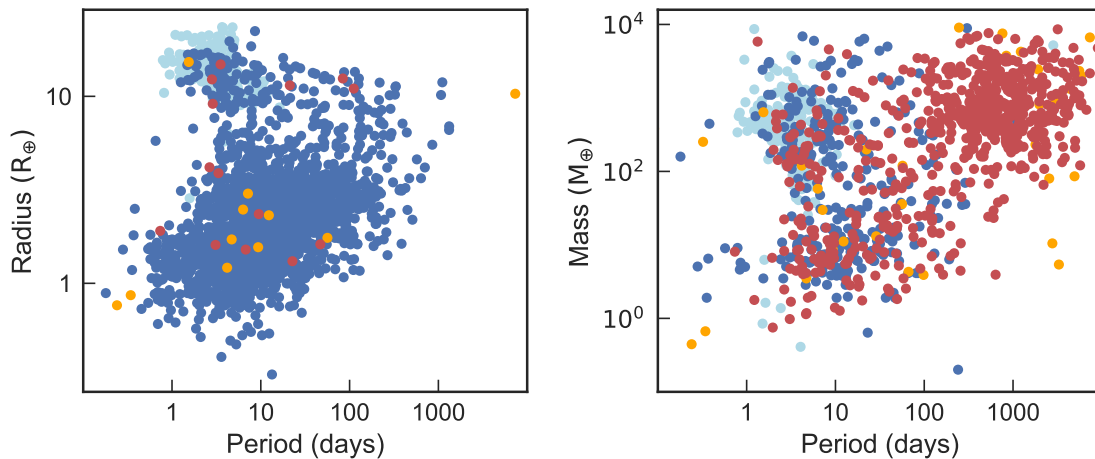
Fig. 1.12 Observed exoplanet populations illustrated as planet radius (left) and mass (right) over period. The different detection techniques are compared: radial velocity (red), ground-based transits (light blue), space-based transits (blue), and other (orange).

1.8.2   Inferring the true population

When inferring the true exoplanet populations, one has to systematically account for the selection effects of the different methods as well as the contamination by false positives (see e.g. Winn, 2018). Comprehensive analyses of *Kepler*'s transiting planet population around F, G and K stars were for example published by Fressin et al. (2013), Santerne et al. (2016), and Petigura et al. (2018). Similar analyses of planets orbiting M stars were performed by Dressing & Charbonneau (2015), and Gaidos et al. (2016). These teams estimated the detection completeness and false positive contamination of the survey depending on the planet radius and orbital period. They then 'de-biased' the actual discoveries and calculated the underlying planet occurrence rates. Similar studies were performed for RV planets, yet for a far more limited sample size (see eg. Cumming et al., 2008; Mayor et al., 2011).

Overall, the studies agree that most stars have planets, and that there is on average circa one planet per star within 1 AU. Out of these, at least half of the Sun-like stars host a planet

with $1-4\,\mathrm{R}_\oplus$. Further, M stars show a higher occurrence rate of terrestrial planets than FGK stars, but a low occurrence of larger planets. In fact, only three M stars are currently known to host gas giant planets, Kepler-45b (Johnson et al., 2012), HATS-6b (Hartman et al., 2015), and NGTS-1b (Bayliss et al., 2018).

The 'holy grail' of exoplanet science has often been seen as answering the question 'how many other Earths are out there?', a property referred to as $\eta_\oplus$. This idea is drawn from the Drake equation, which describes the factors that quantify how many communicative extraterrestrial worlds exist. Therein, $\eta_\oplus$ is defined as the fraction of planets that can support life. In an exoplanet context, this is generally constrained to planets that have a similar size and mass to Earth, and lie in the habitable zone of their host star (although these limits differ from study to study). *Kepler* was the only survey ever designed to answer this question, being sensitive enough to detect an Earth-sized planet transiting a Sun-like star on a 1 year orbit. However, such studies suffer from varying definitions of $\eta_\oplus$ and habitability, and a lack of statistics on wide-orbit exoplanets. The question of $\eta_\oplus$ thus remains widely unanswered. Possible answers range from $\eta_\oplus = 0.04$ to $\eta_\oplus = 11.5$ (Burke et al., 2015).

Two regions of the parameter space are particular interesting: the transition between rocky and icy planets at $1.5-2\,\mathrm{R}_\oplus$, and the transition between giant gas planets and brown dwarfs at $4-10\,\mathrm{R}_\mathrm{J}$. Recent studies have provided evidence for a radius valley for small planets, both from an observational (Fulton et al., 2017) and theoretical (Owen & Wu, 2017) approach. This valley at $1.5-2\,\mathrm{R}_\oplus$ seems to separate the populations of apparently rocky Super-Earths from icy Sub-Neptune-sized objects. It is suggested that the atmospheres of such gas planets get evaporated by the host star, leaving only the rocky core at the end of the process.

The physical processes are less clear for the boundary between giant exoplanets and 'failed stars', such as Brown Dwarfs. The working definition of the International Astronomical Union uses the deuterium burning limit $M > 13\,\mathrm{M}_\mathrm{J}$ as a criterium to draw the line between the two categories (Boss et al., 2007). However, recent studies suggest that this definition might fail, and that a formation-based criterium may be preferable (e.g. Schneider et al.,

2011; Wright et al., 2011). Planets may only form through core accretion, while stars form through gravitational collapse (see Section 1.4.2).

1.9   The Next Generation Transit Survey (NGTS)

1.9.1   Overview and science goals

The Next Generation Transit Survey (NGTS, Wheatley et al. 2018) is a wide-field survey for exoplanets, operating at the European Southern Observatory's (ESO's) site at Cerro Paranal, Chile (Fig. 1.13). Throughout my PhD, I have installed and operated telescopes, optimised the observing strategies (Chapter 3) and data quality assessment, and developed tools for the pipeline and candidate vetting (Chapters 4 and 5).
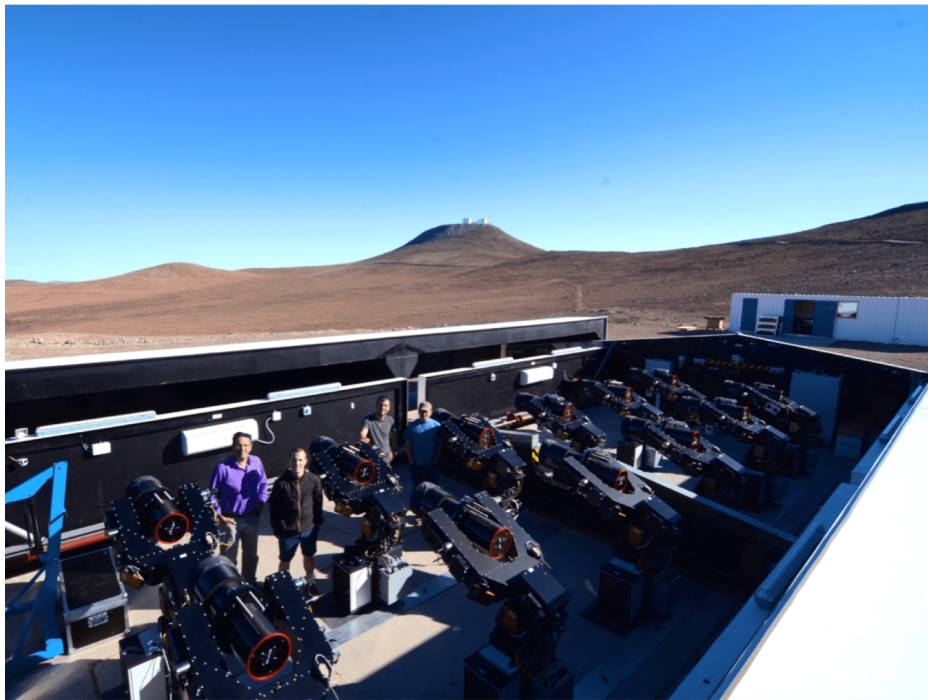
Fig. 1.13 The Next Generation Transit Survey (NGTS), which has been operating from ESO's Paranal Observatory in Chile since 2016. Credit: Gregory Lambert.

NGTS achieved first light in 2015 and began full survey operations in April 2016. The mission's primary goal is the detection of Neptune-sized exoplanets transiting bright stars, which are suitable for further characterisation and mass determination with high-precision

telescopes. These objects are of high interest as they mark two transition regions: Large Neptunes ($4 - 8$ R$_\oplus$) could be either small gas or large ice planets, while Small Neptunes ($2 - 4$ R$_\oplus$) could be either large rocky or small icy planets.

To achieve its science goal, NGTS is designed to be the first ground-based exoplanet survey to reach sub-mmag photometry[10]. NGTS thereby builds on its design studies and prototype (Chazelas et al., 2012; McCormac et al., 2017) and the legacy of previous surveys, most notably WASP (Pollacco et al., 2006). In contrast, previous ground-based facilities have a more limited photometric precision. For example, with $10 - 50$ mmag for HAT (Bakos et al., 2002) and $3 - 30$ mmag for WASP, these missions were more prone to detect hot Jupiters.

1.9.2 Facility

The NGTS facility consists of twelve independent 20 cm f/2.8 telescopes, operated from independent Optical Mechanics, Inc. (OMI) mounts (Wheatley et al., 2018). This enhances tracking of individual fields, and freedom in scheduling observations. Each telescope is coupled to an Andor Ikon-L Camera featuring a 2k×2k e2V back-illuminated deep-depleted CCD with a pixel size of 13.5 μm (4.97 arcsec). The detectors have a constant PSF FWHM of 12 μm across the field of view.

Each telescope has a 7.4 sq deg field of view. The total field of view adds up to 88.8 sq deg, similar to the *Kepler* mission. NGTS covers a new field of this size every few months, allowing it to survey many bright stars for short orbit planets. The sensitivity is optimised between $500 - 900$ nm (Fig. 1.14). This maximises the observation efficiency for K and early-M stars, favouring the detection of small planets.

1.9.3 Observing conditions

ESO's Paranal Observatory site has one of the best observing conditions for ground-based photometry. On average, ~ 78 % of the night time are usable for photometric observations[11].

---

[10]1 mmag corresponds to circa 0.1 % precision on the light curve
[11]https://www.eso.org/sci/facilities/paranal/astroclimate/site.html, online 26 March 2018
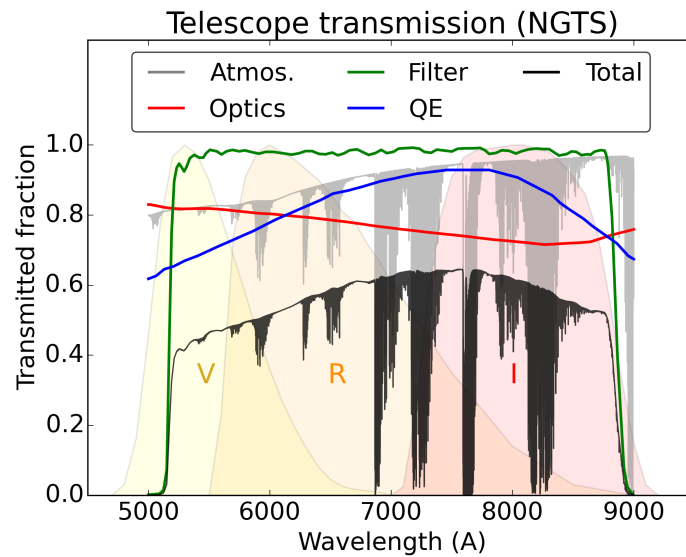
Fig. 1.14 The NGTS transmission function, spanning the V, R and I bands. Shown are the different transmission efficiencies of the NGTS filter, optics and the CCD quantum efficiency, the atmospheric transmission, and the resulting total transmission.

NGTS has operated in science mode since April 2016 (Wheatley et al., 2018). Fig. 1.15 shows the 'on-sky time' since the start of commissioning with four telescopes in September 2015 (marked by the letter 'a' in Fig. 1.15). The term on-sky time here refers to the observable night time multiplied by the number of installed telescopes. By December 2015, four more telescopes were installed, doubling the on-sky time of the facility (b,c). In April 2016, the installation of the final four telescopes was completed (d).

However, NGTS did not have a smooth start after commissioning. Immediately after the beginning of scientific observations with the full twelve telescopes in April 2016, the facility was forced into one month of down-time, due to rodents damaging the telescopes (e). Observations remained limited in May-July 2016, due to bad weather introduced by the climatic phenomenon El Niño (f). This was followed by a roof failure, forcing NGTS into another two weeks of technical downtime (g). In late 2016, major issues with camera shutters had to be resolved (h). Since 2017, the survey has been able to observe without major technical interruptions.
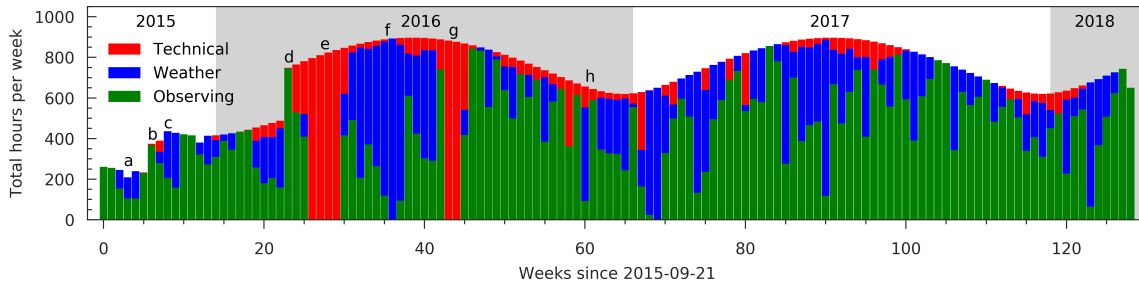
Fig. 1.15 The NGTS on-sky time since start of commissioning in September 2015. Major events a-h are described in the main text. Figure courtesy of James McCormac.

1.9.4   Operations

NGTS is a fully robotic survey (Wheatley et al., 2018). Observations can be scheduled remotely and in advance without requiring further supervision by human observers. Typically, fields are scheduled to be observed with the same telescope continuously over multiple months. To observe as many hours per night as possible, a single telescope observes a maximum of two fields per night. This totals to ~ 250 nights per field, with 2 to 4 hours continuous coverage per night.

The field selection considers the density of stars per field, the frequency of dwarf stars, and the estimated pollution by false positives derived from my yield simulations, which are described in Chapter 3. The survey further avoids the galactic plane to $20°$ and the moon to $25°$. On average, one telescope field contains $10,000$ target stars brighter than $V = 15$.

The survey employs the DONUTS autoguiding software (McCormac et al., 2013) to follow the fields and remain on target during the night. Through this, stars fall on the same CCD pixel during the entire night. This is key for NGTS' high precision photometry. DONUTS operates in real time on the science images, and continuously cross-correlates the positions of stars with a reference image. If a deviation is detected, guiding corrections are calculated and passed on to the telescope. This reduces the drift of stars from multiple pixels to 0.04 pixel on average per night.

1.9.5 Light curve extraction and transit search

NGTS uses a custom data pipeline to extract the light curves of all target stars (Wheatley et al., 2018), which is largely based on the WASP pipeline (Collier Cameron et al., 2006). First, a reference catalogue is produced by extracting the positions of stars from 100 stacked NGTS images using CASUTOOLS[12] (Irwin et al., 2004). Second, images are corrected for bias and flat fielding in the standard way. Next, the astrometry is solved for every image using a custom routine. Light curves are then extracted using CASUTOOLS' aperture photometry.

Light curves are detrended using a customised implementation of the SYSREM algorithm (Tamuz et al., 2005). This removes systematic trends seen in multiple light curves. Additionally, signals with a period of the lunar phase and sidereal day are removed using moving average detrending after phase-folding on these periods. Transit-like features in NGTS' light curves are detected using the ORION software, a custom implementation of the Box-Least-Squares (BLS) algorithm (Kovács et al., 2002).

Transits are vetted using a variety of tools, covering the possible measures discussed in Section 1.6.1. For a first screening and candidate ranking, the CANVAS (CANdidates Vetting, Analysis and Selection; Métrailler 2016) algorithm fits each BLS candidate with an exoplanet transit model using least squares curve fitting. This is based on the BATMAN (Kreidberg, 2015) implementation of the Mandel & Agol (2002) model. CANVAS ranks the candidates according to how well the BLS signal matches the planet model, and penalises for sinusoidal trends, odd-even difference, secondary transits and common periods. Further, the likelihood of the transit model is evaluated for a sliding offset between model and data. This serves to probe whether the signal is real or a reoccurring noise pattern. Moreover, the TRANSITSOM algorithm (Armstrong et al., 2017) is employed to use self-organising maps (an unsupervised machine learning technique) for the characterisation of the transit shape. This proves to be a powerful tool to distinguish between planetary transits and noise features.

NGTS is the first wide-field ground-based transit survey ever to make use of automated centroid vetting.This allows the crucial identification of background eclipsing binaries (see

---

[12]http://casu.ast.cam.ac.uk/surveys-projects/software-release, online 26 March 2018

Sections 1.6 and 1.6.1). Developing this methodology was a substantial part of my PhD project, and is described in detail in Chapter 4.

Finally, a machine-learning driven vetter, AUTOVET, retrieves all the features outlined above (Armstrong et al. 2018; see Section 1.6.2). Using supervised learning and a training set of simulated transits, AUTOVET employs a random forest algorithm to select the most important vetting features. The results are used to rank the candidates and prioritise the best targets for immediate follow-up.

1.9.6 NGTS-1b

In 2017, NGTS announced its first exoplanet discovery. NGTS-1b is a possibly inflated hot Jupiter orbiting an early M-dwarf star in a 2.65 day orbit (Bayliss et al., 2018). With a radius of $1.33^{+0.61}_{-0.33}$ R_J and mass of $0.812^{+0.066}_{-0.075}$ M_J, this is the heaviest and possibly also largest planet ever discovered around an M-dwarf. This makes NGTS-1b one of only three currently known systems of its kind, bringing interesting insights for current theories of planet formation and migration around low-mass stars (see Section 1.8.2).
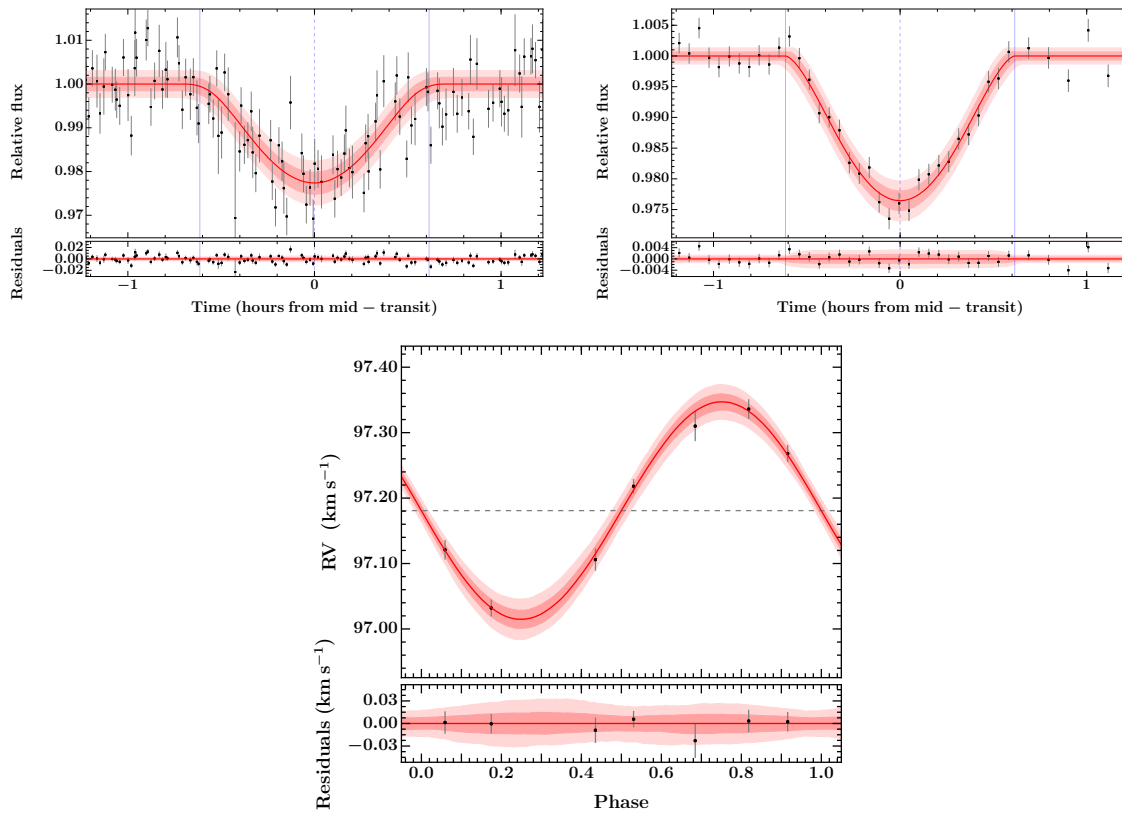
Fig. 1.16 Discovery data and global modelling of NGTS-1b. Top left: discovery light curve from NGTS. Top right: Eulercam z-band follow-up photometry. Bottom: HARPS RV follow-up. Red lines represent the median of the posterior model, and red bands its 1 and 2-sigma uncertainties. Figure from Bayliss et al. (2018).

Chapter 2

Methodology

"Start with what is right rather than what is acceptable."

— Franz Kafka

2.1 Bayes' theorem

Bayes' theorem describes that the conditional probability $P(A|B)$, the likelihood of an event A given an event B, can be calculated as:

$$P(A|B) = \frac{P(B|A)P(A)}{P(B)}, \tag{2.1}$$

where $P(B|A)$ is the conditional probability of B given A, and $P(A)$ and $P(B)$ are the probabilities of A and B (see e.g. MacKay, 2003).

Bayes' theorem can be interpreted in two different ways: in the 'Bayesian interpretation' it represents a 'degree of belief'; in the 'Frequentist interpretation' it is considered a 'frequency of occurrence'. In this thesis, I always approach questions using the 'Bayesian interpretation', unless clearly stated otherwise. As many other scientific fields, the field of exoplanets has moved into this probabilistic view with an interest in likelihoods.

2.2   Bayesian inference

The field of statistical inference derives properties of an underlying probability density func-tion (PDF) from given data (see e.g. MacKay, 2003). In the abstract mathematical definition, a probability density is defined by the differential of the normalised cumulative distribution function F for a given PDF f of a random variable x, given by $f(x) = \frac{d}{dx}F(x)$. For any set A, the PDF can give the probability that the value of y lies within A, as $P(y \in A) = \int_A f(x)dx$.

Bayesian inference is an application of Bayes' Theorem, where the PDF is the conditional probability $P(A|B)$. It describes the probability of set A given set B, which gets updated as more information on B becomes available.

2.2.1   Applied example of Bayesian inference

The principle of Bayesian inference can be illustrated using the example of two rivalling siblings, Alice and Bob. Alice challenges Bob to toss a coin. A heads means that Alice wins money, a tails means that Bob wins money. Bob is suspicious, and wants to know if Alice is trying to trick him. The coin is defined as fair if the probability of heads is 0.5, i.e. $\Theta := P(\text{heads}) = 0.5$. Bob assumes that Alice either has a completely fair coin ($\Theta = 0.5$), or a trick coin that always ends up showing heads ($\Theta = 1$). He demands one trial toss, which results in heads. Using Bayes' theorem, Bob can then infer the probability that the coin is fair via

$$P(\text{fair coin}|\text{trial data}) = \frac{P(\text{trial data}|\text{fair coin})P(\text{fair coin})}{P(\text{trial data})}. \tag{2.2}$$

The four factors are:

- $P(\text{fair coin}|\text{trial data})$ is the 'posterior probability' that the coin is fair, judging from the results of the trial toss.

- $P(\text{fair coin})$ is the 'prior probability' that the coin is fair. Depending on how much Bob mistrusts his sister based on previous experience, he can reflect this in his choice

of prior. Since Alice tricked him three out of five times in the past, he chooses

$$P(\text{fair coin}) = 1 - 3/5 = 0.4.$$

- $P(\text{trial data}|\text{fair coin})$ is the 'likelihood' of the trial outcome under the assumption that the coin is fair. Here this is simply

$$P(\text{trial data}|\text{fair coin}) = 0.5.$$

- $P(\text{trial data})$ is the so called 'Bayesian evidence'. It is the overall probability of getting the trial outcome, derived as the integral over all possible products of prior and likelihood. With the coin being either completely fair ($\Theta = 0.5$) or unfair ($\Theta = 1$), this simplifies to:

$$P(\text{trial data}) = [P(\text{trial data}|\text{fair coin}) \cdot P(\text{fair coin})]$$
$$+ [P(\text{trial data}|\text{unfair coin}) \cdot P(\text{unfair coin})]$$
$$= [0.5 \cdot 0.4] + [1 \cdot (1 - 0.4)] = 0.8$$

Bob can now use Eq. 2.2 to calculate the posterior probability that the coin is fair:

$$P(\text{fair coin}|\text{trial data}) = \frac{0.5 \cdot 0.4}{0.8} = 0.25.$$

He sees his suspicion confirmed, and the posterior likelihood of the coin being fair is now even lower than his prior assumption.

Bob demands two more trial tosses, which both result in heads as well. He started the game with his prior $P(\text{fair coin}) = 0.4$. After the three tosses, he derives the likelihood $P(\text{trial data}|\text{fair coin}) = 0.5^3 = 0.125$. The evidence becomes $P(\text{trial data}) = (0.5^3 \cdot 0.4) + (1^3 \cdot 0.6) \approx 0.65$. When he calculates the posterior probability that the coin is fair, he finds:

$$P(\text{fair coin}|\text{trial data}) = \frac{0.125 \cdot 0.4}{0.65} \approx 0.08.$$

The additional data updates the posterior likelihood, and further decreases his trust in a fair game.

An important aspect in Bayesian inference is the choice of prior. If Bob had fully trusted Alice, he could have chosen, for example, $P(\text{fair coin}) = 0.95$. The likelihood is determined by the trial tosses and would have been the same: $P(\text{trial data}|\text{fair coin}) = 0.125$. The Bayesian evidence would have been $P(\text{trial data}) = 0.5^3 \cdot 0.95 + 1^3 \cdot 0.05 \approx 0.169$. This would have led to $P(\text{fair coin}|\text{trial data}) = \frac{0.125 \cdot 0.95}{0.169} \approx 0.7$. If Bob had not mistrusted Alice based on previous experience, he would have still bet his money on tails.

2.2.2 Application to data modelling

Applied to data modelling within the frame of Bayesian inference, the PDF $P(\Theta|x)$ describes the probability for a set of parameters, Θ, given the set of data, x. It gets updated as more data becomes available (see example in Section 2.2.1). From Bayes' Theorem, this posterior $P(\Theta|x)$ is given by the likelihood $P(x|\Theta)$ for the data given the parameters, the prior $P(\Theta)$ for the parameters, and the Bayesian evidence $P(x)$ for the data:

$$P(\Theta|x) = \frac{P(x|\Theta)P(\Theta)}{P(x)}. \tag{2.3}$$

The Bayesian evidence $P(x)$ is generally unknown. It can be computed as

$$P(x) = \int P(x|\Theta)P(\Theta)\mathrm{d}\Theta, \tag{2.4}$$

but this integral is computationally expensive to solve. It yields a normalization factor for the posterior PDF, which is not needed for optimisation problems of a defined model, where only the relative difference between chosen parameters is evaluated. This is the case in Markov Chain Monte Carlo (MCMC) approaches (see Section 2.5). In this context, it is hence often bypassed:

$$P(\Theta|x) \propto P(x|\Theta)P(\Theta) \tag{2.5}$$

In the context of exoplanet transit modelling, the set of parameters Θ contains for example the orbital period P, epoch of first transit T_0, planet radius R_{p}, stellar radius $R_\star$ and more. The data set x is the light curve, i.e. a time series of flux values. The choice of priors $P(\Theta)$ can be motivated by other information. For example, the stellar radius might be constrained by stellar models and *Gaia* parallax measurements. This could be reflected as a Gaussian prior on this variable, with mean (maximum probability) at the measured value and the standard deviation reflecting the error bars. Direct applications are discussed throughout Chapters 4 and 5.

2.3   Markov chains

A Markov chain is defined as a sequence of variables $x_0, x_1, ..., x_N, n \in \mathbb{N}$ drawn from the distribution $p(x_{t+1}|x_t)$. Each variable x_{t+1} depends only on the current state x_t, and not on any previous history. This is often referred to as being memory-free.

In a more playful approach, a Markov chain can be explained on the example of the childrens' game 'snakes and ladders' (see e.g. Jacob VanderPlas' blog post[1]). The game board consists of 100 fields, numbered 1 to 100. Certain fields are connected with chutes and ladders, which transport the player down- or upwards to another field. For example, a ladder leads from field 1 to field 38, another ladder leads from field 4 to 14. The players take turns throwing a six-sided dice and advancing their tokens with the goal of being the first to reach field 100.

Viewed probabilistically, the dice score translates into six results. The equally probable results after the first throw of the dice are (dice score $\rightarrow$ resulting field): $1 \rightarrow 38$, $2 \rightarrow 2$, $3 \rightarrow 3$, $4 \rightarrow 14$, $5 \rightarrow 5$, $6 \rightarrow 6$. One can set up a probability vector like this for each field, listing the options where the player will land with what probability. All results depend only on the current position of the player, and are independent from any past history of the game. The game is hence memory-free, and can be modelled as a Markov chain.

---

[1]https://jakevdp.github.io/blog/2017/12/18/simulating-chutes-and-ladders/, online 2 June 2018

2.4   Monte Carlo methods

Monte Carlo methods are sampling techniques, generating random samples to solve a deterministic problem. For example, the expectation $E(x)$ of a probability density function (PDF) $P(x)$ can be approximated by sampling N variables x_i from it:

$$E(x) = \lim_{N \to \infty} \left(\frac{1}{N} \sum_{i=1}^{N} x_i \right) = \int x P(x) \mathrm{d}x. \tag{2.6}$$

An illustrative example is the often referenced 'drunk walker', stumbling out of a bar and looking for the way home. For simplicity, here I first assume the one-dimensional case of a narrow road, and the house being just a few steps down the road. Assuming the drunk walker has no spatial awareness, the probability of taking a left or right step is equal. One can then ask the question: 'How many steps will it take the drunk walker in average to get home?'.

This problem can be easily solved analytically, but also via a Monte Carlo simulation. At each step, we can assume a binary jump function: one step left, or one step right, each with a 50% probability. By running many simulations, we can sample the expected value from the PDF.

The power of a Monte Carlo simulation becomes clear when one chooses more complicated examples. What if the drunk walker is located in a real city, with complicated street networks and obstacles? An analytic approach becomes infeasible, yet drawing random steps from a jump function quickly solves the problem. One could also choose a more realistic jump function, such as a two-dimensional Gaussian to reflect the varying step lengths.

2.5   Markov chain Monte Carlo (MCMC)

A Markov chain Monte Carlo (MCMC) now combines the two approaches discussed in Sections 2.3 and 2.4. When sampling PDFs, the MCMC is constructed such that the chain $x_0, x_1, ..., x_N, n \in \mathbb{N}$ converges to the underlying PDF for $N \to \infty$. MCMC methods are powerful tools for sampling PDFs (see e.g. MacKay, 2003).

This can again be explained on the example of the drunk walker. It is now assumed the drunk walker roughly remembers the direction home. This adds the Markov chain aspect. After each step the walker evaluates if the last move was beneficial or not. Instead of drawing steps randomly in all directions, there is now a favourable direction. Speaking in terms of an optimisation problem, the drunk walker will eventually converge to a stationary state (the home). In the following sections, the principle of MCMC walkers is applied to optimisation problems, such as model fitting data.

2.5.1 Sampling with MCMCs

When sampling PDFs with MCMCs in practice, all steps are recorded in the MCMC 'chain'. The part of the chain before reaching convergence to a stationary state is denoted the 'burn-in' phase. Depending on how far the start point (initial parameter guess) for the MCMC lies from the true parameters, the burn-in phase can be long or short. The evaluated part of the chain yields the desired posterior likelihood of the variable. The intrinsic variation in these is then considered the scatter or 'error bars' of the variable.

Computational implementations of MCMC methods use different sampling algorithms to optimise the exploration of the parameter space. These serve to sample a posterior likelihood distribution $P(\Theta|x)$ by computing the values of $f(x) = P(x|\Theta)P(\Theta)$. As discussed in Section 2.2, this bypasses calculating the evidence. Three common MCMC sampling algorithms are discussed below.

Metropolis-Hastings sampling

The Metropolis-Hastings algorithm (Hastings, 1970; Metropolis et al., 1953) is based on the concept of a random walk. It performs random draws of the parameters Θ from a so-called jumping distribution $g(\Theta'|\Theta_i)$. In practice, this is usually a Gaussian function with mean Θ_i, whose variance determines the jump size s. Thus, an update for each parameter Θ is

suggested as

$$\Theta' = g(\Theta'|\Theta_i) = \mathcal{N}(\Theta_i, s). \tag{2.7}$$

Note how this directly translates into the example of the drunk walker above.

Next, the acceptance ratio $\alpha = f(\Theta'|x)/f(\Theta_i|x) = P(\Theta'|x)/P(\Theta_i|x)$ is calculated. To evaluate acceptance or rejection of this step, a uniform random number $u \in \mathcal{U}(0,1)$ is drawn. If $u < \alpha$, the step is accepted and $\Theta_{i+1} = \Theta'$; otherwise if $u > \alpha$, the step is rejected and $\Theta_{i+1} = \Theta_i$. Again, note how this directly translates into the drunk walker remembering the direction home and rejecting bad steps with a certain probability.

Gibbs sampling

Gibbs sampling (Geman & Geman, 1984) is an optimisation of the Metropolis-Hastings algorithm. If Θ is a large set of parameters and $f(\Theta|x)$ is very complex, it can be too computationally expensive to update all parameters conjointly at each step. Instead, Gibbs sampling updates the parameters one by one using the conditional PDF of each, always taking into account the state of all other parameters.

Affine invariant sampling methods

The concept of an affine invariant sampler was introduced by Goodman & Weare (2010). These samplers enable a computationally efficient sampling of highly skewed likelihood distributions, which result from correlated parameters. Goodman & Weare (2010) motivate this on the simple example of sampling from a two-dimensional Gaussian, which has the form:

$$P(x_1, x_2) \propto \exp\left(-\frac{(x_1 - x_2)^2}{2\varepsilon} - \frac{(x_1 + x_2)^2}{2}\right). \tag{2.8}$$

If $\varepsilon << 1$, the standard Metropolis-Hastings or Gibbs sampling would have to use a jump scale $\sqrt{\varepsilon}$ to converge along the (1,-1)-axis, leading to very slow convergence along the

(1,1)-axis. An affine transformation of this expression can resolve this correlation:

$$P(y_1, y_2) \propto \exp\left(-\frac{y_1^2 + y_2^2}{2}\right) \text{ with } y_1 = \frac{x_1 - x_2}{\sqrt{\varepsilon}} \text{ and } y_2 = x_1 + x_2. \tag{2.9}$$

These methods represent so-called 'ensemble' samplers, which consist of various 'walkers'. This makes them intrinsically different from the 'single particle' samplers discussed above. Each walker is updated not only using its own current value, but with respect to the current value of all walkers in the ensemble (or a sub-set of those). In this thesis, I use the EMCEE software for all MCMC models, which utilises the affine invariant sampling method.

Maximising the likelihood

As discussed, the decision of acceptance or rejection of an MCMC step is based on comparing the likelihoods $f(\Theta'|x)$ and $f(\Theta|x)$. This is generally done using maximum likelihood estimation. Practically, MCMC algorithms make use of the logarithmic likelihoods, as the original likelihood function is expensive to differentiate. As the logarithm is monotonically increasing, this transformation does not influence the optimisation problem. For N data points $x_k \in (x_1, ..., x_N)$, a corresponding data function y_k with errors σ_k, and a model function $M(x)$, the logarithmic likelihood is given as

$$\log L = \sum_{k=1}^{N} \left(\frac{y_k - M(x_k)}{\sigma_k}\right)^2. \tag{2.10}$$

This is based on the assumption that errors follow a Gaussian distribution. In this thesis, I generally fit for the error scaling, leading to the expression:

$$\log L = \sum_{k=1}^{N} \left[\left(\frac{y_k - M(x_k)}{\sigma_k}\right)^2 - \log \sigma_k^{-2}\right]. \tag{2.11}$$

2.5.2 Assessing convergence

Proving that the MCMC chains have converged is an important task, yet often not mathematically possible. In this section, two commonly used criteria are introduced.

Autocorrelation analysis

The samples in the MCMC chain are not independent, but each chain shows an intrinsic autocorrelation (see e.g. Foreman-Mackey et al., 2013; Goodman & Weare, 2010). The number of independent samples can be estimated from the total length of the chain divided by its autocorrelation length. The integrated autocorrelation time gives a convergence criterion by quantifying the variance of the MCMC chain.

The MCMC has the aim of estimating the expected value of the model function $f(\Theta)$ in dependency of the model parameters Θ (denoted as A):

$$A := E[f(\Theta)] = \int f(\Theta)P(\Theta)d\Theta. \tag{2.12}$$

The unknown probability density $P(\Theta)$ is estimated through the MCMC sampling approach, in which N samples are drawn. This leads to an estimation of the expected value, given by the estimator $\hat{A}$ as:

$$\hat{A} = \frac{1}{N}\sum_{n=1}^{N} f(\Theta^{(n)}). \tag{2.13}$$

The variance of the estimator can be expressed as

$$\text{var}(\hat{A}) \approx \frac{\text{var}[f(\Theta)]}{N/\tau}, \tag{2.14}$$

where τ is the integrated autocorrelation length. The ratio N/τ can be interpreted as the effective number of independent samples. Knowledge of τ hence allows to estimate the required number of total samples to achieve the desired variance of the estimator. The integrated autocorrelation length τ is defined as

$$\tau = \sum_{t=-\infty}^{\infty} \frac{C(t)}{C(0)}, \tag{2.15}$$

where $C(t)$ is the auto-covariance function at lag t, given by

$$C(t) = \lim_{t'\to\infty} \text{cov}\left[f(X(t'+t)), f(X(t'))\right]. \tag{2.16}$$

For the practical applications presented in this thesis, the approximate calculation of τ incorporated in EMCEE is used. Convergence of the MCMC chain is then suggested if its length is at least $10 - 100\ \tau$ (Foreman-Mackey et al., 2013).

Gelman-Rubin diagnostic

The Gelman-Rubin diagnostic (Gelman & Rubin, 1992) compares the variance between the mean values of multiple chains (denoted as B/N) and the mean variance within each chain (denoted as W). This uses M independently simulated chains, whereby N is the evaluated length of these chains. The mean and variance within the m-th chain are denoted Θ_m and σ_m, respectively. The sample mean is $\hat{\Theta} = \frac{1}{M}\sum_{m=1}^{M}\Theta_m$. A large discrepancy between B and W suggests the chain is not yet converged. Gelman & Rubin (1992) define B and W as:

$$B = \frac{N}{M-1}\sum_{m=1}^{M}(\Theta_m - \hat{\Theta})^2, \tag{2.17}$$

$$W = \frac{1}{M}\sum_{m=1}^{M}\sigma_m. \tag{2.18}$$

From this, the estimated covariance matrix

$$\hat{V} = \frac{N-1}{N}W + \frac{1}{N}B \tag{2.19}$$

can be calculated. Convergence of the MCMC chain is thus indicated when the posterior variance $\hat{V}$ and the within-chain variance W converge. This is denoted by the potential scale reduction factor (PSRF), $\sqrt{\hat{R}}$, which is defined through:

$$\hat{R} \sim \frac{\hat{V}}{W} \to 1. \tag{2.20}$$

Brooks & Gelman (1998) suggests a refined version, in which they define $\hat{R}_c$ as the criterion:

$$\hat{R}_c = \frac{d+3}{d+1}\hat{R} \to 1, \tag{2.21}$$

where d is defined as $d = 2\hat{V}/\text{var}(\hat{V})$. Brooks & Gelman (1998) suggest that convergence is reached if $\hat{R}_c < 1.2$, while a more strict criterion of $\hat{R}_c < 1.1$ is often used in applications of the test in the literature.

2.5.3 Limitations: model comparison

The MCMC approach is limited in cases where different models should be compared. For an example in the context of exoplanets, it is a common problem in RV studies that one might want to compare the fit of RV data between a single planet and multi planet scenario. This model comparison requires knowledge of the 'Bayes factor', the ratio of the evidence of both models. As MCMCs disregard the Bayesian evidence (see definition in Section 2.2), there is no statistically robust way of performing a model comparison. Approximate computations of the evidence have been suggested, but are beyond the scope of this thesis. A detailed discussion is given in e.g. Weinberg (2010) and references therein.

A model comparison is best addressed by using a 'Nested Sampling' approach (Skilling, 2004) instead of MCMCs. Nested Sampling allows to compute the evidence directly. In the exoplanet context, this then enables to robustly compare various RV models (see Hall et al., 2018). The concept of Nested Sampling, however, is beyond the scope of this thesis, and was not needed or applied for any of the presented studies. The interested reader may be referred to e.g. Feroz et al. (2009); Handley et al. (2015); Skilling (2004) and references therein.

2.6 Gaussian Process regression

This section gives a brief introduction to the complex topic of Gaussian Processes (GPs). The interested reader is referred to classic references such as by Rasmussen & Williams (2005) and Bishop (2006) for a detailed discussion. A gentle introduction for the application to time-series data (such as exoplanet data) is given e.g. by Roberts et al. (2013).

Regression problems typically occur if one wants to describe a set of data points with a model function (see Fig. 2.1A). For a data set (x, y), the measured variable y is described as a function $y = f(x)$ of the variable x. The measurements lie off the idealised model function

by an error ε, which is here assumed to be Gaussian:

$$y = f(x) + \varepsilon \text{ with } \varepsilon \sim \mathcal{N}(0, \sigma^2). \tag{2.22}$$

Here, σ^2 is the variance of the measurement. For example, in a linear regression, $f(x)$ is determined by two parameters Θ_0 and Θ_1, which gives $y = f(x) = \Theta_0 x + \Theta_1$. One can then fit for these parameters, for example by using an MCMC approach.
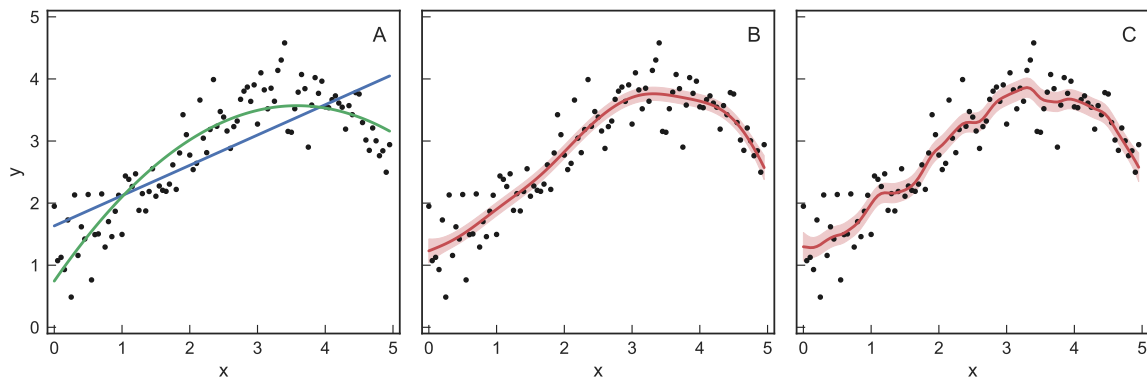
Fig. 2.1 Example of a regression analysis. A) The data set (x, y) is modelled as a linear function $y = f(x) = \Theta_0 x + \Theta_1$ (blue line) and quadratic function $y = f(x) = \Theta_0 x^2 + \Theta_1 x + \Theta_2$ (green line). The model is hence restricted to the chosen parametrisation. B) The data set is modelled via GP regression. An Exponential Squared kernel is chosen, which captures smooth, long-term trends. C) GP regression with a Matern-3/2 kernel, which can capture smooth, long-term trends as well as more stochastic, short-term variations.

The description of the data is restricted to the chosen parametrisation. What if the data is actually a higher-order polynomial, or not a polynomial at all? Extrapolating this fit is hence strongly biased by the chosen fit function.

In GP regression, on the other hand, one does not define an expression for $f(x)$. Instead of fitting for the parameters Θ_i of a chosen model, one fits for a family of functions to determine which $f(x)$ works best (examples in Fig. 2.1B and C). This is a so-called non-parametric approach. This does not imply that there are no parameters; in fact, there are indefinitely many possible functions and parameters. One can therefore think of GP regression as a 'rubber ruler', flexible enough to fit any data set without being constrained to a fixed set of parameters.

In a Bayesian context, a GP can hence be interpreted as a prior on the functions that describe any unknown data set (see e.g. Murphy, 2012). By updating it with measurements of the data y, one gains the posterior of the model. The GP postulates a family of jointly Gaussian functions, in which the relation of data points are described by the covariance matrix, expressed by the kernel $k(x_i, x_j)$. The choice of kernel incorporates that the function values of nearby data points should be very similar. A GP can use different kernels and metrics to evaluate the correlation between data points. The squared distance r^2 between data points x_i and x_j is evaluated for any metric M as

$$r^2 = (x_i - x_j)^T M^{-1} (x_i - x_j). \tag{2.23}$$

In the one-dimensional case (all applications in this thesis), M is simplified to a scalar. One can think of the kernel as determining the 'bendability' of the GP rubber ruler. Certain kernels are well suited to model smooth, long-term variations (a more stiff rubber ruler; see Fig. 2.1B). Other kernels describe more stochastic short-term variations (a very bendable rubber ruler; see Fig. 2.1C).

The choice of GP kernel is a highly non-trivial exercise, and still an active part of ongoing research. A detailed review of kernels can be found in e.g. Duvenaud (2014). In this thesis, I follow common kernel choices which have proven to be robust for problems similar to the ones discussed here. A typical choice to model smooth, long-term variations is for example an 'squared exponential kernel' [2] (Fig. 2.1B):

$$k\left(r^2\right) = e^{-r^2/2}. \tag{2.24}$$

To capture long-term as well as short-term trends, a 'Matern 3/2 kernel' is well suited (Fig. 2.1C):

$$k\left(r^2\right) = \left(1 + 3\sqrt{r^2}\right) e^{-3\sqrt{r^2}}. \tag{2.25}$$

---

[2]also referred to as 'exponentiated quadratic kernel'

This kernel has the advantage that it can describe rougher, more stochastic variations ($\sim |r|$) in addition to a characteristic length/time scale ($\sim e^{-|r|}$).

In practice, the GP is fitted to the data by fine-tuning the so-called 'hyperparameters'. These provide a scaling for r^2 depending on the length/time scales of the data. In a physical context, the hyperparameters can also be interpreted as normalising the data and converting them into dimensionless values.

Expanding on the above examples, one can choose the product of a constant kernel (scaling determined by hyperparameter Θ_1) and a squared exponential kernel (scaling determined by hyperparameter Θ_2) to express the correlation between data points x_i and x_j. This is given as:

$$k\left(x_i, x_j\right) = \Theta_1 e^{-(x_i - x_j)^2/(2\Theta_2)}. \tag{2.26}$$

Likewise, for the product of a constant kernel and a Matern 3/2 kernel we have:

$$k\left(x_i, x_j\right) = \Theta_1 \left(1 + 3\sqrt{(x_i - x_j)^2/\Theta_2}\right) e^{-3\sqrt{(x_i - x_j)^2/\Theta_2}}. \tag{2.27}$$

In both cases, the hyperparameter Θ_1 gives the amplitude of the covariance. The hyperparameter Θ_2 determines the length/time scale of the correlation between data points.

By fitting for the GP hyperparameters, for example with MCMC methods, one can hence explore correlations in the data series. These can then be linked to physical sources, such as stellar variability, weather patterns or systematic instrumental noise.

Chapter 3

Simulating the NGTS Yield of Transiting Planets and False Positives

"Those who do not want to imitate anything, produce nothing."

— Salvador Dalí

3.1 Summary

In this chapter, I present a yield simulator to predict the number and characteristics of planets, false positives and false alarms in transit surveys. The simulator is based on a galactic model and the planet occurrence rates measured by the *Kepler* mission. It takes into account the observation window function and measured noise levels of the investigated survey. Additionally, it includes vetting criteria to identify false positives. I apply this simulator to NGTS, finding that red noise is the main limitation up to 14th magnitude, and that its obtained level determines the expected yield. Assuming a red noise level of $1\,\mathrm{mmag}$, the simulation predicts the following for a four-year survey: 4 ± 3 Super-Earths, 19 ± 5 Small Neptunes, 16 ± 4 Large Neptunes, 55 ± 8 Saturn-sized planets and 150 ± 10 Jupiter-sized planets, along with 4688 ± 45 eclipsing binaries and 843 ± 75 background eclipsing binaries. I characterise the properties of the expected objects, enhancing the early identification of false positives, and discuss follow-up strategies for transiting candidates.

3.2   Introduction

Estimating the yield of a transit experiment provides a way to assess the planet catch, the effect of different observing strategies, and the false positive to planet ratio. Astrophysical objects such as eclipsing binaries (EBs) and background eclipsing binaries (BEBs) frequently mimic transit-like shape variability in the light curve (see Section 1.6). Brown (2003) raised awareness of the contamination impact by false positives in upcoming surveys, but most yield simulations have only focused on the number of planets. As one of the first, Brown & Latham (2008) applied false positive models to predict the yield of the TESS mission. Recently, Sullivan et al. (2015) estimated the planet yield, false positive contamination rates and the success of ad-hoc vetting methods for the TESS mission. In addition to enabling insight into future surveys, yield simulations can be used to evaluate how well current instruments achieve their possibilities, as well as how current observing strategies may be optimised.

I developed a yield simulator with the goal of estimating the planet merit and the impact of false signals applicable to any upcoming transit survey. The simulations specifically take into account red noise[1], false alarms[2] and false positives. In order to assess the impact of various observing strategies, the simulation takes as inputs the target list, telescope parameters, bandpass, field of view, cadence, noise models and detection criteria. It allows to evaluate the impact of various observing strategies and to examine the vetting processes for false positives. I implemented methods examining the transit parameters (depth, shape and duration), secondary eclipses, centroid movement, and the feasibility of planet follow-up and characterisation. I apply the simulator to estimate the yield of planets and false positives for the recent NGTS mission.

This chapter is organised into three major parts. Part one describes the computational layout and the mechanisms of the simulations, which are adaptable to any transit survey. In part two, I verify the simulations on the example of *Kepler*. Part three describes the application of the simulations to NGTS. The simulations and the set of priors are described in Section 3.3. Section 3.4 describes the validation process of my code using the results from

---

[1]systematic noise in the data

[2]transit-like features caused by systematic noise

Kepler. In Section 3.5, I examine the case of NGTS, the effects of different red noise levels and detection criteria, and the expected planets and false positives. I estimated the feasibility to identify false positives with NGTS' photometric data alone, and provide an outlook into the necessary follow-up facilities for planet candidates. Finally, I discuss my findings and draw conclusions in Sections 3.6 and 3.7.

3.3   Layout of the simulations

The overall sketch of the simulation layout as described below is shown in Fig.3.1. The simulation input contains a list of stars in the field of view, as well as the instrument specifications (step 1 in Fig.3.1). An example input file for the application to NGTS can be found in appendix A. From this, I first calculate the collected flux for each object. Second, I randomly assign host stars with planets, and compute the signal characteristics of transiting planets and eclipsing binaries (depth, duration, shape, visibility, and possible dilution; step 2). Third, I calculate the total noise for each observation and compute which systems would be detectable (step 3). Next, I rule out false positives if detectable from photometric data (step 4). This yields the expected planet candidate list. Finally, I assess the feasibility to follow-up planetary signals with RV instruments (step 5).
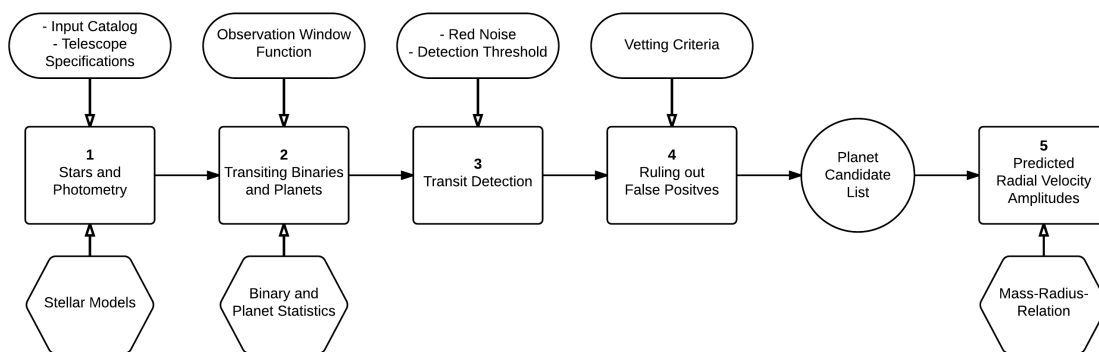
Fig. 3.1 The simulation can be structured in five main modules, containing user input and settings (ovals), observed parameters and models (hexagons), steps of calculations (rectangles), and output files (circle).

3.3.1   Stars and photometry

The simulation considers an input catalog with information about the multiplicity, radius, mass, effective temperature, and magnitude of all stars in the field of view. The input catalog is built using the TRILEGAL galaxy model (Girardi et al., 2005), up to $V = 23$. I keep the preset adjustments of TRILEGAL referring to the standard Milky Way model and simulate binaries with a fraction of 33% (Raghavan et al., 2010). While this value was estimated for solar-type stars, it is also consistent with predictions for low-mass stars given the dispersion reported in the literature (see e.g. Duchêne & Kraus, 2013, and references therein). The binary mass ratio q of the secondary and primary mass, $q = M_s/M_p$, is drawn uniformly between 0.08 and 1. To include higher-order multiples, I randomly select single stars and assign them to be higher-order multiples. This way, in the end the input catalog consists of 56% single stars, 33% binaries and 11% higher order multiples (Raghavan et al., 2010).

From this input catalog, I identify a target list of stars according to magnitude and spectral type. For example, the values for the application to NGTS are listed in Table 3.1 in Section 3.5.1. I assume all input catalog stars are randomly distributed across the field of view. Then I compute the photometric flux using the effective temperatures and V-band magnitudes of the input catalog and the transmission function of the telescope. The stellar parameters are converted into photometric flux using spectrophotometric reference stars from Pickles (1998). The zero-point of the V-band is defined by models of Vega from the Kurucz atlas (Kurucz, 1993). The Johnson V-band model is adopted from Buser & Kurucz (1978). Any other stars lying in the photometric aperture of the target star are considered as background stars for the particular target.

3.3.2   Transiting binaries and planets

Binaries

For all input catalog stars identified as binaries, I draw orbital periods P in days from a log-normal distribution with mean of 4.8 and a standard deviation of 2.3 (Duquennoy & Mayor, 1991). The eccentricities follow a uniform distribution with a maximum eccentricity

given by $e_{max} = 0.4 \cdot \log P - 0.2$ (approximated from Raghavan et al., 2010). Only detached eclipsing binaries are considered using the Roche limits as criteria. Contact eclipsing binaries are evident from the light curves and can be readily ruled out. I do not consider eclipses within triple or higher-order hierarchical eclipsing binaries.

I define orbit and transit parameters following Winn (2011). I consider a binary system, where star 1 denotes the hotter star with higher surface brightness, and star 2 its companion. If star 1 is fully transited by star 2, I compute the transit depth as

$$\delta_1 = \frac{A}{A_1} \cdot \frac{F_1}{F_1 + F_2},$$ (3.1)

where $A = \min(A_1, A_2)$. A_1 and A_2 denote the surface disk area of the two stars, and F_1 and F_2 their flux. In the case of grazing eclipses I replace A with the overlapping area of two circles with radii $R_{1,2}$ and midpoint distance y.

Planets

The planet occurrence rates are based on the results of the *Kepler* mission, as derived by Fressin et al. (2013) for FGK stars, and by Dressing & Charbonneau (2015) for small planets around M dwarfs. While recent results have made progress on long period and small planets (Burke et al., 2015), Fressin et al. (2013) still provides the most complete study in the planet regime targeted by all-sky surveys. The occurrence rates denote the average number of planets per star binned by planet radius and orbital period. In Fressin et al. (2013), these are discretely sampled in radius and period: Earths (< 1.25 $R_\oplus$), Super-Earths (< 2 $R_\oplus$), Small Neptunes (< 4 $R_\oplus$), Large Neptunes (< 6 $R_\oplus$), and giant planets (< 22 $R_\oplus$), as well as ten logarithmically spaced period ranges. I randomly assign a value for period and radius within each discrete interval. The period is drawn within each interval from a logarithmic distribution. I draw the radius within each interval from a uniform distribution, except for the last interval (> 6 $R_\oplus$), in which I draw from a logarithmic distribution for consistency with empirical findings (see e.g. Grether & Lineweaver, 2006, and Exoplanetarchive[3]).

---

[3] http://exoplanetarchive.ipac.caltech.edu/ (online 26 March 2018)

I assign planets to all stars, single or binary, in the input catalog according to the occurrence rate (which may be greater than 1), except when binary systems have orbital periods shorter than 5 days. Although these short-orbit binary systems are frequent (Slawson et al., 2011) and can theoretically host circumbinary planets, these planets are likely undetectable (Martin et al., 2015; Muñoz & Lai, 2015). This is because compact binaries likely migrated in from wider orbits, leading to planets being consumed by their stars or ejected from the system. Surviving planets are expected to be small, low-mass and highly misaligned, and hence difficult to detect, as the stellar signals would dominate. These constrains lead to a smaller number of assigned planets around close-in binaries than for wide binaries or single stars. Note that there is no evidence that wide binaries affect the occurrence rate of short orbit planets (Deacon et al., 2016). I do not consider planets around the 11% of higher order multiples in my target list, as in most cases their transit signals will be diluted too much by the other stars in the system to be detectable. In cases where there is more than one planet assigned to the same star, the orbital parameters of planets are drawn completely independently. This choice is made to avoid influencing the yield by setting orbital stability criteria for multiplanetary systems. This ensures the same statistical average over all stars of the field, in line with the occurence rates representing an average over many systems. For all remaining planets in binary systems I compute stability criteria following Holman & Wiegert (1999) and reject planets in unstable orbits ($< 1\%$ of all planets).

I investigate the impact of eccentric planetary orbits by assigning various mean eccentricities between 0 and 0.5 and find a consistent planet yield as with circular orbits. I therefore employ circular orbits for all planets considering the short orbit sensitivity of all-sky transit surveys. I define orbit and transit parameters following Winn (2011). For grazing geometry, the overlapping area of the two objects is computed instead. If the host system is part of a binary system, I account for dilution by the other star.

Observation Window Function

For each transiting planet I estimate the number of transits that can be detected. The time of the first transit is set randomly between 0 and the orbital period P. To compute the

observation window I calculate the average visibility duration per night of each field. I implement average weather information at the telescope location and reject a certain fraction of nights to simulate bad conditions.

Dilution

Background stars in the aperture of a target star affect its extracted photometry. First, they decrease the transit depth of a planet orbiting the target star and might make the signal undetectable. Second, if the target star or any background star is an eclipsing binary, its eclipse depth will be decreased and it may appear planet-like. The dilution D for a certain source is the ratio of its stellar flux F_0 and the total flux in the aperture $\sum_i F_i$. I evaluate D for each system, with F_0 being either the flux of a single star or the whole multiple system in which the transit/eclipse occurs. The theoretical transit depth δ_0 following Winn (2011) is then reduced to the measured transit depth

$$\delta = \delta_0 \cdot \frac{F_0}{\sum_i F_i}. \tag{3.2}$$

3.3.3   Transit detection

The total noise of the extracted photometric flux can be described as a composition of uncorrelated and correlated noise, referred to as white and red noise (Pont et al., 2006). White noise scales with exposure time, aperture, and flux. I calculate it as the sum of individual white noise sources,

$$\sigma_{\mathrm{white}}^2 = t_{\mathrm{exp}} N_\star + n_{\mathrm{pix}} \left(t_{\mathrm{exp}} N_{\mathrm{sky}} + t_{\mathrm{exp}} N_{\mathrm{dark}} + N_{\mathrm{read}}^2 \right) + \sigma_{\mathrm{scint}}^2, \tag{3.3}$$

where n_{pix} is the number of pixels in the aperture, and t_{exp} the exposure time. $N_\star$ is the photon count received from a given source and N_{sky} the sky background. N_{dark} and N_{read} are the counts contributed by dark and readout noise. σ_{scint} describes the scintillation noise, evaluated following Dravins et al. (1998).

White noise averages out by the square root of the number of exposures per transit, N_{exp}. The total noise in one transit is given by the squared quadratic sum of the binned white noise and the red noise. Red noise is composed of various sources that are not entirely known, such as weather patterns (if ground-based), correlated astrophysical and instrumental noise, and software influence. I assume the driving red noise patterns are correlated on one-night time scales, and are to first order uncorrelated over timescales of multiple days. Therefore, red noise of measurements on different days (or different transits) average out, and I get the total noise

$$\sigma_{\text{tot}}^2 = \frac{\sigma_{\text{white}}^2/N_{\text{exp}} + \sigma_{\text{red}}^2}{N_{\text{tr}}} \tag{3.4}$$

for a phase-folded light curve with N_{tr} transit events.

I require two criteria for the detection of a transit signal. First, at least three transit events must be visible, $N_{\text{tr}} \geq 3$. Second, the signal-to-noise ratio, SNR, of the phase-folded light curve must exceed a minimum requirement. I refer to this minimum SNR as the *detection threshold*, in the following denoted by the acronym DT:

$$SNR = \frac{\delta_{\text{tr/occ}}}{\sigma_{\text{tot}}} > \text{DT}. \tag{3.5}$$

In here, $\delta_{\text{tr/occ}}$ denotes the depth of the transit or occultation signal.

3.3.4 Ruling out false positives

To identify false positives (see Section 1.6) I define criteria based on the work of the *Kepler* team (Batalha et al. 2010 and 2012, Bryson et al. 2013). I consider that a transit signal event originates from a false positive if:

- I measure transit depths greater than a given threshold (2 R_{Jup}), assuming the radius of the host star is known (2 R_{Jup} is the maximum planet size in the simulations) .

- I detect a secondary eclipse δ_{occ} and clearly distinguish it from the transit signal δ_{tra} if both criteria are met:

$$\frac{\delta_{\mathrm{occ}}}{\sigma_{\mathrm{occ}}} > \mathrm{DT} \quad \text{and} \quad \frac{\delta_{\mathrm{tra}} - \delta_{\mathrm{occ}}}{\sqrt{\sigma_{\mathrm{tra}}^2 + \sigma_{\mathrm{occ}}^2}} > \mathrm{DT}. \qquad (3.6)$$

  As introduced in section 3.3.3, DT denotes the detection threshold, and σ_{tra}^2 and σ_{occ}^2 the noise of the transit and occultation signals.

- there are ellipsoidal variations in the light curve, a typical feature of close binaries. I use the criteria from Sullivan et al. (2015) for the simulations of the TESS yield and employ the model of photometric variations from Mazeh (2008), using limb darkening from Claret et al. (2012) and Claret et al. (2013) as well as gravity darkening from Lucy (1967) to calculate the signal caused by ellipsoidal variations.

- a V-shape is clearly detectable in the light curve. I assume this is the case if the in-/egress time equals the transit duration (i.e. no flat bottom), and if the target is less than 10% diluted (i.e. no noise being introduced by blended light). Given that planet transits can be V-shaped as well, this criteria cannot be used alone (see Section 3.5.5).

- during the eclipse the center of flux in the aperture (centroid) shifts more than a given fraction of a pixel. This aims to identify BEBs.

- the transit duration is significantly different than what is expected for a planet. For this purpose I compare the detected transit duration with the maximum transit duration of a gas giant planet (2 R_{Jup}) orbiting the target star with the detected period and impact parameter $b = 0$.

3.3.5 Predicted RV amplitudes

Assessing the feasibility of RV follow-up for transit surveys is important to anticipate follow-up strategies. To estimate planet masses from radii, I try to reflect the empirical

mass-radius distribution of known exoplanets[4]. I assume a radius versus mass relationship following Weiss & Marcy (2014) for objects below 3 $R_\oplus$. For planets of 3-6 $R_\oplus$ I adopt a Neptune density of $\rho_{\text{Neptune}} = 1.64\,\text{g/cm}^3$. For 6-11 $R_\oplus$ I adopt a Jupiter density of $\rho_{\text{Jupiter}} = 1.33\,\text{g/cm}^3$, and for larger planets a Jupiter mass of $M_{\text{Jup}} = 1.898 \times 10^{27}\,\text{kg}$ as a mean value. To reflect the intrinsic diversity of planetary composition and structure, I distribute the masses following a log-normal distribution with deviation 0.5 around the mean. Finally, I estimate the RV semi-amplitude using the parameters assigned to the planet systems and compare to the limits of current facilities.

3.4   Verifying the simulation on the example of *Kepler*

Using my simulations, I estimate the yield of *Kepler* and compare my results to the actual candidates and confirmed planets. I use two approaches: 1) I draw the target stars from version 10 of the *Kepler* Input Catalog (Brown et al., 2011), and use the TRILEGAL galaxy model to simulate background stars and distribute them randomly in the *Kepler* field of view; 2) I solely use TRILEGAL and create an ad-hoc target list from all FGKM stars brighter than $V = 15$. In both cases, the CCD parameters and noise levels of *Kepler* are adopted from Gilliland et al. (2011) and the *Kepler* bandpass from Koch et al. (2010).

I find that the two approaches are consistent in their yield predictions. In both cases I obtain a total of 3000 planets to be discovered with *Kepler*. These comprise 600 Earths, 1000 Super-Earths, 1000 Small Neptunes, 100 Large Neptunes, and 200 giant planets. Currently there are 4500 objects listed as *Kepler* candidates, out of which 2300 have been confirmed as planets so far[5].

When comparing the numbers of *Kepler* candidates and confirmed *Kepler* planets with the simulated yield, I find a good agreement. First, the total number of simulated planets matches the actual findings. Second, the balance of planet types is in agreement with the statistics drawn from both the *Kepler* candidates as well as the confirmed *Kepler* planets. These results hence verify my simulation models and assumptions. The code solely requires

---

[4]http://exoplanetarchive.ipac.caltech.edu/ (online 2 June 2018)
[5]http://exoplanetarchive.ipac.caltech.edu/ (online 26 March 2018)

changing a set of priors to be used for other transit surveys. These priors contain the target list, telescope bandpass, noise levels, as well as the observation window and strategy.

3.5   Estimating the yield of NGTS

3.5.1   NGTS facility, target list and background stars

The ground-based NGTS facility is made of twelve independent 20 cm telescopes, each with a 7.4 sq.deg. field of view (see Section 1.9). In my yield simulation I consider the situation where each telescope observes a separate neighboring field, such that the total field of view is 88.8 sq.deg. combined (hereafter called *NGTS-field*). I assume the survey covers three different NGTS-fields per year within four years of operation. In total, 12 NGTS-fields will be observed. In Paranal, in average 78% of the night time is of photometric quality. Most of the year one night is usually either completely photometric or not. A typical night lasts 10.5 h during winter and 7.5 h during summer[6]. Considering the observation duration of an NGTS-field is four months and detectable transit periods are less than two weeks, I assume all phase-folded light curves will be randomly uniformly sampled. I select a typical NGTS-field at $l = 285°, b = +20°$, which is representative of the targeted stellar population. The target selection criteria are shown in Table 3.1. The simulation input file I employ to model NGTS can be found in appendix A.

3.5.2   Red noise as the dominant limitation

I compute the white noise using Eq. 3.3 and the parameters shown in Table 3.1. Based on the design of NGTS, I consider circular apertures with a 3 pixel radius. Since the sky noise varies strongly with lunar phase, I adopt the median value during a lunar cycle. I compute the scintillation noise using Dravins et al. (1998) for 20 cm telescopes, an average airmass of 1.5 and location at 2400 m above sea level. Scintillation noise is the main white noise component for a single exposure for stars brighter than $V = 11$ (Fig. 3.2). For fainter targets,

---

[6]https://www.eso.org/sci/facilities/paranal (online 26 March 2018)

Table 3.1 Settings for NGTS in the yield simulation, based on observed data from test and commissioning phases (Walker, 2013, and private correspondence within the NGTS consortium).

Target list			Noise levels		
V	< 15		$N_{\text{sky}}^{\text{new moon}}$	$= 65$	$\mathrm{e^- s^{-1} pix^{-1}}$
$R_\star$	< 2	$R_\odot$	$N_{\text{sky}}^{\text{full moon}}$	$= 600$	$\mathrm{e^- s^{-1} pix^{-1}}$
T_{eff}	$< 10^5$	K	$N_{\text{sky}}^{\text{median}}$	$= 125$	$\mathrm{e^- s^{-1} pix^{-1}}$
$\log g$	< 6.5		N_{dark}	$= 0.06$	$\mathrm{e^- s^{-1} pix^{-1}}$
			N_{read}	$= 10$	$\mathrm{e^- pix^{-1}}$
			σ_{red}	$= 0 - 2$	mmag

CCD parameters	
t_{exp}	$= 10$ s
t_{read}	$= 1.49$ s

stellar and background noise become driving factors, with the latter dominating at the faint end for $V > 13.5$.

Correlated noise and systematics, referred to as red noise, affect photometric measurements on timescales comparable to the transit duration (few hours). NGTS tests in Geneva and La Palma demonstrated its ability to achieve 1 mmag sensitivity and better (Wheatley et al., 2013). The upper panel of Fig. 3.3 illustrates the white noise binned up per single transit, $\sigma_{\text{white}}/N_{\text{exp}}$ (Section 3.3.3). Considering a single-transit, a red noise level of 1 mmag dominates the total noise for objects $V < 14$, a red noise of 0.5 mmag dominates for objects $V < 13$. Note that for phase-folded light curves of bright targets, a white noise model would underestimate the total noise by up to an order of magnitude, compared to a model taking 1 mmag of red noise into account (Fig. 3.3, lower panel).

3.5.3 Choosing a minimum detection threshold

The choice of the *detection threshold* DT (introduced in section 3.3.3), the minimum signal-to-noise ratio required to trigger a detection, has a significant impact on the expected yield. A high detection threshold leads to non-detection of small planets. On the contrary, lowering the detection threshold increases the number of false alarms caused by red noise. The impact
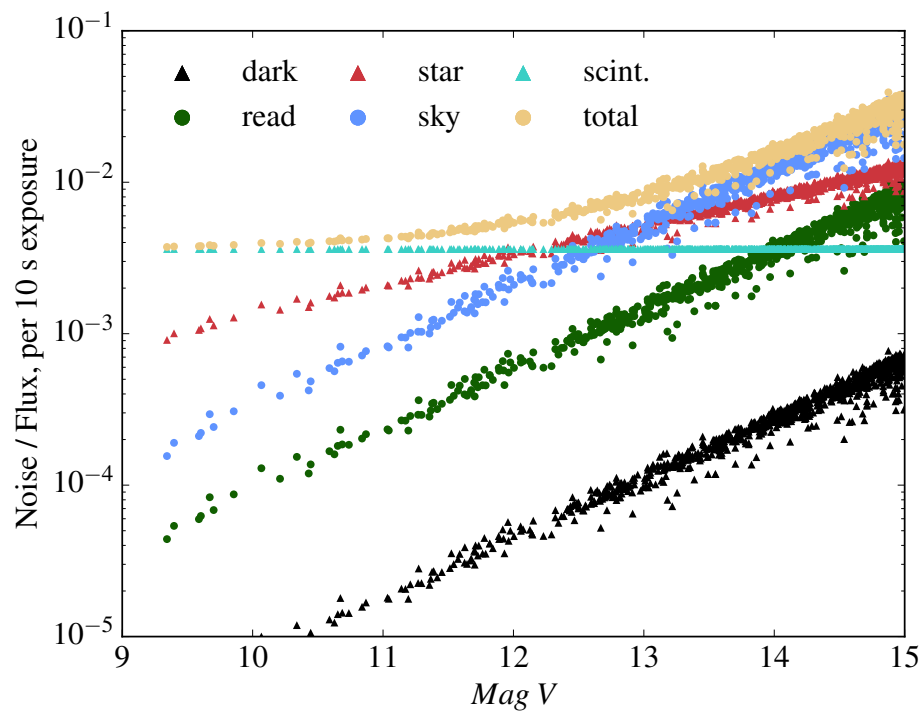
Fig. 3.2 NGTS' white noise components. Values are calculated for each star in the simulated run time using Eq. 3.3, the stellar flux (Section 3.3.1) and empirical values for sky, dark and readout counts (Table 3.1).
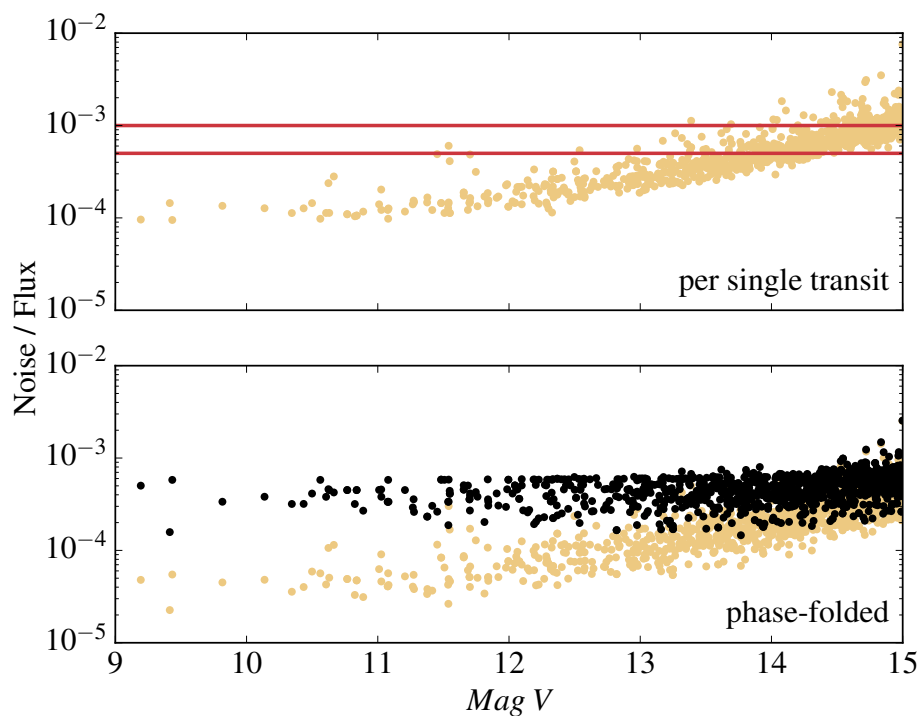
Fig. 3.3 NGTS' white and red noise. Upper panel: white noise (yellow circles) binned over all exposures in one single transit with typical transit timescales of $1-4$ h. Red lines indicate the impact of red noise levels at 0.5 mmag and 1 mmag. Lower panel: white noise (yellow circles) and total noise (i.e. white noise and 1 mmag red noise; black circles) for phase-folded light curves.

of red noise depends on the timescale considered. In this Section, I estimate the optimal detection threshold for NGTS as a function of the estimated number of false alarms.

To estimate the number of false alarms, I begin my argument with a time series that consists of N_{tot} data points. Each point corresponds to an average of the measurements taken over a duration equal to a typical transit duration ($1 - 4$ h). The chance that Gaussian noise causes one data point to lie off the mean (looking like a transit) by a standard deviation more than $x\,\sigma$ is given by

$$p_{\text{outlier}}(x) = \frac{1 - \text{erf}(x/\sqrt{2})}{2}, \tag{3.7}$$

whereby erf denotes the error function. I assume there is a number of $N \geq 3$ outliers in the time series. In order to mimic a transit pattern, these N outliers must be distributed in a time periodic manner. The probability for such a configuration is given by

$$p_{\text{N outliers}} = \left(p_{\text{outlier}}(x) \cdot \frac{N_{\text{tot}}}{N} \right)^2 \cdot p_{\text{outlier}}(x)^{N-2} \quad (N \geq 3). \tag{3.8}$$

In here, the first factor ($p_{\text{outlier}}(x) \cdot \frac{N_{\text{tot}}}{N}$) corresponds to the probability of the first and last outlier. The time periodicity is defined by the total number of outliers and the positions of the first and last outlier in the time series. Consequently, the outliers inbetween have determined locations in the time series and the probability of this to happen is expressed by the second term of the equation.

Fig. 3.4 illustrates this on the example of $N = 3$ transit-like outliers. The data is simulated to mimic one month of NGTS observations, binned into 1 h bins. Each night is simulated to be 7 h long, leading to $N_{\text{tot}} = 210$ data points. The first outlier may thus be located anywhere in the first third of the time series ($N_{\text{tot}}/N = 210/3 = 70$ possible locations), while the last outlier may be located anywhere in the last third of the time series (again $N_{\text{tot}}/N = 210/3 = 70$ possible locations). The second outlier has to lie exactly in the middle

between the first and last outlier to fulfil the periodicity requirement. This leads to

$$p_{3 \text{ outliers}} = \left(p_{\text{outlier}}(x) \cdot \frac{210}{3} \right)^2 \cdot p_{\text{outlier}}(x)^1. \tag{3.9}$$
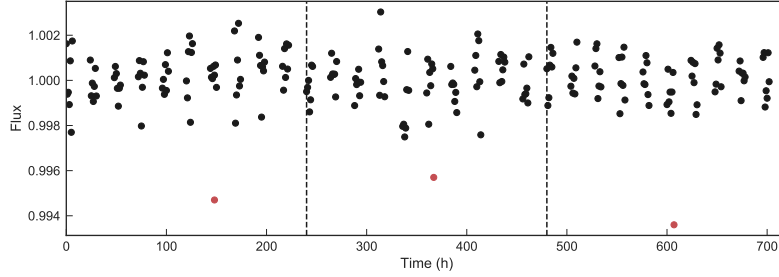
Fig. 3.4 Example of the method to estimate false alarm pollution. To mimic the box-least squares transit search, the simulated data resembles one month of NGTS data in 1 h bins. False alarms may be caused by periodically distributed outliers. In the case of $N = 3$ outliers (red circles), the first and third outlier can lie anywhere at the beginning and end of the light curve. The third outlier has to fulfil the periodicity requirement and hence lie exactly in between.

For NGTS, the total error on each data point is dominated by red noise (see Section 3.5.2). Assuming red noise is uncorrelated on multi-day timescales and follows a Gaussian error distribution, it averages out with the number of transit events, and I can approximate $x \approx DT/\sqrt{N}$. For example, with a detection threshold $DT = 5$ and requiring $N = 3$ outliers, from Eq. 3.7 follows that $p_{\text{outlier}}(x) \approx 1.9 \times 10^{-3}$. In my estimation for NGTS I have $t_{\text{total}} \approx 885 \text{ h}$. Assuming transit-like timescales $T \approx 2 \text{ h}$ this leads to $N_{\text{tot}} \approx 440$. Finally, with the example of $N = 3$ outliers I obtain from Eq. 3.8 that $p_{N=3 \text{ outliers}} \approx 1.7 \times 10^{-4}$.

The false alarm probability for one time series of data points is then the sum over $p_{N \text{ outliers}}$ for all possible N, which happens to converge quickly with increasing N. As a false alarm can be triggered for each object in the target list, the total number of false alarms, N_{FA}, scales with the number of objects in the observed field, N_{obj}, and the number of covered NGTS-fields, leading to

$$N_{FA} = \sum_{\text{fields}} \left[\left(\sum_{N=3}^{N_{max}} p_{N \text{ outliers}} \right) \cdot N_{\text{obj}} \right]. \tag{3.10}$$

I compute Eq. 3.10 for a range of typical transit-like timescales from $T = 1 - 4$ h to evaluate the impact of the detection threshold on the yield versus false alarms. With a total of 12 NGTS-fields in 4 years, each containing $N_{\text{obj}} \sim 10^5$, a detection threshold DT $= 5$ leads to on the order of 10^3 false alarm signals.

3.5.4   Expected yield and major influencing factors

A multitude of Neptunes and giants

I categorise the yield by object categories: EBs, BEBs, and planet types (shown in Table 3.2). Note that this choice is made to match the classification in Fressin et al. (2013), although I point out that recent studies suggest the dividing line between rocky/volatile-rich planets and icy planets lies around 1.6 $R_\oplus$ (Fulton et al., 2017; Owen & Wu, 2017; Rogers, 2015). For the application to NGTS, I subdivide the category of giant planets into Saturns (6-10 $R_\oplus$) and Jupiters (10-22 $R_\oplus$). The simulation over the entire survey time of four years is repeated ten times using the same parameters and input to estimate the mean values and standard deviations of the total number of expected planets and false positives (Fig. 3.5). I account for uncertainties in the planet and binary priors via error propagation. Statistical errors caused by re-running the TRILEGAL galaxy model for the same field are found to be negligible in comparison. NGTS' combined fields over four years contain tens of thousands of planets and binary systems that transit in the line of sight (Fig. 3.5). After accounting for visibility, noise, and detection criteria, only a small fraction triggers a detectable signal. A detection threshold DT $= 5$ for a 1 mmag red noise leads to the detection of ~ 35 small and large Neptunes, as well as 200 giant planets.

Table 3.2 Planet classification based on the radius.

Super-Earths	1.25	$-$ 2	$R_\oplus$
Small Neptunes	2	$-$ 4	$R_\oplus$
Large Neptunes	4	$-$ 6	$R_\oplus$
Saturns	6	$-$ 10	$R_\oplus$
Jupiters	10	$-$ 22	$R_\oplus$
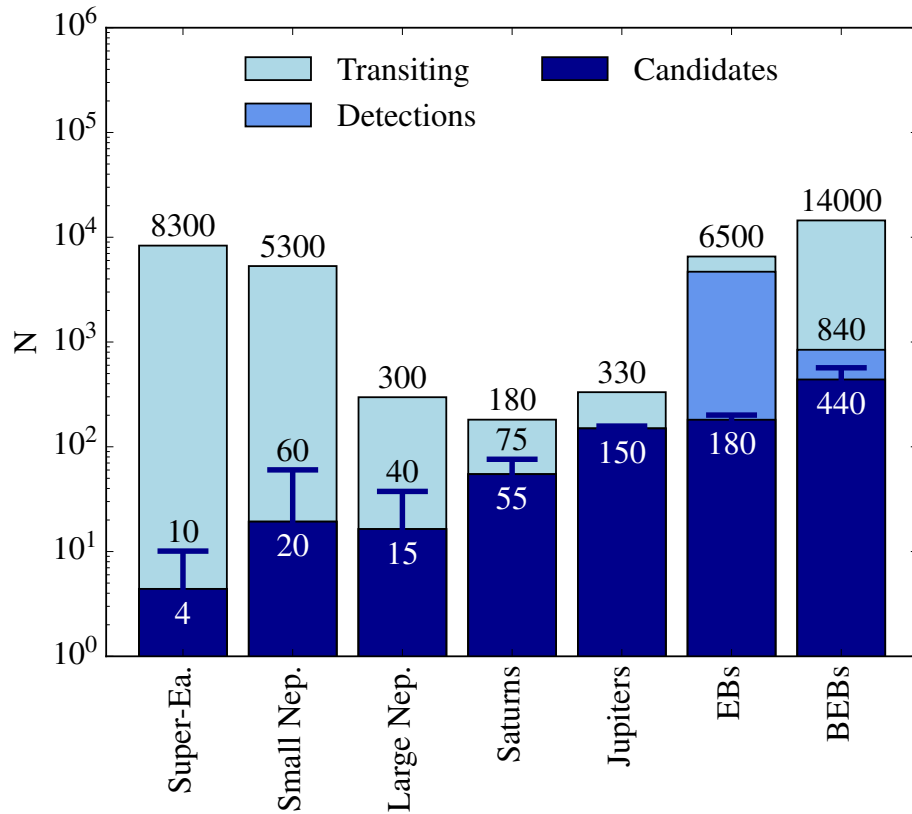
Fig. 3.5 Expected Yield for NGTS' planets (see Table 3.2) and false positives, i.e. EBs and BEBs. Light blue: objects undergoing a transit in the line of sight with orbital periods shorter than 20 days. Blue: Objects that can be detected with a detection threshold DT = 5 for a red noise level of 1 mmag. Dark blue: planetary candidates that remain from the former group after applying the rule-out criteria for false positives described in Section 3.3.4. As all planets pass the rule-out criteria, all planet detections are classified as candidates. The false positives erroneously passing the vetting are misclassified as NGTS planet candidates. They need follow-up with additional instruments before they can be identified. Blue lines indicate the possible yield if a red noise level of 0.5 mmag can be reached. All values are averaged over ten simulation runs. Uncertainties are indicated in Table 3.3.

Impact of red noise and detection criteria

The impact of the red noise level and detection threshold is significant for Neptune-sized planets (Table 3.3). Decreasing the red noise from 1 mmag to 0.5 mmag increases the sensitivity for small planets by a factor of three (see also Fig. 3.5). Completely omitting red noise leads to $250 - 300$ additional small planets. On the other hand, increased red noise levels result in a loss of most small planets.

Maintaining the assumption of a 1 mmag red noise and reducing the detection threshold from DT = 5 to 3 leads to a comparable increase as dividing the red noise by two, but increases the number of false alarms by several magnitudes as discussed in Section 3.5.3. In contrast, increasing the detection threshold from DT = 5 to 7 leads to the loss of small planets comparable to doubling the red noise.

For the following Sections, I assume a detection threshold DT = 5 and, consistent with the design goal of NGTS, a 1 mmag red noise, unless otherwise stated.

Table 3.3 Expected yield for NGTS under different assumptions of the red noise. The table shows all planet classes, false positives before the vetting process described in Section 3.3.4 (EB before, BEB before), and false positives that remain unidentified after the vetting process (EB after, BEB after). Shown values are the mean and standard deviation averaged over 10 simulation runs, including any uncertainties on the priors.

	2 mmag	1 mmag	0.5 mmag	0 mmag
Super-Earths	1 ± 1	4 ± 3	10 ± 3	28 ± 3
Small Nep.	5 ± 2	19 ± 5	60 ± 10	229 ± 20
Large Nep.	4 ± 1	16 ± 4	38 ± 4	69 ± 6
Saturns	28 ± 5	55 ± 8	76 ± 10	86 ± 10
Jupiters	129 ± 9	150 ± 10	158 ± 11	161 ± 10
EB before	4719 ± 45	4688 ± 45	4708 ± 46	4719 ± 45
BEB before	1070 ± 88	843 ± 75	972 ± 83	1070 ± 88
EB after	211 ± 12	181 ± 12	201 ± 12	211 ± 12
BEB after	665 ± 51	439 ± 37	568 ± 47	665 ± 51

3.5.5   False positives and false negatives

NGTS finds a significant number of false positives, consisting of 4700 EBs and 850 of BEBs (Table 3.3, Fig. 3.5). To copy the screening process to identify them, I use the series of criteria described in Section 3.3.4. I only vet target stars for ellipsoidal variations, assuming light curve features of diluted background stars are undetectable with NGTS. The centroiding sensitivity for NGTS is set to 1/100 pixel.

The most efficient criteria are depth, secondary eclipses and ellipsoidal variations for EBs, as well as centroiding and secondary eclipses for BEBs (Fig. 3.6). Overall, I estimate that 96% of EBs and 48% of BEBs can be identified by the vetting process. These values include vetting for the transit duration, which can be used to identify 5% of false positives, including 2% that cannot be detected with another method. V-shaped transits can be detected for 54% of EBs, including 5% that cannot be ruled out with other methods. Here, I do not use the V-shape alone to reject an object, as planets can cause V-shaped transits as well.
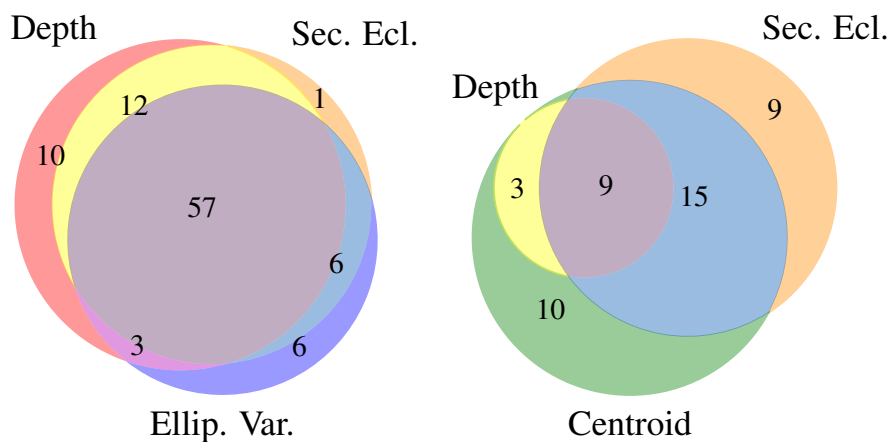
Fig. 3.6 Percentage of false positives identified with different rule-out methods for EBs (left) and BEBs (right). Overlapping regions are designated by color combination. The relative error on all values is $\leq 10\%$. For example, in total 37% (10%+15%+9%+3%) of BEBs can be identified by the centroid method. This includes 10% of BEBs which can only be identified by centroiding. 9% of BEBs can be identified by centroiding, depth and secondary eclipse criteria at the same time.

While individual criteria can already hint towards possible false positives, at least two criteria can be met in parallel for about three quarters of all EBs and one quarter of all BEBs.

All criteria are effective for a wide range of EBs, but are less applicable for systems with faint secondaries. Faint BEBs are strongly diluted, which decreases the ability to identify them with any method.

The search for false positives can lead to false negatives. Giant planets undergoing grazing eclipses can still trigger detectable NGTS signals. I estimate 10% of all planet detections show a distinguishable V-shape. The transit depth is a reliable measure assuming the stellar properties of the target star are well-known. Secondary eclipses, ellipsoidal variations and centroid shifts for planets are not expected to be detectable with NGTS.

3.5.6   Characteristics of NGTS candidates

Distinguishing remaining false positives from planets

After the candidate vetting process described above, the majority of false positives will be identified but the undetected ones may still outnumber the planet candidates. EBs that remain undetected in the candidate list are expected to consist of binaries with low mass companions, such as M-stars or Brown Dwarf secondaries (Fig. 3.7). Small M stars or Brown Dwarfs are the same size as gas giants (Fortney et al., 2011) and hence pollute the sample of giant planets but scarcely affect the population of smaller planets (Fig. 3.8). These systems cannot be ruled out based on a transit light curve, but need RV follow-up and mass measurements.

Remaining BEBs can show more variety due to different degrees of dilution of their transit signals (Fig. 3.7). They can mimic planetary radii over a large range but especially pollute the sample of planets in the Neptune-sized regime (Fig. 3.8). In addition, this is the regime where statistical false alarms will pollute the sample most.

Fig. 3.8 further illustrates that it will be difficult to filter out planets below 2-day orbital periods. The planet occurrence rates suggest planets are unlikely to have orbital periods of less than $1 - 2$ days (Dressing & Charbonneau, 2015; Fressin et al., 2013). Many binary systems, in contrast, are known to orbit on time scales of only a few hours, including detached systems (see e.g. Norton et al., 2011; Soszyński et al., 2015).
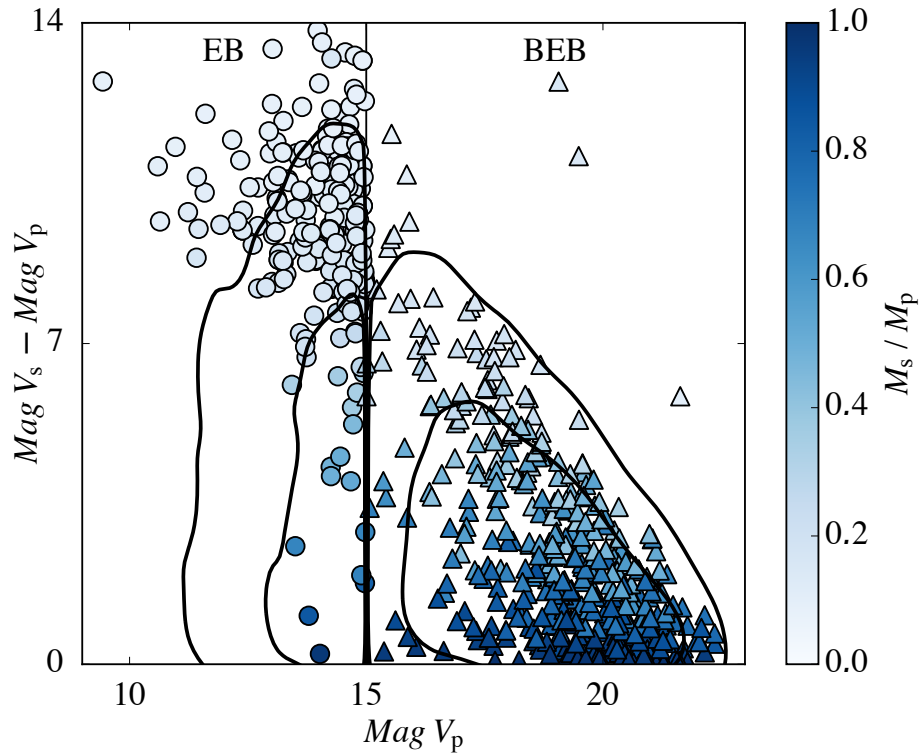
Fig. 3.7 EBs (circles) and BEBs (triangles) that are not identified by the light curve vetting process and need follow-up observations, shown against the magnitudes of the primary and secondary. The color-coding displays the binary mass ratio M_s/M_p of the secondary to primary. Contour lines illustrate the original distribution of false positives before the vetting process. Note that the dividing line at Mag $V_p = 15$ is a consequence of how targets (and thus EBs and BEBs) are defined in the simulation. EBs are targets whose primary is brighter than Mag $V_p \leq 15$. BEBs are blended into the aperture of a target, and have per definition Mag $V_p > 15$.
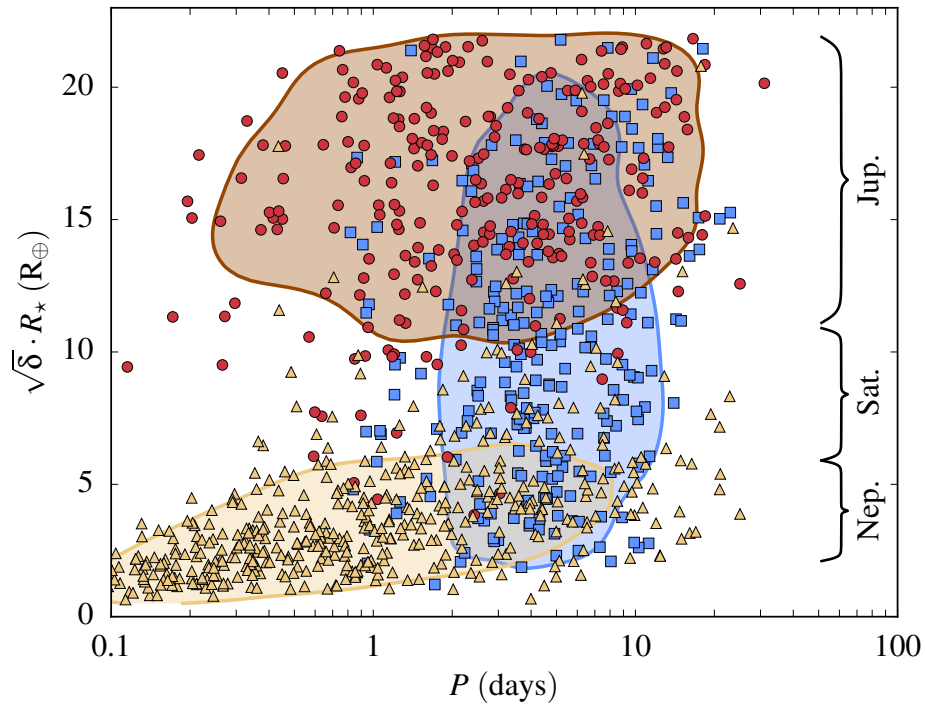
Fig. 3.8 Objects in the expected NGTS candidate list after the photometric vetting process. The measured apparent radius without correction for dilution or grazing eclipses is shown. Planets (blue squares), EBs (red circles) and BEBs (orange triangles) occupy different regions of the parameters space in apparent transit radius and orbital period. Symbols denote the objects in one simulation run for a red noise of 1 mmag, 1 σ contours are calculated over ten simulation runs. Note that the three distinct clumps are a direct consequence of the occurrence rates of each species (planet, EB, BEB) as well as the efficiency of the candidate vetting methods. Planet occurrence rates predict a sparsity of orbits below 1-2 days. EBs that erroneously pass the candidate vetting have low-mass companions with similar sizes to gas giant planets. BEBs passing the vetting will be strongly diluted, mimicking the transit signals of Neptune-sized planets.

Expected planet properties

$97 \pm 1\%$ of all predicted NGTS planets are found at orbital periods shorter than two weeks, and $60 \pm 3\%$ orbit in less than 5 days (Fig. 3.9). Decreasing the red noise by half leads to an increase of NGTS' sensitivity to detect small planets with longer orbital periods. K stars are found to be typical hosts for NGTS' smallest planets, such as Small Neptunes and Super-Earths (Figs. 3.9 and 3.10). Large Neptunes can be detected around G stars. Fig. 3.10 further illustrates the sensitivity cutoff of NGTS as a function of planet over stellar radius. The paucity of giant planets detected around small stars is a direct consequence of the planet occurrence rates estimated from the results of the *Kepler* mission (Dressing & Charbonneau, 2015; Fressin et al., 2013).

I estimate that $57 \pm 17\%$ of planets detected with NGTS orbit single stars, and $34 \pm 12\%$ ($8 \pm 5\%$) orbit the primary (secondary) stars of binary systems. Most of the planets detected in binary systems are Jupiters and inflated giants, as only large planets are still detectable given the strong dilution of the transit signal by the light of the binary companion. Dilution decreases the transit depth by 20% or more for 21% of Jupiters, 11% of Saturns and 8% of smaller planets. Circumbinary planets are not detected due to the limited sensitivity of NGTS for long-period transiting planets.

20 ± 5 planets are detected with NGTS around background stars. These consist of systems with a faint target star and a small background star orbited by an inflated giant planet.

RV follow-up and characterisation of NGTS planets

I estimate the planetary masses and RV signals as per Section 3.3.5. The bulk of detected planets lies in magnitude between Corot 7b and GJ 1214b (Fig. 3.11). Instruments like Coralie (Queloz et al., 2000) are important for vetting false positives, and enable mass measurement of $43 \pm 2\%$ of predicted Jupiter-sized planets. HARPS (Mayor et al., 2003) can confirm $99 \pm 0\%$ of all predicted Jupiter-sized planets, $92 \pm 1\%$ of Saturn-sized planets, and $51 \pm 2\%$ of Large Neptunes. ESPRESSO (Pepe et al., 2014) will reach the sensitivity to measure RV signals of all NGTS planets. It is worth mentioning that most stars hosting small
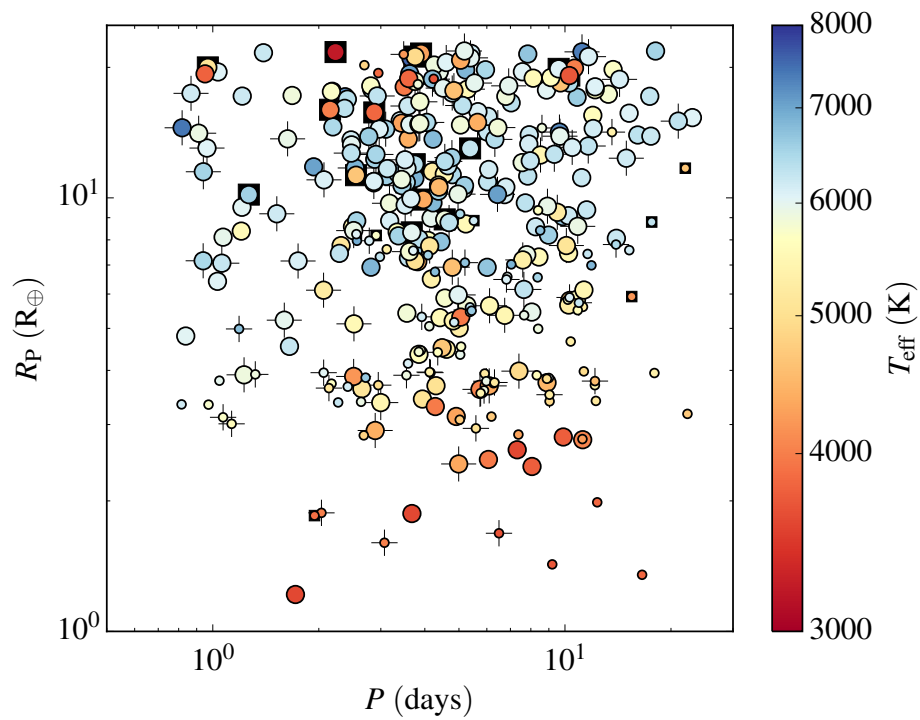
Fig. 3.9 Distribution of detected NGTS planets in period and radius, color-coded according to the host star's effective temperature. Symbol sizes represent detections for red noise levels of 0.5 mmag (small) and 1 mmag (large). An underlying cross (square) marks a planet orbiting the primary (secondary) of a binary system.
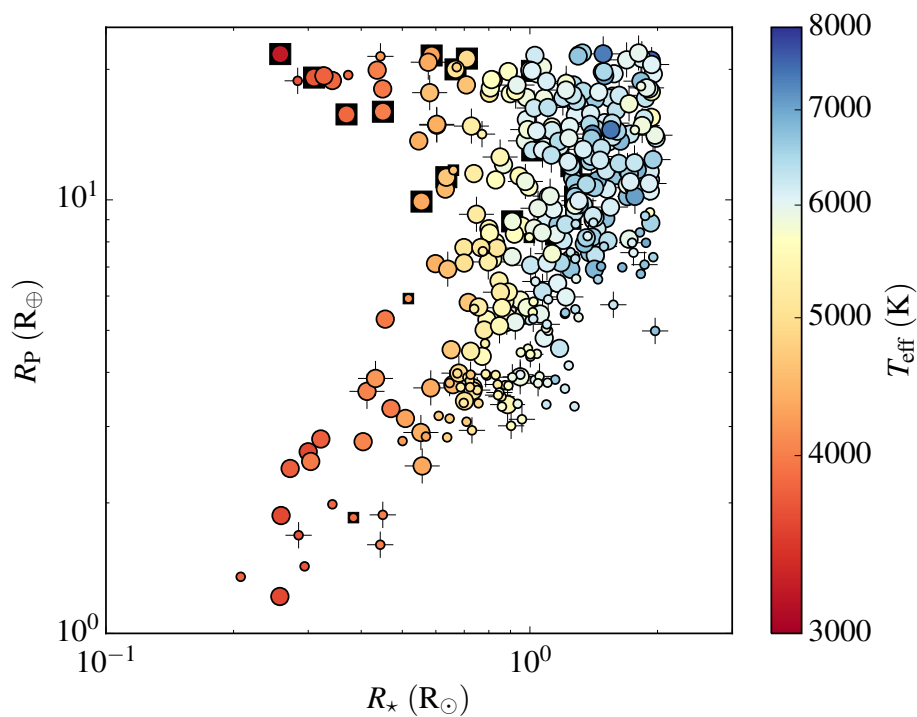
Fig. 3.10 Radius of detected NGTS planets versus radius of their host star, color-coded by the host star's effective temperature. Symbol sizes represent detections for red noise levels of 0.5 mmag (small) and 1 mmag (large). An underlying cross (square) marks a planet orbiting the primary (secondary) of a binary system.

planets are K dwarfs (Fig. 3.10) and are brighter in the infrared. Future characterisation of these objects may hence be easier in that wavelength.
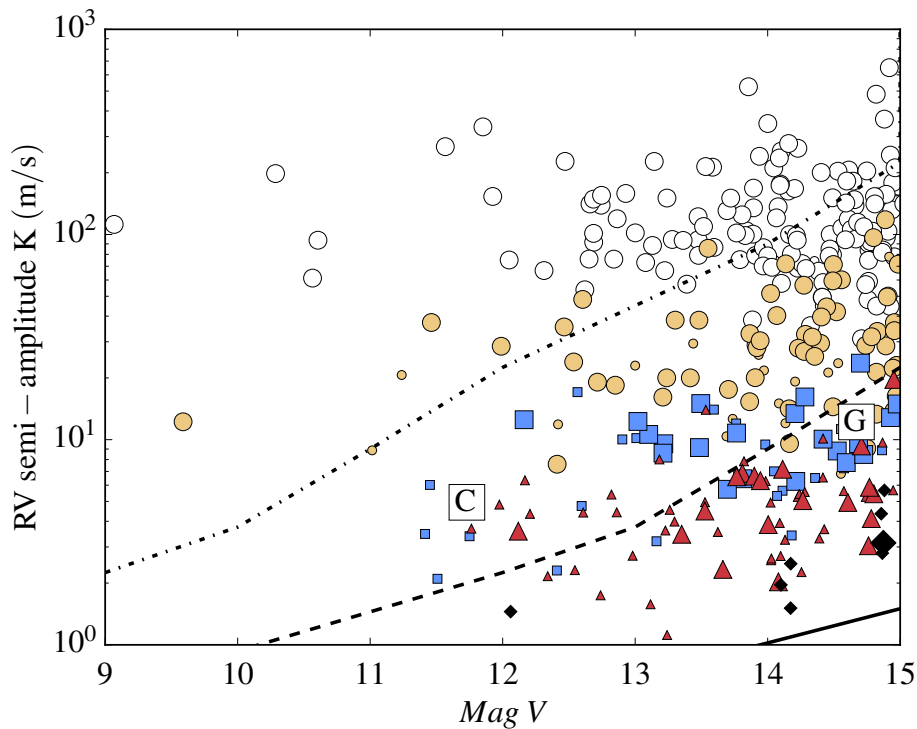
Fig. 3.11 Estimated RV signals of NGTS planets compared to the sensitivity of current and future RV instruments: Coralie (dotted line), HARPS (dashed line) and ESPRESSO (solid line). Planet symbols denote Jupiters (white circle), Saturns (yellow circle), Large Neptunes (blue squares), Small Neptunes (red triangles) and Super-Earths (black diamonds). Symbol sizes represent detections for red noise levels of 0.5 mmag (small) and 1 mmag (large). The sensitivity curve for each instrument corresponds to the criterion $2K > 3 \sigma_{RV}$. This reflects the minimum signal that can be detected with 3σ for an 1 h exposure considering the instrument's sensitivity, implying at least 10 independent RV measurements per target. The ESPRESSO sensitivity is taken from (Pepe et al., 2014), values for HARPS and Coralie are established for 1 h exposures on non-rotating and non-active stars compiled from published results. The planets Corot7b (C) and GJ 1214b (G), for which masses were measured with HARPS, are shown for comparison.

3.6   Discussion

3.6.1   Red noise limitation, detection criteria and planet merit

Red noise is a limiting factor in searching for small planets around bright stars. According to my simulation, at least a 1 mmag precision is necessary to detect Neptune-sized planets (see Table 3.3). In this work, I assume major components of the red noise are only short-time (nightly) correlated and average out over a whole season. This assumption is based on early NGTS test data (private communication within the NGTS consortium), and extrapolated from WASP results (Pollacco et al., 2006) and recent studies with EulerCam at La Silla (Lendl et al., 2013). Early results from NGTS data suggest this assumption is realistic (Wheatley et al., 2018).

Red noise is the dominant factor for bright objects (see Fig. 3.3). Decreasing it by half increases the overall number of small planets and allows to find more of them around bright stars; however, it does not significantly change the number of giant planets, as the detection of giants is limited by the observation window function rather than the noise threshold.

The detection efficiency and false alarm rate depend on the chosen detection criteria, as well as on the final version of detrending and light curve fitting algorithms. Assuming false alarms can be ruled out by automated vetting with AUTOVET and visual inspection, a ratio of 100 false alarms to 1 planet signal is a realistic compromise between a high planet yield and practicality.   In the simulation, I settled for a detection threshold of 5 σ. In systems where a transit has already been found (e.g. by the TESS survey) or other planets are known, additional transit signals with lower signal-to-noise ratio may be considered.

3.6.2   Selecting the target list

The number of transiting planets scales with the number of stars in the field of view and hence decreases with distance form the galactic plane. Conversely, there will be more background stars, leading to increased dilution and therefore a decrease of the transit depth, as well as an increased number of false positives. Specifically, the yield of EBs, BEBs, and giant planets scales with the crowdedness of the field, as their signals are still detectable even in a

crowded environment. In contrast, Neptunes and smaller planets show a saturation behavior since dilution limits the detection of small planets in crowded fields. Sparse fields lead to a higher detection efficiency for small planets but a decreased number of targets. The results suggest these two factors average out for Neptunes and smaller planets. It would therefore be beneficial to stay distant from the galactic plane in order to optimise for a higher yield of Neptunes and Super-Earths, while reducing the contamination by false positives.

3.6.3 Follow-up and characterisation of NGTS candidates

For NGTS, I estimate that the majority of EBs and BEBs can be identified without needing further follow-up measurements. EBs that cannot be identified by the vetting process usually have a low-mass secondary such as an M-dwarf or Brown dwarf, mimicking planets with sizes of Jupiter or greater. It will require RV follow-up to determine the mass of the companion and reject a planet hypothesis. While some of the remaining BEBs can have low-mass companions and hence mimic various planetary signals, the majority consist of binary companions with comparable mass. These systems cause very deep transit signals, but are diluted onto a planetary scale. Follow-up of these systems can be achieved with high-precision multi-color photometry to investigate the color dependence of the transit/eclipse depth.

Here, I focused on EBs and BEBs, but it can be assumed hierarchical eclipsing binaries lead to similar numbers as BEBs, as shown, for example, in the yield simulations for TESS by Sullivan et al. (2015). Additionally considering false alarms on the order of $\sim 10^3$, I expect 97 % of all initially detected NGTS transit signals to be caused by false positives and false alarms. After the candidate vetting, I expect to remain with 82 % of NGTS planet candidates being caused by false positives that need to be identified by follow-up. In comparison, CoRoT's initial detections contained 98 % of false positives (Almenara et al., 2009). After the vetting process, the follow-up candidates included 88 % of false positives. Existing ground-based surveys like WASP and HAT are even more limited in detecting false positives in their photometric data. In the RV and photometric vetting of HAT candidates a typical frequency of 95 % of false positives was found (Hartman et al., 2011; Latham et al., 2009). In their estimations for TESS' full-frame images mode, Sullivan et al. (2015) find a

contamination by false positives of 97 % in the detected signals and 81 % after the ad-hoc vetting process.

Dilution by background stars can lead to an underestimation of planetary radii around target stars. Planets in binary systems are particularly more difficult to detect and may appear smaller, as the light from the binary companion decreases the transit signal further (see Chapter 5 for a detailed study of such a system). Hence, gas giants may be misclassified as Neptunes or Super Earths. Here, I do not treat these diluted planets as false negatives, but the findings raise awareness of the importance of follow-up measurements to resolve multiple star systems and blended objects.

Precise knowledge of neighboring objects as well as target star radii is crucial for the vetting and characterisation of planets. Results from the *Gaia* survey (Gaia Collaboration et al., 2016a) provide astrometric information on more than two million stars, enabling the screening of NGTS targets for nearby background stars. The new *Gaia* DR2 data release (Gaia Collaboration et al., 2018, released during revision of this thesis) provides precise parallax measurements, enhancing the precision of spectroscopic properties of target stars.

3.7   Conclusion

I developed a comprehensive simulation to investigate the impact of observing strategies, target fields, and noise properties on the planet and false positive yields of transit survey programs. I considered the NGTS facility, and showed that the yield is strongly dependent on the red noise level and detection threshold.

According to my simulation, NGTS will fulfil its design purpose by finding $240 - 320$ close-in planets and providing a new sample of $40 - 110$ characterisable Neptune-sized and smaller planets for the anticipated four-year survey.

Chapter 4

Centroid vetting of planet candidates from NGTS

"The unseen enemy is always the most fearsome."

— George R.R. Martin

4.1 Summary

NGTS' sub-mmag photometric precision and ability to identify false positives are crucial. Particularly, variable background objects blended in the photometric aperture frequently mimic transits of potentially habitable exoplanets (see Section 1.9). These objects can best be identified with the centroiding technique: if the photometric flux is lost off-centre during an eclipse, the flux centroid shifts towards the centre of the target star. I developed a fully-automated centroid vetting algorithm for NGTS, enabled by the survey's high-precision auto-guiding. My method allows the detection of centroid shifts with an average precision of 0.75 milli-pixel, and down to 0.25 milli-pixel for specific targets, for a pixel size of 4.97". The algorithm is now part of the NGTS candidate vetting pipeline and is automatically employed for all detected signals. Further, I developed a joint Bayesian fitting model for all photometric and centroid data, allowing to disentangle which object (target or background) is causing the signal, and what its astrophysical parameters are. In this Chapter, I demonstrate

the method on two NGTS objects of interest. These achievements allow NGTS to apply the centroiding technique for automated candidate vetting, enabling the production of a robust candidate list before follow-up.

4.2 Introduction

NGTS' ability to identify false positives, in particular BEBs, is expected to be a major factor for its scientific success (see Section 1.6 and Chapter 3). BEBs can best be identified with the centroiding technique, measuring a shift of the flux centroid towards the centre of the target star during a blended eclipse (Fig. 4.1). Although this method has successfully been employed by the space-based *Kepler* mission (Batalha et al. 2010 and 2012, Bryson et al. 2013), it has previously not been proven feasible for ground-based wide-field transit surveys.

If a BEB lies within the photometric aperture of a target star, the centre of flux in the aperture, ξ, is offset from the true centre of the target (Fig. 4.1). Assuming a symmetric point-spread-function, I introduce the concept of a 'photometric centre of mass'. One can directly translate this principle from classical mechanics into the photometric scenario by replacing the term 'mass' with 'flux', denoted as $F_c(t) = F_c$ for the constant object in the aperture, and $F_e(t)$ for the eclipsing object:

$$\vec{\xi}(t) = \frac{F_c\,\vec{x}_c + F_e(t)\,\vec{x}_e}{F_c + F_e(t)}. \tag{4.1}$$

The CCD position of the two objects is denoted as $\vec{x}_c$ and $\vec{x}_e$, respectively. Consequently, any change in brightness of one object leads to a shift of the centre of flux in the aperture. Any centroid shift is hence dependent on $F_e(t)$:

$$\Delta\vec{\xi}(t) = \vec{\xi}(t) - \vec{\xi}(t = 0) \tag{4.2}$$

A detailed derivation can be found in Section 4.4.1. Note that these equations describe two objects, yet this model can be applied to an arbitrary number of objects, which are described by their common centre of flux.
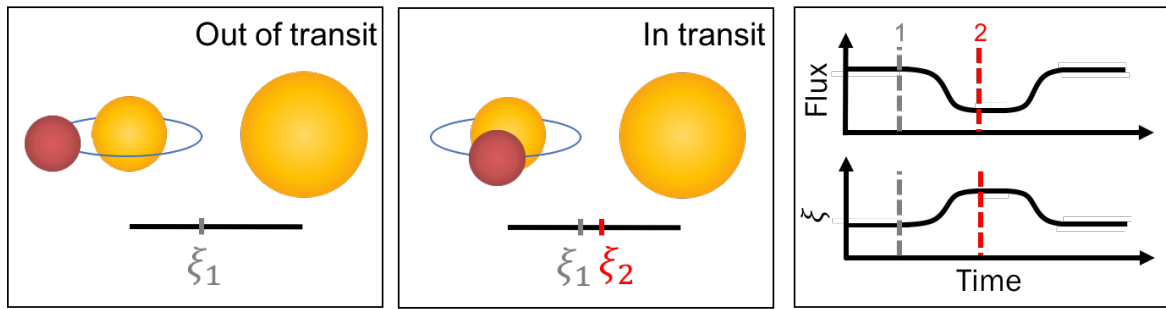
Fig. 4.1 Sketched illustration of a centroid shift $\Delta\xi = \xi_2 - \xi_1$ correlated to a transit-like signal, which is caused by a background eclipsing binary diluted in the aperture of a constant target star. Typically, both systems are photometrically extracted as a single source, and are not visually resolvable in NGTS images. Note that if the system can be visually resolved, the direction of the shift indicates which object undergoes the eclipse.

Below, I distinguish four distinct cases. I assume that the brighter object in the aperture will be identified as the 'target', and refer to the fainter objects in the aperture as 'blended' or 'background objects':

1. Diluted planet (*dilP*): The target hosts a transiting planet, the background objects are constant (on the respective time-scales and period of the detected signal). The planet transit signal is diluted and the measured depth is decreased. For example, a Hot Jupiter might be misidentified as a Neptune-sized planet if the background object is unresolved. Note that this means that detecting a correlation between flux and centroid data is not sufficient to disregard a planet candidate.

2. Diluted eclipsing binary (*dilEB*): The target is an eclipsing binary, the background objects are constant. The binary's eclipse signal is diluted and the measured depth is decreased. If the dilution is high and/or the eclipse is shallow, this can mimic a planetary transit.

3. Background planet (*BP*): The target is constant, one of the background objects hosts a transiting planet. The transit signal is diluted and the measured depth is decreased. The transit depth would be decreased by $> 50\%$, in most cases hindering the detection of the signal.

4. Background eclipsing binary (*BEB*): The target is constant, one of the background objects is an eclipsing binary. The transit signal is diluted and the measured depth is decreased. If the dilution is high and/or the transit is shallow, this can mimic a planetary transit around the target star.

4.3   Computation of the stellar centroid time series data

Each NGTS image pixel has a size of 13.5 μm (4.97"). The default radius of NGTS' circular photometric aperture is 3 pixels, covering a total sky area of 700 sq.arcsec. For all observations, the survey employs the DONUTS auto-guiding algorithm developed by McCormac et al. (2013), which ensures the telescopes stay centred on target over the course of one night.

The centre of aperture per exposure, $\vec{x}_{\mathrm{apt}}(t)$, is determined by a global fit to all reference stars in the field of view. Thereby, the high-precision auto-guiding minimises random scatter of these aperture positions to $\sim$0.1 pixel between subsequent exposures, and a total drift of < 1 pixel over multiple hours. In theory, the centre of flux per exposure, $\vec{x}_{\mathrm{flux}}(t)$, is equal to $\vec{x}_{\mathrm{apt}}(t)$ in the case of isolated stars with a Gaussian point spread function and perfect alignment of the aperture mask. However, in the presence of blended objects or stray light, the two are offset from each other. This offset depends on the magnitude and position of the background object.

Both $\vec{x}_{\mathrm{apt}}(t)$ and $\vec{x}_{\mathrm{flux}}(t)$ are computed for each exposure in the NGTS pipeline using CASUTOOLS[1] (Irwin et al., 2004). I introduce the centroid as a relative value, ξ, relating the two:

$$\vec{x}_{\mathrm{flux}}(t) = \vec{x}_{\mathrm{apt}}(t) + \vec{\xi}(t). \tag{4.3}$$

As a result, the centroid is automatically corrected for any global drift of the grid of apertures across the CCD, and is representing the remaining (local) residuals. Note that $\vec{\xi}(t)$ is a time series containing centroid measurements for all exposures.

---

[1]http://casu.ast.cam.ac.uk/surveys-projects/software-release
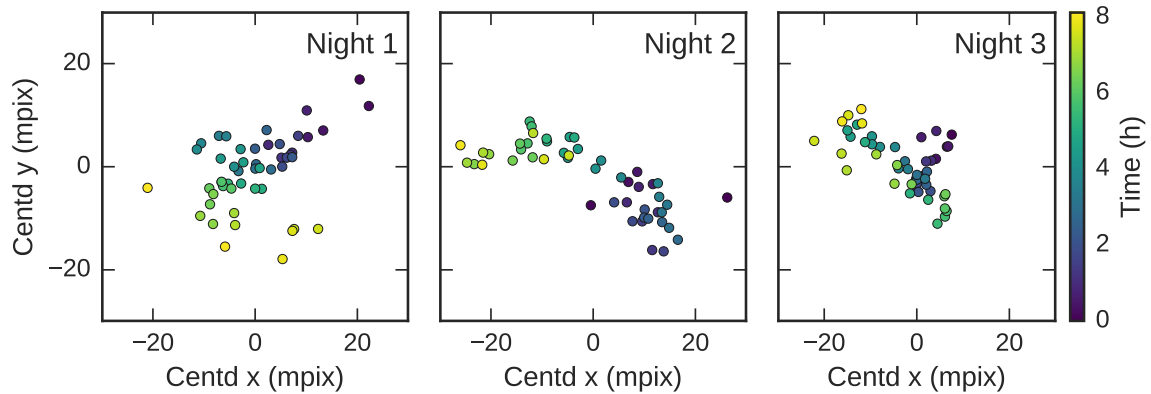
Fig. 4.2 The centroid motion $\vec{\xi}(t)$ (see Eq. 4.3) varies between different observing nights. Centroid values are shown in milli-pixel (mpix). The colour coding illustrates the time from the start of the observations on a given night.

4.3.1   Pre-whitening the flux-centroid time series

NGTS typically observes each field down to an elevation of $30°$ above the horizon. Given NGTS' large ($\sim 3°$) field-of-view (FOV) there is a $\sim 5"$ difference in the atmospheric refraction between the higher and lower elevation sides of the image. This difference ranges from 0.5 pixels at the zenith, to 1.75 pixels at an elevation of $30°$ (see Eq. G in Bennett 1982). This effect is temperature and pressure dependent and acts along the parallactic angle, which rotates as the field crosses the sky. Additionally, small amounts of field rotation may occur due to residual polar misalignment of each NGTS telescope. The centroids display a systematic low-amplitude drift over the course of each night due to atmospheric refraction differences across the image (see Fig. 4.2; Eq. G in Bennett 1982). The strength of this effect varies across the image and may differ night-to-night, but is correlated between neighbouring objects. The correlation between objects decreases as the distance between them increases (see Fig. 4.3). The NGTS autoguider aims to fix the global average position of the field to the same sub-pixel level, and can hence not correct for this. To address this, I instead follow a three-step approach to correct the centroid motion for each target star:

1. *Flattening*: I compute the median centroid of each night and use it to correct the night-to-night offset, in order to combine all nights together.
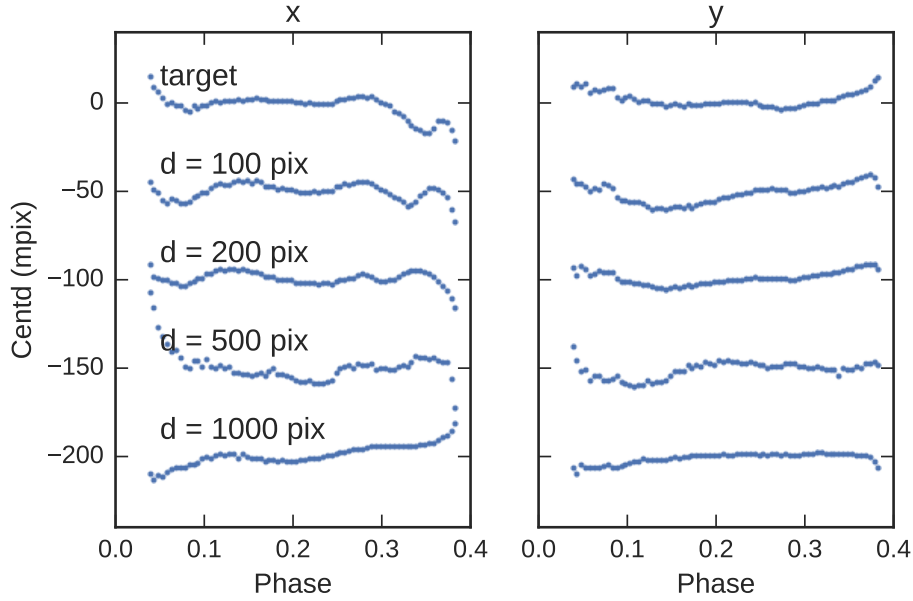
Fig. 4.3 The similarity of the centroid motion $\vec{\xi}(t)$ between objects decreases with distance on the CCD. Examples show the centroid data of randomly selected objects. This data was collected over the course of four months and phase folded on a sidereal day period.

2. *Detrending*: I use the centroid correlation between neighbouring objects to pre-whiten the centroid time series of my planet candidates. For a given target, I select N_{ref} reference stars. I perform a least squares fit to determine which linear combination of these resembles the target's centroid curve best, and remove this trend:

$$\xi_{target,detrended} = \xi_{target,raw} - \sum_{i}^{N_{ref}} c_{i,raw} \cdot \xi_{i,raw}. \tag{4.4}$$

Here, $\xi_{i,raw}$ is the centroid data of the i-th reference star, and $c_{i,raw}$ is the scale parameter that is fitted for. When selecting reference stars, I only regard objects within a certain distance d_{max} (in pixel) from the target on the CCD, based on my observations of decreasing correlation with distance (see Fig. 4.3). Further, I pre-select the most correlated objects to decrease the number of free fit parameters. I phase-fold the centroid time series on the transit period, exclude the in-transit data, and calculate Pearson's correlation coefficient of the target with each selected neighbour. The N_{ref} most correlated objects are selected. Finally, to choose reference stars which are less

affected by residuals of the sky background ($\lesssim$ 50 ADU/s) subtraction and to avoid saturated stars ($\gtrsim$ 50000 ADU/s), only objects with flux of $500 - 10000$ ADU/s are included.

3. *Sidereal day correction*: The observing pattern of ground-based surveys can lead to systematic noise on the period of a sidereal day. As my centroid detrending is applied to data that has been phase-folded on the transit period, residuals of sidereal day systematics may be present in long-period systems. To further enhance my algorithm, I phase-fold the centroid time series of the target on the mean period of a sidereal day and perform a moving average fit to correct for any remaining trends. I only consider data outside of the primary or secondary eclipses. Hence, the correction does not affect the transit signal. Generally, the effect of the sidereal day correction is marginal, as most NGTS targets are found at short periods.

The effect of the different detrending steps is demonstrated in Fig. 4.4 for the NGTS planet candidate NG0409-1941 020057. Since the object has a period of 1.61 days (see Section 4.4.2), which is close to the sidereal day period, these systematics have mostly been removed before this stage, such that their effects are negligible. Note that long-period transits, however, will profit from this additional step. After detrending, a clear centroid signal remains at phase 0, indicating the presence of a background object in the aperture (see Section 4.2).

4.3.2 Global performance: sub-milli-pixel precision

To assess the global performance of my technique, I mimic the centroiding process for planet candidates on $\sim$1200 targets from a typical NGTS field. For each star, I randomly uniformly draw a period between 0.8 and 15 days, on which I phase-fold the centroid time series. This range is based on the minimum value used for the Kepler planet occurrence rates in Fressin et al. (2013) and the period sensitivity of NGTS. I select stars with flux counts of $500 - 10000$ ADU/s, to avoid influence of the sky background ($\sim$50 ADU/s) and saturation (> 50000 ADU/s).
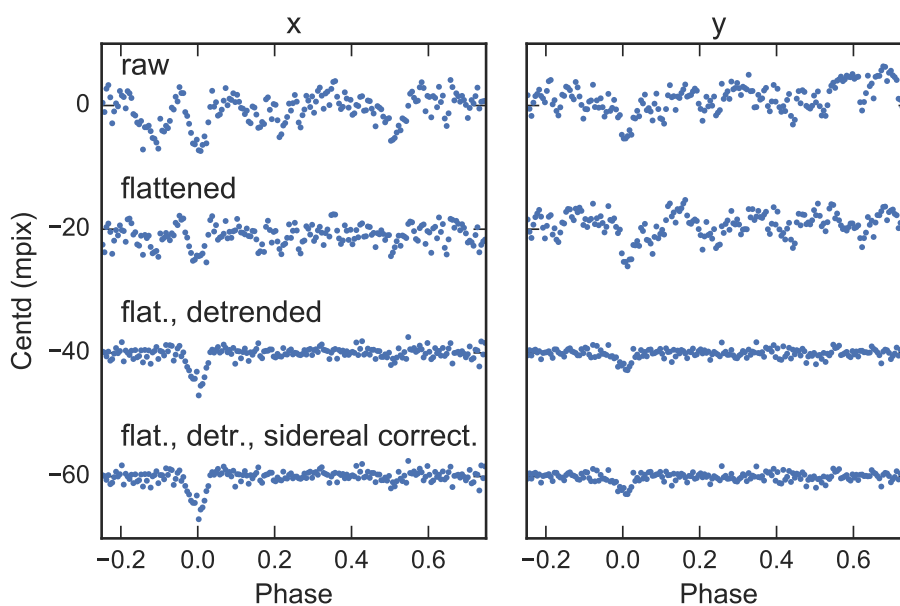
Fig. 4.4 *Improvement of the centroiding systematics with each detrending step (see Section 4.3.1) on the example of NG 0409-1941 020057. Shown are the centroid time series $\vec{\xi}(t)$ phase-folded on the period of the transit-like signal at* 1.61 *days. First, I correct the night-to-night offsets in the time series by subtracting the median value per night ('flattened'). Second, the centroid data is detrended by a reference signal calculated from their most correlated neighbours. Last, a sidereal day correction is applied. Centroid data in x and y direction are shown in the left and right column of the figure, respectively. The time series are offset from each other by* 20 *milli-pixel on the vertical axis for clarity.*

I test the impact of different settings for the maximum distance on the CCD, d_{max}, and maximum number of reference stars, N_{ref} (Fig. 4.5). Selecting the most correlated neighbour as the sole reference object already leads to an average milli-pixel precision. Including more reference objects further increases this precision, yet saturates at $N_{\mathrm{ref}} \approx 20$. Widening the search radius does not yield any improvement, as the correlation of the centroid systematics decreases with distance (see Section 4.3.1 and Fig. 4.3). I find an optimal performance for $d_{\mathrm{max}} \approx 200$ pixel and $N_{\mathrm{ref}} \approx 20$. In theory, additional reference objects add additional information, but can also lead to over-fitting or converging to a local minimum. In any case, pre-selecting a limited number of the most correlated reference stars is advantageous for computational efficiency.

Fig. 4.6 illustrates the remaining root mean squared error (RMSE) of the phase-folded centroid data after detrending. I achieve an RMSE of < 1 milli-pixel for 73% and 75% of all targets in the x and y direction, respectively. 61% show a precision of < 1 milli-pixel in both directions at the same time. I achieve an average centroid precision of ~ 0.75 milli-pixel in both directions, and as low as 0.25 milli-pixel for individual targets.

I identify an increase in the achieved centroid precision for shorter periods (Fig. 4.7, upper panel). This is a direct consequence of the white noise statistics and the amount of data that can be binned up in the phase-folded centroid curve. Similarly, the centroids of fainter host stars are more strongly influenced by sky background variations, leading to higher noise in the phase-folded centroid curves (Fig. 4.7, lower panel).

4.4   Identification of centroid shifts caused by blended sources

To identify centroid shifts caused by blended sources in the aperture of a planet candidate, I phase-fold the detrended centroid time series on the period of the respective transit feature. I compare the flux and centroid phase curves using four methods:

1. Manual inspection of the phase-folded flux and centroid curves (see panel A in Fig. 4.8 and 4.12). This allows a qualitative investigation of the noise in each time series, and
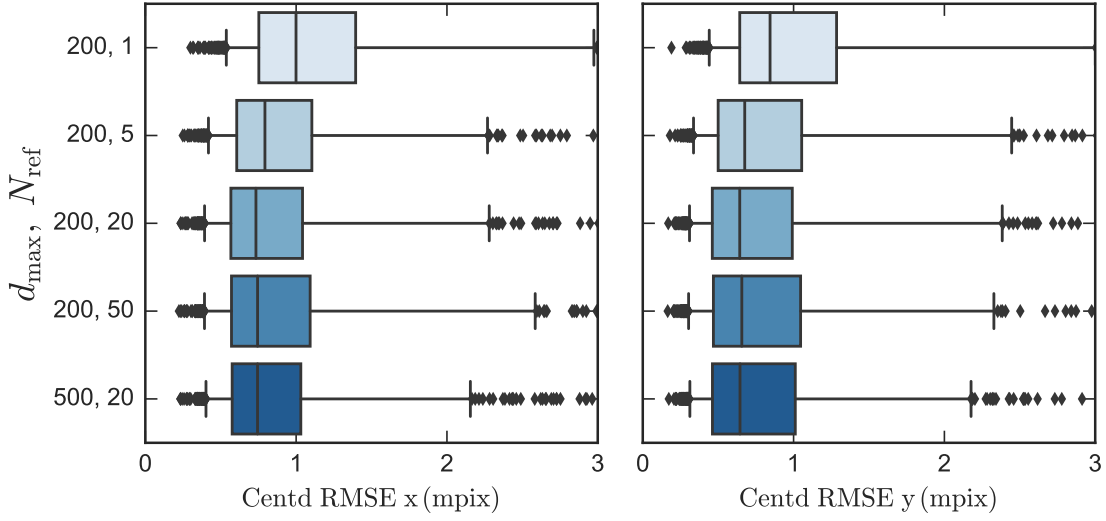
Fig. 4.5 Comparison of different centroid detrending settings. Shown is the root mean squared error (RMSE) of the phase-folded data after detrending. Boxes represent the median, and 25th and 75th percentile of all objects. Whiskers display the 5th and 95th percentile, and outlying objects are plotted as symbols. A search radius of $d_{max} \approx 200$ pixel and choice of $N_{ref} \approx 20$ reference objects is the best compromise between a high precision and computational efficiency.

the identification of any systematic features that might mimic or hide a correlation between flux and centroid.

2. Pearson's correlation for a rolling window[2] (see panel B in Fig. 4.8 and 4.12). The window size should be longer than the signal width. In praxis, I employ multiple window sizes and include all results into my further analyses. I here demonstrate my analyses using a window size of 0.25 in phase. To start, I place this window centred on the transit and calculate Pearson's correlation coefficient between the flux and centroid data. I then slide the window across the data, repeating the measurement for each position.

3. Cross-correlation (see panel C in Fig. 4.8 and 4.12). I calculate Pearson's correlation coefficient between the phase-folded flux and each centroid curve. I then shift one series of data against the other (with periodic bounds), repeating the measurement

---
[2]known as rolling, windowed, or sliding-window correlation
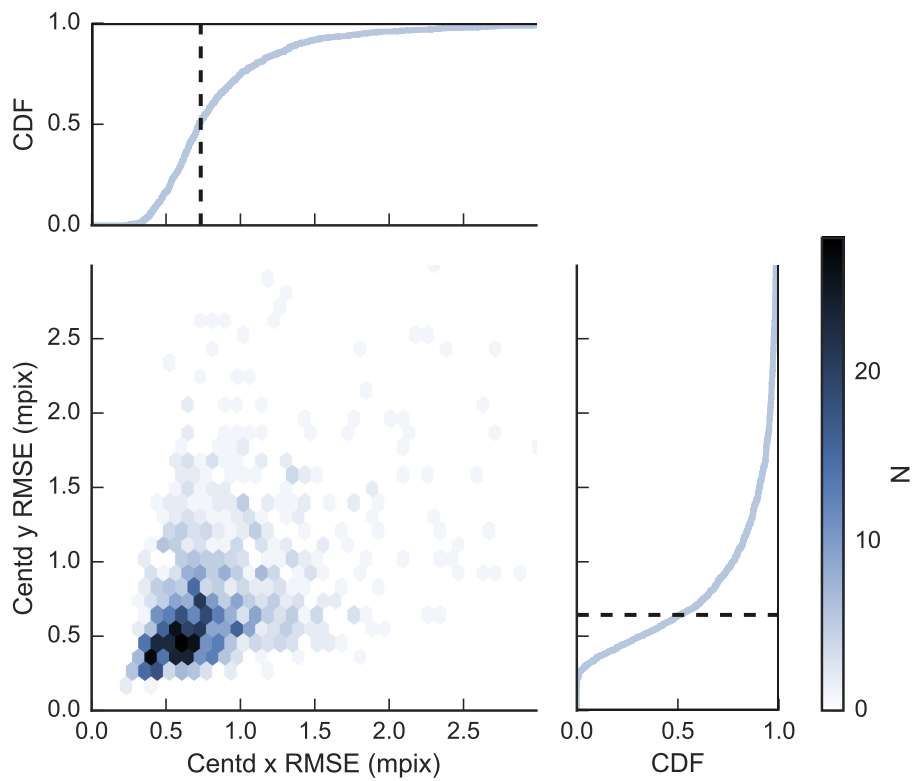
Fig. 4.6 Achieved centroid precision for an analysis run over ~1200 *stars from a typical NGTS field. Each star is given a period, which is randomly uniformly drawn between* 0.8 *and* 15 *days, and the centroid time series is phase-folded on the respective period. Shown is the root mean squared error (RMSE) of the phase-folded data in x and y direction after detrending, as well as the cumulative distribution function (CDF) in each direction.*
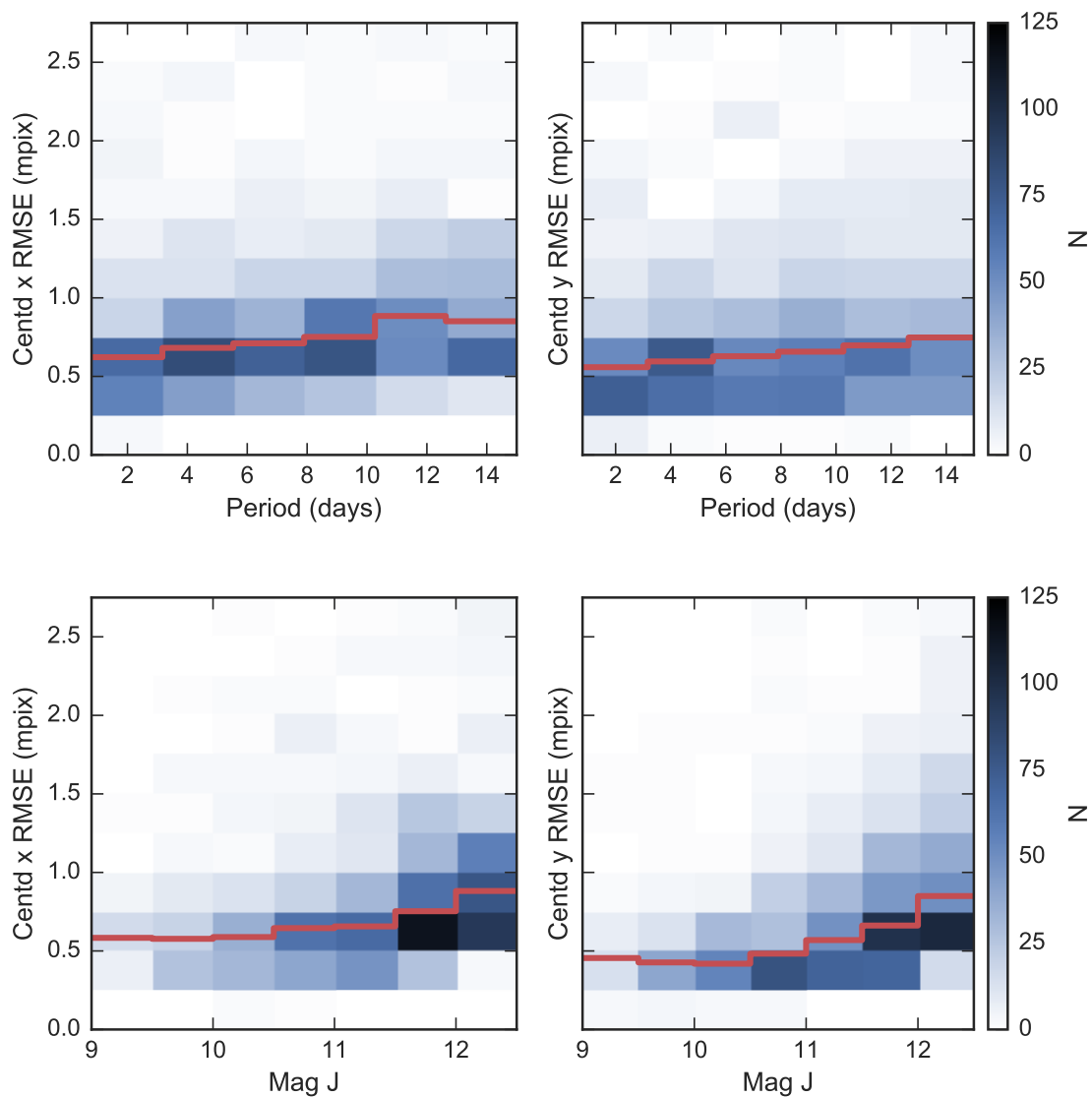
Fig. 4.7 Dependency of the centroid precision on the period of the transit-like signal (upper panel) and the J-magnitude of the host star taken from 2MASS (lower panel), shown for ~1200 targets from a typical NGTS field. Solid red lines indicate the median centroid RMSE for each period and magnitude bin. Long period signals show slightly higher noise in the phase-folded centroid curves. Fainter stars are more influenced by the sky background, leading to increased noise in the phase-folded centroid curves.

for each position. This is equivalent to the cross-correlation function widely used in astronomy, but normalised to a range of -1 to $+1$.

4. Hypothesis tests and manual inspection of the rain plots (see panel D in Fig. 4.8 and 4.12). Rain plots were successfully used to qualitatively identify correlations between the flux and centroid time series for *Kepler* (see e.g. Batalha et al. 2010). While a single target undergoing an eclipse would 'rain' straight down (local centre of flux is unaffected), a blended object causes a trend ('wind') sideways. In my analyses for NGTS, I extract the in-transit data as a subset. I set the Null Hypothesis that this in-transit centroid data is distributed around the mean of the out-of-transit centroid data, i.e. around 0. I perform statistical hypotheses tests, a two-tailed T-test and two-tailed binomial test, and record their p-value. For a chosen significance level, e.g. $\alpha = 0.01$, I test if the Null Hypothesis can be rejected. The two-tailed tests are employed to verify both if the mean is significantly greater or significantly smaller than 0 (whereas a one-tailed test would only test for one direction).

4.4.1 Analysis of blended systems

A detailed study of the centroid signal is needed to determine which scenario causes the transit-like feature (dilP, dilEB, BP, or BEB; see Section 4.2). At this stage in the vetting process, I assume that the period has been identified correctly.

In the first step of the centroid analysis, any information on visually identified nearby objects must be used to identify blended sources. I therefore inspect the NGTS images and cross-match with existing catalogues including *Gaia* DR1 (Gaia Collaboration et al., 2016a,b) and 2MASS (Skrutskie et al., 2006). If the local centre of flux shifts away from (towards) the centre of the target star, this indicates that the target star (background object) is decreasing in brightness, i.e. undergoing the eclipse (see Fig 4.1). However, as discussed in Section 4.2, this alone does not disqualify a planet scenario. Only a detailed, conjoint model of the flux and centroid time series, taking the dilution factor into account, can clarify this situation by establishing the likelihood of all astrophysical parameters.

Below, I model the aperture to contain two sources of light, one that is constant (c) and one that is eclipsing (e). This implicitly models multiple background objects as originating from a single source, located at their centre of light in the aperture. Consequently, $F_e(t)$ is the flux time series of the eclipsing object alone, while $F_c(t) = F_c$ denotes the constant object. The time series of the total flux in the aperture is

$$F_{sys}(t) = F_e(t) + F_c. \tag{4.5}$$

I define the dilution factor out of transit as

$$D_0 = 1 - \frac{F_e(t_0)}{F_{sys}(t_0)}, \tag{4.6}$$

where t_0 is a chosen time out-of-transit.

I have to distinguish between two cases: an eclipsing background object (BP or BEB; Section 4.4.1) and a constant background object (dilP or dilEB; Section 4.4.1). I consider these two cases in turn in the following two subsections.

Constant target, eclipsing background object

The target is constant (located at $\vec{x}_c$) and the signal comes from an eclipsing background source that is offset (located at $\vec{x}_e$). I set the origin of the coordinate system to the target's position, hence $\vec{x}_c = 0$. The centroid out of transit, $\vec{\xi}_0$, is then given following Eq. 4.1 and 4.6 as:

$$\begin{aligned}
\vec{\xi}_0 &= \frac{F_c(t_0)\vec{x}_c + F_e(t_0)\vec{x}_e}{F_{sys}(t_0)} = \frac{F_e(t_0)\vec{x}_e}{F_{sys}(t_0)} \\
&= (1 - D_0)\vec{x}_e. \tag{4.7}
\end{aligned}$$

The centroid at any time is then given as

$$\vec{\xi}(t) = \frac{F_c(t)\vec{x}_c + F_e(t)\vec{x}_e}{F_{sys}(t)} - \vec{\xi}_0$$

$$= \left(\frac{F_e(t)}{F_{sys}(t)} - 1 + D_0 \right) \vec{x}_e. \tag{4.8}$$

For normalised light curves, I can express this as

$$F_e(t) = F_e^{norm}(t) \cdot F_e(0) \tag{4.9}$$

$$F_{sys}(t) = F_{sys}^{norm}(t) \cdot F_{sys}(0) \tag{4.10}$$

$$\frac{F_e(t)}{F_{sys}(t)} = \frac{F_e^{norm}(t)}{F_{sys}^{norm}(t)} \cdot (1 - D_0) \tag{4.11}$$

$$\vec{\xi}(t) = \left(\frac{F_e^{norm}(t)}{F_{sys}^{norm}(t)} - 1 \right) \cdot (1 - D_0) \vec{x}_e. \tag{4.12}$$

Eclipsing target, constant background object

The target undergoes the eclipse (located at $\vec{x}_e$) and is diluted by a constant background source that is offset (located at $\vec{x}_c$). Again, I set the origin of the coordinate system to the target's position, hence $\vec{x}_e = 0$. The centroid out of transit, $\vec{\xi}_0$, is then given following Eq. 4.1 and 4.6 as:

$$\vec{\xi}_0 = \frac{F_c(0)\vec{x}_c + F_e(0)\vec{x}_e}{F_{sys}(0)} = \frac{F_c(0)\vec{x}_c}{F_{sys}(0)}$$

$$= D_0 \vec{x}_c \tag{4.13}$$

The centroid at any time is then given as

$$\vec{\xi}(t) = \frac{F_c(t)\vec{x}_c + F_e(t)\vec{x}_e}{F_{sys}(t)} - \vec{\xi}_0$$

$$= \left(\frac{F_c(t)}{F_{sys}(t)} - D_0 \right) \vec{x}_c. \tag{4.14}$$

For normalised light curves, this can be expressed as

$$F_c(t) = F_c^{\text{norm}}(t) \cdot F_c(0) = 1 \cdot F_c(0) \tag{4.15}$$

$$F_{\text{sys}}(t) = F_{\text{sys}}^{\text{norm}}(t) \cdot F_{\text{sys}}(0) \tag{4.16}$$

$$\frac{F_c(t)}{F_{\text{sys}}(t)} = \frac{1}{F_{\text{sys}}^{\text{norm}}(t)} \cdot D_0 \tag{4.17}$$

$$\vec{\xi}(t) = \left(\frac{1}{F_{\text{sys}}^{\text{norm}}(t)} - 1 \right) \cdot D_0 \vec{x}_c. \tag{4.18}$$

Dependency of the blend position on transit parameters

Rearranging the previous equations allows to express the position of the blended background object in terms of the actually measured transit depth of the system, δ_{sys}:

$$\tilde{x}_{\text{blend}} = \pm \, \tilde{\xi}_{\text{max}} \cdot \left(\frac{\delta_{sys}}{1 - \delta_{sys}} \cdot D_0 \right)^{-1}. \tag{4.19}$$

The sign depends on whether the blended background object is the constant (+) or variable (-) source in the aperture.

Bayesian analysis

A Bayesian analysis enables to explore complex parameter spaces and robustly estimate posterior likelihoods for each parameter. In particular, any information on visually identified objects can be used as priors, such as the position of the blended background object.

I base my fitting model on the EB[3] module by Irwin et al. (2011), which incorporates the possibility of a dilution term. I establish a maximum likelihood function based on a simultaneous fit of the phase-folded flux and centroid time series following Eq. 4.12 and 4.18 (depending on which model is chosen for the fit). The free parameters in my model are the relative CCD position of the blended background object ($\tilde{x}_{\text{blend}}$), the dilution factor D_0, as well as the standard parameters of an EB model, namely the surface brightness ratio J, ratio of the sum of the radii over the orbital distance $(R_1 + R_2)/a$, the radius ratio R_2/R_1,

---

[3]https://github.com/mdwarfgeek/eb, online 26 March 2018

and cosine of the inclination $\cos i$. I also include offset terms for the normalised flux and centroid time series, denoted F_0, $\xi_{x,0}$, and $\xi_{y,0}$. These correct for any remaining offset after the normalisation, and are usually negligible. Additionally, the error bars on the flux and centroid data are free parameters and determined by the fit, $\sigma(F)$, $\sigma(\xi_x)$, and $\sigma(\xi_y)$. When there is no prior information, uniform priors are chosen, where applicable within physical bounds, otherwise with non-restrictive bounds. The priors for the two following case studies are listed in Tables 4.1 and 4.2. Note that all priors are jointly proper, ensuring posterior propriety. None of the priors are unbounded, and the likelihood functions for all models converge to 0 as the model deviates from the data.

I fix the period and epoch to the values determined by the NGTS candidate pipeline. The other parameters of the EB model (limb darkening, gravity darkening, and reflectivity) are left at their standard values. Both stars are assumed to be without spots. The EB model can resemble the Mandel & Agol (2002) planet transit model if surface brightness ratio, mass ratio, light travel time and reflectivity are zero. Hence, I can readily model all scenarios (dilP, dilEB, BP, BEB; see Section 4.2).

To find the best fit, I follow a two-step approach. First, I employ a differential evolution algorithm (Storn & Price, 1997) to explore the parameter space and find a global optimisation. This uses an iterative approach in which different populations of solutions are compared and the best fit is kept. As it does not rely on gradient methods, it is robust against local minima. For this, I implement the SCIPY (Jones et al., 2001) distribution of the algorithm.

Second, I use the result of the differential evolution as the initial guess for an Markov chain Monte Carlo (MCMC) algorithm and adopt priors, to re-fine the fit and establish the likelihood of my parameters. For this, I implement the EMCEE (Foreman-Mackey et al., 2013) package. Initially, the walkers are distributed following a Gaussian distribution around the initial guess with the standard deviation being 1% of the given data range. I first perform several MCMC runs with 10000 steps each, and test for convergence using the Gelman-Rubin statistic (Gelman & Rubin, 1992, see Section 2.5.2). In the final run, I compute 5000 burn-in steps and 45000 evaluation steps, from which I sample every n-th step, whereby n is determined by the maximum of the autocorrelation time of all parameters. The Gelman-

Rubin statistics for all parameters lie well below the recommended value $\hat{R} < 1.1$, suggesting convergence of the MCMC chains.

4.4.2   Case studies

I employ my centroiding technique on the example of two case studies representing different scenarios as follows. First, I consider NG 0522-2518 017220, which is an eclipsing binary slightly diluted by a visually resolved blend. Second, I apply my analyses to NG 0409-1941 020057, which has no prior visual information, yet can be identified as a strongly diluted background eclipsing binary from a joint MCMC fit of photometric flux and centroid data.

NG 0522-2518 017220

The target NG 0522-2518 017220 was first detected with a period of ∼0.83 days. Its sinusoidal out-of-eclipse (OOE) variation unveiled that the true signal originates from a primary and secondary eclipse with a period of ∼1.67 days, which have comparable depths of ∼3 per cent and widths of ∼2.6 hours. With Gmag $= 13.6$ in *Gaia* DR1 (Jmag $= 12.6$ and Kmag $= 12.2$ in 2MASS) the object is bright and well-suited for follow-up and potential characterisation. It is located at RA = 05h 23m 31.6s, DEC = -25d 08m 48.4s and has been identified as 2MASS 05233161-2508484, and *Gaia* 2957881682551005056.

However, the centroid time series shows clear shifts of $5 - 8$ mpix in x and y direction for both the primary and secondary eclipse (see Fig. 4.8). All correlation and hypothesis tests confirm a statistically significant centroid shift correlated to the transit signal (see Table 4.5). On visual inspection, I identify a neighbouring object at ∼18 arcsec separation, which has a similar brightness at Gmag $= 14.0$ (Jmag $= 12.7$, Kmag $= 12.2$) and partly blends into the target's photometric aperture (see Fig. 4.10). The centroid shifts into the positive x and y direction which, combined with the visual information, suggests that the target is undergoing the eclipse while the flux from the blended background object is constant (see Fig. 4.1). A direct comparison of the detrended and phase-folded light curves shows that the eclipses are only visible for NG 0522-2518 017220. In the light curve of the neighbouring object the

Table 4.1 Priors for the global MCMC model of NG 0522-2518 017220.

Δx	$\mathcal{N}(1.9, 0.2)$ pixel
Δy	$\mathcal{N}(1.7, 0.2)$ pixel
D_0	$\mathcal{N}(0.13, 0.02)$
J	$\mathcal{U}(0, 1)$
R_1/R_2	$\mathcal{U}(0, 1)$
$(R_1 + R_2)/a$	$\mathcal{U}(0, 1)$
$\cos i$	$\mathcal{U}(0, 1)$
F_0	$\mathcal{U}(-1, 1)$
$\xi_{x,0}$	$\mathcal{U}(-1, 1)$
$\xi_{y,0}$	$\mathcal{U}(-1, 1)$
$\sigma(F)$	$\mathcal{U}(0, 1000)$ mmag
$\sigma(\xi_x)$	$\mathcal{U}(0, 1000)$ mpix
$\sigma(\xi_y)$	$\mathcal{U}(0, 1000)$ mpix

signals are diluted beyond the noise level, and hence not detectable (Fig. 4.11). This verifies the conclusions drawn from the centroid analysis.

Using the *Gaia* DR1 magnitude and models for the NGTS point-spread-function and bandpass, I calculate a dilution factor of $D_0 = 0.13 \pm 0.02$ for NG 0522-2518 017220. I further compute the centre of flux of the third light in the aperture to be at $\vec{x}_{\text{backg.obj.}} = (1.9 \pm 0.2, 1.7 \pm 0.2)$ pixels. This information on D_0 and $\vec{x}_{\text{backg.obj.}}$ is used as Gaussian priors on these parameters in my MCMC model fit. Table 4.1 lists all priors used for the MCMC model.

The object shows significant out-of-eclipse (OOE) modulation on a $\sim 1\%$ level, which appears to be sinusoidal and in phase with the eclipse signal. First, I analyse the time evolution of the OOE variation by dividing the light curve in equal sections in time, and compare the variability between these sections. Thereby, I find that the OOE modulation significantly changes over the 175 day observing span. Next, I compute Lomb Scargle periodograms for the OOE data. This identifies multiple periods, which relate to the orbital period of the system and systematics on a sidereal day period. With an orbital period of ~ 1.67 days, it can be assumed that the orbit is circular and that the binary components are tidally locked. Hence, I conclude that the OOE modulations may result from a combination

of 1) stellar spots on either or both bodies, 2) a difference in the reflection indices of the two bodies, and 3) systematics introduced by the third light in the aperture.

Before analysing the time series with my MCMC model, I remove the OOE variation from the flux and centroid time series using Gaussian Process Regression. By employing a combination of a Matern 3/2 kernel function, a linear kernel and a white noise kernel, the OOE data of each time series is modelled individually. Next, I extrapolate the model and evaluate it for the eclipse data, resulting in the detrended light curve and centroid curves shown Figs. 4.8A and 4.11.

The results of my MCMC model fit are shown in Fig. 4.8 and Table 4.6. Fig. 4.9 shows the resulting posterior distributions. I find a high inclination $i = 80.14° \pm 0.34°$ of the system and a comparable surface brightness ratio $J = 0.722 \pm 0.010$ of the two components. The radius ratio of the two bodies is estimated to be $R_2/R_1 = 0.2414 \pm 0.0044$.

The example of NG 0522-2518 017220 illustrates how the centroiding technique can help identifying which system in the aperture shows the eclipsing signal. In particular, any visual information on the blend can be input as priors to refine the model fit and establish the physical parameters of the eclipsing system.

NG 0409-1941 020057

The transit-like signal of NG 0409-1941 020057 was initially detected with a period of $\sim$0.8 days and width of $\sim$3.4 hours. However, with additional NGTS photometry the true period could be established as $\sim$1.61 days, with a $\sim$4% primary eclipse and a $\sim$0.5% secondary eclipse. The object is well suited for follow-up at Gmag $= 13.3$, Jmag $= 12.1$ and Kmag $= 11.7$. It is identified as 2MASS 04104778-2031575 and *Gaia* 5091012688012721664, and is located at RA = 04h 10m 47.8s, DEC = -20d 31m 57.5s. The signal, however, is significantly correlated with $\sim$5 mpix and $\sim$2 mpix centroid shifts in x and y, respectively (see Fig. 4.12, Table 4.5).

At the time of this analysis, the target is listed as a single source in all existing catalogues, including 2MASS and *Gaia* DR1. I investigate the archival images, but find no definite indication of two separate sources, despite a marginal ellipticity of the 2MASS point-
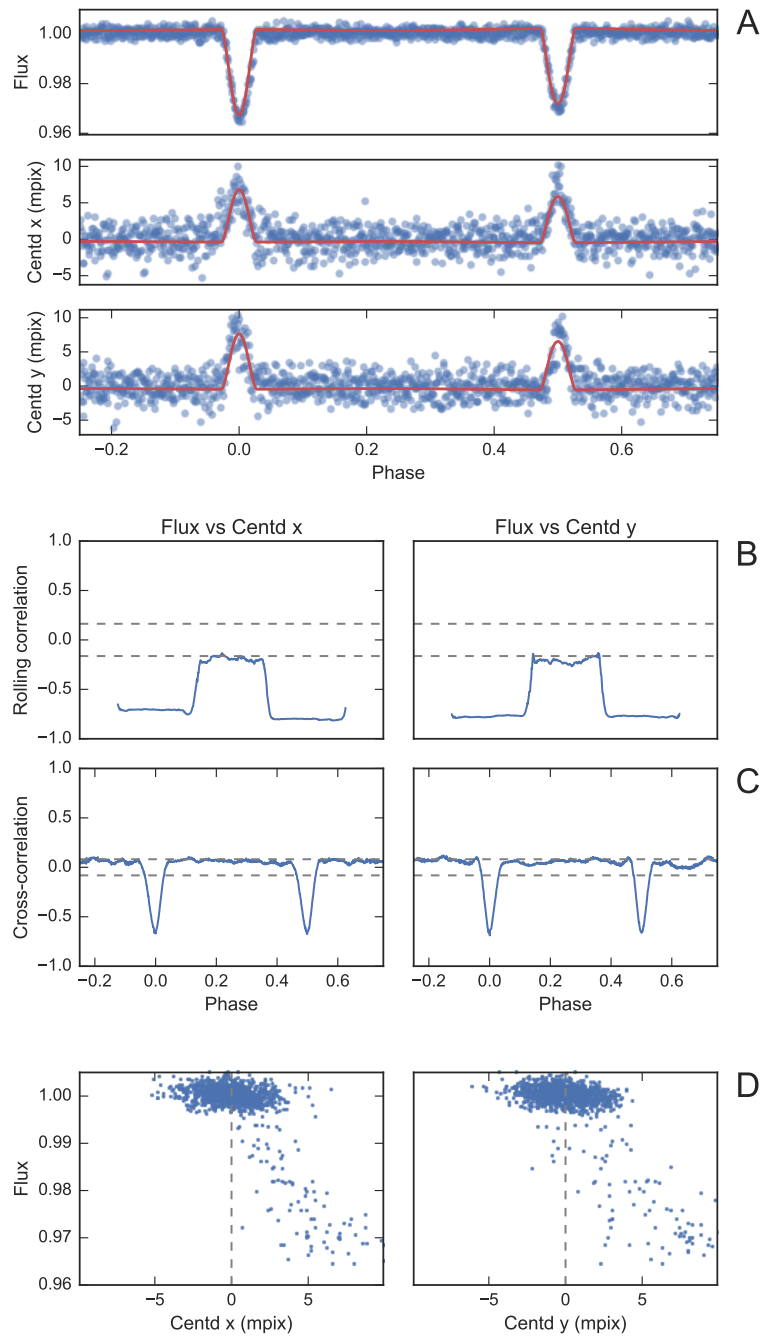
Fig. 4.8 *Identification and model fit of a centroid shift correlated to the transit-like signal in NG 0522-2518 017220. A) The correlation is clearly visible in the manual inspection of the flux and centroid phase curves, even though the centroid shift is at the ~6 mpix level. Red curves represent the result of the MCMC analysis. B) The rolling correlation analysis shows a significant correlation around phase 0. Dashed lines indicate confidence intervals of 99%, calculated as $2.58/\sqrt{w/\Delta t}$ (see Fisher (1921)), whereby w is the window size and Δt is the difference in phase between binned points. C) The cross-correlation shows a significant correlation at lag 0 in phase. Dashed lines show confidence intervals of 99% calculated as $2.58/\sqrt{N}$ (see Fisher (1921)), whereby N is the total number of binned points. D) Rain plots show a clear trend between flux and centroid shift.*
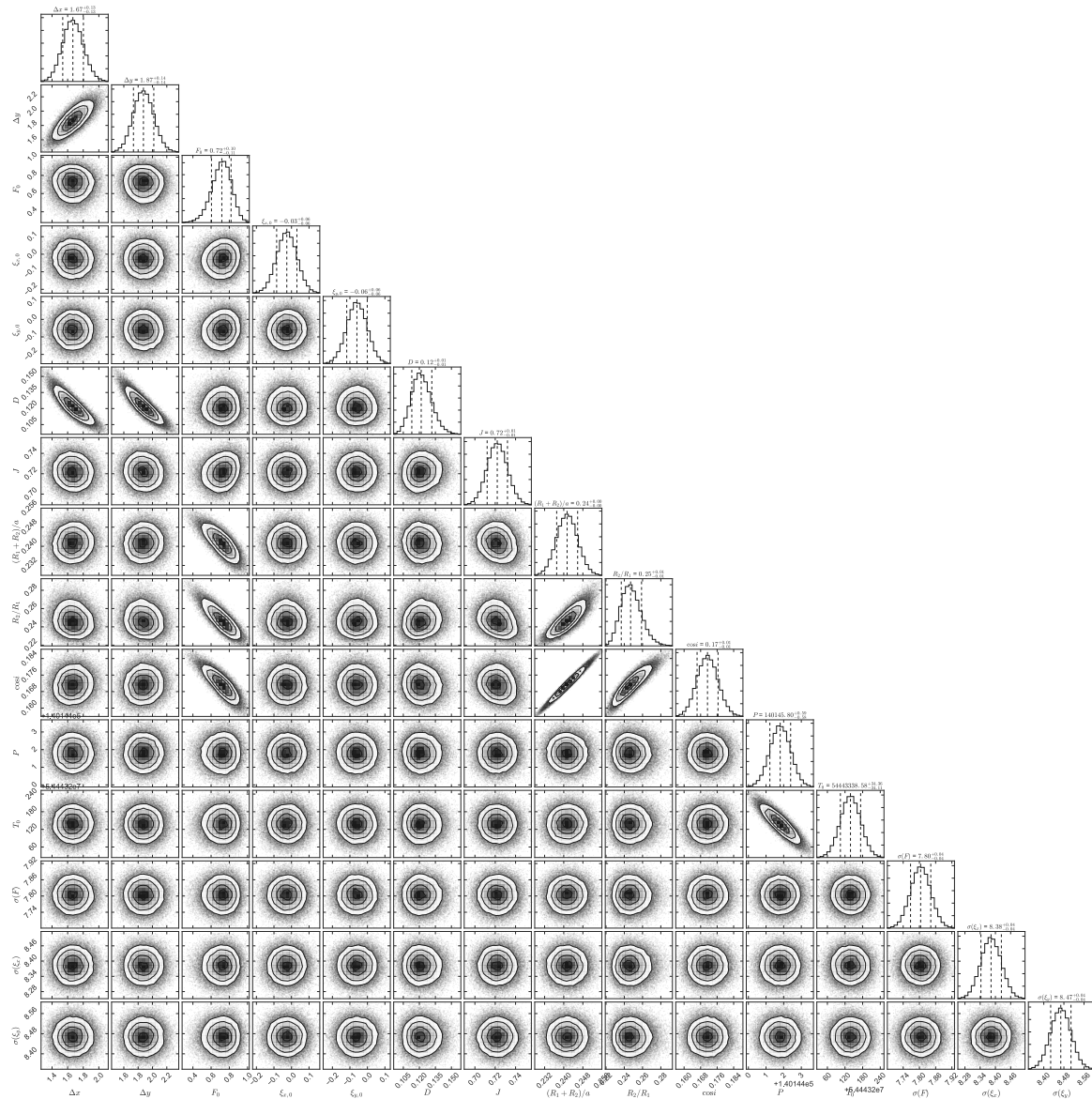
Fig. 4.9 Posterior likelihood distributions for all parameters of the MCMC fit to NG 0522-2518 017220. A description of the model and all parameters can be found in Section 4.4.1. The corner plot allows to represent all samples of high dimensional models, and to evaluate which parameters of the model are correlated. For example, Δx and Δy, the location of the blended source in x and y direction, are correlated. Further, as to be expected, the radius ratio R_1/R_2, sum of radii over semi-major axis $(R_1 + R_2)/a$ and cosine of the inclination $\cos i$ are correlated with each other.
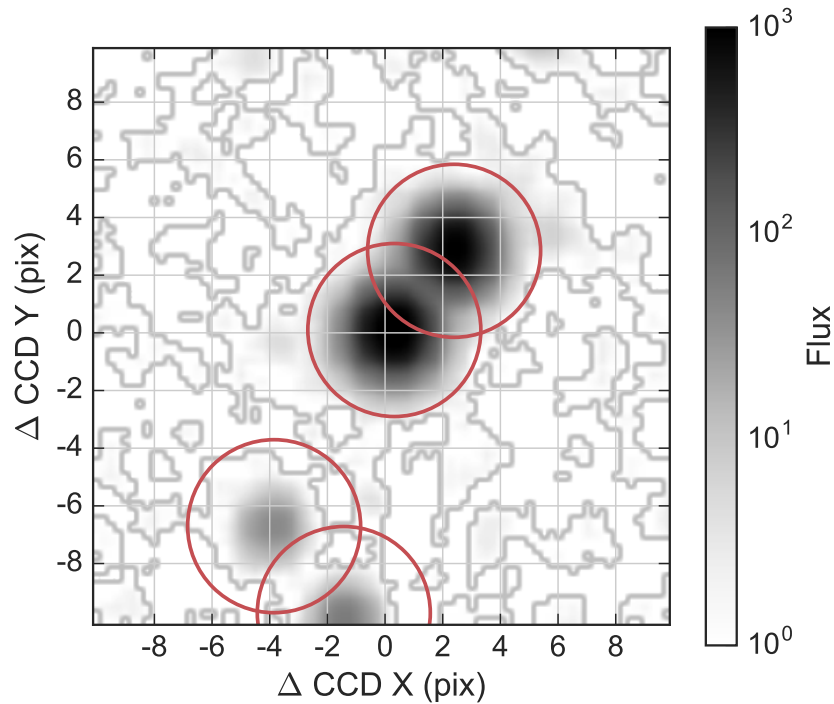
Fig. 4.10 Visual inspection of the NGTS sky images for NG 0522-2518 017220 uncovers that a neighbouring object is blending into the photometric aperture of the target (centred in the image). The size of one NGTS pixel measures 4.97". Red circles illustrate the photometric aperture radius of 3 pixels.
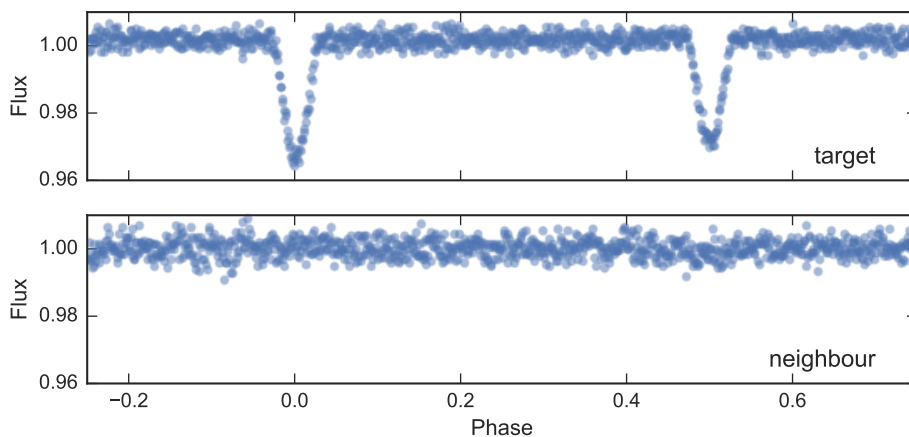
Fig. 4.11 Comparison of the phase-folded light curves for NG 0522-2518 017220 and its blending neighbour. While the primary and secondary eclipse signals are clearly visible in the target, they can not be identified in the blending neighbour. This verifies the outcome of the centroid analysis: the target is undergoing the eclipse, while the neighbouring object is constant.
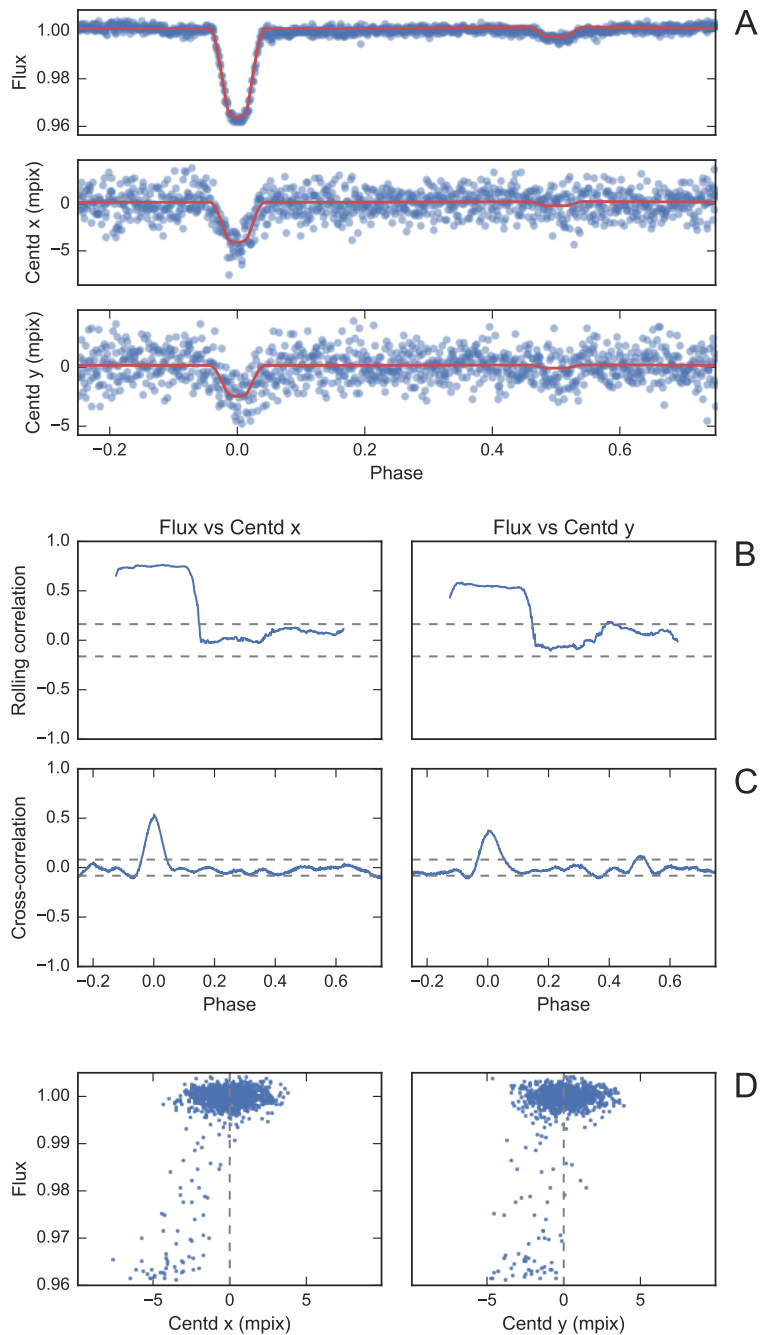
Fig. 4.12 Identification and model fit of a centroid shift correlated to the transit signal in NG 0409-1941 020057. See caption of Fig. 4.8.
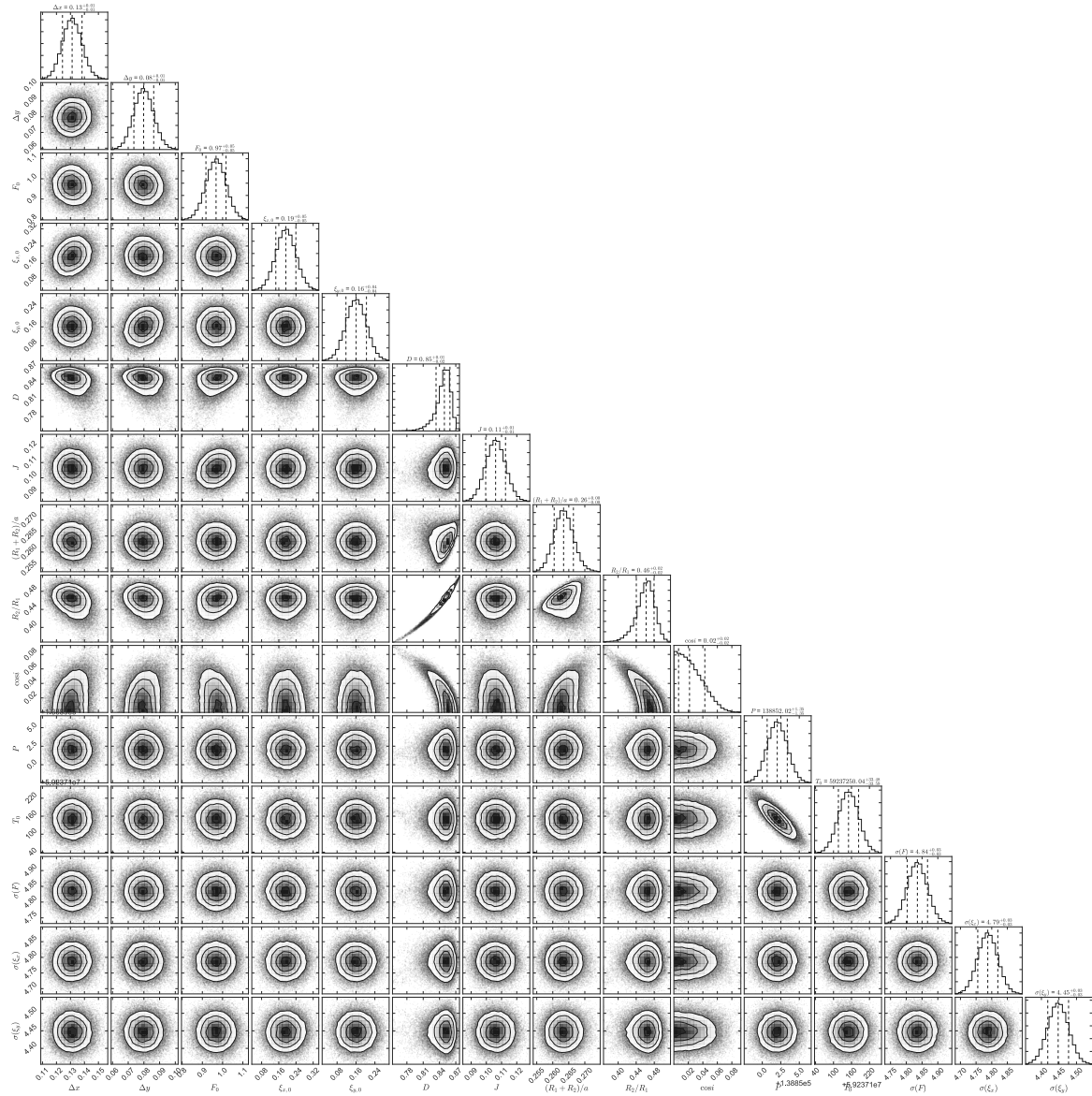
Fig. 4.13 Posterior likelihood distributions for all parameters of the MCMC fit to NG 0409-1941 020057. A description of the model and all parameters can be found in Section 4.4.1. Most notably, there is a strong correlation between the dilution D_0 and the radius ratio R_1/R_2, as both determine the depth of the transit signal.

Table 4.2 Priors for the global MCMC model of NG 0409-1941 020057.

Δx	$\mathscr{U}(-1,1)$ pixel
Δy	$\mathscr{U}(-1,1)$ pixel
D_0	$\mathscr{U}(0,1)$
J	$\mathscr{U}(0,1)$
R_1/R_2	$\mathscr{U}(0,1)$
$(R_1+R_2)/a$	$\mathscr{U}(0,1)$
$\cos i$	$\mathscr{U}(0,1)$
F_0	$\mathscr{U}(-1,1)$
$\xi_{x,0}$	$\mathscr{U}(-1,1)$
$\xi_{y,0}$	$\mathscr{U}(-1,1)$
$\sigma(F)$	$\mathscr{U}(0,1000)$ mmag
$\sigma(\xi_x)$	$\mathscr{U}(0,1000)$ mpix
$\sigma(\xi_y)$	$\mathscr{U}(0,1000)$ mpix

spread-function. However, *Gaia* DR1 is incomplete below $\sim$4" separation[4]. I consider this incompleteness in my MCMC model as an upper limit for uniform priors on the relative CCD position of the background object. Table 4.2 list all priors used for the MCMC model. Due to the short orbital period and the clear secondary eclipse at phase 0.5, I restrict my MCMC model to circular orbits.

The results of my MCMC analysis can be seen in Figs. 4.12 and 4.13, and are summarised in Table 4.6. The object undergoing the eclipse is highly diluted with $D_0 = 0.849^{+0.010}_{-0.015}$, indicating that the signal originates from a blended background object. This background object would hence show an undiluted transit depth of $\delta_e = 24.5^{+2.0}_{-2.6}\%$, and has a surface brightness ratio of $J = 0.1061 \pm 0.0065$ and radius ratio of $0.462^{+0.018}_{-0.022}$.

Before the correct period had been established and my centroiding analysis had been performed, six reconnaissance RV measurements were taken using the *Coralie* spectrograph (Queloz et al., 2001a) on the Swiss 1.2 m telescope at La Silla Observatory, Chile. These measurements are set out in Table 4.3. The RV signal for this system, when phase-folded at the true period, shows an in-phase variation of approximately $50\,\mathrm{m\,s^{-1}}$ (see Fig 4.14). Such a signal is consistent with what may be expected for a typical hot Jupiter. However the bisectors of the RV cross-correlation functions show a significant correlation with the

---

[4]https://www.cosmos.esa.int/web/gaia/dr1 (online 26 March 2018)

Table 4.3 Coralie radial velocities of NG 0409-1941 020057

BJD	RV	RV error	BIS
(-2400000)	(km s^{-1})	(km s^{-1})	(km s^{-1})
57605.906507	103.93259	0.04857	0.08040
57613.901203	103.88342	0.04335	0.06101
57630.852688	103.75888	0.04108	-0.11377
57632.906217	103.86820	0.03938	0.06171
57634.786375	103.82177	0.04350	-0.00728
57638.748983	103.85213	0.04198	0.02030

RV amplitude (see Fig. 4.14) This indicates that the variation seen for this target is due to a blended star that is spectroscopically contaminating the cross-correlation function and is moving in phase with the photometric period.

Note that the acceptance of the *Coralie* fibre is ∼2". The results from my MCMC model predict the blended background object to be offset from the target by 0.653 ± 0.040" in x and 0.396 ± 0.034" in y, further supporting the hypothesis that the *Coralie* signal is affected by the blend. The evidence provided by both the centroid vetting and the RV data are in agreement and suggest a highly diluted BEB scenario.

Gaia DR2 confirms the centroid model of NG 0409-1941 020057

In the revision process for this thesis, *Gaia* DR2 was released (Gaia Collaboration et al., 2018) and indeed resolved the NG 0409-1941 020057 system as two separate stars (see Table 4.4). The measured *Gaia* DR2 positions lead to a separation of 0.523241 ± 0.000050" between the two sources. These results match the predicted separation from the centroid analysis (0.653 ± 0.040" in x and 0.396 ± 0.034" in y). The new insights from *Gaia* DR2 hence confirm the effectiveness of the centroiding technique, again highlighting the high-precision measurements that can be obtained with this method.
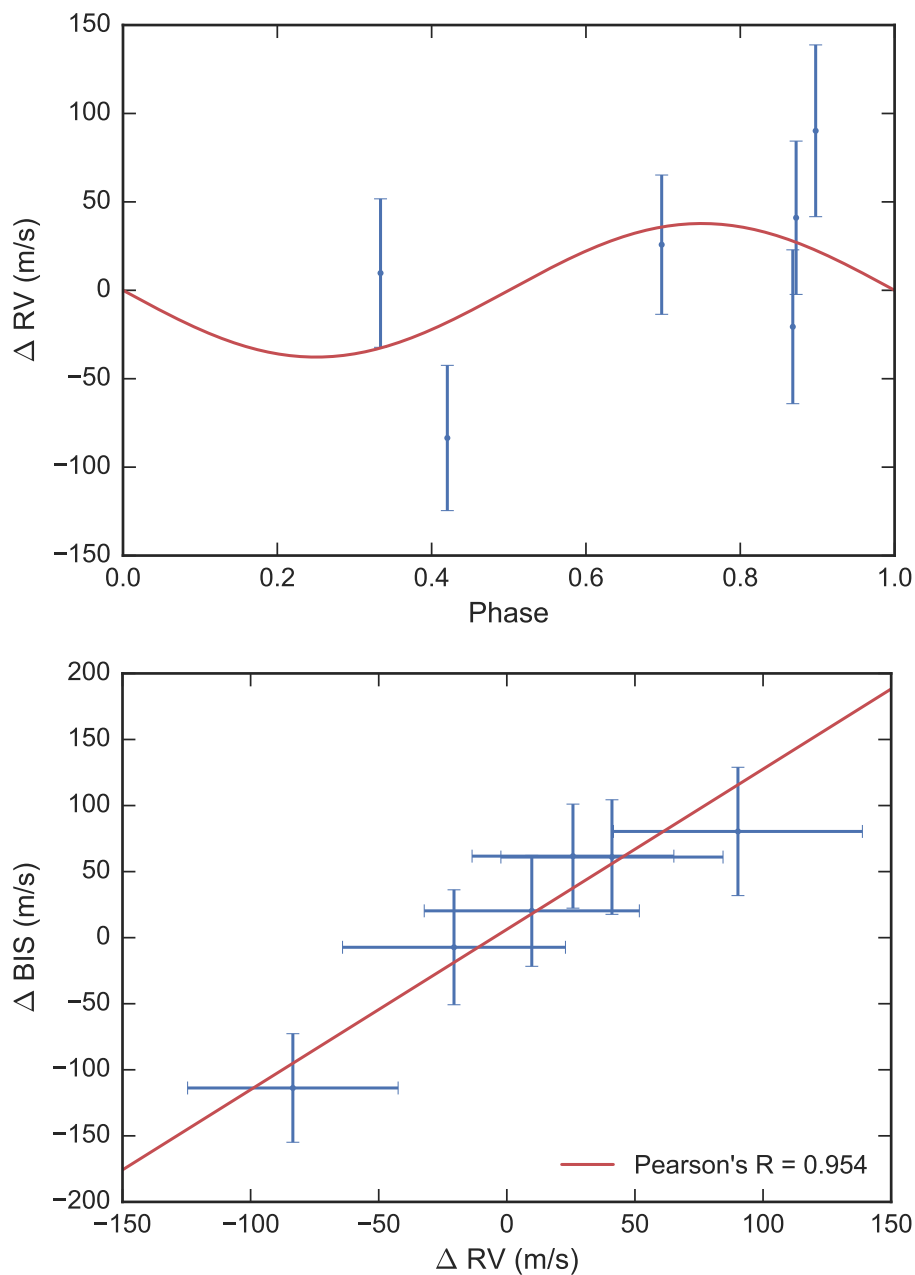
Fig. 4.14 Coralie RV measurements of NG 0409-1941 020057. Upper panel: RV signal phase folded onto the photometric period and epoch. The solid line indicates the best fit Keplerian solution assuming a circular orbit and the photometric period and epoch. Lower panel: RV bisector spans against the measured RV signal. The strong correlation (Pearson's R = 0.954) indicates that the detected RV variations are due to a diluted spectrum shifting at large amplitudes, such as a BEB.

Table 4.4 Gaia DR2 confirms the centroid model predictions for NG 0409-1941 020057, and resolves that the system consists of two stars.

Gaia DR2 ID	5091012688014057088	5091012688012721792
RA	62.6992509469°	62.6989893509°
σ_{RA}	0.0000000056°	0.000000012°
Dec	$-20.53261496288°$	$-20.53275731863°$
σ_{Dec}	0.0000000057°	0.000000013°
Parallax	0.981 ± 0.034 mas	0.785 ± 0.060 mas
*G*mag	13.467	14.500
BP - RP colour	0.741	1.071
T_{eff}	5191 K	5095 K
Angular separation	0.523241 ± 0.000050"	

Table 4.5 Statistical identification of a centroid shift correlated to the transit-like signals in NG 0522-2518 017220 and NG 0409-1941 020057. The table displays the signal-to-noise ratio (SNR) of the rolling correlation and cross-correlation analyses, displayed in Fig. 4.8 and 4.12. Further, it lists the resulting p-values from a T-test and binomial test of the in-transit centroid data, testing the Null Hypothesis that the centroid is distributed around the mean of the out-of-transit data, i.e. around 0.

	x	y
NG 0522-2518 017220		
SNR roll. corr.	41.43	43.01
SNR cross-corr.	53.28	26.55
p-value T-test	$4.01 \cdot 10^{-32}$	$5.69 \cdot 10^{-26}$
p-value Binomial test	$6.62 \cdot 10^{-24}$	$9.96 \cdot 10^{-18}$
NG 0409-1941 020057		
SNR roll. corr.	51.66	44.06
SNR cross-corr.	15.75	12.28
p-value T-test	$7.92 \cdot 10^{-26}$	$4.34 \cdot 10^{-16}$
p-value Binomial test	$8.67 \cdot 10^{-19}$	$5.65 \cdot 10^{-12}$

Table 4.6 Parameters of the blended eclipsing systems NG 0522-2518 017220 and NG 0409-1941 020057.

		NG 0522-2518 017220	NG 0409-1941 020057
Catalogue values			
Coordinates		RA = 05h 23m 31.6s	RA = 04h 10m 47.8s
		DEC = -25d 08m 48.4s	DEC = -20d 31m 57.5s
2MASS ID		2MASS 05233161-2508484	2MASS 04104778-2031575
Gaia ID		*Gaia* 2957881682551005056	*Gaia* 5091012688012721664
Magnitudes		$G = 13.6, J = 12.6, K = 12.2$	$G = 13.3, J = 12.1$ and $K = 11.7$
Colour		$J - K = 0.4$	$J - K = 0.4$
Fitted parameters			
Δx	Relative CCD x position of the blend in pixel	1.67 ± 0.14	0.1312 ± 0.0071
Δy	Relative CCD y position of the blend in pixel	1.87 ± 0.14	0.0798 ± 0.0064
F_0	Offset in normalised flux	$(7.2 \pm 1.1) \cdot 10^{-4}$	$(9.68 \pm 0.50) \cdot 10^{-4}$
$\xi_{x,0}$	Offset in centroid in x in pixel	$(-2.7 \pm 5.8) \cdot 10^{-5}$	$(1.93 \pm 0.47) \cdot 10^{-4}$
$\xi_{y,0}$	Offset in centroid in y in pixel	$(-6.0 \pm 5.9) \cdot 10^{-5}$	$(1.61 \pm 0.44) \cdot 10^{-4}$
D	Dilution	$0.1217^{+0.0099}_{-0.0088}$	$0.849^{+0.010}_{-0.015}$
J	surface brightness ratio	0.722 ± 0.010	0.1061 ± 0.0065
$(R_1 + R_2)/a$	Sum of radii over semi-major axis	0.2414 ± 0.0044	0.2634 ± 0.0031
R_2/R_1	Ratio of radii	0.247 ± 0.012	$0.462^{+0.018}_{-0.022}$
$\cos i$	Cosine of the inclination	0.1713 ± 0.0051	$0.022^{+0.021}_{-0.015}$
P	Period in seconds	140145.80 ± 0.59	138852.0 ± 1.4
T_0	Epoch in seconds	54443339 ± 35	59237250 ± 34
e	Eccentricity	0.0 (fixed)	0.0 (fixed)
ω	Argument of periastron in degree	0.0 (fixed)	0.0 (fixed)
$\sigma(F)$	Error on normalised flux	$(7.805 \pm 0.037) \cdot 10^{-3}$	$(4.835 \pm 0.032 \cdot 10^{-3}$
$\sigma(\xi_x)$	Error on centroid in x	$(8.383 \pm 0.041) \cdot 10^{-3}$	$(4.787 \pm 0.032) \cdot 10^{-3}$
$\sigma(\xi_y)$	Error on centroid in y	$(8.468 \pm 0.041) \cdot 10^{-3}$	$(4.448 \pm 0.03) \cdot 10^{-3}$
Derived parameters			
i	Inclination in degree	80.14 ± 0.34	$88.61^{+0.86}_{-1.26}$
R_1/a	Radius of the primary over semi-major axis	0.1935 ± 0.0027	$0.1800^{+0.0037}_{-0.0020}$
R_2/a	Radius of the secondary over semi-major axis	$0.0478^{+0.0030}_{-0.0027}$	$0.0830^{+0.0030}_{-0.0033}$
T_2	Midpoint of secondary eclipse in s	54513413 ± 41	59306676 ± 36
$T_{dur,1}$	Duration of primary eclipse in s	185700 ± 2100	281100 ± 3600
$T_{dur,2}$	Duration of secondary eclipse in s	185700 ± 2100	281100 ± 3600
$\delta_{1,dil}$	Diluted depth of the primary eclipse	$3.252^{+0.043}_{-0.051}$	$3.628^{+0.032}_{-0.047}$
$\delta_{2,dil}$	Diluted depth of the secondary eclipse	$2.798^{+0.041}_{-0.052}$	0.238 ± 0.023
$\delta_{1,undil}$	Undiluted depth of the primary eclipse	$3.716^{+0.067}_{-0.073}$	$24.5^{+2.0}_{-2.6}$
$\delta_{2,undil}$	Undiluted depth of the secondary eclipse	$3.197^{+0.063}_{-0.070}$	2.10 ± 0.26
Δx_{sky}	Relative sky position of the blend in arcsec	8.29 ± 0.76	0.653 ± 0.040
Δy_{sky}	Relative sky position of the blend in arcsec	9.29 ± 0.84	0.396 ± 0.034

4.5   Discussion

4.5.1   Impact of the centroiding technique on NGTS candidate vetting

NGTS is successfully employing the centroid technique for automated and routine candidate vetting. I achieve an average centroid precision of 0.75 milli-pixel for all candidates, and as low as 0.25 milli-pixel for individual objects. This precision depends on the photometric data quality as a direct consequence of Eq. 4.12 and 4.18. I therefore expect to observe an increase of the centroiding utility with higher signal-to-noise ratios of the detected transit-like signal.

The obtained centroid precision exceeds the previous assumptions in my yield estimations by an order of magnitude (see Chapter 4). The yield simulator is based on a galactic model and the planet occurrence rates estimated by the Kepler mission. It considers the measured noise levels and observation window function of NGTS, and simulates vetting criteria to identify false positives. I previously assumed all centroid shifts > 10 mpix could be detected, and predicted that $\sim 38\%$ of all BEBs can be identified with NGTS alone. Considering the achieved centroid precision of 0.75 mpix, I update my yield simulator and repeat this analysis. I assume that all centroid signals $> 3\sigma$ above the noise level can be detected. This is motivated by the detection of a ~ 2 mpix centroid shift for NG 0409-1941 020057 (Section 4.4.2 Fig. 4.12). I estimate that this allows to directly identify $\sim 80\%$ of all BEBs (see Fig. 4.15).

To verify these estimations, I test my implementation on eclipsing systems from the latest NGTS pipeline run. I restrict this comparison to a sample of obvious astrophysical signals with eclipse depths $> 2\%$ to avoid the influence of spurious signals. Note that this sample mostly comprises undiluted EBs due to their high occurrence rates. I find that $16 \pm 8\%$ of this sample show a significant correlation between their photometric flux and centroid data. The given confidence interval is the standard error of the mean of a sample of binomial random variables. In comparison, the simulations suggest the identification of a centroid shift for $12 \pm 2\%$ of such a sample. These values are in agreement, and highlight the expected success of the centroid algorithm for the automated candidate vetting pipeline.
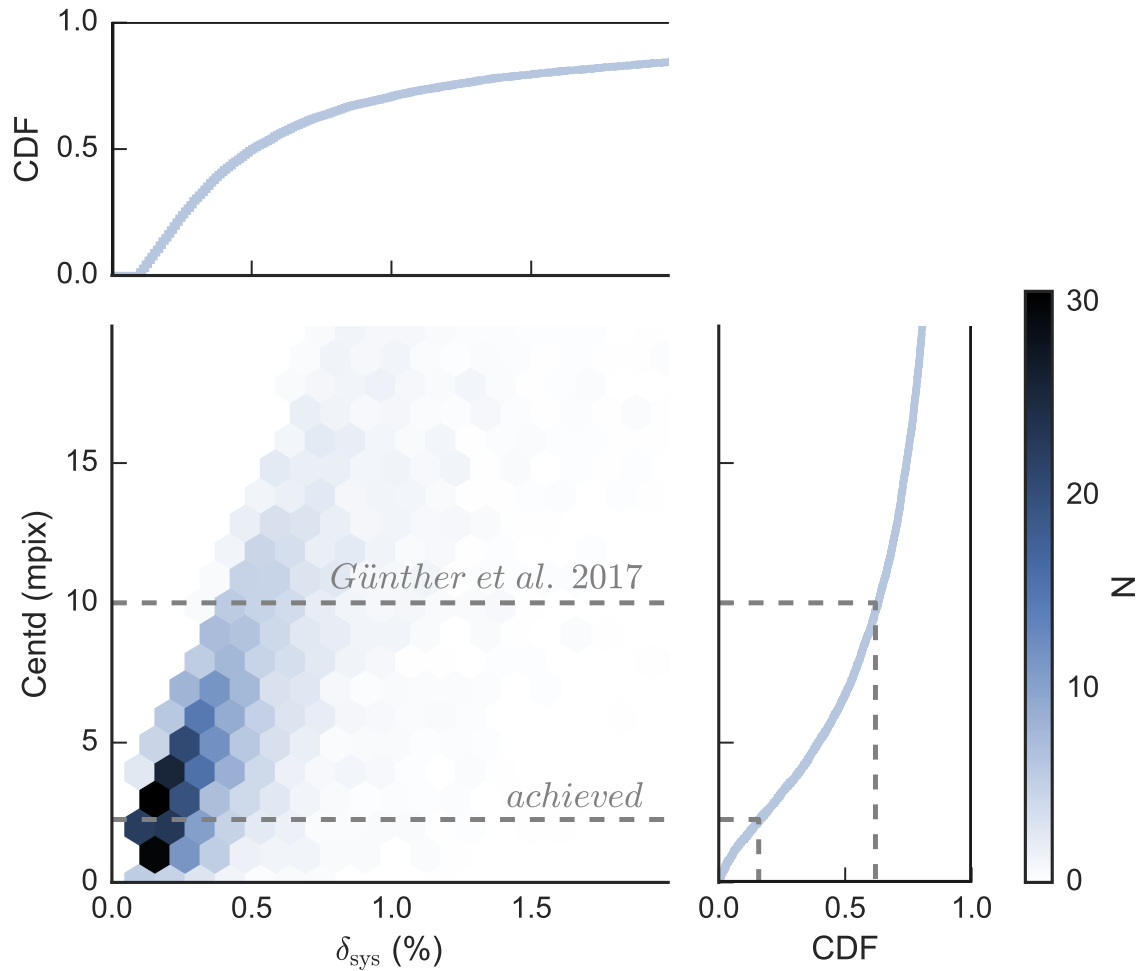
Fig. 4.15 *The impact of the centroiding algorithm for automated planet candidate vetting in NGTS, based on the simulated yield for four years of survey operation. Shown is the total number of BEBs triggering a signal as a function of the measured (diluted) transit depth of the system, δ_{sys}, and the caused centroid shift, $\Delta \xi$, as well as the cumulative distribution function (CDF) of each parameter. Assuming that all centroid signals $> 3\sigma$ above the noise level of 0.75 mpix can be detected, the achieved centroiding detection threshold exceeds my previous assumptions by an order of magnitude. This will allow to directly identify $\sim 80\%$ of all BEBs.*

4.5.2   Investigated candidates

In sections 4.4.2 and 4.4.2, I demonstrated my method in two case studies. First, visual information on NG 0522-2518 017220 allowed us to identify which blended object is undergoing the eclipse. I identify out-of-eclipse modulation, which is likely due to either a) star spots, b) the reflection effect, or c) systematics from the blended contaminant, or a combination of these effects. The eclipsing system is shown to be a grazing low-mass binary, likely consisting of a *K* star primary and *M* star or brown dwarf secondary.

Second, an analysis of NG 0409-1941 020057 reveals that its signal in fact originates from a highly diluted source, and thus suggests a deep background eclipsing binary (undiluted depth of $24.5^{+2.0}_{-2.6}\%$) as a cause. RV data previously collected with *Coralie* shows a correlation in the bisectors of the RV cross-correlation function, which supports the results of my centroiding method. The blended objects are estimated to be < 1" separated, such that at the time of analysis no existing catalogue had resolved the system. During the revision of this Thesis, *Gaia* DR2 was released, and indeed resolves the system, confirming the centroid model predictions (see Section 4.4.2). This demonstrates the effectiveness of the centroid technique, as it predicts the relative position of blended background objects even if they are unknown.

The parameter space was thoroughly explored using differential evolution algorithms and multiple MCMC runs from different starting positions. Additionally, care was taken to reach convergence of all walkers and to not fall into local minima. However, systematics in the flux and centroid time series may still be present after the detrending procedure, and could potentially restrict the exploration of the parameter space. This could lead to the underestimation of MCMC posterior likelihood distributions. Hence, a future refinement of the presented work could be the implementation of a joint MCMC model directly incorporating Gaussian Process Regression (see e.g. Gillen et al., 2017; Pepper et al., 2017).

4.6   Conclusion

I develop a comprehensive framework to extract and detrend flux centroid information from NGTS data. The introduced algorithms are part of an automated vetting pipeline for all NGTS candidates. I achieve an average precision of 0.75 milli-pixel on the phase-folded centroids over an entire field, and 0.25 milli-pixel for specific targets. This enables the identification of systems that are currently too close (< 4 arcsec) to be resolved with any photometric or astrometric all-sky survey. Case studies of NGTS candidates illustrate that different scenarios can lead to a centroid motion, yet my robust MCMC fitting procedure is able to determine the true origin of a given transit-like signal. In total, I estimate to be able to rule out $\sim 80\%$ of all blended variable background objects with NGTS data alone. These systems would otherwise have to be followed up with higher-resolution imaging, or may potentially be misidentified as planet candidates. While the centroiding technique has previously been employed for the space-based *Kepler* mission, we here develop this method for the ground-based wide-field NGTS mission.

Chapter 5

Unmasking the hidden NGTS-3Ab: a hot Jupiter in an unresolved binary system

"Know thy blend, know thy planet.

A thousand stars, a thousand diluted planets."

— freely based on a quote from Sun Tzu

5.1   Summary

In this chapter, I present the discovery of NGTS-3Ab, a hot Jupiter found transiting the primary star of an unresolved binary system. I develop a joint analysis of multi-colour photometry, centroids, RV cross-correlation function (CCF) profiles and their bisector inverse slopes (BIS) to disentangle this three-body system. This analysis is based on data gathered with NGTS, SPECULOOS and HARPS and makes use of my newly developed BLEND-FITTER software. I find that the binary consists of NGTS-3A (G6V-dwarf) and NGTS-3B (K1V-dwarf) at < 1" separation. NGTS-3Ab orbits every $P = 1.6753728 \pm 0.0000030$ days. The planet radius and mass are $R_{\mathrm{planet}} = 1.48 \pm 0.37$ R$_J$ and $M_{\mathrm{planet}} = 2.38 \pm 0.26$ M$_J$, suggesting the planet is potentially inflated. This analysis emphasises that systems like NGTS-3 can be resolved by combining all the information from multi-colour photometry, centroids and RV CCF profiles. Such systems cannot be disentangled from single-colour photometry

and RV measurements alone. Importantly, the presence of a BIS correlation indicates a blend scenario, but is not sufficient to determine which star is orbited by the third body. Moreover, even if no BIS correlation is detected, a blend scenario cannot be ruled out without further information. This further cautions that the choice of methodology for calculating the BIS can influence the measured significance of its correlation. The findings presented in this chapter are crucial to consider for wide-field transit surveys, which require wide CCD pixels (> 5") and are hence prone to contamination by blended objects. With TESS on the horizon, it is pivotal for the candidate vetting to incorporate all available follow-up information from multi-colour photometry and RV CCF profiles.

5.2   Introduction

NGTS and the upcoming TESS mission will soon further increase the sample of small planets orbiting bright stars, delivering prime targets for follow up studies. Naturally, such wide-field exoplanet surveys require wide CCD pixels (> 5"). This can influence the observation in two ways (see Section 1.6): 1) circa 44 per-cent of main sequence F6-K3 systems (Raghavan et al., 2010) and $20 - 50$ per-cent of late K and M dwarfs (Fischer & Marcy, 1992; Ward-Duong et al., 2015) are actually binary and triple systems. A given target might hence be a multi-star system, whose companions remain unresolved. 2) A single CCD pixel often contains multiple background objects, whose light (and signals) influence the observations. Both scenarios can lead to the underestimation of planet radii or to false positives.

In this chapter, I evaluate an interesting signal observed with NGTS, that initially seemed to originate from the transit of a hot Jupiter around a Sun-like star. After gathering HARPS follow-up spectroscopy, a planet-like RV signal was confirmed, but a bisector correlation was detected. Usually, bisector correlations are seen as indicators of BEBs (see Section 1.7), and as such, the system was nearly disregarded as a false positive. Through careful analysis of all data and false positive scenarios, and development of a new routine, the BLENDFITTER modelling toolbox, I am able to disentangle this system.

I present the discovery of NGTS-3Ab, a hot Jupiter found orbiting a star in a still visually unresolved binary system. This chapter attempts to provide a comprehensive case study to unmask an unresolved three-body system by combining all the information from multi-colour photometry, centroids, RV measurements and their bisectors. This study is based on data gathered with NGTS, SPECULOOS and HARPS, and enhanced by my advances with the centroiding technique for NGTS (Chapter 4). Here, I develop a new algorithm, BLENDFITTER, to conjointly model multi-colour photometry, centroids and the RV extraction process. For this, I simulate the RV CCFs and study correlations of the BIS. My findings highlight the value of a thorough inspection and modelling of multi-colour photometry, centroids, RV CCFs and BISs for exoplanet surveys.

5.3   Blendfitter

The BLENDFITTER code is a global MCMC modelling framework. It incorporates the analysis of transit light curves from multiple instruments, centroid time series, and radial velocity (RV) data. It can directly extract all relevant information from a radial velocity (RV) cross-correlation function (CCF). This bypasses the extraction step in the standard pipelines of RV surveys, which potentially could treat blended systems incorrectly. By modelling the CCF with a single Gaussian (one source of light) or the sum of two Gaussians (two sources of light), BLENDFITTER can readily capture blend scenarios. The information BLENDFITTER extracts includes the RV, full-width at half maximum (FWHM), Contrast and CCF bisector. From this, the bisector inverse slope (BIS) can be computed.

Based in a Bayesian framework, any prior information can be included. These can be, for example, different telescope bandpasses, the properties of the host star, or constrains on the blend separation. Finally, BLENDFITTER allows to model baseline functions through Gaussian Process (GP) regression or as polynomials. Each step of the BLENDFITTER routine is elaborated on the example of NGTS-3 throughout the following Sections.

Table 5.1 Summary of all observations of NGTS-3 used in this work, including the discovery photometry, the follow-up photometry and the spectroscopic observations.

Facility	Date	Notes
NGTS	2016 Aug 18 - 2017 Dec 6	78572 points, 10s exp.
SPECULOOS-Callisto	2018 Jan 26	301 points, 30s exp., r' band
SPECULOOS-Io	2018 Feb 9	471 points, 30s exp., i'+z' band
SPECULOOS-Europa	2018 Feb 9	457 points, 30s exp., i'+z' band
SPECULOOS-Callisto	2018 Feb 15	445 points, 35s exp., g' band
SPECULOOS-Europa	2018 Feb 15	469 points, 30s exp., r' band
HARPS	2017 Feb 1 - 2017 Mar 5	7 spectra

5.4   Observations

NGTS-3 (NGTS J061746.7-354222.9; see Table 5.5) was photometrically discovered by NGTS, and followed up using high precision photometry from SPECULOOS during its commissioning period, and spectroscopy from HARPS. All of these observations are detailed in this Section and a summary is provided in Table 5.1.

5.4.1   NGTS photometry

The presented data on NGTS-3 was observed on a single NGTS telescope over a photometric campaign conducted between 18 August 2016 and 6 December 2016, and detrended with the 'TEST18' pipeline version. This contains 78572 exposures of 10 s in the NGTS bandpass (550 – 927 nm) over a total of 89 observation nights. The autoguider's RMSE of the field tracking errors was 0.136 pixels over the 89 nights. This slightly elevated RMSE (compared to the typical value of ~ 0.05 pixels) was due to a mechanical issue with the right ascension bearing in the mount, whereby the telescope occasionally jumped by ~ 1 pixel. The autoguiding then recentered the field after few exposures. Image reduction, aperture photometry, reduction of systematic effects, and transit search were performed as described Section 1.9. I further extracted and reduced the flux centroids of NGTS-3 as described in Chapter 4.

NGTS-3's transit-like signal of 2% was detected with a period of 1.675 days and width of 2 hours. No centroid shift was detected. Initially, these photometric observations alone made NGTS-3 a strong hot Jupiter candidate. Table 5.2 provides the full photometry and centroid

Table 5.2 NGTS photometry and centroid data of NGTS-3. For guidance, ten observations are shown here.

Time days (HJD-2450000)	Flux (normalised)	Centd x pixel	Centd y pixel
...	...	...	...
7619.901516	1.021527545	-0.11709990	0.06187227
7619.901667	1.000179888	-0.04072431	0.04446441
7619.901806	0.957097368	-0.02046733	0.04210692
7619.901956	1.076526278	0.07883140	0.03817588
7619.902106	0.996836033	-0.03235835	0.03558102
7619.902257	1.123472365	0.10736324	0.00703842
7619.902419	1.010499832	0.09472378	-0.01132131
7619.902569	0.943342956	-0.06200864	0.05012148
7619.90272	1.019069713	-0.00554865	-0.03038287
7619.90287	0.961933312	0.03336356	-0.09503899
...	...	...	...

time series after detrending. Figures 5.1A-D show this data phase-folded at the best-fitting transit period as determined via the global modelling (outlined in Section 5.5.8).

5.4.2   SPECULOOS photometry

SPECULOOS is located at ESO's Paranal Observatory in Chile and currently undergoing commissioning. The facility consists of four robotic 1-meter Ritchey-Chretien telescopes. Each telescope is equipped with an Andor Peltier-cooled deeply depleted 2K×2K CCD camera with a 13.5 μm pixel size. The field of view of each telescope is 12'×12'(0.35"/pixel), with optimal sensitivity in the near-infrared (700 to 1000 nm).

NGTS-3 was observed in the g', r' and i'+z' bands during the commissioning of the first three SPECULOOS telescopes, Europa, Io and Callisto. A summary of these observations is provided in Table 5.1. The images were calibrated using standard procedures (bias, dark, and flat-field correction) and photometry was extracted using the IRAF/DAOPHOT aperture photometry software (Stetson, 1987), as described by Gillon et al. (2013). For each observation, a careful selection of both the photometric aperture size and stable comparison stars was performed manually to obtain the most accurate differential light curve of NGTS-3.
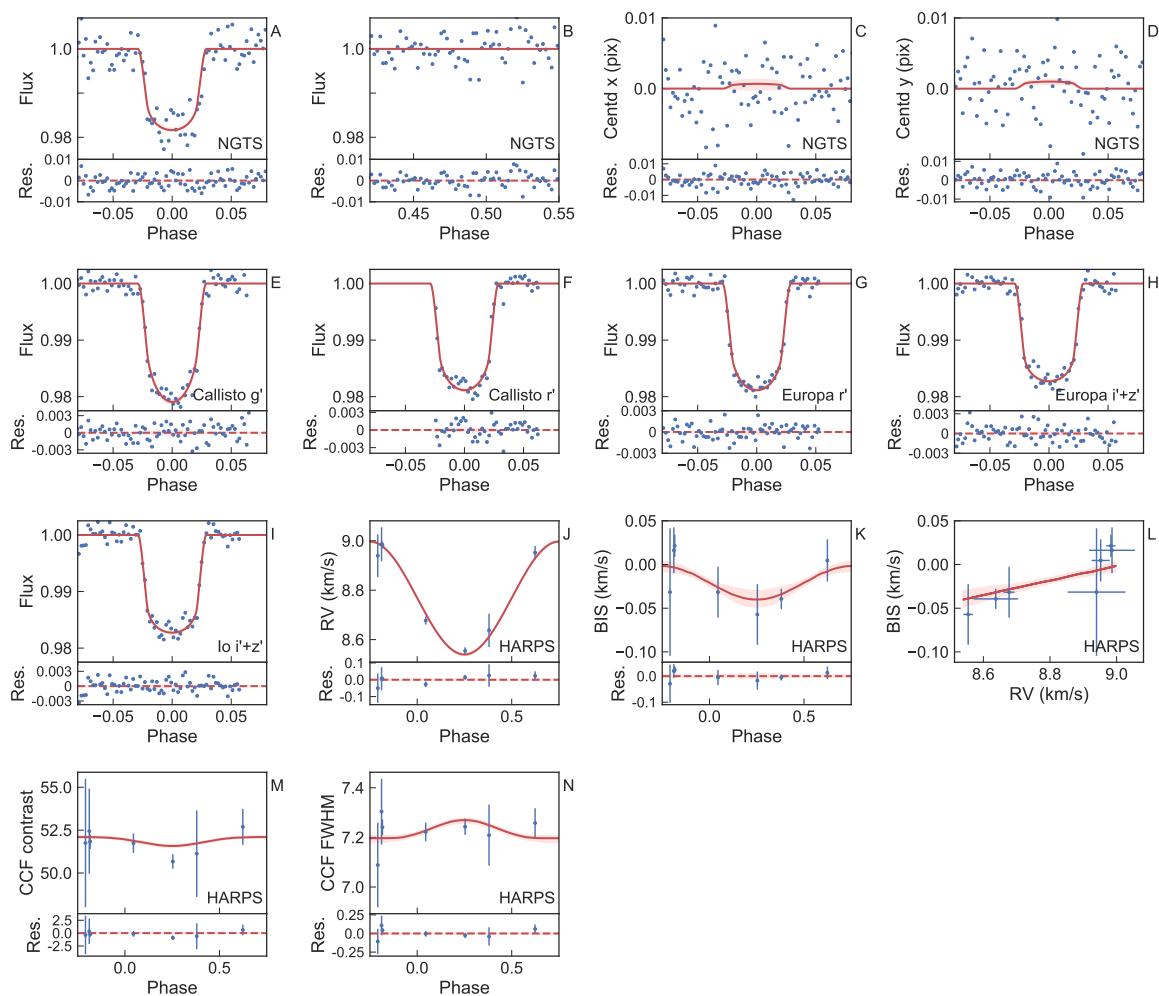
Fig. 5.1 Data and global model of NGTS-3, phase-folded at the best-fitting period of 1.675 d. A) NGTS light curve, B) NGTS light curve around phase 0.5, C) NGTS centroid in x, D) NGTS centroid in y, E) SPECULOOS Callisto g'-band, F) SPECULOOS Callisto r'-band, G) SPECULOOS Europa r'-band, H) SPECULOOS Europa i'+z'-band, I) SPECULOOS Io i'+z'-band, J) HARPS RV measurements, K) HARPS bisector inverse slope (BIS), L) HARPS BIS versus RV, M) HARPS Contrast measurements, and N) HARPS FWHM measurements. Photometric measurements are binned equally in phase with a spacing of 0.002 (total of 500 phase-folded points). I randomly draw 100 samples from the MCMC chain and calculate the models. Red curves in A)-N) display the median and 16th / 84th percentile of all drawn models. The global, joint modelling is described in Section 5.5.8.

Table 5.3 SPECULOOS Callisto r' band photometry for NGTS-3, as an example of the SPECULOOS observations with Europa, Io and Callisto. For guidance, ten observations are shown here.

Time days (HJD-2450000)	Flux (normalised)	Flux error (normalised)
8144.51886	0.99634245	0.00306679
8144.51931	0.99873645	0.00303029
8144.51976	0.9895214	0.00292396
8144.52021	0.99279671	0.0029041
8144.52067	0.99233135	0.00286985
8144.52112	0.99131786	0.00286618
8144.52157	0.98893842	0.00277872
8144.52202	0.99065349	0.00284851
8144.52247	0.98691918	0.00285377
8144.52292	0.98281773	0.00297856
...	...	...

Table 5.3 provides the full photometry of one of the observations as an example. Figs. 5.1 E-I show the data with the best fit determined via the global modelling (see Section 5.5.8).

5.4.3 HARPS spectroscopy

RV follow-up for NGTS-3 was obtained with HARPS (Mayor et al., 2003) on the ESO 3.6 m telescope at La Silla Observatory in Chile between 1 February 2017 and 5 March 2017. The data was reduced using the standard HARPS data reduction software (DRS). RVs were calculated for each epoch via cross-correlation of the HARPS data reduction pipeline with a G2 mask. Results along with their associated error, full width at half maximum (FWHM), contrast, and bisector slope are listed in Table 5.4. Early RV results were encouraging, with an in-phase variation of K$\approx$230 m s^{-1} at a very high significance (see Fig. 5.1 J). However, the bisector span of the RV cross-correlation function showed a strong correlation with the measured RV (see Fig. 5.1 K and L). As discussed in Section 1.7, this can be a sign of a contaminating spectrum with large RV shifts (e.g. due to a blended binary), which is responsible for the apparent RV variation of the target.

Table 5.4 HARPS radial velocities for NGTS-3 as retrieved by the standard data reduction software (HARPS DRS 3.5).

Time days HJD-2450000	RV km/s	RV error km/s	FWHM km/s	Contrast per-cent	BIS km/s
7785.721175	8.98228	0.01635	7.23903	52.138	0.02101
7790.705903	8.93196	0.02892	7.00693	51.672	-0.00334
7791.692363	8.62082	0.01606	7.08774	50.959	-0.04371
7811.584627	8.55463	0.01448	7.2421	51.021	-0.05955
7814.586319	8.67687	0.01237	7.22015	52.134	-0.01864
7815.555984	8.94451	0.01069	7.22257	52.785	0.01179
7817.545532	8.98783	0.01712	7.24024	52.212	0.01667

5.5   Analysis

5.5.1   Stellar properties

The NGTS-3 system is located at RA = 06h 17m 46.8s, DEC = -35d 42m 22.3s, and is identified as NGTS J061746.7-354222.9, with magnitudes $G = 14.4$, $J = 13.3$, $K = 12.8$ (Table 5.5). The HARPS data shows a positive bisector correlation (Fig. 5.1K and L), which is a direct indicator for contamination of the spectrum of NGTS-3A by at least one other stellar object in the system (see Section 1.7).

A spectral fit of the seven obtained HARPS spectra is performed to determine the parameters of the brightest object in the aperture, denoted as NGTS-3A (Table 5.5). The overall signal-to-noise ratio is relatively low (23:1), leading to large uncertainties on the derived parameters. The co-added spectrum shows no sign of contamination due to the other star in the aperture. Using methods similar to those described by Doyle et al. (2013), values for the stellar effective temperature $T_{\mathrm{eff},A}$, surface gravity $\log g_A$, the stellar metallicity $[Fe/H]_A$, and the projected stellar rotational velocity $(v \sin i)_A$ are derived. To constrain the latter, a macroturbulence value of 2.7 km s^{-1} is obtained using the Doyle et al. (2014) asteroseismic calibration. The effective temperature of $T_{\mathrm{eff},A} = 5600 \pm 150$ K from the spectra analysis, is consistent with the results using the infrared flux method (IRFM). Lithium is not seen in the spectra, giving an upper-limit of $\log A(\mathrm{Li})_A < 1.1$. The measured $T_{\mathrm{eff},A}$ suggests that NGTS-3A is most likely a G6V dwarf, but consistent with a G2V to G8V dwarf (see e.g. Pecaut & Mamajek, 2013).

Table 5.5 Stellar Properties for the NGTS-3 system

Property	Value	Source
Astrometric properties of the system		
R.A.	94.444801	2MASS
Dec	-35.706394	2MASS
NGTS I.D.	J061746.7-354222.9	NGTS
2MASS I.D.	J06174675-3542230	2MASS
Gaia I.D.	2885350546895266432	*Gaia* DR2
$\mu_{\text{R.A.}}$ (mas y^{-1})	-7.4 ± 1.2	UCAC5
$\mu_{\text{Dec.}}$ (mas y^{-1})	8.6 ± 1.3	UCAC5
Photometric properties of the system		
V (mag)	14.642 ± 0.047	APASS
B (mag)	15.451 ± 0.049	APASS
g (mag)	15.002 ± 0.028	APASS
r (mag)	14.423 ± 0.043	APASS
i (mag)	14.252 ± 0.01	APASS
G_{GAIA} (mag)	14.488	*Gaia* DR2
NGTS (mag)	14.109	This work
J (mag)	13.281 ± 0.029	2MASS
H (mag)	12.965 ± 0.029	2MASS
K (mag)	12.814 ± 0.03	2MASS
W1 (mag)	12.798 ± 0.023	WISE
W2 (mag)	12.820 ± 0.023	WISE
B-V colour	0.809 ± 0.068	APASS
J-H colour	0.316 ± 0.042	2MASS
H-K colour	0.151 ± 0.042	2MASS
Derived properties for NGTS-3A		
$T_{\text{eff,A}}$ (K)	5600 ± 150	HARPS spectra
$T_{\text{eff,A}}$ (K)	5570 ± 140	IRFM fitting
$[Fe/H]_{\text{A}}$	$+0.12 \pm 0.15$	HARPS spectra
$(v \sin i)_{\text{A}}$ (km s^{-1})	1.0 ± 0.7	HARPS spectra
$\log g_{\text{A}}$	4.5 ± 0.2	HARPS spectra
$\log A(\text{Li})_{\text{A}}$	< 1.1	HARPS spectra
M_{A} (M$_{\odot}$)	1.017 ± 0.093	ER
R_{A} (R$_{\odot}$)	0.93 ± 0.23	ER
ρ_{A} (g cm^{-3})	1.09 ± 0.29	ER
Spectral type, A	G6V (G2V-G8V)	ER2

2MASS (Skrutskie et al., 2006); UCAC5 (Zacharias et al., 2017); APASS (Henden & Munari, 2014); WISE (Wright et al., 2010); *Gaia* DR1 (Gaia Collaboration et al., 2016b); ER: empirical relations using Torres et al. (2010); ER2: empirical relations using Pecaut & Mamajek (2013).

Table 5.6 No statistical identification of a centroid shift in NGTS-3, using the analysis methods described in Chapter 4. The table displays the signal-to-noise ratio (SNR) of the rolling correlation and cross-correlation analyses, which are well below the threshold SNR=5 in all cases. Further the table lists the resulting p-values from a T-test and binomial test of the in-transit centroid data, testing the Null Hypothesis that the centroid is distributed around the mean of the out-of-transit data, i.e. around 0. *All p-values are well above the threshold p=0.01 for rejecting the Null Hypothesis.*

	x	y
SNR roll. corr.	1.88	1.35
SNR cross-corr.	2.23	2.21
p-value T-test	0.0692	0.1672
p-value Binomial test	0.0649	0.1189

5.5.2 Centroiding

NGTS-3 is registered as a single source in all existing archival data. As part of the NGTS candidate vetting pipeline, a centroiding analysis is performed. No centroid shift is observed for NGTS-3 (Fig. 5.2; Table 5.6). Concurring with the NGTS photometry, this initially made a planet scenario very likely. It is important to emphasise that the non-detection of a centroid shift minimises the risk of blends, but only completely rules out blends at more than ~1" separation (dependent on the magnitude difference and signal depth). In any case, the non-detection of a centroid shift allows to place upper-limits on the possible location of this blend and the dilution it causes.

5.5.3 HARPS CCF, RV and bisector model

The RV of a star is measured as the Doppler shift of spectral lines (see Section 1.3). The obtained stellar spectrum is cross-correlated with a reference spectrum, and the CCF is fitted with a Gaussian profile to extract the RV, FWHM and Contrast (see Section 1.7). From the CCF, the bisector and BIS can be extracted. Correlations of the BIS with the RV curve can unveil star spots and background binaries mimicking exoplanet signals. The left column in Fig. 5.3 shows the seven CCFs obtained from cross-correlating the HARPS measurements with a reference spectrum of a G2-type star (HARPS DRS has the option of a K5 and G2 mask for cross-correlations).
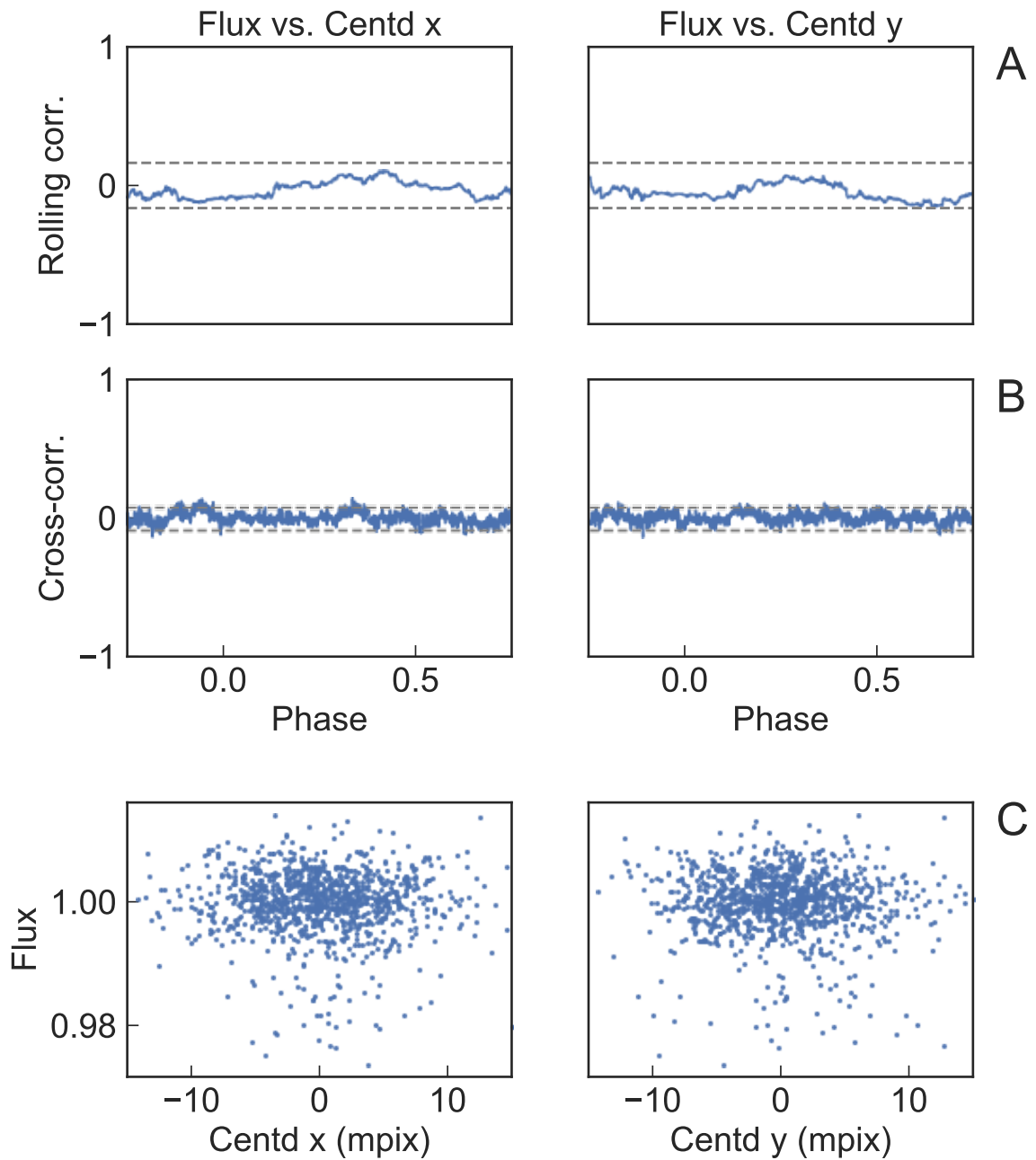
Fig. 5.2 No identification of a centroid shift correlated to the transit signal for NGTS-3Ab, using the analysis methods described in Chapter 4. The upper panels show the rolling (window) correlation (A) and cross-correlation (B) between flux and centroid, phase-folded on the best-fitting transit period. Neither shows signs of a correlation. Dashed lines indicate the 99% confidence intervals in each case. Panel C) shows the 'rain plots', a graphical illustration of the relation between flux and centroids. Here, the 'rain' falls straight down, meaning there is no sign of a correlation.
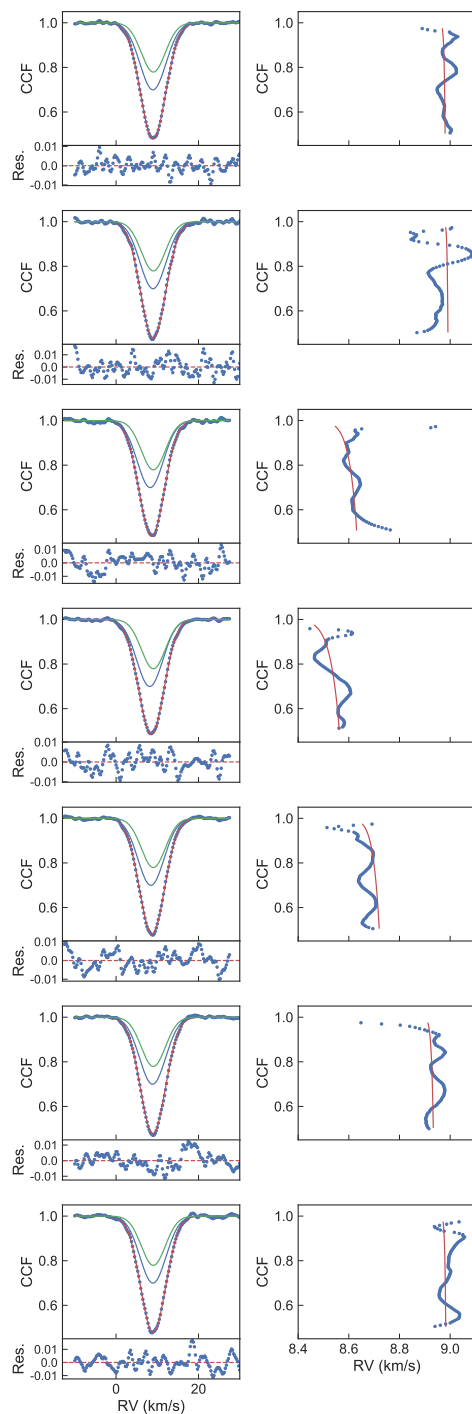
Fig. 5.3 The seven HARPS CCF profiles (left column), and zoom onto their extracted bisectors (right column). Left column: the shown CCF profiles are corrected for the best-fit baseline from the global BLENDFITTER MCMC model. Red lines show the MCMC results for the best fit of the movement of two stars, modelled as two Gaussian profiles. The model for star A is shown in green, star B in blue and their sum in red. Sub-panels show the residuals of the fit. Right column: bisectors were extracted by BLENDFITTER using the second derivatives of the Gaussian fit.

Comparison of approaches to extract the RV, FWHM and Contrast

The most recent HARPS data reduction software (HARPS DRS 3.5) fits an inverse Gaussian function with a constant offset to the CCF profile. By modelling the baseline of the CCF profile as a constant offset, linear or higher order trends are not regarded. The RV, FWHM and Contrast measurements are then extracted as the mean, FWHM and amplitude of the Gaussian. I implement two approaches in the BLENDFITTER code. The first choice follows the exact HARPS DRS procedure. As expected, the results match the HARPS results exactly, with a deviation of $< 10^{-4}$. In all cases, this precision is by a factor of 100 within the parameters' error bars.

I find that the approach of the HARPS DRS fit (i.e. fitting a Gaussian with a constant offset) leaves strong systematic trends in the residuals of the CCF profiles. I hence implement a second method in the BLENDFITTER code. Instead of using a constant baseline, this employs a Gaussian Process (GP) model jointly with the Gaussian fit, and performs an MCMC fit. The MCMC and GP are implemented using EMCEE (Foreman-Mackey et al., 2013) and GEORGE (Ambikasaran et al., 2016). The GP kernel is chosen to be

$$k\left(r^2\right) = c\left(1 + 3\sqrt{r^2}\right)e^{-3\sqrt{r^2}}, \tag{5.1}$$

which represents the product of a constant kernel c and a Matern 3/2 kernel (see Section 2.6). This kernel can describe variations which display a rougher (i.e. more stochastic) behaviour in addition to a characteristic length scale, such as it is the case in the CCF profiles. A fit for white noise is also performed.

I perform an MCMC fit for each CCF profile, using 50 walkers to explore the 6 dimensions (amplitude, mean, standard deviation, c, M, and a white noise scale factor). Two separate burn-in phases of 2000 steps each, a third burn-in of 5000 steps, and an evaluation of 5000 steps are run. The maximum autocorrelation length for all data sets is < 100 steps, and hence all chains are considered to be converged. The chains are thinned by a factor of 10, which leads to a total of $50 \times 5000/10 = 25000$ samples.

Fig. 5.4 compares the resulting parameters from BLENDFITTER and HARPS DRS. Reported values and error bars represent the median and 16th/84th percentile of the resulting posterior likelihood distributions. The GP approach improves the fit and reduces the systematic baseline trend visible in the residuals of the HARPS DRS approach. This shows that in the presence of strong systematics to the CCF profile, especially in the tails of the CCF profile, a constant baseline fit can be too restricting. This can lead to a high bias with low variance. The GP model allows an evaluation with lower bias and higher ('fairer') variance. I consequently use the parameters extracted with the GP model for the global modelling in Section 5.5.8.

Here, I purposely use a single Gaussian model to fit the measured HARPS CCF profiles. This is to match the standard HARPS data analysis (assuming a single planet model). In contrast, in the global MCMC model (see Section 5.5.8) I outline the detailed analysis of the HARPS CCFs with a bimodal Gaussian model (for an unresolved blended system).

Comparison of approaches to extract the bisector and BIS

Throughout the literature, the CCF bisectors have been calculated using slightly different methods. Three examples are outlined here. First, the original implementation for exoplanets by Queloz et al. (2001b) builds on the approach used in studies of binary stars (e.g. Gray, 1989; Toner & Gray, 1988) for individual spectral lines. It uses the sampling on the left wing of the CCF peak. At each measured point, a horizontal line is drawn to intersect with the right wing. The intersection value on the right wing is calculated from a linear interpolation between the two nearest points. The bisector at this level is then calculated as the mean between the left and right value. Second, a cubic spline interpolation can be used to interpolate both sides of the CCF, and calculate the bisector at any chosen value. Last, the most recent HARPS data reduction pipeline (HARPS DRS 3.5) further minimises the impact of outlying points. The routine fits a Gaussian function to the CCF, and calculates the line bisectors from the second derivatives of this fit.

In the BLENDFITTER code, I implement these three methods of calculating the bisector: linear interpolation, cubic spline interpolation and second derivatives of a Gaussian fit. I
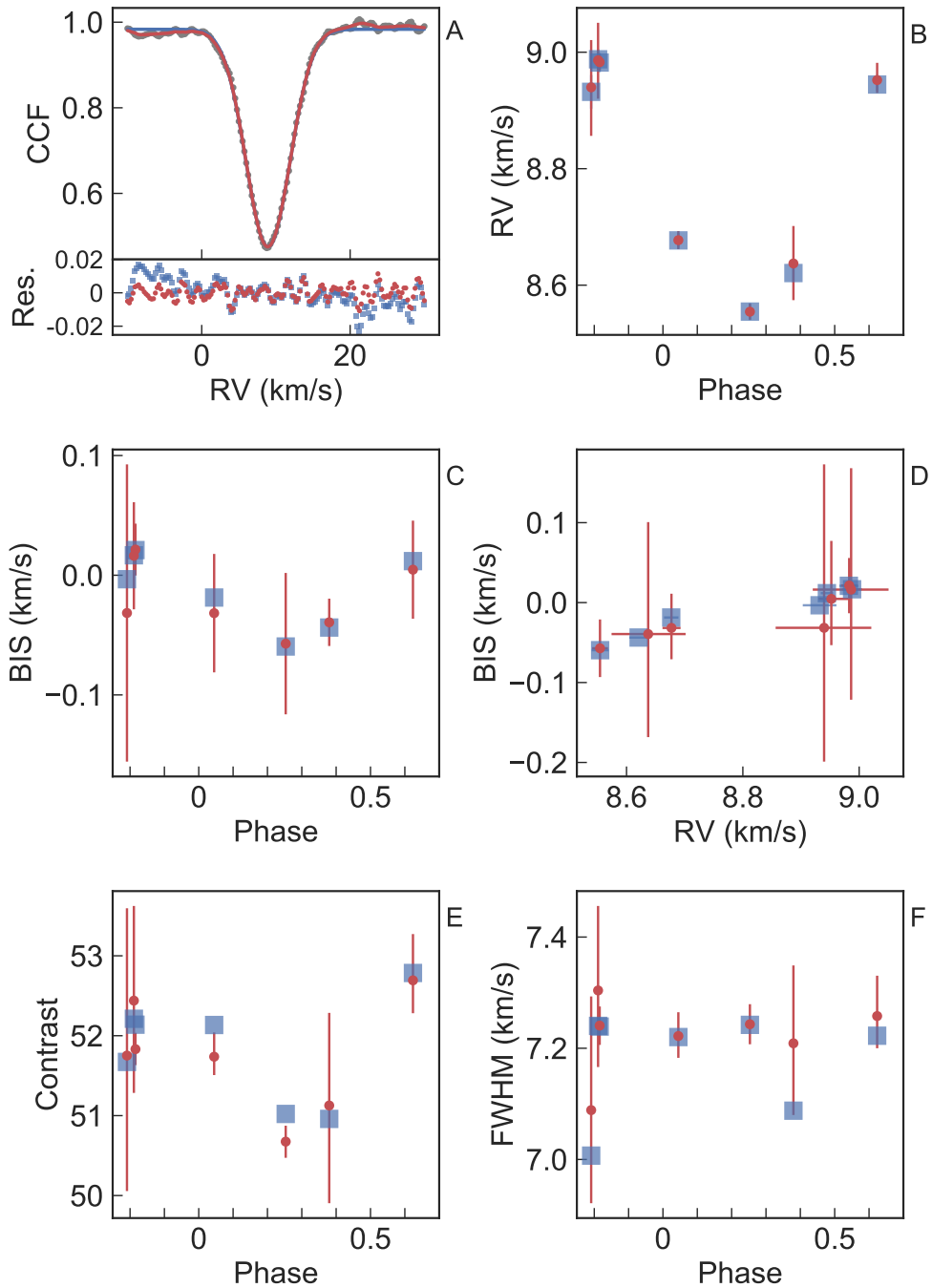
Fig. 5.4 Comparison of the fit and residuals (A) and the extracted parameters (B-F) between the standard HARPS DRS pipeline with a constant baseline (DRS 3.5; blue squares), and the BLENDFITTER *code using a Gaussian Process model for the baseline (red circles). The latter allows an evaluation of the parameters and error bars which is less biased due to systematic noise in the tails of the CCF profile. Values and error bars are thereby estimated with an MCMC fit and represented as the median and 16th/84th percentile of the resulting posterior likelihood distributions.*

re-analyse the HARPS CCFs to verify that the implementation reproduces the reported HARPS results, and to compare the three methods with each other. The right column in Fig. 5.3 shows the extracted bisectors using the same approach as HARPS DRS. Note that all analysed HARPS spectra show a 'serpentine shape' in their bisectors, which can introduce systematic errors into the BIS calculation.

All three methods result in almost identical shapes of the bisectors. However, the linear interpolation approach leads to systematic deviations of the bisector near the top and bottom of the CCF profile. When extracting the BIS from the bisectors, I find that for low-noise CCF profiles all three methods agree in their BIS measurements to a few meters per second, well within their error bars. However, for high-noise CCF profiles, the cubic spline solution differed from the DRS approach by up to ~ 10 m/s, and the linear interpolation approach by up to ~ 100 m/s. This was mainly driven by the discrepancy in extracted bisectors towards the top and bottom of the CCF profile.

A BIS correlation is detected with all three methods. The DRS approach proves to be the most robust way to extract the BIS, while the linear interpolation is strongly affected by noise in the CCF profile. The BLENDFITTER software includes the choice between all three methods, but as the DRS approach proved to be the most robust, I use this setting for all following analyses. This raises caution that the choice of methodology for calculating the bisectors can influence the measured significance of a BIS correlation.

Modelling the CCFs of blended systems

I assume a three body system in which star A is the brightest object, star B is the second star and object C is a third body orbiting one of the stars. The light from object C is assumed to be negligible in comparison to star A and B. Then the overall CCF extracted from a blended system can be modelled as the sum of the CCF from star A and B. As the true shapes of their CCFs are unknown, I represent them as two Gaussian functions, which is the general approximation in RV data analysis. The amplitudes A_A and A_B (of the Gaussians representing star A and B) depend on the product of two factors: 1) the amount of light entering the fibre from each star, F_A and F_B, and 2) the intrinsic CCF contrast in dependency of the stellar

spectral type, C_A and C_B. These are directly connected to the dilution for the RV data. The dilution of star B and star A are calculated as:

$$D_{0,B}^{RV} = 1 - \frac{A_B}{A_A + A_B} = 1 - \frac{C_B F_B}{C_B F_A + C_B F_B}, \tag{5.2}$$

$$D_{0,A}^{RV} = 1 - D_{0,B}^{RV} \tag{5.3}$$

The values for F_A and F_B are retrieved from the dilution model (see Section 5.5.4). I further study the dependency of the contrast C_A and C_B on the stellar spectral type. Sousa et al. (2008) performed a study of 451 potential exoplanet hosts with HARPS, and estimated their effective temperatures, surface gravities and metallicities. The original CCFs are retrieved from the HARPS archives, and the measured amplitudes of these targets are extracted. The CCF contrast strongly depends on the metallicity. I assume that star B has a comparable metallicity to star A, and select only objects with Fe/H between -0.03 and 0.27 (see Table 5.5). Further, only objects analysed with the HARPS CCF G2 mask are selected, to be consistent with the data set. This limits the sample to stars $\gtrsim$ 5000 K. Note that the contrast also strongly depends on the $v \sin i$ of the star. The sample from Sousa et al. (2008) only considers $v \sin i \lesssim 3$ km/s, and is hence biased in this regard. Due to these sample limitations, it is not possible to formulate an empirical relation between the CCF contrast and the stellar type for all possible parameter ranges in the global model. Therefore, I choose to instead propagate the range of possible contrast values from 40% to 60% as an uncertainty onto the prior for the dilution via Eq. 5.3.

Similar to the analysis by Santos et al. (2002), I use the CCF model to investigate the effect of two blend scenarios on the RV and BIS measurements in a 'toy model'. Fig. 5.5 displays all six simulated scenarios, which are outlined below:

Scenarios 1-3: star B is orbited by object C. Two Gaussians are simulated with $D_0^{RV} = 0.8$ and RV semi-amplitude $K_B = 2$ km/s. $FWHM_A$ is fixed at 7 km/s, and $FWHM_B$ is varied between 6.8 km/s, 7 km/s, and 7.2 km/s. The BLENDFITTER toolbox is then used to extract the RV and bisector measurements.

(1) $FWHM_B < FWHM_A$: The measured BIS is anti-correlated with the RV value. This cautions that this scenario can mimic BIS anti-correlations introduced by atmospheric turbulence.

(2) $FWHM_B = FWHM_A$: In practice, the BIS correlation would be covered by noise and not be measurable. This cautions that blended objects with similar FWHM can remain undetected and result in the misclassification of object C. This can lead to a wrong planet mass or false positives.

(3) $FWHM_B > FWHM_A$: The measured BIS is correlated with the RV value.

Scenarios 4-6: star A is orbited by object C. Two Gaussians are simulated with $D_0^{RV} = 0.8$ and RV semi-amplitude $K_A = 0.45$ km/s. $FWHM_A$ is again fixed at 7 km/s, and $FWHM_B$ is varied between 6.8 km/s, 7 km/s, and 7.2 km/s.

(4) $FWHM_B < FWHM_A$: The measured BIS is correlated with the RV value.

(5) $FWHM_B = FWHM_A$: In practice, the BIS correlation would be covered by noise and not be measurable. This cautions that blended objects with similar FWHM can remain undetected and lead to the misclassification of object C. This can result in a wrong planet mass or false positives.

(6) $FWHM_B > FWHM_A$: The measured BIS is anti-correlated with the RV value. This cautions that this scenario can mimic BIS anti-correlations introduced by atmospheric turbulence.

I emphasise that there is no difference between the extracted RV curves of all scenarios (Fig. 5.5). This highlights that including a precise bisector analysis in a global model is pivotal to minimise the false positive risk for exoplanet candidates. If a BIS correlation is detected, the signal can still originate from either star A or star B. Disentangling such a system requires global analysis conjoint with multi-color information, as presented below. However, even in cases where no bisector correlation is detected, scenarios 2 and 5 show that a blend scenario can not be ruled out without further information.
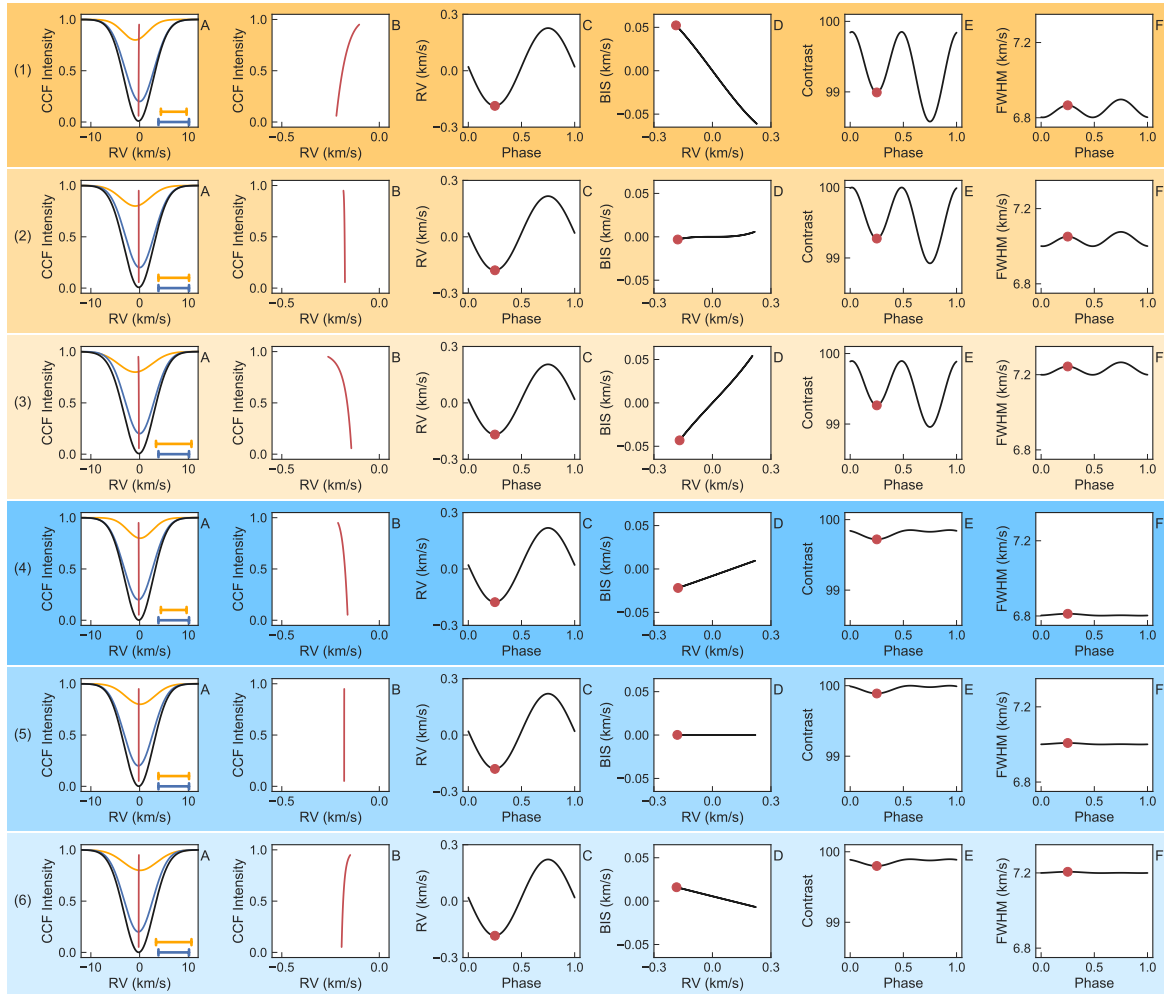
Fig. 5.5 Example scenario of an unresolved binary system, where one star is orbited by a gas giant planet or brown dwarf. The primary was set to a systemic RV of 0 km/s and the secondary to 0.1 km/s, reflecting the orbital motion of the two binary stars. The numbering of the scenarios refers to Section 5.5.3. The top three panels (orange background) display the scenario of a brown dwarf orbiting star B with $K = 1$ km/s. The FWHM or star B varies. First panel: $FWHM_B < FWHM_A$; second panel: $FWHM_B = FWHM_A$; third panel: $FWHM_B > FWHM_A$. The bottom three panels (blue background) display the scenario of a gas giant planet orbiting star A with $K = 0.25$ km/s. The FWHM or star A varies. Fourth panel: $FWHM_B < FWHM_A$; fifth panel: $FWHM_B = FWHM_A$; sixth panel: $FWHM_B > FWHM_A$. A) Simulated CCF profile (black) and bisector (red). The profile is modelled as the sum of two Gaussian functions representing star A (blue) and star B (orange). The horizontal lines at the bottom right indicate the ratio of the FWHM. B) Close-up of the bisector, measured from a single Gaussian fit. C) The RV signal, measured from a single Gaussian fit, resembles a typical hot Jupiter observation in all cases. D) The correlation of the BIS with the RV signal is a function of dilution, offset in systemic RV, and FWHM of the two stars. E) Total CCF contrast, measured from a single Gaussian fit. F) Total FWHM, measured from a single Gaussian fit. The red circles in C-F) denote the time at which the snapshot shown in A) and B) was taken. The offset from (0,0) in D) and the different peak height in E) and F) result from the different RV zero-points of the primary and secondary. All measurements were extracted with the BLENDFITTER *tools.*

Model of the CCF FWHM of NGTS-3A and NGTS-3B

The HARPS CCF profile's FWHM is a function of the stellar rotation and spectral type. From empirical calibrations, it can be expressed as a function of the star's $v \sin i$ and B-V colour (personal correspondence with Francois Bouchy):

$$\sigma^2 = \left(\frac{v \sin i}{1.95}\right)^2 + \sigma_0^2 \tag{5.4}$$

$$\sigma_0^2 = \Big(8.625 - 20.037[B-V] + 23.388[B-V]^2 \\ - 10.364\,[B-V]^3 + 1.273\,[B-V]^4\Big)^2 \tag{5.5}$$

$$\text{FWHM} = 2\sqrt{2\ln(2)\sigma^2}. \tag{5.6}$$

This relation is only valid for main-sequence FGK stars with effective temperatures $T_{\text{eff}} \gtrsim$ 3900 K.

I next use the relations by Sekiguchi & Fukugita (2000) to relate the B-V colour to the effective temperature T_{eff}, metallicity $[Fe/H]$ and surface gravity $\log g$.

$$\begin{aligned}
[B-V] = &-813.3175 + 684.4585\log T_{\text{eff}} \\
&- 189.923\log T_{\text{eff}}^2 + 17.40875\log T_{\text{eff}}^3 \\
&+ 1.2136[Fe/H] + 0.0209[Fe/H]^2 \\
&- 0.294[Fe/H]\log T_{\text{eff}} - 1.166\log g \\
&+ 0.3125\log g\log T_{\text{eff}}
\end{aligned} \tag{5.7}$$

Together with the values and uncertainties for star A from the spectral analysis (see Table 5.5), these relations are used to calculate a prior on the FWHM of star A (shown in Fig. 5.6A).
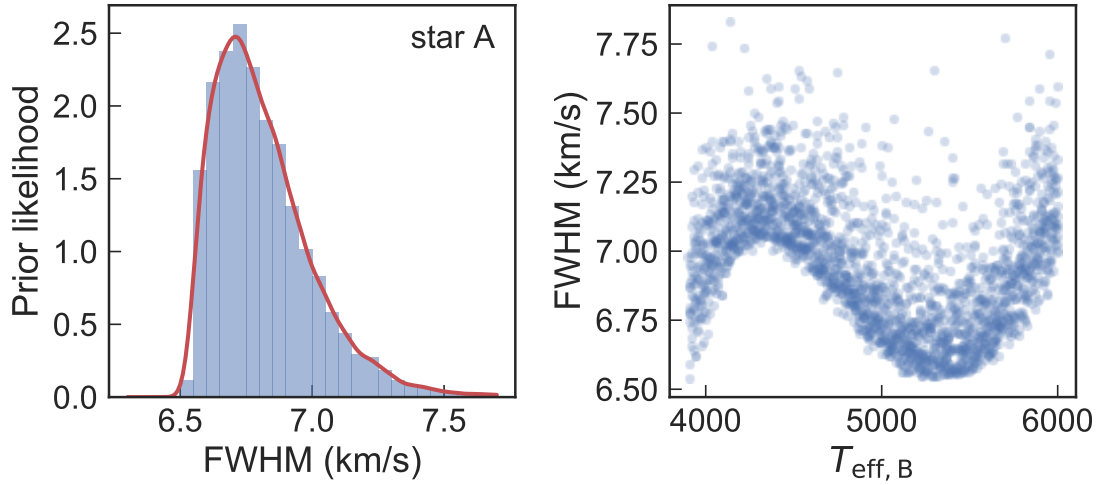
Fig. 5.6 Prior likelihood distributions for the FWHM of star A (A) and star B (B), the latter expressed as a function of $T_{\rm eff,B}$. Note the minima of the FWHM relation for early K-type stars.

Next, I establish a prior on star B in dependency of $T_{\rm eff,B}$, which is calculated from the dilution relation (Section 5.5.4) and updated at each step in the MCMC. It is assumed that both stars formed in the same system, and hence that star B has a similar metallicity to star A. Further, as there are no signs of strong stellar line broadening, it is assumed that star B is a slow rotator like star A. The above relations are then evaluated for a range of $T_{\rm eff,B}$ from $3900 - 6000$ K in steps of 1 K. Fig. 5.6B shows a sampling of the resulting prior on $FWHM_B$. Note the minima of the FWHM relation for early K-type stars.

5.5.4 Global dilution model

It is assumed that NGTS-3A dominates the observed light, and that the spectral analysis of the HARPS data constrains the properties of NGTS-3A. Additionally, the joint modelling of photometry and RV allows to make use of some informative priors and constraints on star B.

This is incorporated in the dilution terms for star A and star B for the photometric data:

$$D_{0,\mathrm{B}}^{\mathrm{phot}} = 1 - \frac{F_{\mathrm{B}}}{F_{\mathrm{A}} + F_{\mathrm{B}}}, \tag{5.8}$$

$$D_{0,\mathrm{A}}^{\mathrm{phot}} = 1 - D_{0,\mathrm{B}}^{\mathrm{phot}}. \tag{5.9}$$

With the knowledge of the spectral type of NGTS-3A, I can simulate the dilution originating from different stellar companions using the telescope transmission functions and stellar model spectra. This makes use of the PHOENIX stellar models (Allard & Hauschildt, 1995; Husser et al., 2013). These are given in a grid, encompassing the effective temperature T_{eff} in steps of 100 K, $\log g$ in steps of 0.5, and $[Fe/H]$ in steps of 0.5 for the range of possible properties. In practice, I employ the PYSYNPHOT software package (STScI Development Team, 2013), which allows to retrieve an interpolated spectrum for any requested property.

The transmission functions of the NGTS, SPECULOOS and HARPS instruments (ESO, 2011; Wheatley et al., 2018, private correspondence with the SPECULOOS consortium) are employed, and multiplied with a model of Earth's atmospheric absorption. Fig. 5.7 shows all resulting transmission functions, and the model spectra of a G6V and K4V dwarf overlayed as examples.

I study the dilution as a function of the spectral type of NGTS-3B by simulating NGTS-3A with the PHOENIX model for the properties (and errors) listed in Table 5.5. Next, I simulate all possibilities for NGTS-3B by passing each PHOENIX model spectra in T_{eff} steps of 200 K through the HARPS and NGTS transmission functions. From this, the dilution of star B, $D_{0,\mathrm{B}}$, is calculated via Eq. 5.9 as a function of the effective temperature of NGTS-3B, $T_{\mathrm{eff,B}}$. When modelling a planet orbiting star A, the dilution of the planet signal on star A is calculated as $D_{0,\mathrm{A}} = 1 - D_{0,\mathrm{B}}$. Fig. 5.8 shows the resulting dilution as function of $T_{\mathrm{eff,B}}$ for HARPS, NGTS and all used SPECULOOS filters. A 5th-order polynomial fit is performed to all mean points and error bars. This fit can then be used to predict the dilution and its error at any chosen $T_{\mathrm{eff,B}}$.
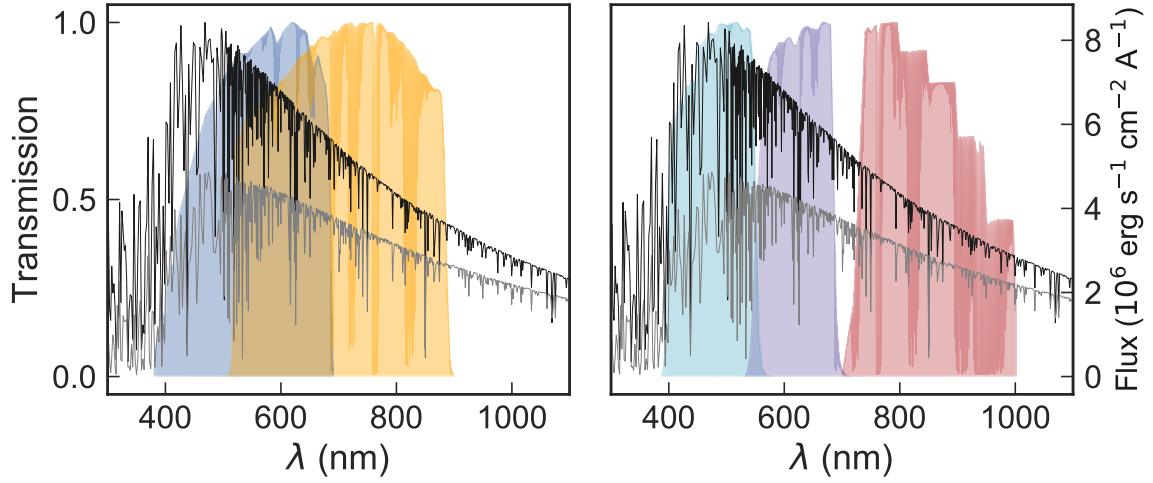
Fig. 5.7 Dilution is a function of the instrument transmission and stellar spectral types. Left axis: Transmission efficiency of HARPS (blue), NGTS (orange) and the SPECULOOS g'-band (light blue), r'-band (purple), and i'+z'-band (red), all including atmospheric absorption. Right axis: luminosity of a G6V (top) and a K4V (bottom) star. The different bandpasses lead to a different dilution of the planetary signal for each instrument.

5.5.5 Inferring properties of NGTS-3B

Without visual information on NGTS-3B, there is no a priori knowledge of its spectral type and properties. It was not possible to constrain the spectrum of NGTS-3B from the HARPS spectra analysis (Section 5.5.1) nor from a spectral energy distribution (SED) fit without prior information. However, one can employ the global MCMC model of the photometric and RV data to estimate the effective temperature of NGTS-3B, $T_{\rm eff,B}$, from the dilution model (Section 5.5.4). At each step in the MCMC chain of the global modelling, I sample the dilution values for all instruments. These are passed into the dilution model, allowing to sample the likelihood distribution of $T_{\rm eff,B}$. Next, empirical relations are employed to use $T_{\rm eff,B}$ for estimating the likelihood distribution of the radius $R_{\rm B}$ and mass $R_{\rm B}$ (see Sections 5.5.6 and 5.5.9). When inferring properties of NGTS-3B, I assume that it is a main sequence star. A giant star would dominate the light and would have been identified in the HARPS spectra analysis. Moreover, low mass main sequence stars are the most abundant objects in the night sky, and frequent companions in binary systems with a G-type primary.
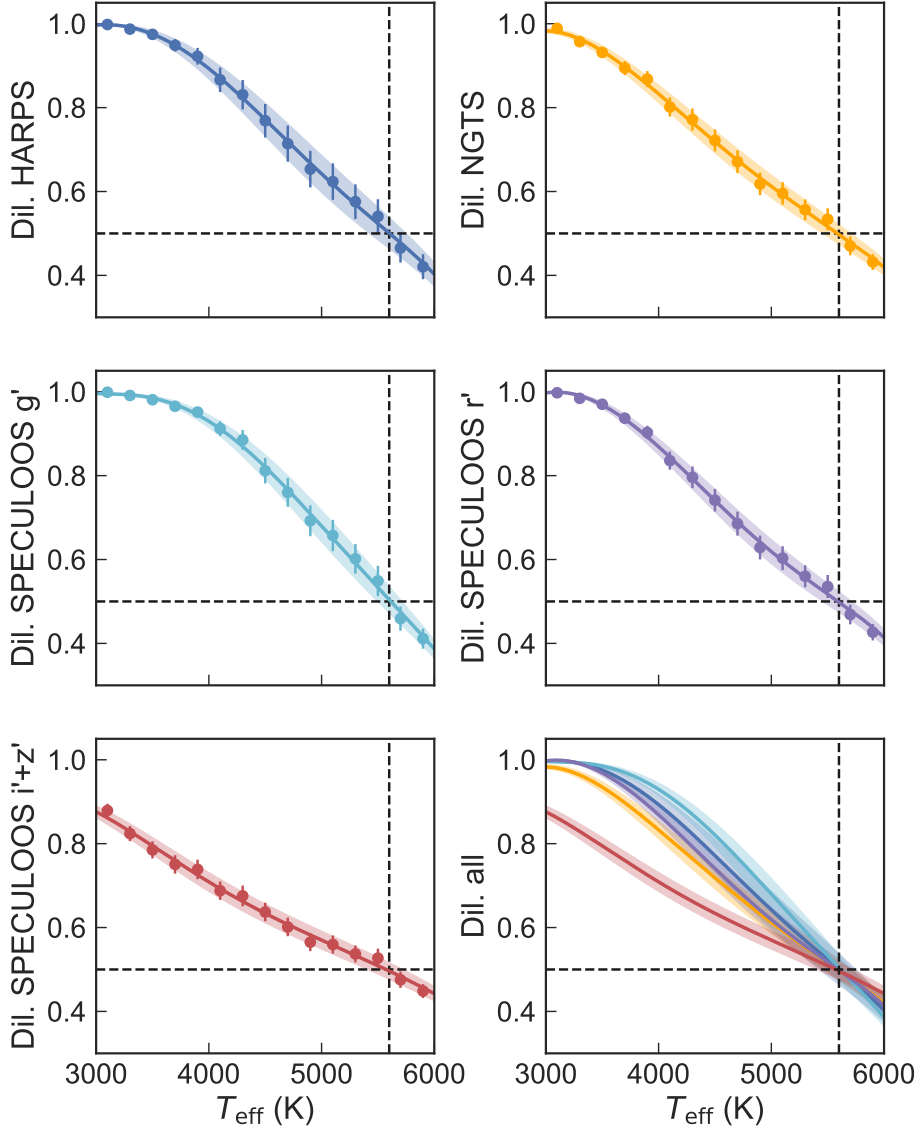
Fig. 5.8 HARPS, NGTS and SPECULOOS dilution of star B, $D_{0,B}$, as a function of the effective temperature of NGTS-3B, $T_{eff,B}$. I derive the dilution by passing PHOENIX model spectra through the telescope bandpasses. I fit the resulting trend with a 5th-order polynomial, which can then be used to predict the dilution for each instrument at any chosen $T_{eff,B}$. Dashed lines at dilution 0.5 and $T_{eff} \approx 5600$ K indicate the properties of star A. Note that, when modelling a planet on star A, the dilution of the planet signal on star A is calculated as $D_{0,A} = 1 - D_{0,B}$.

5.5.6 Model of the RV offset between NGTS-3A and NGTS-3B

In order to model the two CCFs, the systemic radial velocities of NGTS-3A and NGTS-3B are needed. I will use both as free parameters to the fit in Section 5.5.8. However, they are tied to each other by astrophysical constraints, which I can calculate and include into the MCMC modelling.

The RV semi-amplitude for each star, $K_{A,B}$, in the binary system is calculated as

$$K_{A,B} = \frac{M_{B,A} \sin i_{binary}}{(M_A + M_B)^{2/3}} \frac{(2\pi G)^{1/3}}{P_{binary}^{1/3} (1 - e_{binary}^2)^{1/2}}. \tag{5.10}$$

Here, M_A and M_B are the masses of NGTS-3A and NGTS-3B, respectively. P_{binary}, i_{binary} and e_{binary} are the period, inclination and eccentricity of the binary system (not to be confused with the parameters of the planet's orbits). G is the gravitational constant.

As there is no prior knowledge about this binary system, I employ a series of empirical relations to sample the likelihood space for $K_{A,B}$ using a Monte Carlo approach. The result for M_A is used as a normal prior on this parameter (see Table 5.5). The inclination $i$binary is randomly drawn from a uniform distribution in $\cos i_{binary}$ between 0 and 90 degree. The logarithm of the period P_{binary} is randomly drawn from a normal distribution with mean 5.03 and standard deviation 2.28 (Raghavan et al., 2010). The eccentricity e_{binary} is randomly drawn from the results of Tokovinin & Kiyaeva (2016). I do not use their linear fit solution, but instead calculate an empirical cumulative distribution function (CDF) of e_{binary} from their tabulated data. I interpolate the CDF with a cubic spline function, and perform random sampling from the inverse CDF. In total, 1000 random binary systems are generated.

I then calculate the measured RV difference depending on the relative orbital position of the binary system, using

$$RV_{A,B}(t) = K_{A,B}(\cos(\nu(t) + \omega_{A,B}) + e \cos(\nu(t))), \tag{5.11}$$

$$\Delta RV(t) = |RV_A(t) - RV_B(t)|. \tag{5.12}$$

Here, ΔRV denotes the difference in systemic RV that is expected between the two stars, which is the direct result of their gravitational pull on each other. ν is the true anomaly of the system, and $\omega_{A,B}$ the argument of periastron with $\omega_B = \omega_A - 180\,\mathrm{deg}$.

The parameter ω_A is sampled from a uniform distribution between 0 and 360 degree. For each system, I compute ν as a function of time. This is done by calculating the mean anomaly, and then solving Kepler's equation for the eccentric anomaly. Finally, ν is computed from the eccentric anomaly and evaluated for 100 uniformly spaced times in the range from 0 to P_{binary}, sampling the entire orbit for each system.

By combining all this in Eq. 5.12, I derive ΔRV as a function of the unknown mass of NGTS-3B. Fig. 5.9A shows the distribution of ΔRV of all simulated distributions of binary systems with a G6V primary and K1V secondary. To generate priors for the global MCMC fit, I evaluate Eq. 5.12 for 100 different probe masses for star B, uniformly spaced in the range 0.1-1 $M_\odot$. This leads to a total of 1000 binaries $\times$100 time points $\times$100 probe masses $= 10^7$ samples.

Next, I link mass to effective temperature using the empirical catalogue of mean dwarf stars by Pecaut & Mamajek (2013). This mean dwarf model is chosen to rely on as few prior assumptions as possible for the global MCMC fit, as initially there was no information on the spectral type of NGTS-3B. It relies only on the assumption that NGTS-3B is a main sequence star (see Section 5.5.5). I use GP regression with a squared exponential kernel and a constant kernel to fit the data in Pecaut & Mamajek (2013):

$$k\left(r^2\right) = c\,\mathrm{e}^{-r^2/2} \tag{5.13}$$

(see Section 2.6). The resulting fit is then used to predict $T_{\mathrm{eff,B}}$ for any requested M_B, translating the prior on ΔRV to be a function of $T_{\mathrm{eff,B}}$. Its value is calculated at each step in the MCMC chain as described in Section 5.5.5.

Next, I fit the resulting logarithmic distribution of ΔRV with a Gaussian function. When studying the mean $\mu\left(\log_{10}\Delta\mathrm{RV}\right)$ and standard deviation $\sigma\left(\log_{10}\Delta\mathrm{RV}\right)$ of this Gaussian function dependent on $T_{\mathrm{eff,B}}$, there is a clear trend (Fig. 5.9B and C). The parameter

$\mu\left(\log_{10}\Delta\text{RV}\right)$ can be described with a second order polynomial and $\sigma\left(\log_{10}\Delta\text{RV}\right)$ by its mean value. Substituting $x = \left(T_{\text{eff,B}} - 3000\text{ K}\right)/3000\text{ K}$ leads to the following relations:

$$\mu\left(\log\Delta\text{RV}\right) = -0.144x^2 + 0.212x + 0.262 \tag{5.14}$$

$$\sigma\left(\log\Delta\text{RV}\right) = 0.887. \tag{5.15}$$

These equations are then used in the MCMC model (Section 5.5.8) to constrain the systemic velocities in relation to each other for any evaluated $T_{\text{eff,B}}$. Additionally, an upper limit on ΔRV is set by the fact that both systems remain unresolved in HARPS. Hence, their separation has to be $\lesssim 7$ km/s, constrained by the measured FWHM. I hence implement a truncated Gaussian prior on ΔRV as a function of $T_{\text{eff,B}}$.

5.5.7 Detrending NGTS' photometric and centroid data with Gaussian Process regression

To decrease the influence of systematic noise, I pre-whiten the photometric and centroid data from NGTS. First, all data during primary and secondary eclipse is masked. Then, a GP regression fit using the product of a Matern 3/2 kernel and a constant kernel (see Section 2.6) is employed. The light curve and centroid time series are detrended with the resulting GP.

5.5.8 Global MCMC model

I perform a global, joint MCMC modelling of all data sets: the GP detrended photometric and centroid data from NGTS, the HARPS CCFs for the seven exposures, and the extracted HARPS RV and bisector measurements.

Priors. In multiple initial MCMC test-runs the scenario of a planet or sub-stellar object orbiting either star A or star B is modelled. Further, the parameter space is explored from different starting points, with different priors and more free parameters. All approaches converge to the scenario of a planet orbiting star A. Given the previous analyses (Sections 5.5.1-5.5.6),
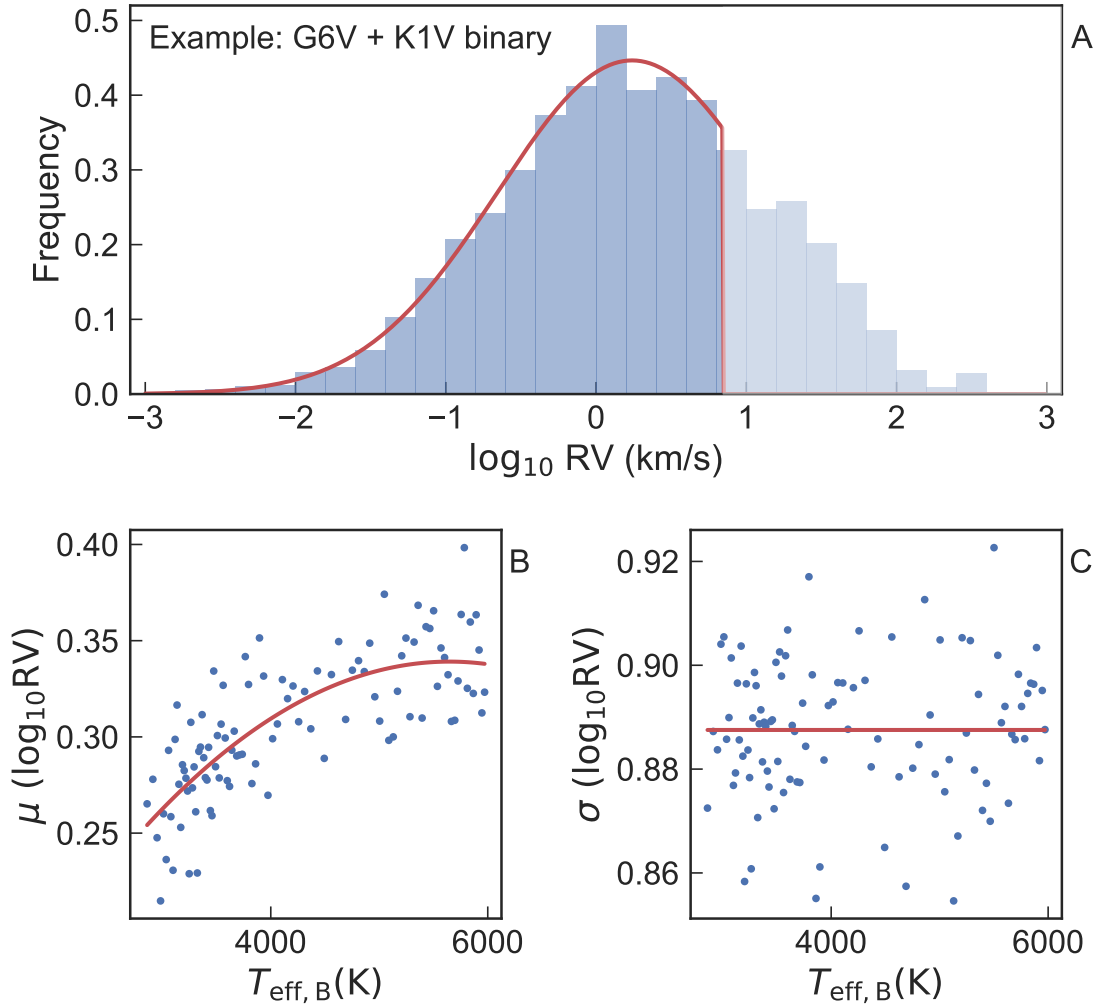
Fig. 5.9 A) RV difference between the two stars of a G6V-K1V binary system from 1000 simulations and sampled at 100 points in phase. The truncation is set by the fact that both systems remain unresolved in HARPS. Hence, their separation has to be $\lesssim 7$ km/s, given by the measured FWHM. The red curve shows a truncated Gaussian fit to the logarithm of the measured RV differences. I fix star A to the properties of NGTS-3A and simulate 1000 binary systems for M_B ranging from $0.1 - 1 M_{\odot}$ in steps of $0.01 M_{\odot}$. I sample each system at 100 points in phase. I calculate $T_{eff,B}$ from M_B, using the empirical relation described in Section 5.5.5. I then calculate the mean (B) and standard deviation (C) of the Gaussian fit to $\log \Delta RV$ for all sampled $T_{eff,B}$. Red curves in B) and C) show a second-order polynomial (constant) fit to the mean (standard deviation) as a function of $T_{eff,B}$.

I can adopt the following priors and constraints (Table 5.7; see Table 5.9 for a description of the parameters):

1. an upper limit of 1" projected separation between NGTS-3A and NGTS-3B (acceptance of the HARPS fibre) as a uniform, informative prior constraining the centroid model. One NGTS pixel spans 4.97", leading to limits of $\Delta x \in (-0.2, 0.2)$ pixel and $\Delta y \in (-0.2, 0.2)$ pixel.

2. the dilution relation from Section 5.5.4, linking the different instruments. As the scenario of a planet on star A is modelled (constrained by the colour difference in transit depth), the dilution is further restricted to $D_{0,\mathrm{A}} \in (0, 0.5)$.

3. the RV offset relation from Section 5.5.6.

4. uniform priors on all other parameters, where applicable within physical bounds, otherwise with non-restrictive bounds.

Note that all the priors are jointly proper, ensuring posterior propriety. None of the priors are unbounded, and the likelihood functions for all models converge to 0 as the model deviates from the data.

Fixed values. The eccentricity is fixed to $e = 0$, as there is no evidence for eccentricity from the HARPS RV data (see e.g. discussion in Anderson et al., 2012). The surface brightness ratio, gravitational darkening and reflectivity are also fixed to 0, following a planet scenario. For each bandpass, I compute quadratic limb darkening parameters for star A from the values in Table 5.5 using the open-source code by Espinoza & Jordán (2015) and the PHOENIX model spectra (Husser et al., 2013). To reduce free parameters in the model, the limb darkening parameters α and β are fixed to the values shown in Table 5.8.

Baselines. From the re-analysis of the HARPS CCFs in section 5.5.3, I find that for all studied CCFs the GP model favours a simple and continuous baseline trend, which can be closely reproduced by a low-order polynomial baseline. To minimise the complexity and number of dimensions of the MCMC model, I therefore opt to use polynomial baselines instead of GPs in the global modelling. In particular, a fourth order polynomial is used for

Table 5.7 Priors for the global MCMC model of NGTS-3. Parameters are described in Table 5.9.

Δx	$\mathcal{U}(-0.2, 0.2)$ pixel
Δy	$\mathcal{U}(-0.2, 0.2)$ pixel
$D_{0,A}$ for each instrument	see Section 5.5.4; in $(0, 0.5)$
P	$\mathcal{U}(0, 10^{12})$ min
$T_0 - 2450000\,d$	$\mathcal{U}(0, 10^{12})$ min
R_p/R_A	$\mathcal{U}(0, 1)$
$(R_A + R_p)/a$	$\mathcal{U}(0, 1)$
$\cos i$	$\mathcal{U}(0, 1)$
$RV_{sys,A}$	see Section 5.5.6; in $(0, 100)$ km/s
$RV_{sys,B}$	see Section 5.5.6; in $(0, 100)$ km/s
K	$\mathcal{U}(-100, 100)$ km/s
A_{CCF}	$\mathcal{U}(0, 1)$
$FWHM_{CCF,A}$	$\mathcal{U}(0, 100)$ km/s
$FWHM_{CCF,B}$	$\mathcal{U}(0, 100)$ km/s
all photometric errors	$\mathcal{U}(0, 1000)$ mmag
all centroid errors	$\mathcal{U}(0, 1000)$ mpix
RV and BIS errors	$\mathcal{U}(0, 1)$ km/s
FWHM error	$\mathcal{U}(0, 10)$ km/s
Contrast error	$\mathcal{U}(0, 1)$
CCF errors	$\mathcal{U}(0, 10)$

Table 5.8 Limb darkening parameters for the global MCMC model of NGTS-3.

	α	β
NGTS:	0.4294	0.2019
SPEC. g':	0.6993	0.0946
SPEC. r':	0.4869	0.1927
SPEC. i'+z':	0.3339	0.2199

the baseline of the HARPS CCFs, and a second order polynomial for the baseline of the SPECULOOS data. As the NGTS data covers mostly out-of-transit data, I remove any global variation using a GP regression fit beforehand (see section 5.5.7), and include only a constant baseline for any NGTS data in the global model. In fitting the baseline polynomials, I do not implement the polynomial values as jump parameters in the MCMC, but instead perform an algebraic least squares fit to the residuals of each MCMC fit at each step in the MCMC chain. This approach was proven robust and effective in multiple previous studies (see e.g. Gillon et al., 2012).

MCMC. A detailed introduction to MCMC modelling is given in Chapter 2. Here, the MCMC is implemented using EMCEE (Foreman-Mackey et al., 2013) and the EB binary star model (Irwin et al., 2011). I run the MCMC analysis on 37 dimensions with 500 walkers for 200,000 total steps. 19 of these dimensions are scaling factors for the errors of each data set. Across all chains, the median (maximal) autocorrelation length is 2,400 ($\sim 3,400$) steps. The total chain is ~ 83 (~ 59) times its median (maximal) autocorrelation length, which is considered as sufficient for convergence. I discard the first $\sim 50,000$ steps as the burn-in phase, and thin the chain by a factor of 2,500. This results in $(200,000 - 50,000)/2,500 * 500 = 30,000$ independent samples.

Results. The hot Jupiter NGTS-3Ab is orbiting NGTS-3A with a period of 1.675 days. The planet radius and mass are $R_{\mathrm{planet}} = 1.48 \pm 0.37$ R$_J$ and $M_{\mathrm{planet}} = 2.38 \pm 0.26$ M$_J$, conform with a potentially inflated gas giant planet. I find a dilution of $0.38 - 0.43$ of the transit signal, depending on the instrument bandpass. NGTS-3Ab has an undiluted transit depth of $\delta_{\mathrm{undil.}} = (R_{\mathrm{planet}}/R_{\mathrm{A}})^2 = 2.68 \pm 0.15\%$. The planet introduces an undiluted RV signal of $K = -0.404 \pm 0.035$ km/s on NGTS-3A. The systemic velocities of NGTS-3A and B are $RV_{\mathrm{sys,A}} = 8.566 \pm 0.049$ km/s and $RV_{\mathrm{sys,B}} = 9.032^{+0.085}_{-0.064}$ km/s, respectively. All results of the MCMC analysis can be found in Fig. 5.1 and 5.11, and Table 5.9.

5.5.9 Identifying NGTS-3B

Using the approach outlined in Section 5.5.5, I estimate the effective temperature of NGTS-3B from the dilution model, and find $T_{\mathrm{eff,B}} = 5230^{+190}_{-220}$ K. This places NGTS-3B most likely as

an K1V dwarf (ranging G9V-K2V; see e.g. Pecaut & Mamajek 2013). From this, I calculate the final radius and mass of NGTS-3B, but deviate here from Section 5.5.6. The approach in Section 5.5.6 was chosen to find the mass for mean dwarf stars in relation to $T_{\text{eff,B}}$ only, as no prior information on NGTS-3B was available. This does not allow to estimate uncertainties, and, particularly, it is not possible to propagate uncertainties on $\log g_{\text{B}}$ and $[Fe/H]_{\text{B}}$.

For the calculation of uncertainties, I here estimate R_{B} and M_{B} from $T_{\text{eff,B}}$ by using the empirical relations by Torres et al. (2010). These relations depend on $T_{\text{eff,B}}$, $\log g_{\text{B}}$ and $[Fe/H]_{\text{B}}$. I estimate a prior on $\log g_{\text{B}} \in \mathcal{N}(4.6, 0.2)$ using the data by Pecaut & Mamajek (2013) for the result $T_{\text{eff,B}} = 5230^{+190}_{-220}$ K. Further, it is assumed that NGTS-3A and B formed in the same system, and hence show similar metallicity. I hence set a metallicity prior of $[Fe/H]_{\text{B}} \in \mathcal{N}(0., 0.5)$.

This analysis gives $R_{\text{B}} = 0.77^{+0.22}_{-0.16}$ R$_\odot$ and $M_{\text{B}} = 0.88^{+0.14}_{-0.12}$ M$_\odot$. Table 5.9 summarises all inferred results. Fig. 5.12 shows the inferred distributions for all parameters.

5.5.10 Identifying NGTS-3Ab

I use the MCMC chains and the inference of the systems dilution to calculate the properties of NGTS-3Ab, the object orbiting NGTS-3A. One can estimate the radius of NGTS-3Ab directly from the MCMC samples of the ratio of radii, R_C/R_A, and the prior on R_A. This results in $R_{\text{planet}} = 1.48 \pm 0.37$. The mass of NGTS-3Ab can be estimated with the binary mass function f for spectroscopic single-lined binaries:

$$f := \frac{PK^3(1-e^2)^{\frac{3}{2}}}{2\pi G} = \frac{M_C^3 \sin i^3}{(M_C + M_A)^2} \tag{5.16}$$

I solve this equation for all MCMC samples (P, K, i) and the prior on M_A, finding $M_{\text{planet}} = 2.38 \pm 0.26$. Table 5.9 summarises all derived results. Fig. 5.12 shows the inferred distributions for all parameters. Fig. 5.10 gives an illustration of the NGTS-3 system.
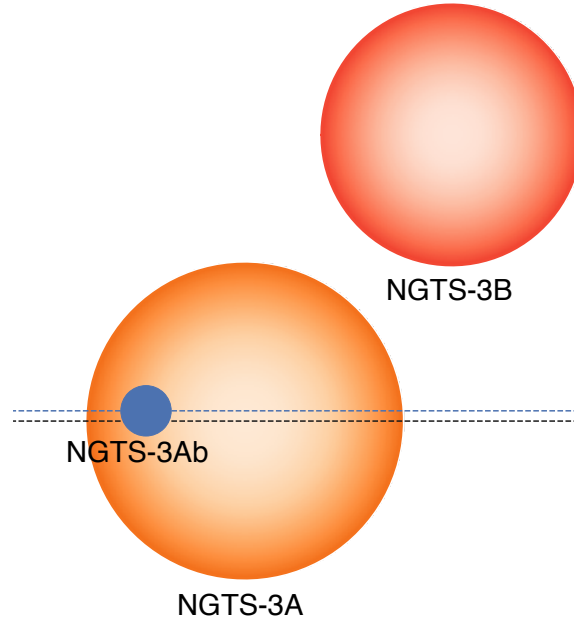
Fig. 5.10 Illustration of the NGTS-3 system. The planet NGTS-3Ab orbits the primary of an unresolved binary system. The black dashed line indicates the mid-line of the stellar disk, the blue dashed line shows the planet's orbit.

5.5.11 Identifying the binary orbit

A significant difference in systemic RV for NGTS-3A and B (Table 5.9) is detected, but it is not straightforward to use this to constrain the orbital separation; the likelihood space for ΔRV spans orders of magnitudes and depends on its orbital parameters, which remain unconstrained (see Section 5.5.6). However, the centroid information can constrain the projected separation. With an estimate of the distance to the system, this can be translated into an orbital separation.

An SED fit to the magnitudes reported in Table 5.5 is performed following the method presented in Gillen et al. (2017). For modelling of NGTS-3A and NGTS-3B, two separate stellar model spectra from PHOENIX are used. As priors, the results of the spectral analysis for NGTS-3A ($R_A, T_{\text{eff,A}}, \log g_A$; see Table 5.5), and the inferred posterior likelihoods for NGTS-3B ($R_B, T_{\text{eff,B}}$; see Table 5.9) are employed. The prior on the surface gravity is again chosen to be $\log g_B \in \mathcal{N}(4.6, 0.2)$ (see Section 5.5.9). $[Fe/H]_{\text{A,B}} = 0$ is fixed to avoid

interpolation over wide ranges of metallicity (the PHOENIX spectra are given in steps of 0.5 in metallicity). This results in a distance of $d = 1010^{+150}_{-130}$ pc to the binary system.

Alternatively, the distance can be determined via the *Gaia* DR2 parallaxes. The reported parallax of $p = (1.315 \pm 0.019)$ mas translates into a distance of $d = 760 \pm 11$ pc. This is significantly smaller than the SED fit result. The discrepancy might result from an intrinsic bias in the spectral analysis, introduced by the light from the blended source.

Using either result for the distance, I can translate the projected sky separation of $\Delta x_{\mathrm{sky}} = 0.42^{+0.36}_{-0.43}$ arcsec and $\Delta y_{\mathrm{sky}} = 0.66^{+0.23}_{-0.35}$ arcsec (constrained by the centroid data in the global MCMC model; see Table 5.9) into AU. This gives a lower limit on the orbital semi-major axis of the binary, which is $a_{\mathrm{binary}} > 500$ AU. Using Kepler's third law, I determine that the binary period is $P_{\mathrm{binary}} > 11000$ yr . At this orbital separation, no detection of transit-timing variations (TTVs) is expected. Indeed, there was no evidence for any TTVs in the data. The resulting binary orbit agrees well with typical scenarios of a planet in a binary system, further supporting the evidence for NGTS-3Ab.

5.6   Discussion

5.6.1   NGTS-3 as a cautionary tale of careful vetting

Only careful modelling of multi-colour photometry, centroids and RV CCF profiles and their bisectors enabled the verification of NGTS-3Ab. From single-colour photometry, centroids and RV measurements alone, NGTS-3Ab would have been misclassified as an undiluted hot Jupiter orbiting an isolated G-type star. On the other hand, a simpler consideration of the bisector correlation would have led to it being rejected as a planet. This finding is important to consider, as the bisector correlation is a common planet vetting criterion. It might have previously led to the erroneous rejection of bona fide planets in unresolved binary systems.

I particularly raise caution that single-colour photometry alone, even if combined with precision centroiding, was not sufficient to identify the three-body nature of this system. Only if combined with multi-colour information and an analysis of the RV CCF profiles and BIS measurements, it was possible to unmask the hidden nature of this system. I caution that

Table 5.9 Parameters of the NGTS-3 system. Values and error bars are the median and 16th / 84th percentile of the MCMC posterior likelihood distributions.

	Fitted parameters (astrophysical)		
Δx	Relative CCD x position of the blend	85^{+72}_{-87}	milli-pixel
Δy	Relative CCD y position of the blend	133^{+47}_{-71}	milli-pixel
$D_{0,\text{A,NGTS}}$	Dilution of star A in NGTS	$0.434^{+0.030}_{-0.032}$	
$D_{0,\text{A,SPEC.g'}}$	Dilution of star A in SPECULOOS g' band	$0.409^{+0.035}_{-0.038}$	
$D_{0,\text{A,SPEC.r'}}$	Dilution of star A in SPECULOOS r' band	$0.432^{+0.031}_{-0.034}$	
$D_{0,\text{A,SPEC.i'+z'}}$	Dilution of star A in SPECULOOS i'+z' band	0.449 ± 0.027	
$D_{0,\text{A,HARPS}}$	Dilution of star A in HARPS	$0.424^{+0.045}_{-0.051}$	
P	Period	1.6753728 ± 0.0000030	days
T_0	Epoch (HJD-2450000)	7620.16790 ± 0.00095	days
$R_{\text{planet}}/R_{\text{A}}$	Ratio of radii	0.1638 ± 0.0045	
$(R_{\text{A}} + R_{\text{planet}})/a$	Sum of radii over the semi-major axis of the planet's orbit	$0.1792^{+0.0012}_{-0.0011}$	
$\cos i$	Cosine of the inclination	$0.0077^{+0.0085}_{-0.0054}$	
$RV_{\text{sys,A}}$	Systemic RV of NGTS-3A	8.566 ± 0.049	km/s
$RV_{\text{sys,B}}$	Systemic RV of NGTS-3B	$9.032^{+0.085}_{-0.064}$	km/s
K	RV semi-amplitude	-0.404 ± 0.035	km/s
	Fitted parameters (other)		
A_{CCF}	Maximal amplitude of the CCF profile	$0.52147^{+0.00076}_{-0.00070}$	
$\text{FWHM}_{\text{CCF,A}}$	FWHM of the CCF profile of NGTS-3A	7.436 ± 0.082	km/s
$\text{FWHM}_{\text{CCF,B}}$	FWHM of the CCF profile of NGTS-3B	$6.857^{+0.078}_{-0.090}$	km/s
$\sigma(F_{\text{NGTS}})$	Error of the flux in NGTS	10.247 ± 0.079	mmag
$\sigma(\xi_x)$	Error of the centroid in x	12.114 ± 0.097	milli-pixel
$\sigma(\xi_x)$	Error of the centroid in y	11.926 ± 0.095	milli-pixel
$\sigma(F_{\text{SPEC.Callisto,g'}})$	Error of the flux in SPEC. Callisto g' band	$2.846^{+0.099}_{-0.093}$	mmag
$\sigma(F_{\text{SPEC.Callisto,r'}})$	Error of the flux in SPEC. Callisto r' band	$3.03^{+0.13}_{-0.12}$	mmag
$\sigma(F_{\text{SPEC.Europa,r'}})$	Error of the flux in SPEC. Europa r' band	$2.597^{+0.087}_{-0.082}$	mmag
$\sigma(F_{\text{SPEC.Europa,i'+z'}})$	Error of the flux in SPEC. Europa i'+z' band	$2.512^{+0.085}_{-0.080}$	mmag
$\sigma(F_{\text{SPEC.Io,i'+z'}})$	Error of the flux in SPEC. Io i'+z' band	2.517 ± 0.084	mmag
$\sigma(\text{RV})$	Error of the RV	$0.043^{+0.017}_{-0.010}$	km/s
$\sigma(\text{BIS})$	Error of the BIS	$0.0317^{+0.015}_{-0.0097}$	km/s
$\sigma(\text{FWHM})$	Error of the FWHM	$0.084^{+0.037}_{-0.023}$	km/s
$\sigma(\text{Contrast})$	Error of the Contrast	$1.61^{+0.66}_{-0.41}$	
$\sigma(\text{CCF})$	Error of the CCF 1	$0.00322^{+0.00019}_{-0.00018}$	
$\sigma(\text{CCF})$	Error of the CCF 2	$0.00611^{+0.00036}_{-0.00033}$	
$\sigma(\text{CCF})$	Error of the CCF 3	$0.00574^{+0.00035}_{-0.00031}$	
$\sigma(\text{CCF})$	Error of the CCF 4	$0.00397^{+0.00025}_{-0.00022}$	
$\sigma(\text{CCF})$	Error of the CCF 5	$0.00436^{+0.00026}_{-0.00024}$	
$\sigma(\text{CCF})$	Error of the CCF 6	$0.00484^{+0.00030}_{-0.00027}$	
$\sigma(\text{CCF})$	Error of the CCF 7	$0.00518^{+0.00030}_{-0.00028}$	
	Derived parameters for NGTS-3B		
$T_{\text{eff,B}}$	Effective temperature of NGTS-3B	5230^{+190}_{-220}	K
R_{B}	Radius of NGTS-3B	$0.77^{+0.22}_{-0.16}$	$R_\odot$
M_{B}	Mass of NGTS-3B	$0.88^{+0.14}_{-0.12}$	$M_\odot$
ρ_{B}	Density of NGTS-3B	$1.13^{+0.29}_{-0.23}$	$\rho_\odot$
	Derived parameters for NGTS-3Ab		
R_{planet}	Radius of the planet	1.48 ± 0.37	R_{J}
M_{planet}	Mass of the planet	2.38 ± 0.26	M_{J}
ρ_{planet}	Density of the planet	$0.31^{+0.41}_{-0.15}$	ρ_{J}
i	Inclination	$89.56^{+0.31}_{-0.48}$	deg
R_{planet}/a	Planet radius over semi-major axis of the planet's orbit	0.02523 ± 0.00071	
R_{A}/a	Radius of NGTS-3A over semi-major axis of the planet's orbit	$0.15398^{+0.00082}_{-0.00069}$	
a	Semi-major axis of the planet's orbit	$5.0^{+1.4}_{-1.0}$	$R_\odot$
T_{1-4}	Total duration of transit	138.15 ± 0.82	min
T_{2-3}	Transit width	98.82 ± 0.63	min
$\delta_{\text{undil.}} = (R_{\text{planet}}/R_{\text{A}})^2$	Undiluted (real) depth of the transit	2.68 ± 0.15	%
b_{tra}	Impact parameter of the transit	$0.050^{+0.055}_{-0.035}$	
	Derived parameters for the NGTS-3 binary system		
Δx_{sky}	Relative sky position of the blend in x	$0.42^{+0.36}_{-0.43}$	arcsec
Δy_{sky}	Relative sky position of the blend in y	$0.66^{+0.23}_{-0.35}$	arcsec
d	Distance to the system	1010^{+150}_{-130}	pc
a_{binary}	Orbital separation between the stars	> 500	AU
P_{binary}	Orbital period of the binary stars	> 11000	yr

Fig. 5.11 Posterior likelihood distributions for all astrophysical parameters of the MCMC fit to NGTS-3. For better visibility, the error scaling parameters are not shown here. Parameters are described in Table 5.9.
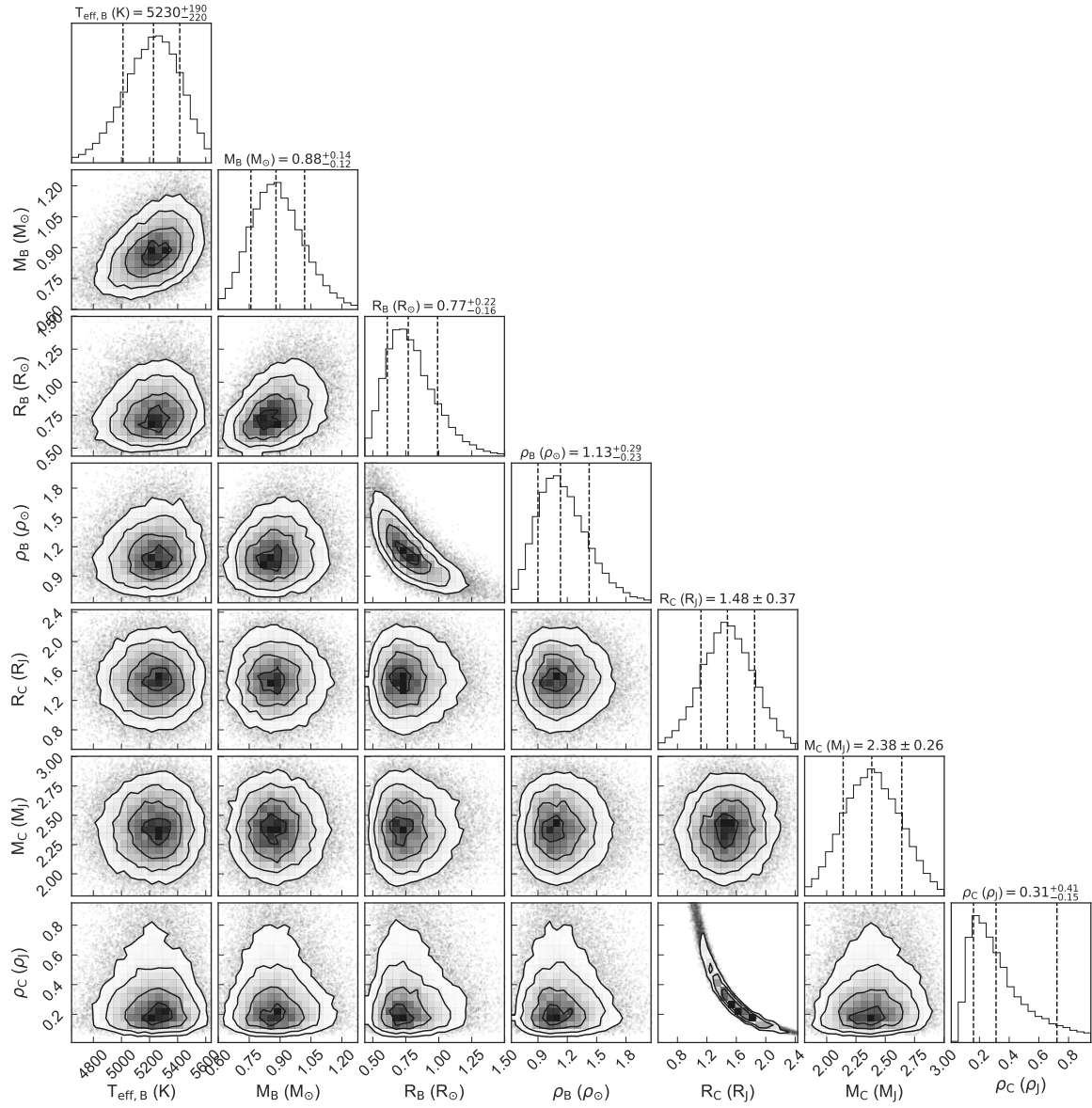
Fig. 5.12 *Likelihood distributions for the derived parameters for NGTS-3B and NGTS-3Ab, as inferred from the results of the MCMC fit. Parameters are described in Table 5.9.*

this scenario might be more common than currently anticipated. Diluted gas giant planets or Brown Dwarf companions in unresolved binary systems can also mimic Neptune-sized and rocky exoplanets.

NGTS-3 is not resolved in *Gaia* DR2, which was released during revision of this thesis. *Gaia* DR2 is complete to an angular resolution of 0.4"-0.5" separation (Gaia Collaboration et al., 2018). The non-identification of the companion in *Gaia* DR2 is in agreement with the results of our global MCMC model, predicting a separation around the completeness limit of *Gaia* DR2 (see Tab. 5.9). This highlights that hidden companion stars to exoplanet hosts in multi-star systems can remain unresolved in *Gaia* DR2. Moreover, there was no sign of the companion in the SPECULOOS images, nor the HARPS guider images. It is hence crucial for transit surveys like NGTS and the upcoming TESS mission to account for the resolution limits of follow-up instruments and catalogues like *Gaia* DR2.

The most robust way to identify hidden systems is a systematic lucky imaging or adaptive optics follow-up. Ideally, this would be conducted for any exoplanet system. In the case of NGTS-3, this will also allow to verify the accuracy of our modelling. I therefore aim to propose for high-resolution imaging of NGTS-3. Exploring this system further will place constraints on its binary companions, consequently refining the planetary parameters.

5.6.2   Caveats and prospects

Priors on star A and B

The priors on star A are drawn from the HARPS spectral analysis. I caution that this is only correct if the flux from star A dominates the spectrum. In the case of similar luminosity of star A and B, the spectrum will be significantly influenced by both stars. The spectral analysis then approximately reflects the mean value between the two stars. As the findings indicate that star B contributes to the overall spectrum, this might underestimate the effective temperature of star A.

Due to lack of information about star B, it has to be assumed that it is a slow-rotating main-sequence star, which has the same prior on its metallicity as star A. While reasonable, this assumption might cause a slight bias.

Calibration of the HARPS CCF G2 mask

There is no calibration of the HARPS CCF G2 mask covering the entire range of effective temperatures from $3000 - 6000$ K. In particular, the model will profit from the following two calibrations:

$$\text{Contrast} = f\left(T_{\text{eff}}, \log g, [Fe/H]\right), \tag{5.17}$$

$$\text{FWHM} = f\left(T_{\text{eff}}, \log g, [Fe/H]\right). \tag{5.18}$$

In Section 5.5.3, I studied these relations. While the current HARPS calibrations allow to constrain the relationship for the FWHM for effective temperatures $\gtrsim 3900$ K, there is no such calibration for the contrast. The analysis of data from Sousa et al. (2008) only allowed to constrain the contrast for effective temperatures $\gtrsim 5000$ K. To avoid introducing a bias into the fit due to the break at this temperature, I decided to use uniform priors instead (which, however, by itself introduces some bias).

5.7   Conclusion

In this chapter, I report the disentanglement of a previously unresolved three-body system, NGTS-3, from multi-colour photometry, centroiding and RV cross-correlation profiles. I present the discovery of NGTS-3Ab, a potentially inflated hot Jupiter ($R_{\text{planet}} = 1.48 \pm 0.37$ R$_J$ and $M_{\text{planet}} = 2.38 \pm 0.26$ M$_J$) in a 1.675 days orbit around the primary of an unresolved binary system. This provides an interesting testbed for planet formation, migration and orbital stability, as well as stellar multiplicity and metallicity.

Binary and triple systems are numerous. They frequently mimic exoplanet signals in photometric and RV observations. I develop a thorough analysis framework, packaged

in the BLENDFITTER tool, to unmask such false positives and identify the true cause of detected signals. In particular, I analyse the photometric flux centroid as well as the RV cross-correlation functions and their bisectors.

Chapter 6

Conclusion and future vision

"We adore chaos because we love to produce order."

— M. C. Escher

The aim of my PhD research was to optimise the efficacy of the Next Generation Transit Survey (NGTS) by enhancing the planet characterisation and minimising the risk of false positives. My work focused on three key areas, which are presented in this thesis along with my key achievements:

1. I designed a new yield estimator to maximise the science merit of transit surveys (Chapter 3). By applying it to NGTS, I characterised the expected contamination by false positives and prepared candidate vetting strategies.

2. I developed an automated centroid analysis of NGTS targets to disentangle planets from false positives and accurately identify blend scenarios (Chapter 4).

3. I introduced a novel approach to accurately characterise diluted planets (Chapter 5). This increased our understanding of false positive scenarios mimicking planets, and raised caution that only a combined modelling of multi-colour photometry, centroids and RV CCF profiles allows an accurate characterisation of exoplanets.

6.1   The importance of characterising the yield and efficacy

In Chapter 3, I showed that a flexible, realistic yield estimator enables to quantify the detection limitations and candidate vetting efficiency. I estimated that the contamination with false positives in NGTS stems from 4688 ± 45 EBs and 843 ± 75 BEBs. Additionally, thousands of false alarms can be expected. All together, non-transit events outnumber the yield of $240 - 320$ planets by nearly two orders of magnitude. For the chosen NGTS survey strategy, I find that EBs mainly pollute the regime of gas giant planets and are mostly ruled out by standard vetting procedures. BEBs, on the other hand, frequently mimic Neptune- and Earth-sized transits, the main targets of NGTS.

My results for NGTS agree with empirical findings for the planet-to-false-positive-ratio of exoplanet surveys. For example, studies with HAT and CoRoT (see e.g. Almenara et al., 2009; Hartman et al., 2011) and yield estimations for TESS (Sullivan et al., 2015) report a similar fraction of $95 - 99\%$ of false positives in the initial candidate lists.

My quantification of the expected false positives particularly benefited the NGTS survey, as it informed the preparation of follow-up strategies. In particular, these findings set the focus on developing the centroid technique for NGTS. This method had - although successfully employed from space - never been proven feasible for ground-based wide-field transit surveys; a fact which naturally led to the next step in my PhD research (see Section 6.2). Generally, the major advantages of a yield estimator are that it enables to a) quantify various survey strategies (such as the choice of target fields, observing window functions, and signal-to-noise thresholds), b) gain insight into the properties of these false positive systems and c) optimise for the desired outcome. The resulting science merit of an exoplanet survey is always a trade-off between the total number of planets and the planet-to-false-positive ratio.

While yield simulations mimic reality as close as possible, they are limited by the models, assumptions and prior information used. Some of the major limiting factors are:

- **Planet occurence rates.** As discussed in Section 1.8, a variety of studies have been published on this topic (Cumming et al., 2008; Dressing & Charbonneau, 2015; Fressin et al., 2013; Mayor et al., 2011; Petigura et al., 2018; Santerne et al., 2016). While all

agree to some degree, the occurrence rates are often defined over very wide bins of orbital period, planet radius/mass, and host star type and metallicity. They can therefore differ by an order of magnitude between different studies. Moreover, information for multi-planetary systems and planets in multi-star systems is currently limited.

- **Red noise model.** Based on prototype data, I approximated that NGTS noise is uncorrelated over multiple days. In reality, the influence of the moon, long-term weather pattern, instrumental failures and detrending software have since shown to introduce long-term patterns in NGTS data, and are accounted for in current versions of the pipeline.

- **Transit detection model.** I made the approximation that a transit is detected if SNR> 5. While this is a reasonable proxy, it is impossible to simulate the human factor, namely how the manual eyeballing, fitting and vetting stages are performed. With the introduction of automated vetting tools, future yield estimations will mimic this step more precisely.

- **Observability.** The down-time due to damage by rodents and El Niño, and failures of individual telescopes (see Section 1.9) caused gaps in the observing pattern which could not be anticipated.

- **Empirical knowledge.** For example, WASP used a strategy of switching frequently between observing fields to maximise the covered sky area. This strategy could also be simulated for NGTS. Assuming this would only double the white noise (halve the photon counts), the effect on the total noise budget is negligible (since NGTS is mostly red noise limited). It would double the sky area and hence the number of observed targets. The yield estimator would thus predict almost double the number of planets, clearly favouring this strategy. However, the problem is that, in reality, the precise autoguiding of NGTS relies on a continuous observation. Without it, each target would fall on different CCD image pixels whenever switching fields. The red noise would increase, minimising the yield of the smallest planets. Furthermore, it would make high-precision centroiding impossible, increasing the contamination by BEBs.

All this emphasises that a yield estimator is a powerful way of gaining insight into a survey, but has to be well informed by empirical studies. If this is the case, the gained insight is invaluable for the optimisation of a survey's science merit.

In the future, I aim to apply my yield estimator to upcoming transit surveys such as TESS and PLATO to a) compare with existing predictions (e.g. Sullivan et al., 2015), and b) study the impact of different occurrence rates and survey strategies. In this process, I will also make my software publicly available.

Developing the yield estimator gave me an in-depth insight into all aspects influencing transit surveys (design considerations, survey strategies, red noise patterns, observing window functions, weather, occurrence rates, properties of planets and eclipsing binaries, false positives, candidate vetting, and more). Everything I learned from this study informed and enhanced my subsequent research.

6.2 Automated centroid vetting as an efficient tool for resolving blend scenarios

6.2.1 Automated centroid shift detection

Motivated by my finding that BEBs can be a major limitation for NGTS, I developed a centroiding algorithm to enhance the identification of prime planet candidates (Chapter 4). By measuring the shift of light within an CCD image pixel during an eclipse, this can identify variable and constant background objects blended into the photometric aperture. My method achieved a precision of 0.25 milli-pixel, unprecedented for ground-based surveys. It is estimated to readily rule out 80% of BEBs without requiring further follow-up. This exceeded what was hoped to be feasible from the ground by a hundredfold, almost reaching space-based precision. At a CCD pixel size of 13.5 μm, this precision corresponds to $\sim$6 silicon unit cells (lattice spacing of 5.43 Å), highlighting that these achievements are pushing towards a physical limit.

6.2 Automated centroid vetting as an efficient tool for
resolving blend scenarios
173

It is important to caution, however, that the absence of a centroid shift does not completely rule out blended objects. While the method is near-complete in ruling out blends at > 1" projected separation from the NGTS target, nearby or faint objects cannot always be resolved. This is exactly the case for NGTS-3Ab, which is further discussed in Section 6.3.

Within a short time, the centroiding technique has already proven to be an invaluable tool for the NGTS candidate vetting pipeline. The < 1 mpix precision is of importance for NGTS (5 arcsec pixel size), as follow-up observations of blended candidates are time-limited and costly. While my centroiding code was specifically developed for the NGTS data reduction pipeline, future applications will be possible by integrating an adapted system into the candidate vetting pipelines of other surveys. Centroiding will be particularly crucial for the scientific merit of the TESS mission. Considering its large 21 arcsec pixels, TESS will have an even higher contamination from blended objects than *Kepler* or NGTS. High-precision centroid vetting for TESS will minimise the risk of false positives and provide a prime target list of exoplanets.

6.2.2 Bayesian modelling framework for photometry and centroids

It was initially anticipated to include the centroid shift detection as a candidate vetting feature in the NGTS AUTOVET code (see Section 1.6.2). However, the centroid shift can stem from various scenarios:

- a background eclipsing binary
- a hierarchical triple star system
- a foreground eclipsing binary, diluted by a background star
- a planet transiting a background star
- a planet transiting a foreground star, diluted by a background star
- a planet in a wide-orbit binary star system

This emphasises that the initial detection of a centroid shift (without further investigation) only informs about a hidden blend. It is important to caution that a centroid shift does not imply a false positive scenario; it does not rule out a planetary origin of the signal. It was hence decided to separate the centroid detection from the automated vetting procedure. A

transit-like signal may still be ranked as a top planet candidate, despite the detection of a centroid shift.

Building up on my centroiding algorithm, I further designed a joint Bayesian fitting framework for photometric and centroid data to disentangle the true nature of the signal (Chapter 4). The Bayesian modelling framework I developed is able to disentangle which object (target or background) is causing the signal. It can readily include prior information (e.g. from *Gaia*), and retrieve the posterior likelihood of all astrophysical parameters.

Without a detailed study of the origin of the transit signal and centroid shift, blended systems would have to be identified with high-resolution imaging or RV measurements. Even then, they could potentially be erroneously disregarded.

With the release of GAIA DR2 in April 2018, astrometric information on all NGTS targets will become available. It is expected that this will resolve a large fraction of hidden binary companions, and also identify background objects down to ~ 1" separation (private correspondence with the *Gaia* team). From this, the priors on the Bayesian modelling of photometric and centroid data can be constrained more precisely.

The methodology I developed could benefit the candidate investigation in the upcoming TESS mission. I will hence work on implementing my Bayesian modelling framework to identify hidden objects in the TESS planet candidates, enabling to characterise targets for follow-up.

When working on these models, I found that the analysis is limited by a simplified view of the RV data. In particular, the RV CCF profiles harbour a lot of important information which is linked to blend scenarios. This naturally led to the extension of my work and the analysis of NGTS-3Ab, as presented in Chapter 5 and summarised in the following Section 6.3.

6.3 Unmasking hidden systems through multi-colour photometry, centroiding and RV CCF analyses

NGTS-3Ab initially passed all vetting steps (including the absence of a centroid shift) as a hot Jupiter candidate orbiting a single, Sun-like star. It was hence scheduled for spectroscopic

follow-up with HARPS. However, the detection of a correlation between the bisector inverse slope (BIS) and the RV signal showed clear signs of a blend. This postulated that the blended object had to be part of an unresolved binary system. The systemic velocity between the two objects could not have been detected in the HARPS CCF if it were larger than ~ 7 km/s.

The proposed BLENDFITTER analysis in Chapter 5 requires a very detailed target-by-target modelling, somewhat going against the recent trend towards automated candidate verification (Section 1.6.2). Considering that these candidates have already passed all steps of the vetting and follow-up at this point, however, this is not a strong limitation to its usability. The BLENDFITTER analysis is mainly driven by the data itself, but also relies on different assumptions and approximations:

- **Gaussian model of the HARPS CCF profiles.** The profiles of both primary and secondary were modelled as a Gaussian function, and the total shape computed as their sum. While this is a simplification of the true shape, which is affected by variability in the stellar atmosphere, it is commonly considered a valid approximation (see e.g Santos et al., 2002) and used in the data reduction pipelines of major RV surveys (e.g. HARPS DRS 3.5).

- **Object separation and fibre acceptance.** As there was strong evidence for NGTS-3 being a binary system (from centroiding and HARPS CCF profiles), it was assumed that the light from both primary and secondary fully enter the HARPS fibre. In other scenarios, it might be possible that one of the stars lies slightly off the fibre, and hence only contributes marginally. In that case, the HARPS dilution could not be linked directly to the effective temperatures of the stars, but would additionally have to be a function of the distance and light entering the HARPS fibre.

- **Possibility of a multiple star system.** The presented analysis was limited to a hidden binary star system. It is not unlikely that NGTS-3 actually contains three or more stars. 33% of all known systems are binary stars, and 11% are triple or multiple-star systems (Raghavan et al., 2010). As there is no prior information on NGTS-3, it was

best to keep the model as simple as possible, and limit it to the scenario of a binary star system.

Usually, systems with BIS correlations get disregarded as false positives without further investigation. The example of NGTS-3Ab therefore raises caution that other planets might have been misclassified or erroneously disregarded. In different systems, the impact of a hidden secondary can mask brown dwarfs transiting the secondary as giant planets transiting the primary; most importantly, it can even mask the transit of potentially rocky bodies. Without a detailed modelling of multi-colour photometry, centroiding and RV CCF analyses, this system would have been identified as a hot Jupiter around a single star.

Considering these findings, it could be pivotal for upcoming surveys like TESS and PLATO to account for this in their candidate vetting and follow-up strategies. Employing sufficient instrument time for multi-colour photometry, enhancing the centroid vetting of the surveys, and analysing the RV CCF profiles of the spectrographic measurements could be crucial. Moreover, it could be an important effort to revise previously published planets with updated methodology, and gain additional observations where necessary. Resolving blend scenarios and correcting the classification of planets might impact our conclusions on the true exoplanet demography.

If the proposed analyses are conducted for each planet before publication, releasing large numbers of planets at once will not be feasible. On the other hand, while relying solely on automated vetting to verify planets can produce large numbers, it carries the high risks of misclassifying blended exoplanet systems. It might be beneficial to rename auto-vetted targets into 'prime candidates' (instead of bona-fide 'planets'). Through a stricter naming convention, these objects could be clearly distinguished from bona-fide planets that have their radii and masses thoroughly measured in an analysis based on multi-colour photometry, centroids and RV CCF profiles.

In the future, routine direct imaging follow-up of exoplanet systems might also be conducted, for example with a dedicated adaptive optics instrument. While costly, this could resolve multi-star systems, and retrieve constrains on the stellar types of stars A and B, and the projected separation between both.

6.4   The search for extraterrestrial life - a prospect

Over the past few years, the search for an Earth-analogue has been moving from observing Sun-like stars to a new target: M-dwarf stars. Many researchers nowadays believe that these are the most promising hosts for habitable exoplanets. Targeting these small and cool stars might accelerate our search for extraterrestrial life. M-stars are of highest interest as they constitute $\sim$73% of the stellar population (Dole, 1964) and their small radii and low temperatures favour the detection of habitable planets on short orbits and studies of their atmospheres (Kaltenegger & Traub, 2009). Recently, three exo-Earths have been detected in the habitable zones of the M-star TRAPPIST-1 (Gillon et al., 2017), and another one orbiting Proxima Centauri (Anglada-Escudé et al., 2016). Yet, the true habitability of these worlds currently remains unknown.

Importantly, M-stars undergo explosive eruptions ('flares'), capable of stripping off their planets' atmosphere and extinguishing existing biology (Seager, 2013) - but also of triggering prebiotic chemistry and initiating life in the first place (Airapetian et al., 2016; Björn et al., 2015). Laboratory experiments suggest that the UV radiation wavelength, intensity and timing have a significant impact on the potential to trigger prebiotic chemistry on exoplanets (Rimmer et al., submitted).

The TESS mission will observe an unprecedented number of M-stars. Manually analysing these candidates, as it used to be the case for ground-based surveys, will not be feasible anymore. *Kepler* already pointed the way towards the future: using state-of-the-art machine learning methods to analyse the high-precision data collected on millions of objects. Expertise in big data, machine learning and Bayesian statistics will be pivotal to analyse the incoming complex and challenging data sets. Automated vetting algorithms will generate an unprecedented list of prime targets for missions to follow up and further characterise these exo-solar systems. Soon, JWST, CHEOPS, the Extremely Large Telescopes and other high-precision missions will be able to follow up exoplanets and analyse their atmospheres in detail, advancing our search for potential biosignatures (e.g. water, oxygen, methane). Since these observations will be time-limited and very costly, it is crucial for such programmes

to prioritise a selection of the most promising targets, and ensure that findings are promptly shared among the exoplanet community.

To achieve the ambitious goal of finding habitable exoplanets, we will need to merge exoplanet and origin of life science. For this, the already multidisciplinary field of exoplanet research will soon require to strengthen collaborations between astrophysics, biophysics, chemistry, geology, computer science and statistics. Only an open, international and multi-disciplinary exchange of knowledge, supported by machine-learning data analysis, will truly enable a leap forwards in our understanding of the origin of life - on exoplanets and our own Earth.

What once was fiction, is already becoming reality.

References

ALMA Partnership et al., 2015, The Astrophysical Journal Letters, 808, L3

Agol E., Fabrycky D. C., 2017, Transit-Timing and Duration Variations for the Discovery and Characterization of Exoplanets. Springer International Publishing, Cham, pp 1–20, doi:10.1007/978-3-319-30648-3_7-1

Agol E., Steffen J., Sari R., Clarkson W., 2005, Monthly Notices of the Royal Astronomical Society, 359, 567

Airapetian V. S., et al., 2016, Nature Geoscience, 9, 452

Allard F., Hauschildt P. H., 1995, The Astrophysical Journal, 445, 433

Almenara J. M., et al., 2009, Astronomy and Astrophysics, 506, 337

Ambikasaran S., Foreman-Mackey D., Greengard L., Hogg D. W., O'Neil M., 2016, The Institute of Electrical and Electronics Engineers Transactions on Pattern Analysis and Machine Intelligence, 38, 252

Anderson D. R., et al., 2012, Monthly Notices of the Royal Astronomical Society, 422, 1988

Anglada-Escudé G., et al., 2016, Nature, 536, 437

Armitage P. J., 2017, Lecture notes on the formation and early evolution of planetary systems (arXiv:astro-ph/0701485)

Armstrong D., et al., 2013, Monthly Notices of the Royal Astronomical Society, 434, 3047

Armstrong D. J., Pollacco D., Santerne A., 2017, Monthly Notices of the Royal Astronomical Society, 465, 2634

Armstrong D. J., et al., 2018, Monthly Notices of the Royal Astronomical Society, p. sty1313

Baglin A., et al., 2002, in Battrick B., Favata F., Roxburgh I. W., Galadi D., eds, ESA Special Publication Vol. 485, Stellar Structure and Habitable Planet Finding. pp 17–24

Bakos G. Á., Lázár J., Papp I., Sári P., Green E. M., 2002, Publications of the Astronomical Society of the Pacific, 114, 974

Ballard S., et al., 2011, The Astrophysical Journal, 743, 200

Batalha N. M., Kepler Team 2012, in American Astronomical Society Meeting Abstracts #220. p. 306.01

Batalha N. M., et al., 2010, Astrophysical Journal Letters, 713, L103

Batalha N. M., et al., 2011, The Astrophysical Journal, 729, 27

Bate M. R., Lubow S. H., Ogilvie G. I., Miller K. A., 2003, Monthly Notices of the Royal Astronomical Society, 341, 213

Bayliss D., et al., 2018, Monthly Notices of the Royal Astronomical Society, 475, 4467

Beitz E., Güttler C., Blum J., Meisner T., Teiser J., Wurm G., 2011, The Astrophysical Journal, 736, 34

Bennett G. G., 1982, Journal of Navigation, 35, 255

Binnendijk L., 1974a, Vistas in Astronomy, 16, 61

Binnendijk L., 1974b, Vistas in Astronomy, 16, 85

Bishop C., 2006, Pattern Recognition and Machine Learning. Springer-Verlag New York

Bitsch B., Lambrechts M., Johansen A., 2015, Astronomy and Astrophysics, 582, A112

Björn L. O., et al., 2015, Role of Ultraviolet Radiation in the Origin of Life. Springer New York, pp 415–420

Boisse I., Bouchy F., Hébrard G., Bonfils X., Santos N., Vauclair S., 2011, Astronomy and Astrophysics, 528, A4

Borucki W. J., et al., 2010, Science, 327, 977

Boss A. P., et al., 2007, Transactions of the International Astronomical Union, Series A, 26, 183

Breiman L., 2001, Machine Learning, 45, 5

Broeg C., et al., 2013, in European Physical Journal Web of Conferences. p. 3005 (`arXiv:1305.2270`), doi:10.1051/epjconf/20134703005

Brooks S. P., Gelman A., 1998, Journal of Computational and Graphical Statistics, 7, 434

Brown T. M., 2003, Astrophysical Journal Letters, 593, L125

Brown T. M., Latham D. W., 2008, preprint, (`arXiv:0812.1305`)

Brown T. M., Latham D. W., Everett M. E., Esquerdo G. A., 2011, The Astronomical Journal, 142, 112

Brown D. J. A., et al., 2012, Monthly Notices of the Royal Astronomical Society, 423, 1503

Bryson S. T., et al., 2013, Publications of the Astronomical Society of the Pacific, 125, 889

Burke C. J., et al., 2015, The Astrophysical Journal, 809, 8

Burrows A. S., 2014, Nature, 513, 345

Buser R., Kurucz R., 1978, Astronomy and Astrophysics, 70

C. D. Murray A. C. M. C., 2011, Keplerian Orbits and Dynamics of Exoplanets. In S. Seager (Ed.) *Exoplanets*. University of Arizona Press

Cameron A. C., 2012, Nature, 492, 48

Campbell B., Walker G. A. H., Yang S., 1988, The Astrophysical Journal, 331, 902

Chambers J., 2007, in AAS/Division of Dynamical Astronomy Meeting #38. p. #06.04

Chambers J., 2011, Terrestrial Planet Formation. In S. Seager (Ed.) *Exoplanets*. University of Arizona Press

Charbonneau D., Brown T. M., Latham D. W., Mayor M., 2000, Astrophysical Journal Letters, 529, L45

Charbonneau D., Brown T. M., Noyes R. W., Gilliland R. L., 2002, The Astrophysical Journal, 568, 377

Charbonneau D., et al., 2005, The Astrophysical Journal, 626, 523

Chazelas B., et al., 2012, in Society of Photo-Optical Instrumentation Engineers (SPIE) Conference Series. p. 0, doi:10.1117/12.925755

Claret A., 2000, Astronomy and Astrophysics, 363, 1081

Claret A., Hauschildt P. H., 2003, Astronomy and Astrophysics, 412, 241

Claret A., Hauschildt P. H., Witte S., 2012, Astronomy and Astrophysics, 546, A14

Claret A., Hauschildt P. H., Witte S., 2013, Astronomy and Astrophysics, 552, A16

Collier Cameron A., et al., 2006, Monthly Notices of the Royal Astronomical Society, 373, 799

Coughlin J. L., et al., 2016, The Astrophysical Journal Supplement, 224, 12

Crossfield I. J. M., et al., 2014, Nature, 505, 654

Cumming A., Butler R. P., Marcy G. W., Vogt S. S., Wright J. T., Fischer D. A., 2008, Publications of the Astronomical Society of the Pacific, 120, 531

Deacon N. R., et al., 2016, Monthly Notices of the Royal Astronomical Society, 455, 4212

Deming D., Seager S., Richardson L. J., Harrington J., 2005, Nature, 434, 740

Diaz-Cordoves J., Gimenez A., 1992, Astronomy and Astrophysics, 259, 227

Díaz R. F., Almenara J. M., Santerne A., Moutou C., Lethuillier A., Deleuil M., 2014, Monthly Notices of the Royal Astronomical Society, 441, 983

Dole S., 1964, Habitable planets for man. Blaisdell book in the pure and applied sciences, Blaisdell Pub. Co.

Doyle L. R., et al., 2011, Science, 333, 1602

Doyle A. P., et al., 2013, Monthly Notices of the Royal Astronomical Society, 428, 3164

Doyle A. P., Davies G. R., Smalley B., Chaplin W. J., Elsworth Y., 2014, Monthly Notices of the Royal Astronomical Society, 444, 3592

Dravins D., Lindegren L., Nordlund A., 1981, Astronomy and Astrophysics, 96, 345

Dravins D., Lindegren L., Mezey E., Young A. T., 1998, Publications of the Astronomical Society of the Pacific, 110, 610

Dressing C. D., Charbonneau D., 2015, The Astrophysical Journal, 807, 45

Duchêne G., Kraus A., 2013, Annual Review of Astronomy and Astrophysics, 51, 269

Duquennoy A., Mayor M., 1991, Astronomy and Astrophysics, 248, 485

Duvenaud D. K., 2014, PhD thesis, University of Cambridge

ESO 2011, Technical Report 3P6-MAN-ESO-90100-0005, HARPS User Manual 2.1. ESO

Ehrenreich D., et al., 2015, Nature, 522, 459

Espinoza N., Jordán A., 2015, Monthly Notices of the Royal Astronomical Society, 450, 1879

Etzel P. B., 1981, in Carling E. B., Kopal Z., eds, Photometric and Spectroscopic Binary Systems. p. 111

Fabrycky D., Tremaine S., 2007, The Astrophysical Journal, 669, 1298

Feroz F., Hobson M. P., Bridges M., 2009, Monthly Notices of the Royal Astronomical Society, 398, 1601

Fischer D. A., Marcy G. W., 1992, The Astrophysical Journal, 396, 178

Fisher R. A., 1921, Metron, 1, 3

Foreman-Mackey D., 2016, The Journal of Open Source Software, 24

Foreman-Mackey D., Hogg D. W., Lang D., Goodman J., 2013, Publications of the Astronomical Society of the Pacific, 125, 306

Fortney J., Baraffe I., Militzer B., 2011, Giant Planet Interior Structure and Thermal Evolution. In S. Seager (Ed.) *Exoplanets*. University of Arizona Press

Fressin F., et al., 2013, The Astrophysical Journal, 766, 81

Fulton B. J., et al., 2017, The Astronomical Journal, 154, 109

Gaia Collaboration et al., 2016a, Astronomy and Astrophysics, 595, A1

Gaia Collaboration et al., 2016b, Astronomy and Astrophysics, 595, A2

Gaia Collaboration Brown A. G. A., Vallenari A., Prusti T., de Bruijne J. H. J., Babusiaux C., Bailer-Jones C. A. L., 2018, preprint, (arXiv:1804.09365)

Gaidos E., Mann A. W., Kraus A. L., Ireland M., 2016, Monthly Notices of the Royal Astronomical Society, 457, 2877

Gardner J., et al., 2006, Space Science Reviews, 123, 485

Gaudi S. B., 2011, Exoplanetary Microlensing. In S. Seager (Ed.) *Exoplanets*. University of Arizona Press

Gelman A., Rubin D. B., 1992, Statistical Science, 7, 457

Geman S., Geman D., 1984, IEEE Transactions on Pattern Analysis and Machine Intelligence, PAMI-6, 721

Gillen E., Hillenbrand L. A., David T. J., Aigrain S., Rebull L., Stauffer J., Cody A. M., Queloz D., 2017, The Astrophysical Journal, 849, 11

Gilliland R. L., et al., 2011, The Astrophysical Journal Supplement, 197, 6

Gillon M., et al., 2012, Astronomy and Astrophysics, 542, A4

Gillon M., et al., 2013, Astronomy and Astrophysics, 552, A82

Gillon M., et al., 2017, Nature, 542, 456

Gilmore G., et al., 2012, The Messenger, 147, 25

Girardi L., Groenewegen M. A. T., Hatziminaoglou E., da Costa L., 2005, Astronomy and Astrophysics, 436, 895

Goodman J., Weare J., 2010, Communications in Applied Mathematics and Computational Science, Vol.~5, No.~1, p.~65-80, 2010, 5, 65

Gould A., et al., 2014, Science, 345, 46

Gray D. F., 1989, Publications of the Astronomical Society of the Pacific, 101, 832

Grether D., Lineweaver C. H., 2006, The Astrophysical Journal, 640, 1051

Günther M. N., Queloz D., Demory B.-O., Bouchy F., 2017a, Monthly Notices of the Royal Astronomical Society, 465, 3379

Günther M. N., et al., 2017b, Monthly Notices of the Royal Astronomical Society, 472, 295

Günther M. N., et al., 2018, Monthly Notices of the Royal Astronomical Society, p. sty1193

Hall R. D., Thompson S. J., Handley W., Queloz D., 2018, Monthly Notices of the Royal Astronomical Society, p. 1405

Handley W. J., Hobson M. P., Lasenby A. N., 2015, Monthly Notices of the Royal Astronomical Society, 453, 4384

Hartman J. D., Bakos G. Á., Torres G., 2011, in European Physical Journal Web of Conferences. p. 2002 (`arXiv:1011.5659`), doi:10.1051/epjconf/20101102002

Hartman J. D., et al., 2015, The Astronomical Journal, 149, 166

Hastings W. K., 1970, Biometrika, 57, 97

Hatzes A. P., Cochran W. D., Endl M., McArthur B., Paulson D. B., Walker G. A. H., Campbell B., Yang S., 2003, The Astrophysical Journal, 599, 1383

Haywood R. D., et al., 2016, Monthly Notices of the Royal Astronomical Society, 457, 3637

Henden A., Munari U., 2014, Contributions of the Astronomical Observatory Skalnate Pleso, 43, 518

Henry G. W., Marcy G. W., Butler R. P., Vogt S. S., 2000, Astrophysical Journal Letters, 529, L41

Hilditch R. W., 2001, An Introduction to Close Binary Stars. Cambridge University Press

Holczer T., et al., 2016, The Astrophysical Journal Supplement, 225, 9

Holman M. J., Murray N. W., 2005, Science, 307, 1288

Holman M. J., Wiegert P. A., 1999, The Astronomical Journal, 117, 621

Hunter J. D., 2007, Computing in Science & Engineering, 9, 90

Husser T.-O., Wende-von Berg S., Dreizler S., Homeier D., Reiners A., Barman T., Hauschildt P. H., 2013, Astronomy and Astrophysics, 553, A6

Irwin M. J., et al., 2004, in Quinn P. J., Bridger A., eds, Proc. SPIE Vol. 5493, Optimizing Scientific Return for Astronomy through Information Technologies. pp 411–422, doi:10.1117/12.551449

Irwin J. M., et al., 2011, The Astrophysical Journal, 742, 123

Johnson J. A., et al., 2012, The Astronomical Journal, 143, 111

Jones E., Oliphant T., Peterson P., et al., 2001, SciPy: Open source scientific tools for Python, http://www.scipy.org/

Kaltenegger L., Traub W. A., 2009, The Astrophysical Journal, 698, 519

Kley W., Nelson R. P., 2012, Annual Review of Astronomy and Astrophysics, 50, 211

Klinglesmith D. A., Sobieski S., 1970, The Astronomical Journal, 75, 175

Koch D. G., et al., 2010, The Astrophysical Journal Letters, 713, L79

Kohonen T., 1982, Biological Cybernetics, 43, 59

Kopal Z., 1950, Harvard College Observatory Circular, 454, 1

Kovács G., Zucker S., Mazeh T., 2002, Astronomy and Astrophysics, 391, 369

Kreidberg L., 2015, Publications of the Astronomical Society of the Pacific, 127, 1161

Kurucz R., 1993

Lambrechts M., Johansen A., 2012, Astronomy and Astrophysics, 544, A32

Latham D. W., et al., 2009, The Astrophysical Journal, 704, 1107

Laughlin G., Bodenheimer P., Adams F. C., 2004, The Astrophysical Journal Letters, 612, L73

Léger A., et al., 2009, Astronomy and Astrophysics, 506, 287

Lendl M., Gillon M., Queloz D., Alonso R., Fumel A., Jehin E., Naef D., 2013, Astronomy and Astrophysics, 552, A2

Lin D. N. C., Bodenheimer P., Richardson D. C., 1996, Nature, 380, 606

Lovis C., Fischer D., 2011, Radial Velocity Techniques for Exoplanets. In S. Seager (Ed.) *Exoplanets*. University of Arizona Press

Lucy L. B., 1967, Zeitschrift für Astrophysik, 65, 89

MacKay D. ., 2003, Information Theory, Inference, and Learning Algorithms. Cambridge University Press

Mandel K., Agol E., 2002, The Astrophysical Journal Letters, 580, L171

Martin D. V., Mazeh T., Fabrycky D. C., 2015, Monthly Notices of the Royal Astronomical Society, 453, 3554

Mayor M., Queloz D., 1995, Nature, 378, 355

Mayor M., et al., 2003, The Messenger, 114, 20

Mayor M., et al., 2011, preprint, (arXiv:1109.2497)

Mazeh T., 2008, in Goupil M.-J., Zahn J.-P., eds, EAS Publications Series Vol. 29, EAS Publications Series. pp 1–65 (arXiv:0801.0134), doi:10.1051/eas:0829001

McCormac J., Pollacco D., Skillen I., Faedi F., Todd I., Watson C. A., 2013, Publications of the Astronomical Society of the Pacific, 125, 548

McCormac J., et al., 2017, Publications of the Astronomical Society of the Pacific, 129, 025002

McKinney W., 2010, in van der Walt S., Millman J., eds, Proceedings of the 9th Python in Science Conference. pp 51 – 56

Métrailler L., 2016, Master's thesis, Ecole Polytechnique Federale de Lausanne

Metropolis N., Rosenbluth A. W., Rosenbluth M. N., Teller A. H., Teller E., 1953, The Journal of Chemical Physics, 21, 1087

Milne E. A., 1926, Monthly Notices of the Royal Astronomical Society, 87, 43

Morbidelli A., Raymond S. N., 2016, Journal of Geophysical Research: Planets, 121, 1962

Morton T. D., 2012, The Astrophysical Journal, 761, 6

Morton T. D., 2015, VESPA: False positive probabilities calculator, Astrophysics Source Code Library (ascl:1503.011)

Morton T. D., Bryson S. T., Coughlin J. L., Rowe J. F., Ravichandran G., Petigura E. A., Haas M. R., Batalha N. M., 2016, The Astrophysical Journal, 822, 86

Muñoz D. J., Lai D., 2015, Proceedings of the National Academy of Science, 112, 9264

Murphy K. P., 2012, Machine Learning: A Probabilistic Perspective. The MIT Press

Nelson R. P., Papaloizou J. C. B., Masset F., Kley W., 2000, Monthly Notices of the Royal Astronomical Society, 318, 18

Neveu-VanMalle M., et al., 2014, Astronomy and Astrophysics, 572, A49

Norton A. J., et al., 2011, Astronomy and Astrophysics, 528, A90

Nutzman P., Charbonneau D., 2008, Publications of the Astronomical Society of the Pacific, 120, 317

Ormel C. W., Klahr H. H., 2010, Astronomy and Astrophysics, 520, A43

Owen J. E., Wu Y., 2017, The Astrophysical Journal, 847, 29

Parmentier V., Crossfield I. J. M., 2017, Exoplanet Phase Curves: Observations and Theory. Springer International Publishing, Cham, pp 1–22, doi:10.1007/978-3-319-30648-3_116-1

Pecaut M. J., Mamajek E. E., 2013, The Astrophysical Journal Supplement, 208, 9

Pepe F., et al., 2014, preprint, (arXiv:1401.5918)

Pepper J., et al., 2017, The Astronomical Journal, 153, 177

Perryman M., 2011, The Exoplanet Handbook

Pessah M., Gressel O., eds, 2017, Formation, Evolution, and Dynamics of Young Solar Systems. Springer International Publishing

Petigura E. A., et al., 2018, The Astronomical Journal, 155, 89

Piazzi G., 1801, Risultati delle osservazioni della nuova stella scoperta il di' 1. Gennaio all'Osservatorio Reale di Palermo, doi:10.3931/e-rara-8730.

Pickles A. J., 1998, Publications of the Astronomical Society of the Pacific, 110, 863

Plavchan P., Bilinski C., 2013, The Astrophysical Journal, 769, 86

Pollacco D. L., et al., 2006, Publications of the Astronomical Society of the Pacific, 118, 1407

Pont F., Zucker S., Queloz D., 2006, Monthly Notices of the Royal Astronomical Society, 373, 231

Popper D. M., Etzel P. B., 1981, The Astronomical Journal, 86, 102

Queloz D., et al., 2000, Astronomy and Astrophysics, 354, 99

Queloz D., et al., 2001a, The Messenger, 105, 1

Queloz D., et al., 2001b, Astronomy and Astrophysics, 379, 279

Queloz D., et al., 2009, Astronomy and Astrophysics, 506, 303

Quintana E. V., et al., 2014, Science, 344, 277

Raghavan D., et al., 2010, The Astrophysical Journal, 190, 1

Randich S., Gilmore G., Gaia-ESO Consortium 2013, The Messenger, 154, 47

Rasmussen C. E., Williams C. K. I., 2005, Gaussian Processes for Machine Learning (Adaptive Computation and Machine Learning). The MIT Press

Rauer H., et al., 2014, Experimental Astronomy, 38, 249

Ricker G. R., et al., 2014, in Society of Photo-Optical Instrumentation Engineers (SPIE) Conference Series. p. 20 (`arXiv:1406.0151`), doi:10.1117/12.2063489

Roberts S., Osborne M., Ebden M., Reece S., Gibson N., Aigrain S., 2013, Philosophical Transactions of the Royal Society of London A: Mathematical, Physical and Engineering Sciences, 371

Rogers L. A., 2015, The Astrophysical Journal, 801, 41

Rossum G., 1995, Technical report, Python Reference Manual. Amsterdam, The Netherlands, The Netherlands

STScI Development Team 2013, pysynphot: Synthetic photometry software package, Astrophysics Source Code Library (ascl:1303.023)

Santerne A., et al., 2012, Astronomy and Astrophysics, 545, A76

Santerne A., et al., 2015, Monthly Notices of the Royal Astronomical Society, 451, 2337

Santerne A., et al., 2016, Astronomy and Astrophysics, 587, A64

Santos N. C., et al., 2002, Astronomy and Astrophysics, 392, 215

Schlaufman K. C., 2018, The Astrophysical Journal, 853, 37

Schneider J., Dedieu C., Le Sidaner P., Savalle R., Zolotukhin I., 2011, Astronomy and Astrophysics, 532, A79

Schwarz G., 1978, The Annals of Statistics, 6, 461

Schwarz R., Funk B., Zechner R., Bazsó Á., 2016, Monthly Notices of the Royal Astronomical Society, 460, 3598

Schwarzschild K., Villiger W., 1906, The Astrophysical Journal, 23, 284

Seager S., 2013, Science, 340, 577

Seager S., Sasselov D. D., 2000, The Astrophysical Journal, 537, 916

Seager S., Kuchner M., Hier-Majumder C. A., Militzer B., 2007, The Astrophysical Journal, 669, 1279

Seager S., Bains W., Petkowski J. J., 2016, Astrobiology, 16, 465

Sekiguchi M., Fukugita M., 2000, The Astronomical Journal, 120, 1072

Shallue C. J., Vanderburg A., 2018, The Astronomical Journal, 155, 94

Sing D. K., 2010, Astronomy and Astrophysics, 510, A21

Sing D. K., et al., 2016, Nature, 529, 59

Skilling J., 2004, in Fischer R., Preuss R., Toussaint U. V., eds, American Institute of Physics Conference Series Vol. 735, American Institute of Physics Conference Series. pp 395–405, doi:10.1063/1.1835238

Skrutskie M. F., et al., 2006, The Astronomical Journal, 131, 1163

Slawson R. W., et al., 2011, The Astronomical Journal, 142, 160

Soszyński I., et al., 2015, Acta Astronomica, 65, 39

Sousa S. G., et al., 2008, Astronomy and Astrophysics, 487, 373

Southworth J., Maxted P. F. L., Smalley B., 2004a, Monthly Notices of the Royal Astronomical Society, 351, 1277

Southworth J., Zucker S., Maxted P. F. L., Smalley B., 2004b, Monthly Notices of the Royal Astronomical Society, 355, 986

Southworth J., Wheatley P. J., Sams G., 2007, Monthly Notices of the Royal Astronomical Society, 379, L11

Stetson P. B., 1987, Publications of the Astronomical Society of the Pacific, 99, 191

Storn R., Price K., 1997, Journal of Global Optimization, 11, 341

Sullivan P. W., et al., 2015, The Astrophysical Journal, 809, 77

Tamuz O., Mazeh T., Zucker S., 2005, Monthly Notices of the Royal Astronomical Society, 356, 1466

Tokovinin A., Kiyaeva O., 2016, Monthly Notices of the Royal Astronomical Society, 456, 2070

Toner C. G., Gray D. F., 1988, The Astrophysical Journal, 334, 1008

Torres G., Konacki M., Sasselov D. D., Jha S., 2004, The Astrophysical Journal, 614, 979

Torres G., Andersen J., Giménez A., 2010, Astronomy and Astrophysics Reviews, 18, 67

Torres G., et al., 2011, The Astrophysical Journal, 727, 24

Torres G., et al., 2015, The Astrophysical Journal, 800, 99

Traub W. A., Oppenheimer B. R., 2011, Direct Imaging of Exoplanets. In S. Seager (Ed.) *Exoplanets*. University of Arizona Press

Triaud A. H. M. J., et al., 2010, Astronomy and Astrophysics, 524, A25

Udalski A., Zebrun K., Szymanski M., Kubiak M., Soszynski I., Szewczyk O., Wyrzykowski L., Pietrzynski G., 2002, Acta Astronomica, 52, 115

Vanderburg A., et al., 2015, Nature, 526, 546

Vidal-Madjar A., Lecavelier des Etangs A., Désert J.-M., Ballester G. E., Ferlet R., Hébrard G., Mayor M., 2003, Nature, 422, 143

Wakeford H. R., et al., 2018, The Astronomical Journal, 155, 29

Walker S., 2013, PhD thesis, University of Warwick

Ward W. R., 1997, Icarus, 126, 261

Ward-Duong K., et al., 2015, Monthly Notices of the Royal Astronomical Society, 449, 2618

Weinberg M. D., 2010, Astronomy Department Faculty Publication Series

Weiss L. M., Marcy G. W., 2014, Astrophysical Journal Letters, 783, L6

Wheatley P. J., et al., 2013, in European Physical Journal Web of Conferences. p. 13002 (arXiv:1302.6592), doi:10.1051/epjconf/20134713002

Wheatley P. J., et al., 2018, Monthly Notices of the Royal Astronomical Society, 475, 4476

Winn J. N., 2011, Exoplanet Transits and Occultations. In S. Seager (Ed.) *Exoplanets*. University of Arizona Press

Winn J. N., 2018, preprint, (arXiv:1801.08543)

Wolszczan A., Frail D. A., 1992, Nature, 355, 145

Wright J. T., 2017, Radial Velocities as an Exoplanet Discovery Method. Springer International Publishing, Cham, pp 1–13, doi:10.1007/978-3-319-30648-3_4-1

Wright E. L., et al., 2010, The Astronomical Journal, 140, 1868

Wright J. T., et al., 2011, Publications of the Astronomical Society of the Pacific, 123, 412

Zacharias N., Finch C., Frouard J., 2017, The Astronomical Journal, 153, 166

de Wit J., Seager S., 2013, Science, 342, 1473

van der Walt S., Colbert S. C., Varoquaux G., 2011, Computing in Science & Engineering, 13, 22

Appendix A

Input file for the NGTS yield simulation

```
##############################################################################################################
# Target list criteria
##############################################################################################################
15.            #MagV_target = 15.                      #upper limit on MagV for target stars
22.5           #magV_limit = 22.5                      #upper limit on MagV for background stars
2.             #Rs_limit = 2.                          #upper limit on stellar radius of target stars (in Rsun)
10000.         #Teff_limit = 10000.                    #upper limit on effective temperature of target stars (in K)
6.5            #logg_limit = 6.5                       #upper limit on logg of target stars
##############################################################################################################
# CCD resolution
##############################################################################################################
50331648.      #pixel_number = 12. * 2048.**2          #number of pixels in total; 12 cameras with 2048^2 pixel
4194304.       #pixel_per_ccd = 2048*2048              #number of pixels per CCD; 1 camera with 2048^2 pixel
##############################################################################################################
# Observing strategy
##############################################################################################################
88.8           #FoV = 12. * 7.4.                       #FoV that is observed (in sq.deg.)
122.           #FoV_duration = 365./3.                 #time spent per FoV (in days)
12.            #N_FoVs = 4.*3.                         #number of FoVs surveyed in total (4 years * 3 fields per year)
7.             #hours_per_night = 7.                   #average number of hours observed per night
##############################################################################################################
# Instrument parameters, noise, aperture
##############################################################################################################
10.            #exposure = 10.                         #exposure (in s)
1.49           #readout = 1.49                         #CCD readout time (in s)
0.2            #D_tel = 0.2                            #telescope aperture (in m)
1.5            #airmass = 1.5                          #average airmass
2400.          #h_tel = 2400.                          #height of the telescope above sea level (in m)
125.           #noise_sky = 125.                       #sky noise (in e- per s per pixel)
0.06           #noise_dark = 0.06                      #dark noise (in e- per s per pixel)
10.            #noise_readout = 10.                    #readout noise (in e- per pixel)
28.2743338823  #N_apert_pixel = np.pi*(3.**2.)         #number of pixels in aperture (in average)
##############################################################################################################
# Detection criteria
##############################################################################################################
5.             #detection_threshold = 5.               #detection threshold DT (planet detected if signal-to-noise > DT)
0.001          #red_noise = 1./1000.                   #as fraction (1/1000 ~ 1 mmag)
3.             #num_transits_threshold = 3.            #minimum number of visible transits required for detection
```